Forschungszentrum Jülich
in der Helmholtz-Gemeinschaft

Institut für Sicherheitsforschung und Reaktortechnik

Properties of ATR-2E Graphite and Property Changes due to Fast Neutron Irradiation

Gerd Haag

Jül-4183

Properties of ATR-2E Graphite and Property Changes due to Fast Neutron Irradiation

Gerd Haag

Berichte des Forschungszentrums Jülich ; 4183
ISSN 0944-2952
Institut für Sicherheitsforschung und Reaktortechnik Jül-4183

Zu beziehen durch: Forschungszentrum Jülich GmbH · Zentralbibliothek
D-52425 Jülich · Bundesrepublik Deutschland
☎ 02461 61-5220 · Telefax: 02461 61-6103 · e-mail: zb-publikation@fz-juelich.de

Eigenschaften der Graphitsorte ATR-2E und die Veränderung ihrer Eigenschaften bei Bestrahlung mit schnellen Neutronen

Kurzfassung

Die Graphitsorte ATR-2E wurde als Referenzmaterial für künftige Hochtemperatur-Reaktoren (HTR) von der damaligen Firma Sigri Elektrographit GmbH im Rahmen des vormaligen F+E-Programms „HTR mit kugelförmigen Brennelementen“ entwickelt und von der Kernforschungsanlage Jülich GmbH in den Jahren 1975 bis 1990 eingehend untersucht und in zahlreichen Bestrahlungsexperimenten bis zu sehr hohen schnellen Neutronenfluenzen bestrahlt. Die Untersuchungen erstreckten sich insbesondere auf die physikalischen Eigenschaften Rohdichte, dynamischer Elastizitätsmodul, thermischer Ausdehnungskoeffizient, elektrische Leitfähigkeit und Wärmeleitfähigkeit, auf die Veränderung der Abmessungen der bestrahlten Probekörper sowie auf das durch die Bestrahlung mit schnellen Neutronen unter mechanischer Belastung hervorgerufene Kriechen. Der Bericht enthält nicht nur eine phänomenologische Beschreibung des Bestrahlungsverhaltens von ATR-2E Graphit, er liefert auch alle Zahlenangaben, die derzeit verfügbar sind.

Properties of ATR-2E Graphite and Property Changes due to Fast Neutron Irradiation

Abstract

The graphite grade ATR-2E was developed as a reference material for future High-Temperature Reactors (HTR) in the framework of Germany‘s former R&D Programme „HTR with Spherical Fuel Elements“ by the former company Sigri Elektrographit GmbH. From 1975 to about 1990, the former Kernforschungsanlage Jülich GmbH investigated and tested this graphite in detail including numerous irradiation experiments up to very high fast neutron fluences. The investigations involved in particular the physical properties of apparent density, dynamic Young’s modulus, thermal expansivity, electrical resistivity, and thermal conductivity, the linear dimensional changes, and fast neutron-irradiation-induced creep under mechanical load. The report is not only a phenomenological description of the irradiation behaviour of ATR-2E graphite, but also presents all numerical data available at present.

Contents

Figures

Tables

1. INTRODUCTION

After the year 2000, when new High-Temperature Reactor (HTR) projects were discussed seriously in several countries, the availability of appropriate moderator graphite turned out to be a major problem. Numerous isotropic and near-isotropic graphites had been developed and tested 20 to 40 years ago, but none of them was still on the market when development work on the high-temperature reactor was resumed after a break of about 10 years.

All efforts to cope with this difficulty are based on knowledge and experience still existing from earlier research. However, for reasons of age, many excellent specialists are no longer involved in the new development programmes. Therefore it is all the more important to conserve existing information.

This report presents some findings from the history of graphite as a reactor material which induced the carbon industry to develop isotropic polycrystalline graphite as needed for high-temperature gas-cooled reactors. It took a considerable time until it became clear that only isotropic graphite would meet the needs of modern graphite-moderated nuclear reactors. Because of the fundamental anisotropy of its crystallographic structure (see section 5.1) it was not at all obvious that the manufacturing of chemically pure, highly graphitised, and nevertheless isotropic graphite could be feasible. Finally, the German company Sigri Elektrographit GmbH (later SGL Carbon) succeeded in producing the extruded pitch-coke-based graphite ATR-2E, which from 1975 to about 1990 was extensively tested in numerous irradiation experiments in different material test reactors in order to prove its ability to serve as a moderator as well as a reflector material in gas-cooled power reactors.

Now, many years later when ATR-2E graphite can no longer be produced since the special pitch coke it was made from is no longer available, ATR-2E serves as a model for new nuclear graphites to be used in nuclear reactor designs in the near future. Its data – as-manufactured as well as after irradiation with fast neutrons to extremely high fluences – may still be used as design data until irradiation data for modern nuclear graphites are available. Therefore, the existing data on ATR-2E graphite and the changes of its physical properties due to fast neutron irradiation are published in this report as far as they are still known.

1.1 Early Graphites in Nuclear Reactor Technology

In 1942, Enrico Fermi decided to use graphite as the moderator when he made his first attempt to produce a self-sustaining nuclear chain reaction. Graphite was the only suitable material available in the USA at that time. Earlier they had built a first experimental pile which was an 8-ft cube assembled from graphite blocks and containing about seven tons of uranium oxide in iron containers. By that time, the multiplication factor k_∞ for an infinite lattice of this type was estimated to be only about 0.87. However, it was assumed that this value could be increased – maybe even above 1 – using purer graphite and fuel, and hence purity was the most important property of nuclear graphite at that early stage.

The next pile was constructed from AGX graphite, a product from the National Carbon Company made of petroleum coke and coal-tar pitch, and graphitised by the Acheson process yielding $k_\infty = 0.944$. It was estimated that $k_\infty > 1$ could be realised with highly purified graphite and uranium oxide if the air were removed to reduce neutron absorption by nitrogen. Finally, on December 2nd, 1942, the first nuclear chain reaction was produced in the CP-1 (Chicago Pile 1), which was a major step towards the utilisation of nuclear power in general and towards graphite-moderated reactors in particular.

Similar work had been undertaken in the USSR leading to findings similar to those in the USA. In particular, the negative temperature coefficient of reactivity was found, which became a major argument in favour of graphite-moderated reactors. Unlike the promising results in the US and in the USSR, German investigators came to the conclusion that graphite could not be used with natural uranium to produce a nuclear chain reaction. The purest graphite available to them at that time was a product from the Siemens Plania company, which exhibited a neutron absorption cross section of about 7.5 mb. Compared to that the graphites used in CP-1 exhibited average thermal absorption cross sections of 6.68 mb (AGX, National Carbon Company), 5.51 mb (Speer Carbon Company), and 4.97 mb (AGOT, National Carbon Company) [1].

Already in December 1942, Eugene P. Wigner first called attention to the effects of fast particles on solids. It was suggested that neutrons from fission would displace atoms from their lattice sites by momentum transfer with effects on most of the properties of graphite, which has become known as the Wigner Effect. The possibility was even suggested that graphite bars might fuse together as valence bonds at the surface of the bars are opened and closed again [2], and during operation of a reactor enough energy would be deposited in the graphite to open all the chemical bonds several times. Even the possibility that the graphite parts might very quickly break into small pieces could not be ruled out. However, the first power-producing reactors

(X-10 Reactor and Hanford Reactor) had to be built without such knowledge. Cyclotrons, which were the only fast-neutron sources available, would need several months of irradiation to produce damaging effects equivalent to one day in a Hanford reactor.

This was the starting point for large-scale research programmes to investigate the property changes due to fast particle radiation and to predict their influence on the safety and the lifetime of graphite reactors to be built. Influences of fast neutron radiation on strength, electrical and thermal conductivity, thermal expansivity, dimensional stability, on the storage of internal energy (Wigner energy) and on many other properties have been observed many times and in many countries after the first results emerged from the X-10 reactor in 1944.

It will be demonstrated in later chapters of this report that, although catastrophic behaviour such as fusion or crumbling of graphite pieces, has never occurred, large changes in many properties do result from fast neutron irradiation which need to be taken into account when graphite components of nuclear reactors are designed. Although not all effects are well understood yet, more than 100 graphite reactors have successfully been operated during the last 60 years. A few severe accidents in graphite reactors can in no case be attributed to a lack of knowledge or insufficient properties of the graphite in use.

1.2 Graphite Grades for the First Gas-cooled Power Reactors

Even if the old graphite grades from the 1950s and early 1960s are no longer available on the market to be used in today's nuclear reactor projects, some of them will be briefly discussed to show how much progress in nuclear graphite manufacturing has been made during the last 40 years. It has already been mentioned that for a long time chemical purity was the most important property of reactor graphite when enriched fuel was not available at reasonable cost.

In Europe, a long series of graphite-moderated reactors began in 1956 with the Calder Hall reactors in the UK. This type of reactor (Magnox) was fuelled with U_{nat} and used CO_2 as a cooling gas. Its moderator is PGA graphite (Table 1), an anisotropic (CTE_{perp}/CTE_{par} = 1.95), medium density (1.65 ... 1.75 g/cm^3), extruded petroleum coke graphite manufactured by BAEL (British Acheson Electrodes, Ltd.) and AGL (Anglo Great Lakes). The best way to demonstrate the influence of anisotropy on the behaviour under fast neutron irradiation is to plot the irradiation induced dimensional changes parallel and perpendicular to the extruding direction, as shown in Fig. 1a and Fig. 1b at temperatures 150°C to 250°C. In the direction perpendicular to extrusion, length changes increase continuously with increasing fluence (number of neutrons

per cm^2 with a particular energy distribution). Carbon atoms are knocked from their normal position in the graphite lattice, come to rest in the interlayer space, and cause the graphite crystallites to expand in the direction of the hexagonal axes, whereas parallel to the layer planes the crystallites shrink, as can be seen from Fig. 1b (see also chapter 5). Increasing the ambient temperature increases the mobility of the interstitial carbon atoms so that annealing processes become more and more likely. Therefore, in the direction of the hexagonal axes the expansion effect decreases with increasing temperature, and parallel to the basal planes the dimensional changes due to irradiation decrease with increasing temperature, too.

The next set of diagrams (Fig. 2a and 2b) shows irradiation-induced dimensional changes of PGA graphite at higher temperatures from 300°C to 650°C. Perpendicular to extrusion (Fig. 2a), the influence of expansion in the c-direction still decreases with increasing irradiation temperature until (around 400 to 500°C) a new mechanism appears. Now, the vacancies (within the basal planes) also gain mobility and migrate to the crystallite boundaries where they simply disappear. As a consequence, the annealing rate decreases and, in addition, the increased mobility of the interstitial atoms leads to the formation of interstitial clusters which can no longer be annealed. The result is a decreased shrinkage (or an increased tendency towards expansion) at 650°C in both crystallographic directions (Fig. 2a and b).

Table 1 Properties of early anisotropic reactor graphites

Graphite Grade	**Manufacturer**	**Forming Method**	**Thermal Expansivity** (10^{-6}/K)		**Thermal Conductivity** (W/m K)		**Young's Modulus** (GPa)	
			parallel	*perpend.*	*parallel*	*perpend.*	*parallel*	*perpend.*
PGA	BAEL	Extruding	0.9	3.0	164	105	10.9	5.4
TSX	NCC	Extruding	1.2	3.7			12.5	5.3
CSF	NCC	Extruding	1.2	3.1	155	97	8.0	4.8
TSGBF	NCC	Extruding	2.6	3.8			10.9	5.9

(Data are mean values of pre-irradiation properties of a random set of irradiation specimens; 'perpendicular' and 'parallel' refer to the pressing direction.)

TSX graphite (Table 1) is another example of nuclear graphite in use in the early developmental stages of graphite power reactors. It was manufactured by the National Carbon Company, USA, from a fine-grain petroleum needle coke. Its high purity ($\sigma \approx 3.8$ mb [3]) was achieved by graphitisation at 3000°C, and its anisotropy factor $CTE_{perp}/CTE_{par} > 3$ [4]. Nevertheless, it was used as the moderator and reflector in the Hanford N Reactor, which went into operation in 1961. This enormous anisotropy is reflected by the dimensional changes shown in Fig. 3.

In Germany, the development of high-temperature reactor technology for the AVR Experimental Nuclear Reactor – the first pebble-bed reactor in history – started in parallel to similar projects in the UK (Winfrith), and in the USA (Peach Bottom). Compared to the preceding generation of gas-cooled and graphite-moderated reactors, these projects aimed at higher temperatures, which could only be achieved by replacing metallic structures by graphite and ceramic structures, by using helium as the cooling gas, and by introducing the coated particle concept. Again, the reflector of the AVR was made from an extruded, anisotropic petroleum (needle) coke graphite, ARS/AMT, manufactured by Sigri Elektrographit GmbH. Only very few irradiation data are available for this graphite. Fig. 4 clearly shows a very anisotropic dimensional behaviour at temperatures above 900°C. Fortunately, the highest temperatures occurred only in the upper parts of the graphite structures where, for example, the top reflector had accumulated a fast neutron fluence of only about 1.7 dpa ($\cong 1.3 \cdot 10^{21}/cm^2$ (EDN))* at 1000°C during the first 16 years of operation, whereas the most highly loaded parts of the side reflector receiving a four times higher fluence were exposed to lower temperatures where a rather isotropic dimensional behaviour was observed until final shutdown. [5]

The above-mentioned examples show that until the beginning of the 1960s only highly anisotropic graphites with low thermal expansivity were considered for use in graphite reactors. At that time, it was the agreed philosophy that the dimensional changes would be kept small by low thermal expansion coefficients. If the much higher thermal expansivity of the graphite crystallites perpendicular to the basal planes was balanced by expansion into adjacent pores, the overall thermal expansion coefficients would be much lower. The same effect was expected for the expansion of the crystallites due to irradiation damage. However, linear expansions of about 10% at fluences as low as 14 dpa in combination with such a large spacing between the curves for dimensional changes parallel and perpendicular to extrusion caused problems for the design of graphite components for larger power reactors.

The high anisotropy of the old reactor graphites is caused by the structure and shape of the filler coke (mostly petroleum needle coke) which consists of elongated (“anisometric”) particles. These filler particles are made of graphite crystallites with a preferred orientation of the basal planes along the longitudinal axis of the coke particles. During the extrusion process the filler particles, for their part, take on a preferred orientation parallel to the extrusion direction. If the filler particles were spherical instead of elongated, their orientation after pressing would be

* dpa = displacements per atom; the fluence of 1 dpa is equivalent to the number of (fast) neutrons causing statistically one displacement per C-atom in the piece of graphite under irradiation. “EDN” is another fluence scale which is based on the neutron energy spectrum of the former DIDO reactor.

random, and the physical properties of the whole piece of graphite would be more or less the same in all directions, i.e. near-isotropic.

Early nuclear graphites used, for example, in the first generation of British graphite-moderated reactors (called Magnox) were highly anisotropic and exhibited large dimensional changes due to fast neutron irradiation, as can be seen from Fig. 1. That precluded their use in the next generation of reactors. Therefore, the two major UK producers of nuclear graphites (Anglo Great Lakes, AGL, and British Acheson Electrodes, BAEL) in co-operation with the United Kingdom Atomic Energy Authority (UKAEA) developed much more isotropic graphites with higher dimensional stability under irradiation despite their high thermal expansion compared to PGA graphite, for example. Other high-temperature reactor programmes in Germany and the United States included the development of appropriated core and reflector graphites, too.

The problems arising from manufacturing isotropic graphite seemed to be completely solved when Gilsonite coke became available from a natural but very special carbon source. Gilsonite coke consists of near-spherical particles (Fig. 6) which should avoid a preferred orientation with respect to the direction of pressing or extruding.

The dimensional changes of Gilsonite graphites (Table 2) due to irradiation are demonstrated in Fig. 7 and Fig. 8. In Fig. 7, the linear dimensional changes of an extruded Gilsonite graphite is shown in the two main directions. According to its rather small anisotropy factor $CTE_{perp}/CTE_{par} \approx 1.16$, a remarkable anisotropy still exists. Another Gilsonite graphite, IM 2-24, with an anisotropy factor of $CTE_{perp}/CTE_{par} \approx 1.06$ exhibits less anisotropic dimensional change, although the remaining anisotropy is still visible.

Table 2 Properties of nearly isotropic Gilsonite graphites

Graphite Grade	**Manufacturer**	**Forming Method**	**Thermal Expansivity** (10^{-6}/K)		**Thermal Conductivity** (W/m K)		**Young's Modulus** (GPa)	
			parallel	*perpend.*	*parallel*	*perpend.*	*parallel*	*perpend.*
IM 1-24	AGL	Moulding	4.4	4.4	112	116	10.2	10.5
IM 2-24	AGL	Moulding	5.5	5.2	111	113	10.4	10.5
GCMB	BAEL	Moulding	4.4	4.6			9.4	9.8
GCMD	BAEL	Moulding	4.3	4.2	94	94	7.7	8.1
IE 1-24	AGL	Extruding	4.3	5.0	122	123	12.3	10.8

(Data are mean values of pre-irradiation properties of a random set of irradiation specimens. ‘perpendicular’ and ‘parallel’ refer to the pressing direction.)

Evaluating irradiation data on different Gilsocarbon graphites brings to light the fact that this class of reactor graphites may sometimes be rather inhomogeneous. Fig. 7 and Fig. 8 deal with one or two specimens only. Therefore, the appearance of the graphs is satisfactory. Data points exhibit low scatter confirming that the accuracy of the measurement of the dimensions is high and the irradiation temperature of the four successive irradiations is sufficiently constant. However, if in special cases several specimens have been involved, the picture changes considerably. Fig. 9 shows the dimensional changes of eight specimens – four parallel and four perpendicular to the forming direction – which have been irradiated at almost the same temperatures in the narrow range from 360 to 390°C. Each specimen nicely follows its own regression curve. However, the differences between curves describing the dimensional behaviour of the same material are very large. This can only be attributed to a lack of homogeneity of this graphite and from Fig. 9 it would be difficult to decide how IM 1-24 graphite changes its dimensions in the given temperature range.

The performance of the graphites made from Gilsonite coke and the fact that the supply of sufficiently pure Gilsonite coke to nuclear graphite manufacturers was discontinued in the course of the 1970s in several countries has lead to a great effort to produce isotropic graphites with conventional raw materials and to demonstrate their irradiation behaviour. In the United States, petroleum coke was still the favourite coke despite its higher anisotropy.

In Germany, coal tar pitch coke was chosen as a domestic raw material since the oil crisis in 1973/74 had revealed that the long-range supply with petroleum coke might not be reliable enough. Moreover, pitch coke particles are per se more isotropic. This decision was supported by a feasibility study showing that very isotropic graphites can be manufactured from pitch coke just by extrusion and their irradiation behaviour may be as good as or even better than that of Gilsocarbon graphite.

As an example, irradiation data of a British pitch coke graphite determined in the Dounreay Fast Reactor were communicated, and a piece of this graphite could serve to produce irradiation specimens for several German irradiation capsules to be inserted in the High Flux Reactor at Petten, the Netherlands, at irradiation temperatures of 300, 400, 500, and 600 °C. For the anisotropy factor the value of $CTE_{perp}/CTE_{par} \approx 1.05$ was reported.

After up to five irradiation steps and a maximum fast neutron fluence of 33.3 dpa (at 400°C), the data showed an excellent dimensional behaviour as displayed in Fig. 10a to d. From this finding, it was undoubtedly clear that isotropic graphite can be manufactured from pitch coke and, moreover, by the common extruding technique. These are two important characteristics of ATR-2E graphite, too.

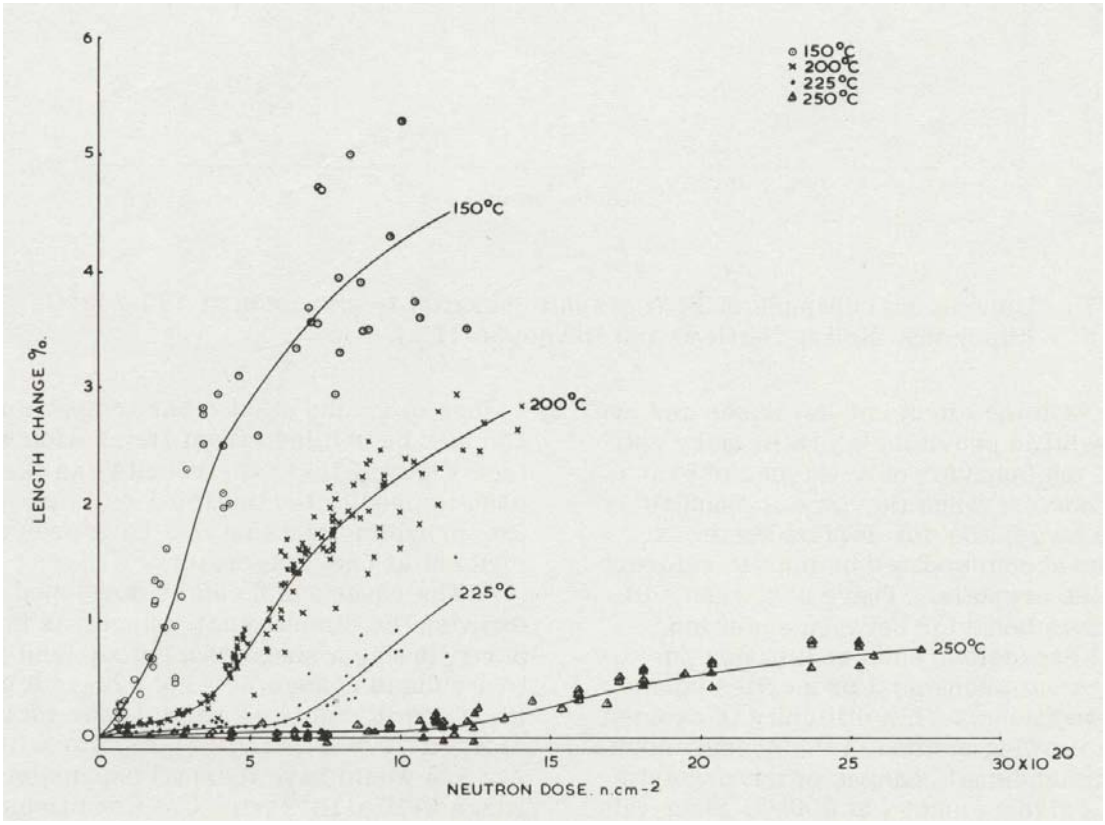

Fig. 1a Dimensional changes of PGA graphite at 150-250°C perpendicular to extrusion

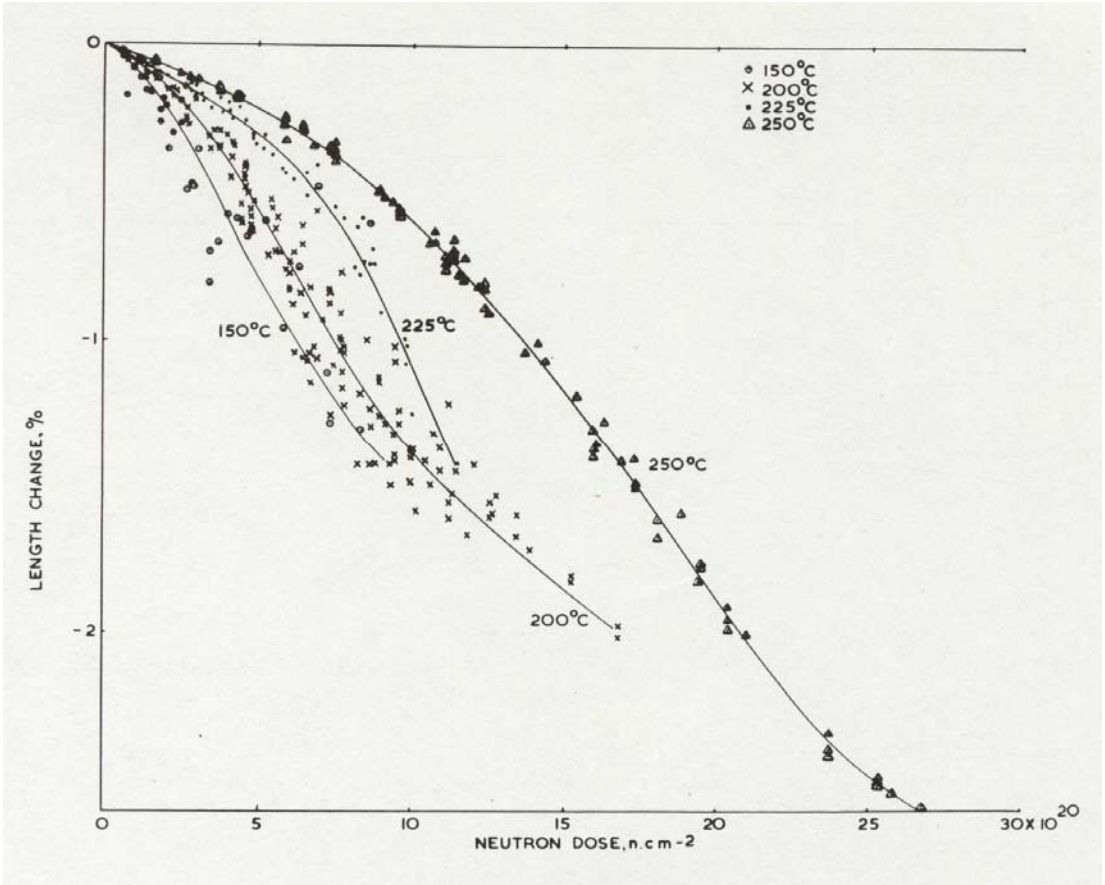

Fig. 1b Dimensional changes of PGA graphite at 150-250°C parallel to extrusion

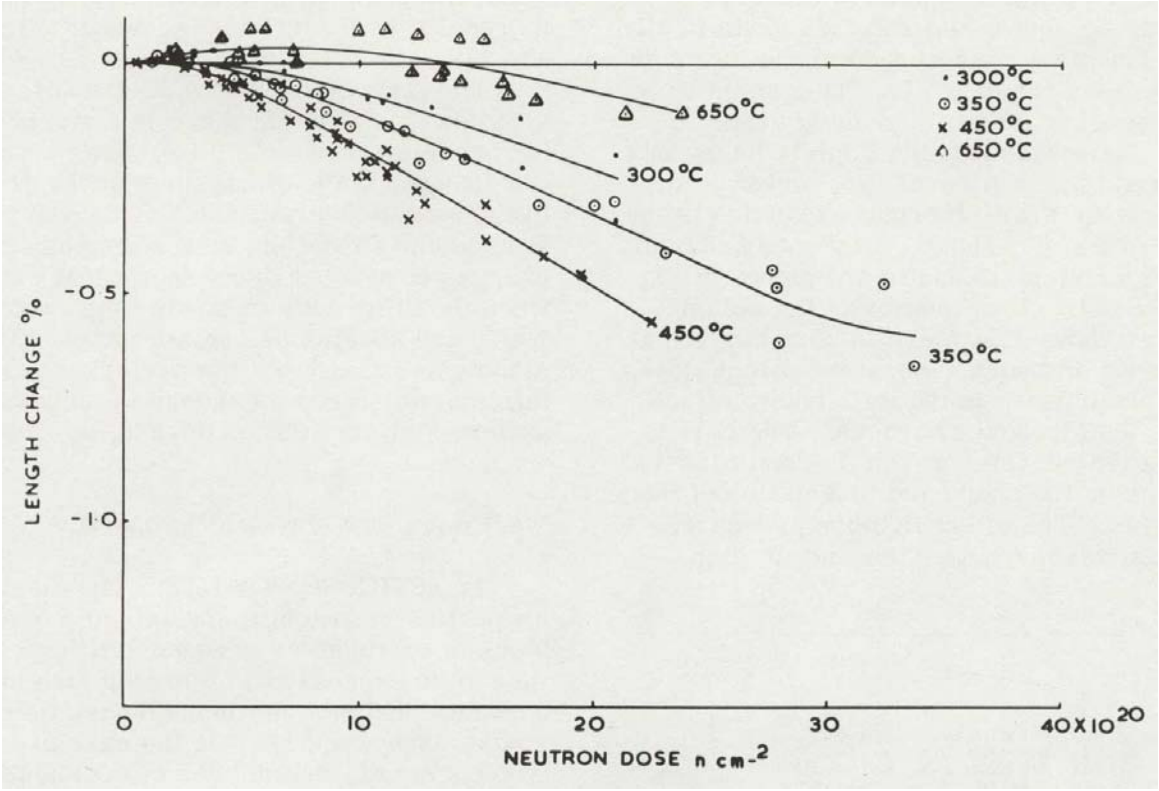

Fig. 2a Dimensional changes of PGA graphite at 300-650°C perpendicular to extrusion

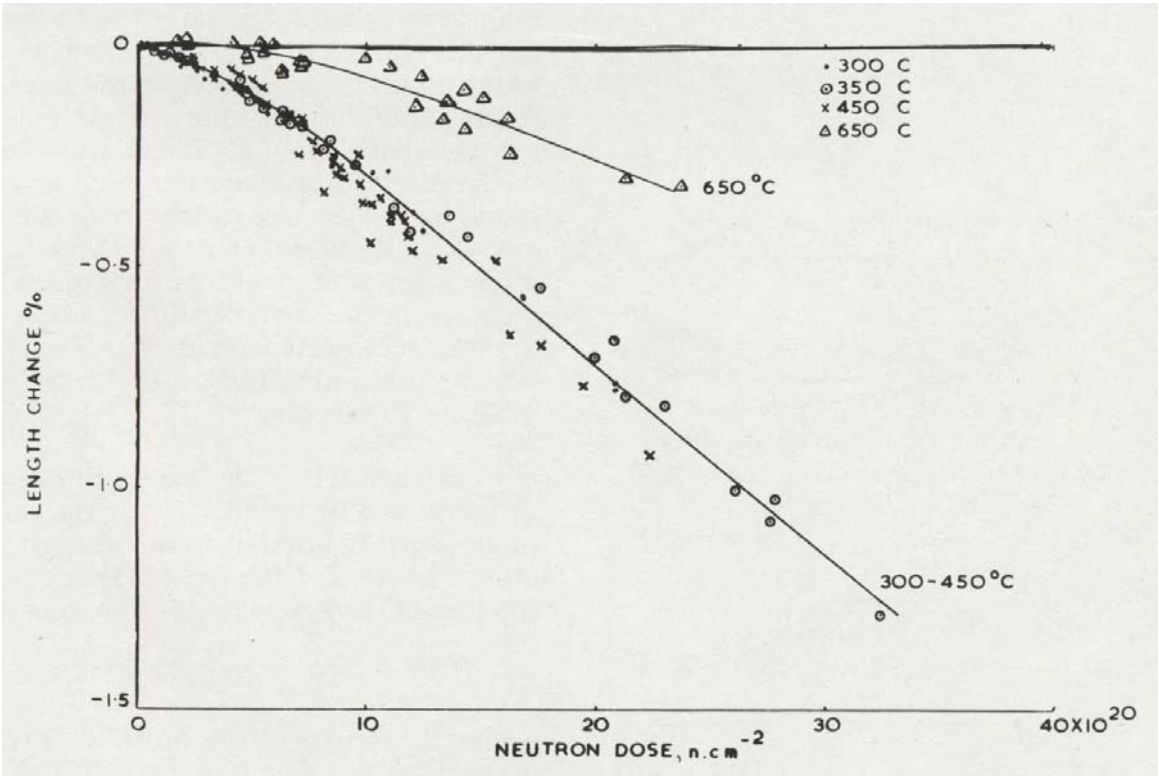

Fig. 2b Dimensional changes of PGA graphite at 300-650°C parallel to extrusion

(Figs. 1a to 2b from [6])

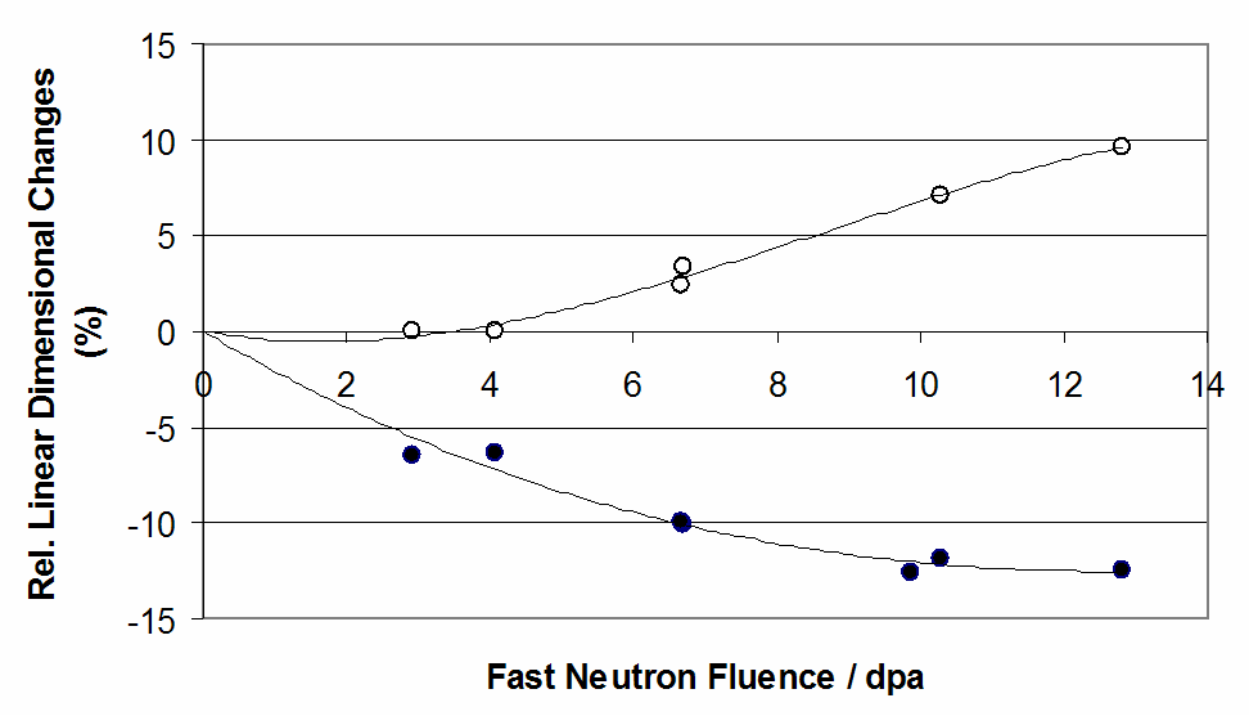

Fig. 3 Dimensional changes of TSX graphite at 1200-1225°C parallel (dark symbols) and perpendicular (light symbols) to extrusion[7]. The original fluence units (E > 0.18 MeV) have been converted to dpa applying the ratio γ(E>0.18 MeV)/cm^2 · 8.9E-22 = γ/dpa

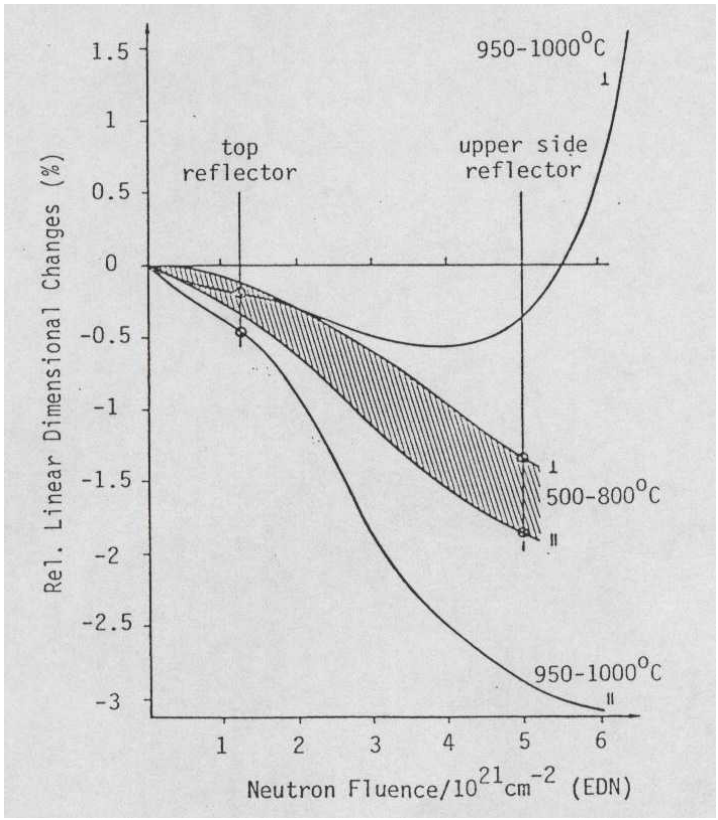

Fig. 4 Dimensional changes of ARS/AMT graphite due to irradiation with fast neutrons

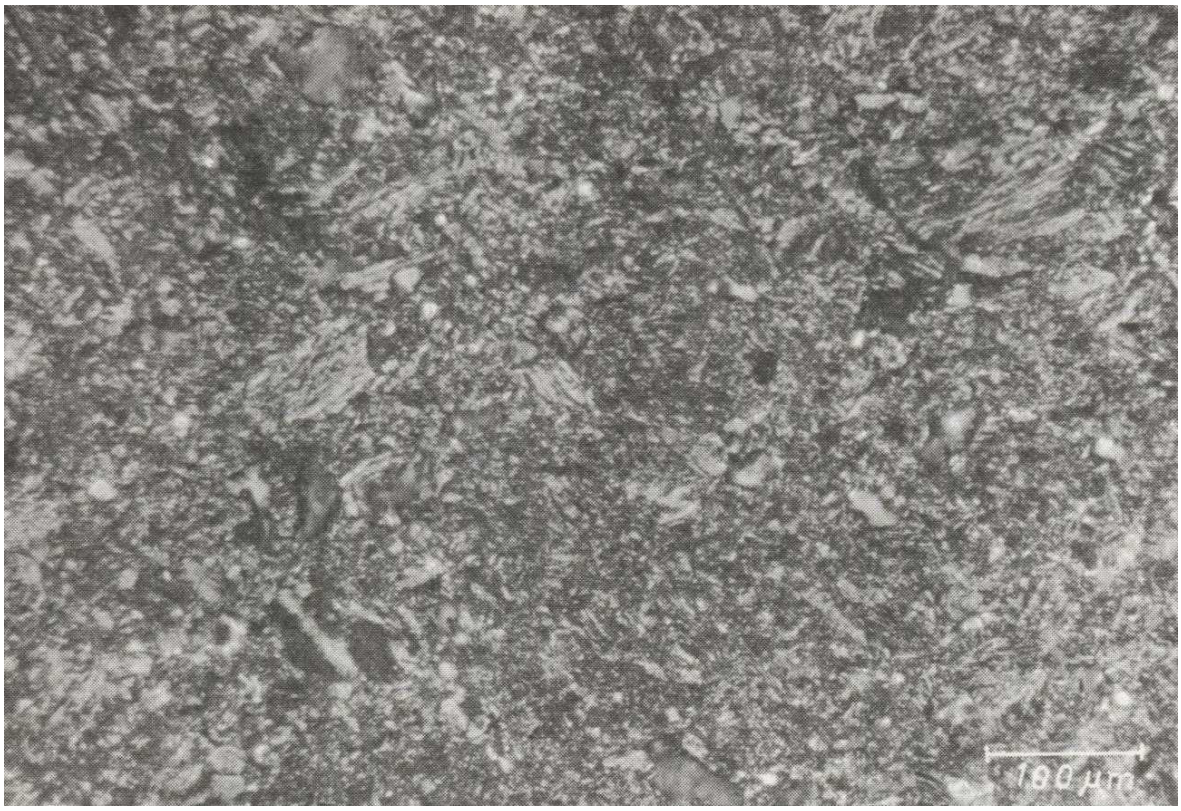

Fig. 5 Micrograph showing a fine-grain petroleum coke graphite

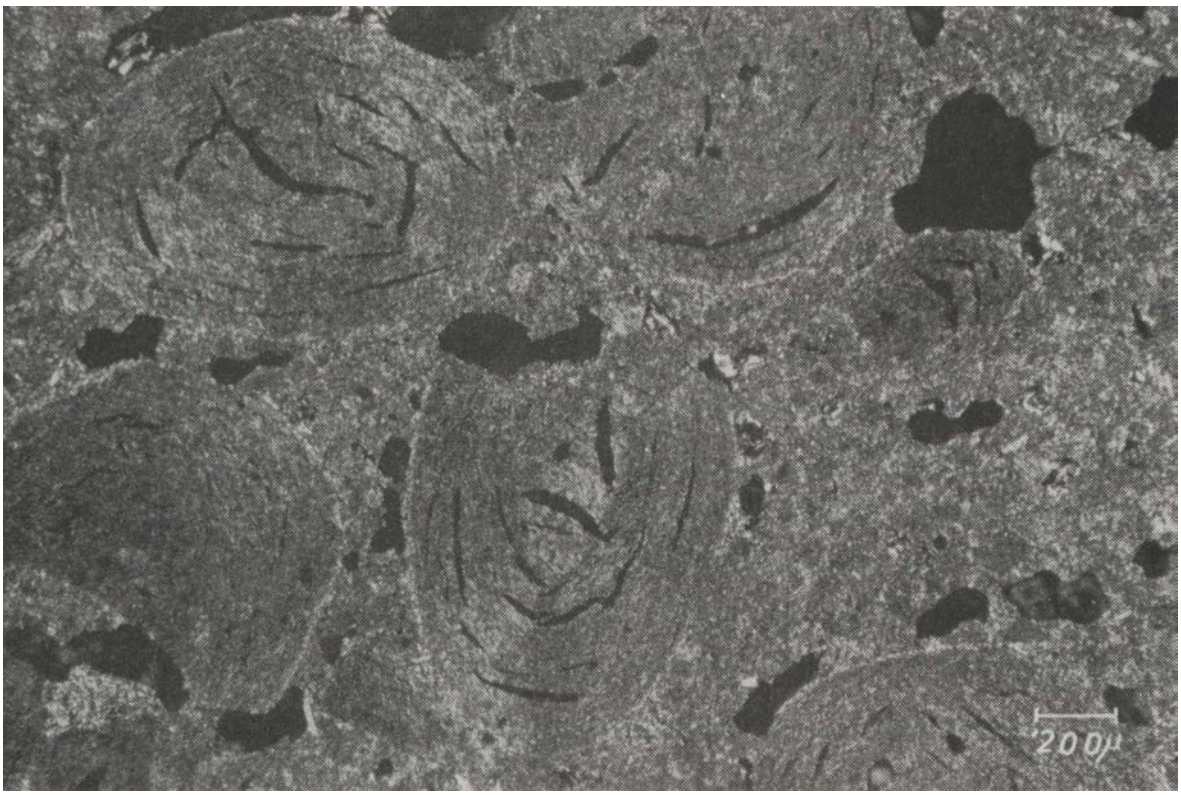

Fig. 6 Micrograph showing a Gilsonite coke graphite

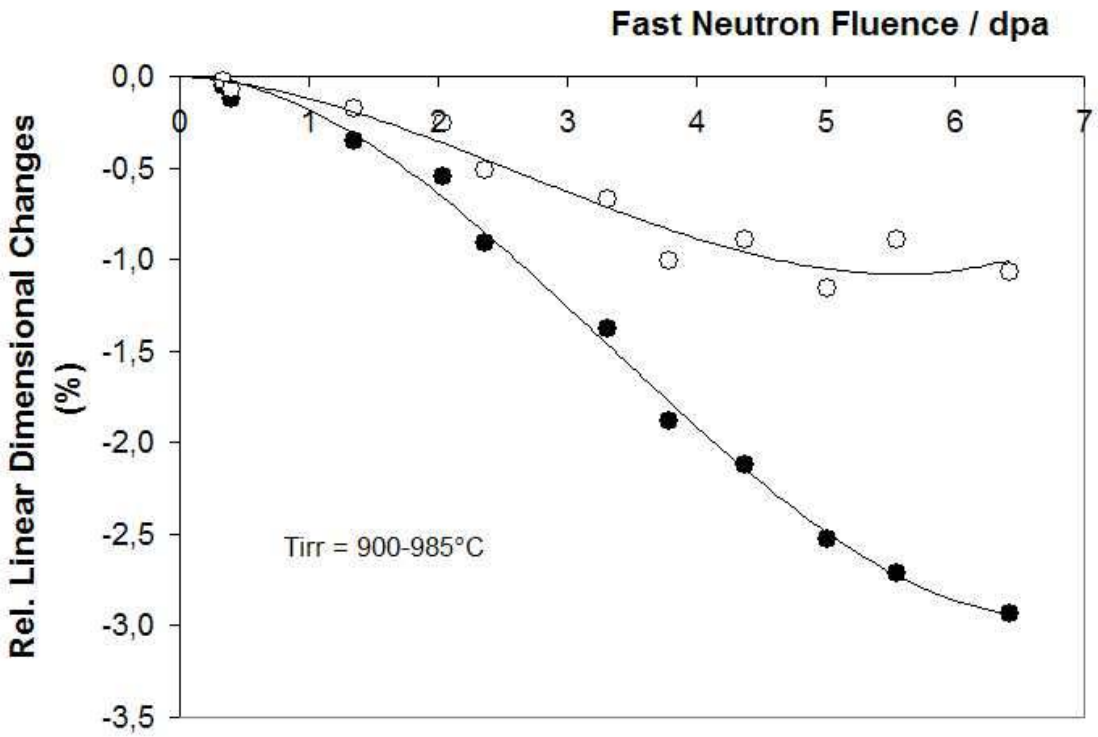

Fig. 7 Irradiation-induced linear dimensional changes of Gilsocarbon graphite IE 1-24 at about 950°C irradiation temperature parallel (dark symbols) and perpendicular (light symbols) to extrusion.

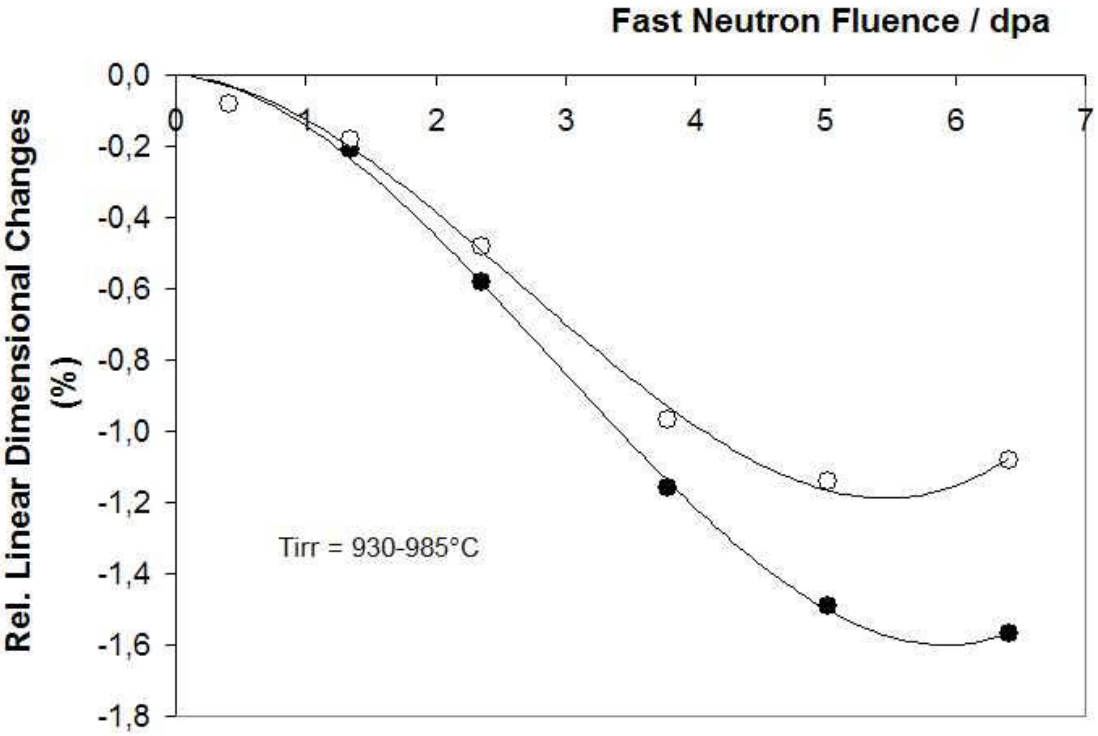

Fig. 8 Irradiation-induced linear dimensional changes of Gilsocarbon graphite IM 2-24 at about 950°C irradiation temperature parallel (dark symbols) and perpendicular (light symbols) to moulding direction.

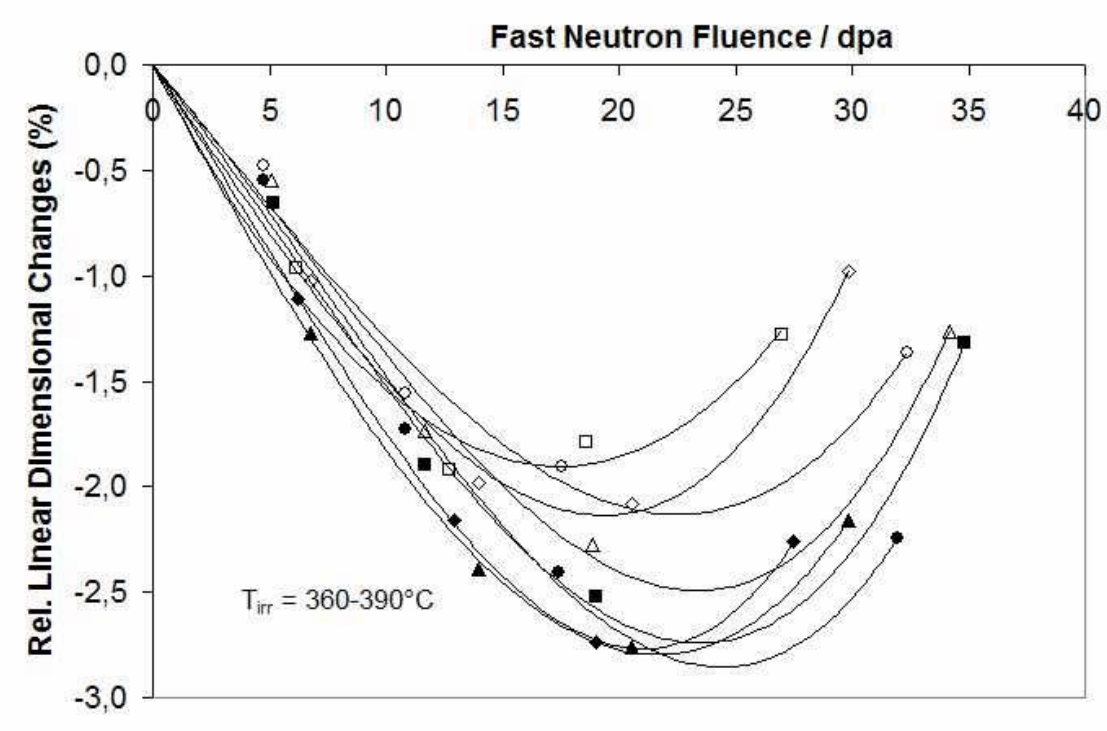

Fig. 9 Irradiation-induced linear dimensional changes of Gilsocarbon graphite IM 1-24 at about 360-390°C irradiation temperature parallel (dark symbols) and perpendicular (light symbols) to moulding direction.

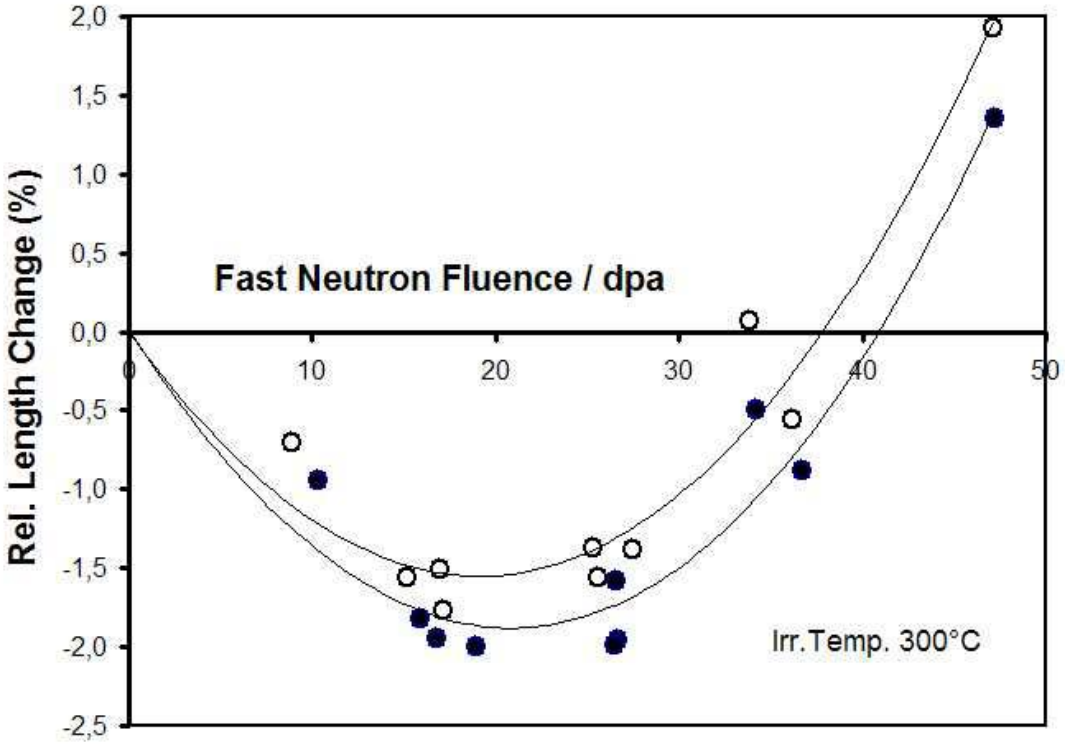

Fig. 10a Irradiation-induced linear dimensional changes of an extruded pitch coke at about 300°C irradiation temperature parallel (dark symbols) and perpendicular (light symbols) to extruding direction.

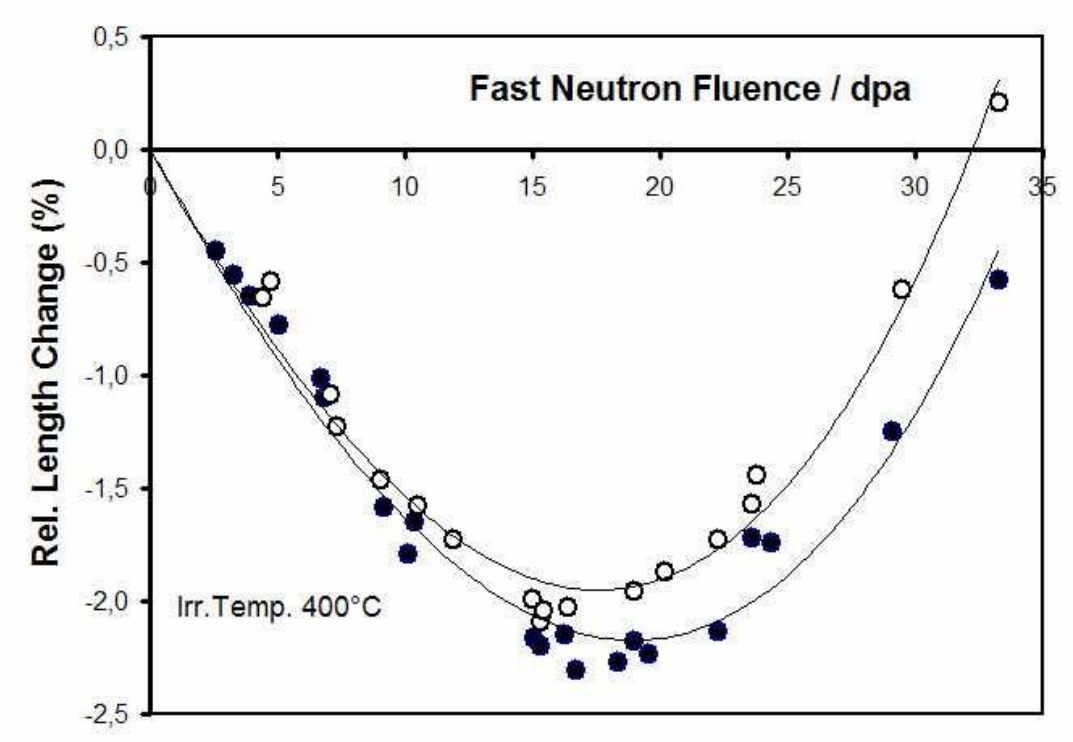

Fig. 10b Irradiation-induced linear dimensional changes of an extruded pitch coke at about 400°C irradiation temperature parallel (dark symbols) and perpendicular (light symbols) to extruding direction.

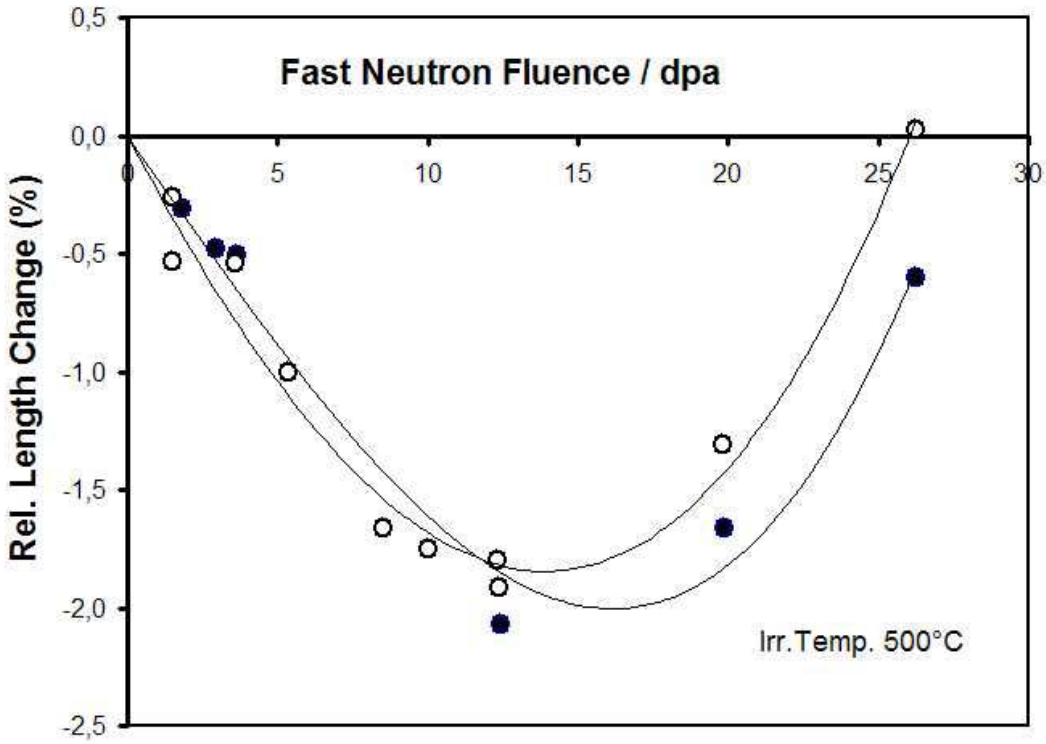

Fig. 10c Irradiation-induced linear dimensional changes of an extruded pitch coke at about 500°C irradiation temperature parallel (dark symbols) and perpendicular (light symbols) to extruding direction.

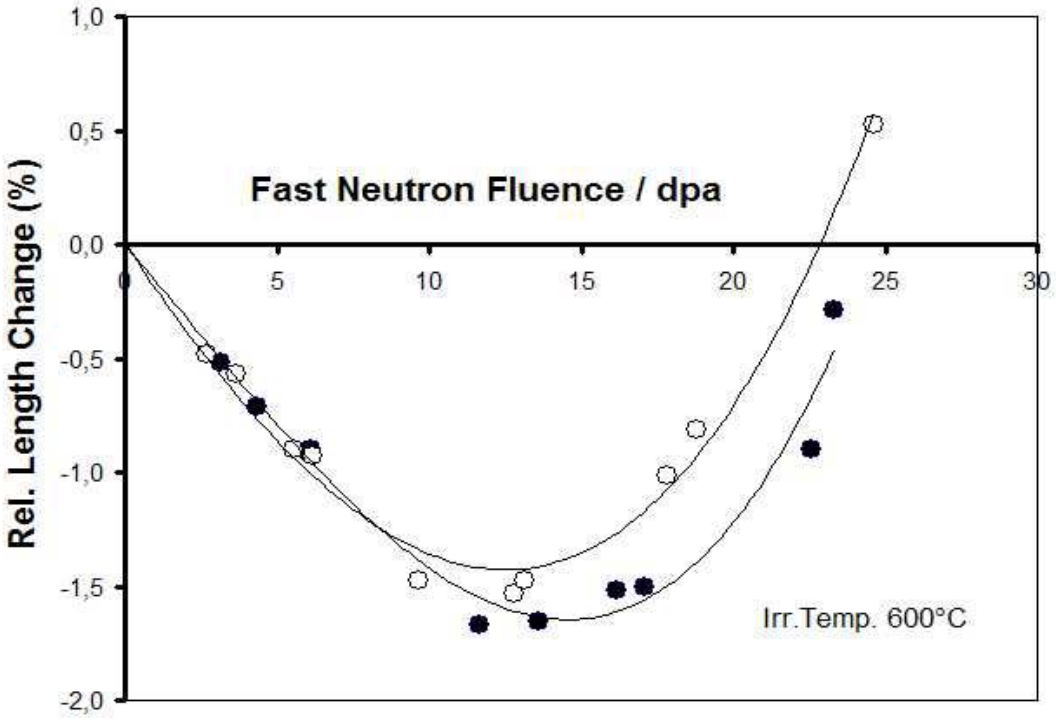

Fig. 10d Irradiation-induced linear dimensional changes of an extruded pitch coke at about 600°C irradiation temperature parallel (dark symbols) and perpendicular (light symbols) to extruding direction.

2. ATR-2E GRAPHITE

As already mentioned in the previous chapter, the German graphite development programme for high-temperature gas-cooled reactors was based on the assumption that reactor graphite for core components with sufficiently high end-of-life fluences can be manufactured from regular pitch coke. Small anisotropy, high strength, and high purity (in view of corrosion) were regarded as important properties of reactor graphite. In the subsequent period, a variety of graphite grades have been manufactured and tested in fast neutron irradiation experiments.

Table 3 presents some of the manufacturing parameters as well as some physical properties. For the use of graphite as structural reactor material, the mechanical stability - primarily the tensile strength - has turned out to be very important. As a result of the Wigner effect and of temperature transients, internal stresses are created in the components and these might be damaged severely if the stresses exceed the strength. Therefore, some other physical properties were assumed to satisfy limiting conditions such as dynamic Young's modulus not exceeding 12 kN/mm^2, thermal conductivity being higher than 90 W/m·K at room temperature, and the coefficient of linear thermal expansion (CTE) being smaller than $6 \cdot 10^{-6}$/K (measured from 20 to 500 °C). Only isotropic graphites with anisotropy factors smaller than 1.15 were thought to be able to fulfil the requirements resulting from stress generation during reactor operation. A compromise had to be found between small CTE values, which can be achieved more easily using anisotropic coke, and isotropic products based on coke with a higher CTE.

The different manufacturing parameters show that there are three different ways of achieving the goals. Forming graphite blocks by extrusion as for ATR-2E graphite is a conventional technique yielding isotropic material only if the filler particles are at least isometric. For extremely large but still homogeneous graphite parts, however, the achievable diameter of extruded graphite blocks may be too small. Therefore, the vibration moulding technique was introduced[8] which, in principle, is able to yield larger block dimensions with good homogeneity and low anisotropy. The graphite grade ATR-2R represents the respective graphite which is comparable to the extruded ATR-2E since it is made from the same special pitch coke.

The two graphites, ASR-1RS and ASR-2R, are also vibration-moulded graphites made from a pitch coke which was rather anisometric as delivered, but was treated according to the so-called secondary coke technique to yield isometric coke particles [9, 10]. However, this treatment of anisometric coke causes additional costs which have to be taken into account depending upon the cost sensitivity of the actual application.

The third way of manufacturing isotropic graphite is isostatic moulding. However, this technique uses very fine coke particles and results in graphites which exhibit non-desirable fracture mechanical properties even though their strength is extremely high. This type of graphite is represented in Table 3 by grades V 483 and V 356. They were included in the programme at a point when their fracture mechanical behaviour had not yet been investigated.

However isotropic a graphite may be, its suitability for reactor purposes can finally only be demonstrated by irradiation testing. Therefore, a screening test was performed in the High Flux Isotopes Reactor (HFIR) at Oak Ridge, TN, in co-operation with Oak Ridge National Laboratory (ORNL, USA) and the General Atomic Company, San Diego (USA).[11] The aim of a series of three irradiation experiments was to determine the 'end-of-life fluence' of the six different graphite grades at a constant temperature of about 600°C. It needs to be pointed out that 'end-of-life fluence' in this case means the fast neutron fluence at which after the shrinkage phase the graphite samples re-attain their original volume and net volume expansion begins. (The expression 'end-of-life fluence' according to this definition is used to compare different graphites with respect to their dimensional behaviour and is not the same as the real 'operational end-of-life' of graphite parts in the reactor core.)

The High Flux Isotopes Reactor has a higher flux ($8.3 \cdot 10^{18}/(m^2 \cdot s)$ (EDN)) than most other test reactors. Therefore, relevant results on the irradiation behaviour of graphites can be attained after shorter irradiation periods. However, high flux irradiation experiments sometimes encourage a discussion about the influence of the neutron spectrum on irradiation results. But in the present case the results are only used to compare different graphites, and not to obtain design data.

The dimensional changes measured after three subsequent irradiations are given in Fig. 11. The initial shrinkage rate is more or less dependent upon the initial coefficient of thermal expansion with the petroleum coke graphite V 356 exhibiting the highest shrinkage rate related to the lowest CTE. The main objective of these irradiations, i.e., to compare the 'end-of-life fluences' (as defined above) of the six graphites has clearly been achieved, and the result is in favour of ATR-2E graphite. A clear disadvantage of the two iso-moulded graphites V 483 and V 356 is also apparent. After having gone through the highest maximum shrinkage (turn around) at a rather high fluence, they expand so fast that they reach end-of-life fluence earlier than ATR-2E, which exhibits a much lower maximum shrinkage at a similar fluence.

The comparison of ATR-2E to ATR-2R will be discussed in more detail in chapter 7 to find out whether the influence of the two different pressing techniques (extruding and vibration mould-

ing) can be resolved. This is an important issue since vibro-moulding in some respect (for example, cost, manufacturing large blocks) may have an advantage over extruding.

In the screening test in HFIR, ATR-2E graphite turned out to have the highest 'end-of-life fluence', a low initial shrinkage rate, and a medium maximum shrinkage at a high fluences. This behaviour was the basis for the decision that ATR-2E should be a candidate graphite for the reflector of future gas-cooled reactors.

Around 1979, when this decision was made the irradiation testing of ATR-2E in the High Flux Reactor at Petten had only advanced to a fast neutron fluence of about 6.5 dpa (equivalent to $\approx 5 \cdot 10^{21}/cm^2$ (EDN)). As shown in Fig. 12, there was no difference between HFR and HFIR data at that time. In the late 1980s, when the final data from the 600°C irradiations at Petten became available (see Tables in App. B), it turned out that under HFR irradiation conditions the 'end-of-life fluence' is about $19 \cdot 10^{21}/cm^2$ (EDN). As mentioned before, the discussion is still going on as to whether this higher 'end-of-life fluence' achieved at a lower flux density has to be explained by a flux density effect.

ATR-2E was the first German isotropic graphite available on a large scale, and has therefore been incorporated in all German irradiation experiments from the very beginning. Its good physical properties and above all its low anisotropy were based on a special pitch coke which was produced by the Rütgerswerke company (Germany) as a mass product for the German aluminium industry. Using this raw material of German origin along with a large-scale consumer at that time provided good prospects for long-term availability. However, an increasing debate on environmental issues and their impact on the future of coking plants in Germany has proven that the availability of the secondary coke technology which is able to make isotropic coke from any primary coke may be an even better long-term solution for the future manufacturing of isotropic nuclear graphite, but at a higher cost.

Graphite Grade			ATR-2E	ATR-2R	ASR-1R	ASR-2R	V 483	V 356
Manufacturer			SIGRI				Ringsdorff	
Coke			Special pitch coke		Pitch coke		Pitch coke	Petroleum coke
Max Grain Size	mm		1	1	1	1	0.1	0.1
Forming Method			Extrusion	Vibrational Molding			Isostatic pressing	
Dimensions	mm		450ϕx2000	400 x 400 x 1000			300x370x900	or 370ϕx900
Apparent Density	g/cm^3		1.80	1.71	1.78	1.70	1.75	1.74
Dynamic Young's Modulus	10^3 n/mm^2	∥	9.6	8.9	9.9	8.5	9.4	10.5
		⊥	8.4	8.3	9.2	7.3	9.3	8.8
Flexural Strength	n/mm^2	∥	23.0	22.3	26.0	18.8	30.8	32.3
		⊥	18.9	20.4	23.0	16.0	30.4	29.4
Compressive Strength	n/mm^2	∥	55.9	56.5	67.1	45.4	73.9	64.8
		⊥	57.8	56.3	63.1	44.9	74.9	65.5
Tensile Strength	n/mm^2	∥	12.6	15.0	14.9	11.5	21.1	22.0
		⊥	12.4	13.3	13.5	9.6	18.8	20.6
Coefficient of Thermal Expansion (20-500°C)	10^{-6}/K	∥	4.4	5.1	4.7	4.3	4.1	3.2
		⊥	4.9	5.5	4.9	5.0	4.3	3.6
Anisotropy of CTE			1.11	1.08	1.04	1.16	1.05	1.13
Thermal Conductivity	W/m K	∥	179	117	125	115	109	128
		⊥	163	110	125	109	109	124
Ash	ppm		170	490	390	<500	520	360

Table 3 Properties of nuclear graphites from the German graphite development programme[12].

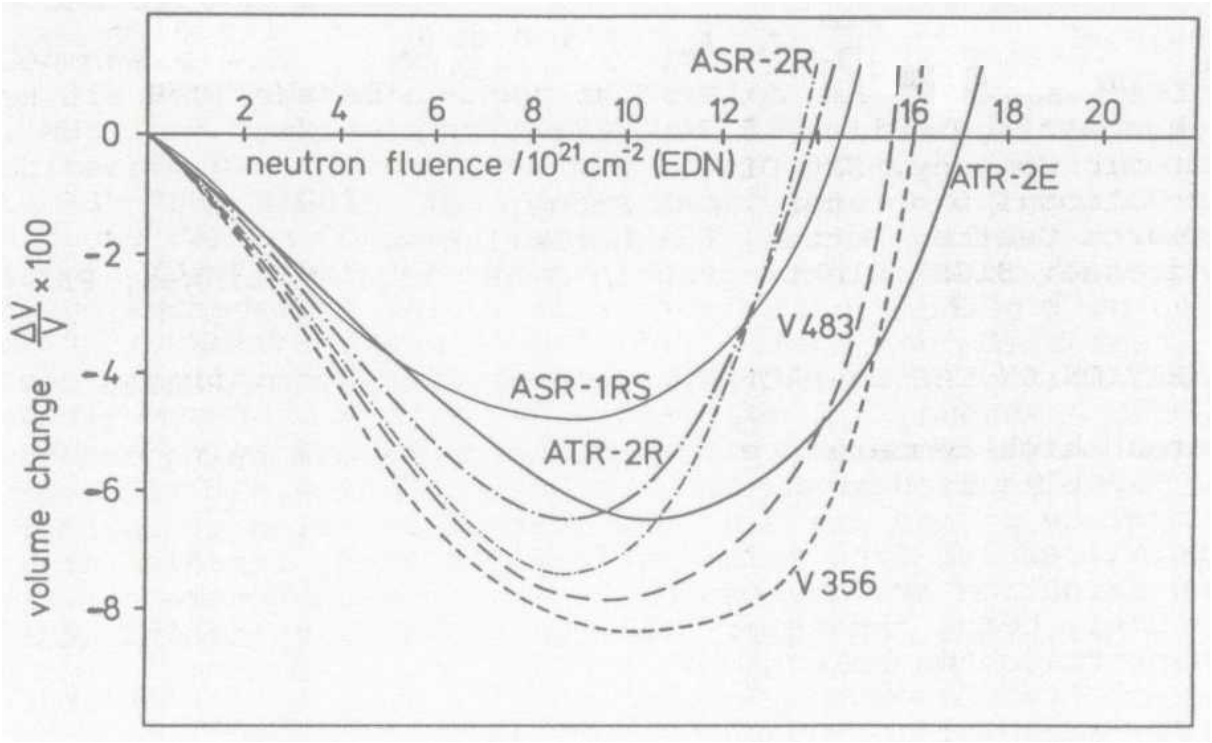

Fig. 11 Irradiation-induced volume changes of six nuclear graphites in HFIR at 600°C [11]

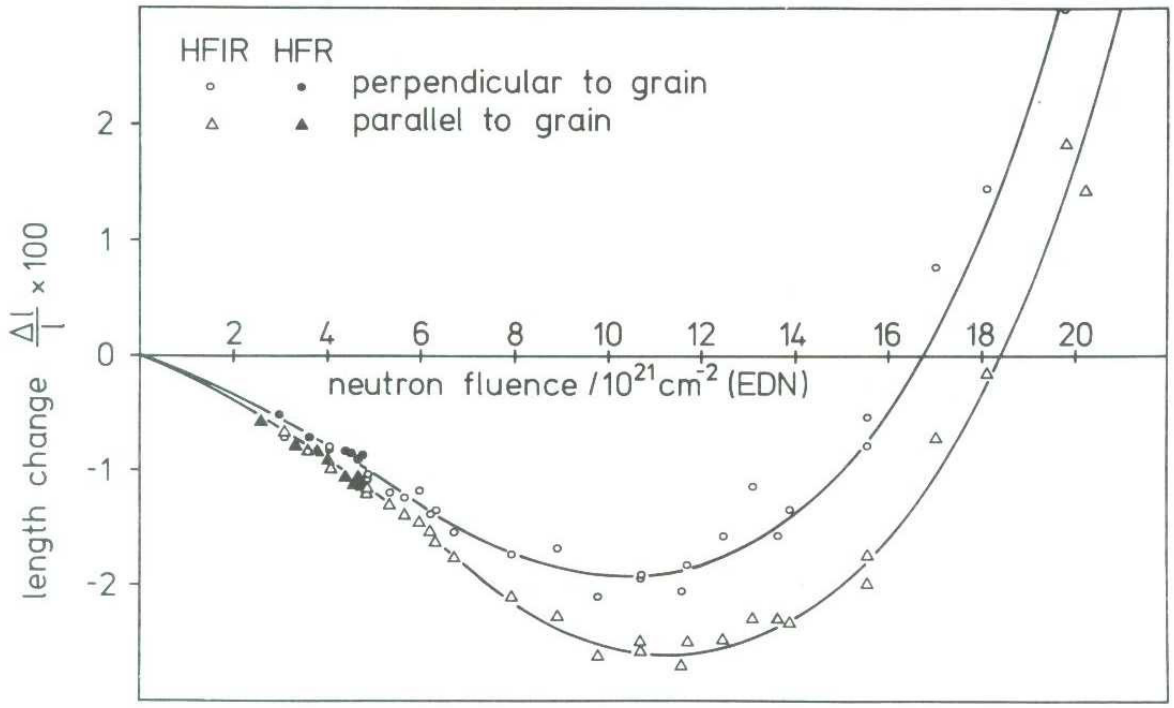

Fig. 12 Dimensional changes of ATR-2E graphite in HFIR Oak Ridge and HFR Petten at 600°C

3. THE HIGH FLUX REACTOR AT PETTEN (NL) AND ITS IRRADIATION FACILITIES

All design data for ATR-2E graphite were obtained from irradiation experiments in the High Flux Reactor (HFR) at Petten, the Netherlands.

The Petten Establishment was founded in 1961 on the basis of an agreement between the Dutch Government and the Commission of the European Communities. The HFR was taken over by the Commission in 1962, and since that time the reactor has been operated under contract by ECN (Energy Centrum, the Netherlands) for the Commission of the European Communities.

The HFR is a materials testing reactor which is water-cooled and -moderated (Fig. 13). During its more than 40 years of existence, the reactor and its equipment have been continuously modernised and upgraded. In 1970, for example, the power was increased from 30 to 45 MW. In 1984, the reactor was shut down for about 14 months for the replacement of the reactor vessel and its peripheral installations.

The core lattice (Fig. 14) is a 9x9 array (729 mm x 750.4 mm) containing 33 fuel assemblies, 6 control members, 19 experiment positions, and 23 beryllium reflector elements. The HFR is operated for 10 reactor cycles or 270 days per year. In a central irradiation position, such as E5, C3, or C7 (Fig. 14), a fast neutron fluence of about $0.5 \cdot 10^{25}/m^2$ (E > 1 MeV) per reactor cycle can be achieved.

This reactor has been used extensively for the German graphite irradiation programme for more than 25 years. Irradiations of cylindrical specimens to investigate the physical property changes due to fast neutron irradiation (so-called ‘basic properties tests’) were performed either in reloadable facilities of the TRIO or QUATTRO type (Fig. 15 and 16)[13,14], and irradiation-induced creep behaviour was observed by means of DISCREET facilities (Fig. 19 to 21).

3.1 Basic Properties Irradiation Tests

TRIO and QUATTRO capsules contained sample holders made of aluminium (sample holder type 1; 300°C to 450°C; Fig. 17) with 9 cylindrical boreholes or of POCO graphite (sample holder type 2; 450° to 650°C; Fig. 18) with 7 cylindrical boreholes to take the irradiation speci-

mens. The sample holders were centred inside a stainless steel tube. They were designed for use in all central positions (C3, C5, C7, E3, E5 and E7; see Fig. 14). In the “hottest” position, C5, the maximum unperturbed thermal neutron flux was $1.9 \cdot 10^{18}/m^2 \cdot s$, the maximum unperturbed fast neutron flux was $2.7 \cdot 10^{18}/(m^2 \cdot s)$, and the maximum nuclear heating in graphite samples was 12 800 W/kg. With this maximum fast flux the fast neutron fluence achieved during 24.7 days (= 1 reactor cycle) is about $5.75 \cdot 10^{25}/m^2$, which is equivalent to about 0.835 dpa in graphite.

3.2 Irradiation Creep Tests

3.2.1 Tensile Sample Carrier

A column of five tensile samples together with reference half-shells and fluence monitors were held in POCO graphite drums which were retained by a stainless steel tube. Pinned connections at the upper and lower end of the column facilitated removal of the samples for the dimensional measurement.

The column was axially loaded in tension by a pneumatic bellows system, positioned directly above the sample column in order to minimise frictional losses. Sample failure is detected by contacts which were actuated by an abnormal extension of the bellows. Heat generated in the sample carrier from gamma irradiation was rejected radially to the reactor primary cooling system. A stepped gas gap between the stainless steel tube and the irradiation thimble (TRIO capsule) compensated the axial variation of gamma flux and ensured a constant temperature profile along the sample column. Variation of gas mixture (He, Ne) in the gas gap provided a range of temperature control.

Two thermocouples per sample were located in the POCO graphite container. Radial temperature gradients within the sample holder resulted in a temperature difference between the samples and the thermocouples. Linear functions relating the two temperatures were derived from heat transfer calculations and the validity of these functions was checked in the first rigs by fitting a reference thermocouple on the centre line of the upper sample.

3.2.2 Compressive Sample Carrier

A column of 10 compressive samples together with reference pieces and fluence monitors was supported directly in a stainless steel sample carrier tube. The arrangement ensured a good

axial alignment and eliminated the possibility of buckling. The samples were retained at the lower end of the tube by a pinned connection.

The column was axially loaded in compression by a pneumatic bellows system located directly above the sample column. A sample failure device was not considered necessary for the compressive rig due to the considerably higher strength of graphite in compression.

A small diameter extraction tube, flanged at the upper end, ran axially up a central hole in the reference pieces and was provided for withdrawing the samples after irradiation. Temperature control was the same as for the tensile sample carrier.

3.3 Irradiation Temperature – Determination and Control

The irradiation temperature was achieved by utilising the reactor gamma heating, absorbed by the rig components as the heat source, the primary cooling circuit as a heat sink, and tailored gaps as heat flow barriers. The maximum heat flux, including the TRIO or QUATTRO thimble, towards the primary circuit water was ± 34 000 W/m for sample holder type 1, and ± 37 000 W/m for sample holder type 2. The thermal analysis was performed by means of a 2-dimensional heat transfer computer code, WRZ1[15]. The irradiation temperature was controlled by means of a double gas gap, one between the drums and the carrier tube, the other one between the carrier tube and the TRIO or QUATTRO thimble. The gas gaps were stepped in order to obtain a homogeneous temperature distribution over the length of the carrier. The He/Ne gas mixture was provided by the standard HFR gas feeding system via the so-called TRIO or QUATTRO panels. Gas circulation was not foreseen. The gas composition could be varied from 100% helium, the lowest possible temperature condition, to 100% neon yielding the maximum possible temperature.

The temperatures of the samples were measured by thermocouples with an accuracy of about ± 5%. They were placed in bores of the drums along the length of the sample carrier. All thermocouples had chromel/alumel thermoelectric wires with AISI 316 sheaths of 1.0 mm O.D. and MgO or Al_2O_3 as insulator. The total length was 4.5 m. There were 12 thermocouples in each carrier. They were supplied with X-ray photographs of the junction and certificates on loop and insulation resistances. Upon supply, the X-ray photographs were examined under a microscope. Loop and insulation resistances were measured and checked against the certificates. They were measured again after degreasing and pickling of the sheath, after hard soldering, after welding of the penetration into the carrier, and before and after brazing to the connectors.

The thermocouples' readings were recorded by means of NEFF data loggers connected to the HFR central computer system DACOS and stored on floppy discs. Final results after evaluation were plots of temperature vs. time, statistical compilation of temperature vs. time distribution, both in graphical and numerical form.

All sample holders were displaced vertically in order to adjust the temperature distribution and to follow the neutron flux shift during the cycle.

3.4 Neutron Dosimetry

The neutron fluence measurement[16] was usually limited to the fast neutrons with E > 1 MeV. It was performed by means of Ni/Co, Fe, Ti, and Nb activation detectors which were placed in an Al_2O_3 cylinder with four holes, in which the four different monitor materials were loaded. Encapsulated into quartz glass boxes, there were normally seven detectors per sample holder placed at fixed vertical distances in the central channel of the experiment before the start of the irradiation.

After the irradiation was finished and the activation monitors were removed from the sample holder in the dismantling cells of the HFR, they were usually evaluated by the ECN Neutron Metrology Department. (In some cases, dosimeters were provided and evaluated by KFA Jülich.) The monitors were received in aluminium capsules coded with the monitor set number. After preparation, the counting procedure was started using an HPGe counting chain. The counting results were processed with appropriate computer programs which yielded irradiation parameters like neutron fluence and fluence rate data.

For the neutron metrology, the following activation reactions were used:

^{59}Co (n,γ) ^{60}Co	for thermal fluence, thermal fluence rate and spectrum index,
^{58}Fe (n,γ) ^{59}Fe	for thermal spectrum index,
^{54}Fe (n,p) ^{54}Mn	for fast fluence, fast fluence rate, and spectrum index,
^{46}Ti (n,p) ^{46}Sc	for fast spectrum index,
^{93}Nb (n,n') ^{93}Nb	for thermal spectrum index,
^{93}Nb (n,γ) ^{94}Nb	for thermal fluence, thermal fluence rate and spectrum index.

The saturation activities per target atom of the product nuclei of the activation reactions, valid for a reference power of 45 MW, were calculated with the VILLA program[17]. Some ratios of these

saturation activities, called spectrum indices, were calculated as a check on the numerical results.

Systematic uncertainties in the EDN fluences amounted to 7%, mainly arising from the method used to derive the damage-to-activation ratio for graphite. Random uncertainty was generally of the order of 2.4% giving a combined uncertainty of ± 7.4% (95% confidence level).

3.5 Handling, Dismantling, Transport

The irradiation capsules were transferred into the hot cell where the sample holder was extracted. After opening the sample holder by cutting its suspension, or in the case of an older version by cutting the top and/or bottom end of the carrier, the samples and the neutron fluence monitors were recovered. In case of difficulties during the standard dismantling procedure, when recovery of the samples was not possible by means of the available equipment, the debris of the sample holder was loaded into a standard ‘waste’ box for transport to another hot cell, where more sophisticated procedures for dismantling could be applied.

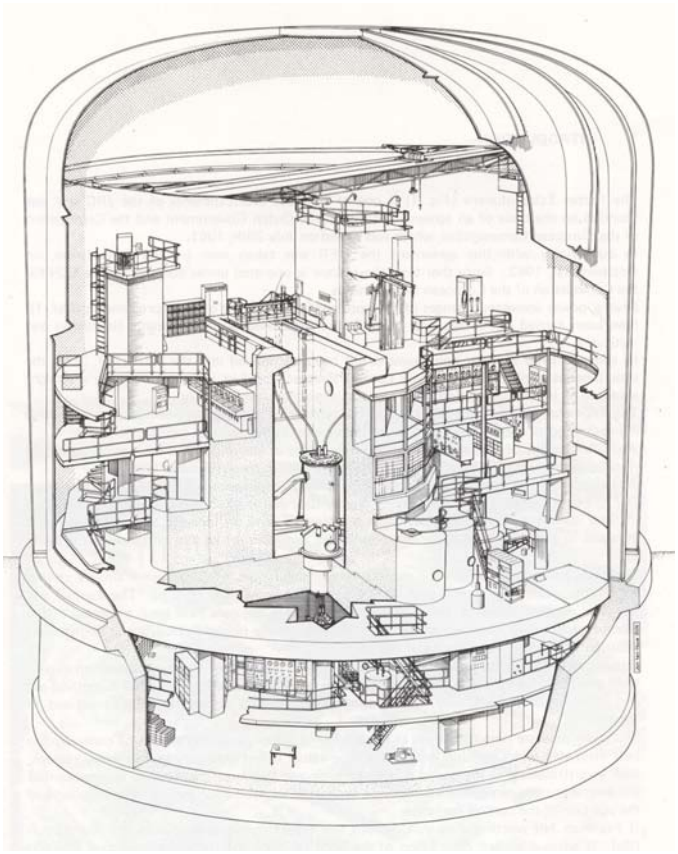

Fig. 13 High Flux Reactor (HFR) Petten (The Netherlands); sketch of the internals

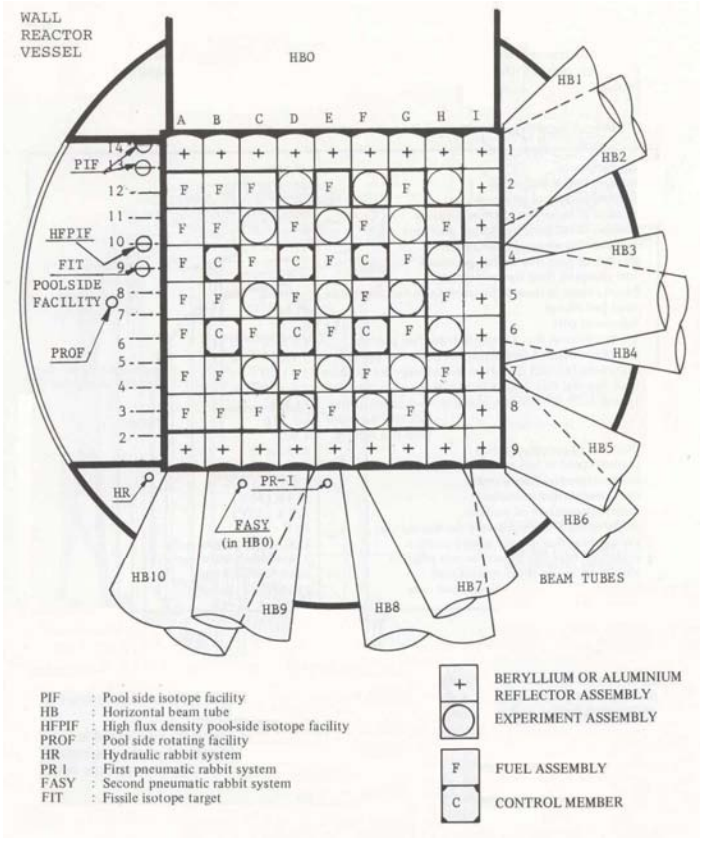

Fig. 14 High Flux Reactor (HFR) Petten (The Netherlands); core configuration

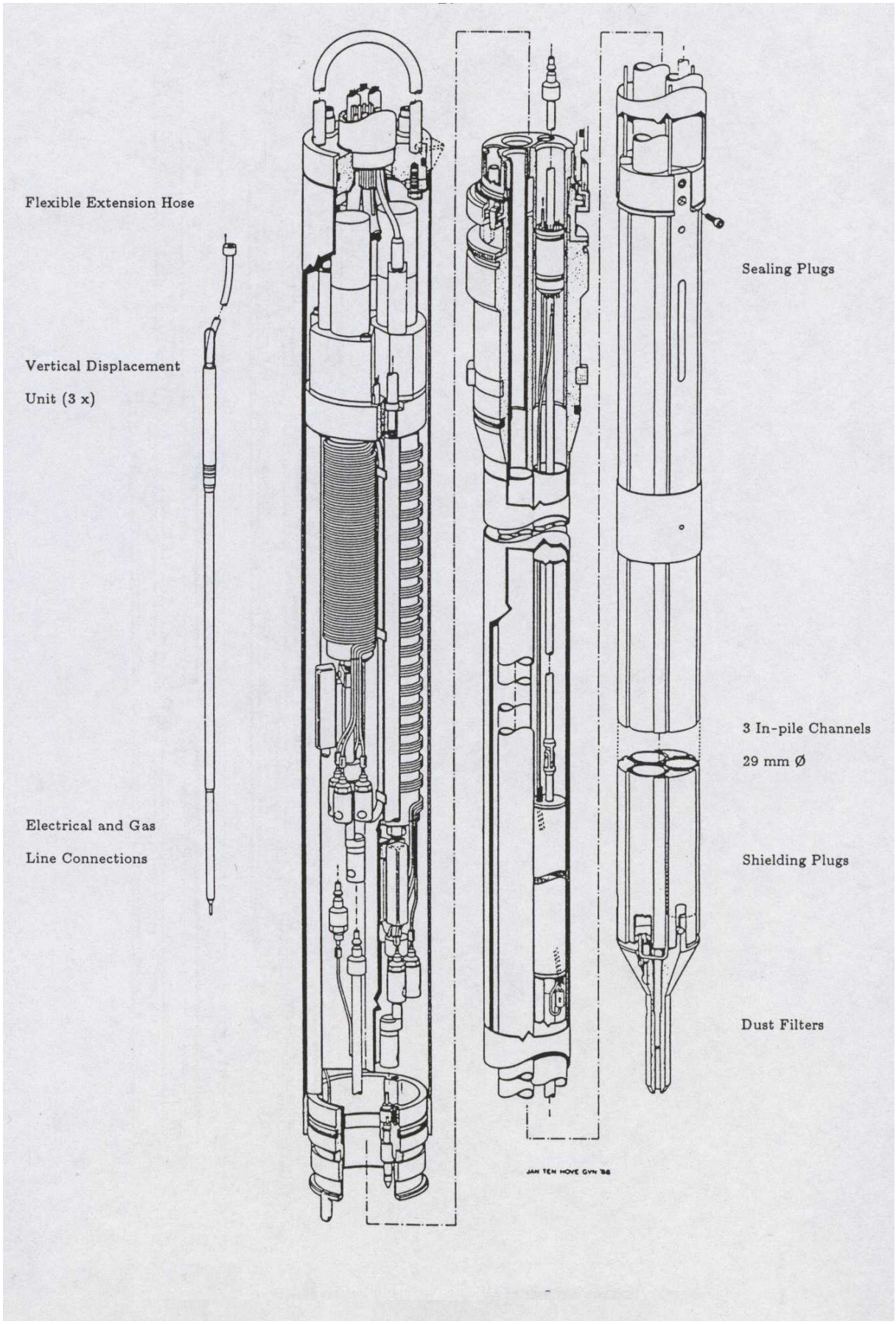

Fig. 15 Standard irradiation capsule TRIO – 129

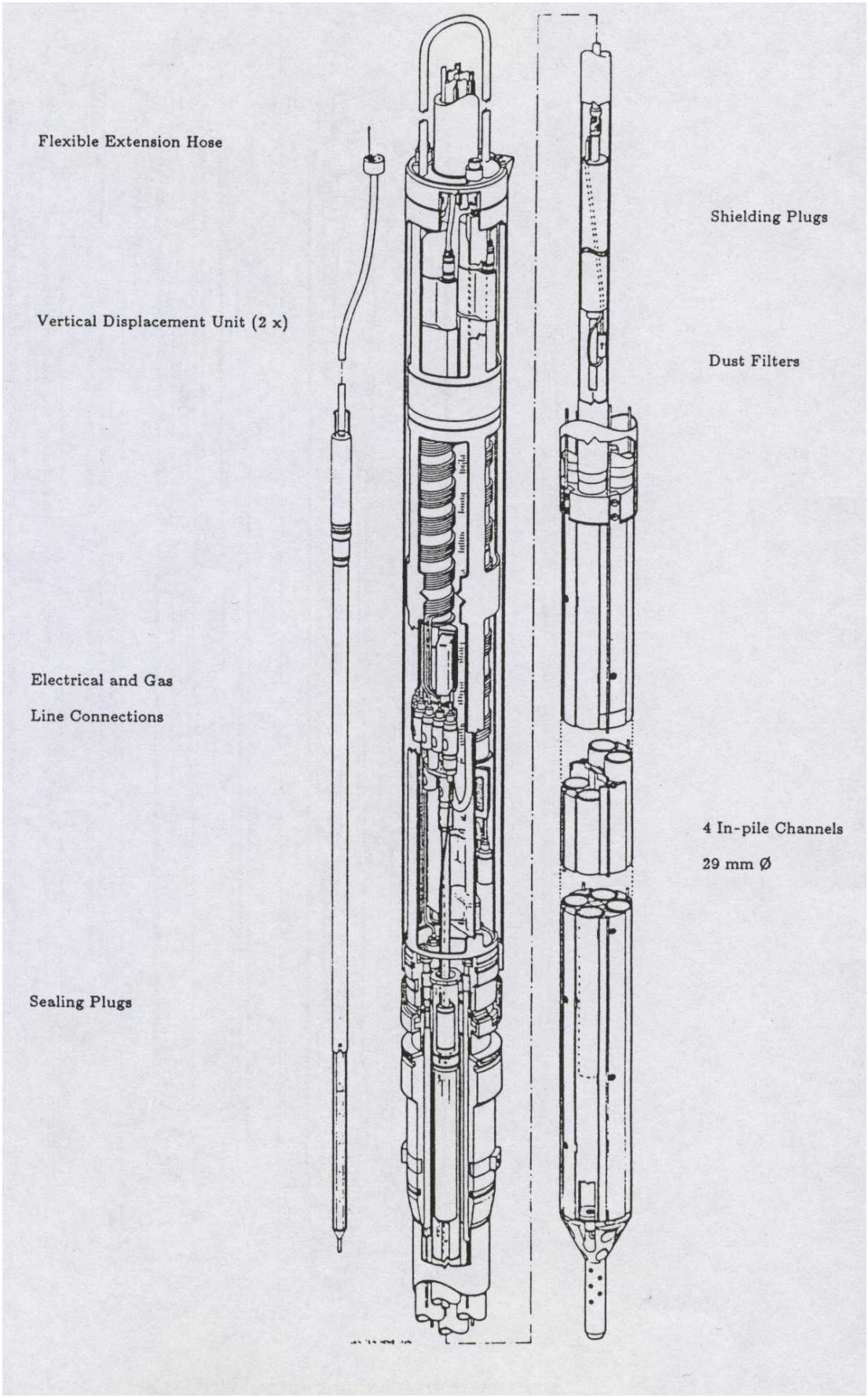

Fig. 16 Standard irradiation capsule QUATTRO – 129

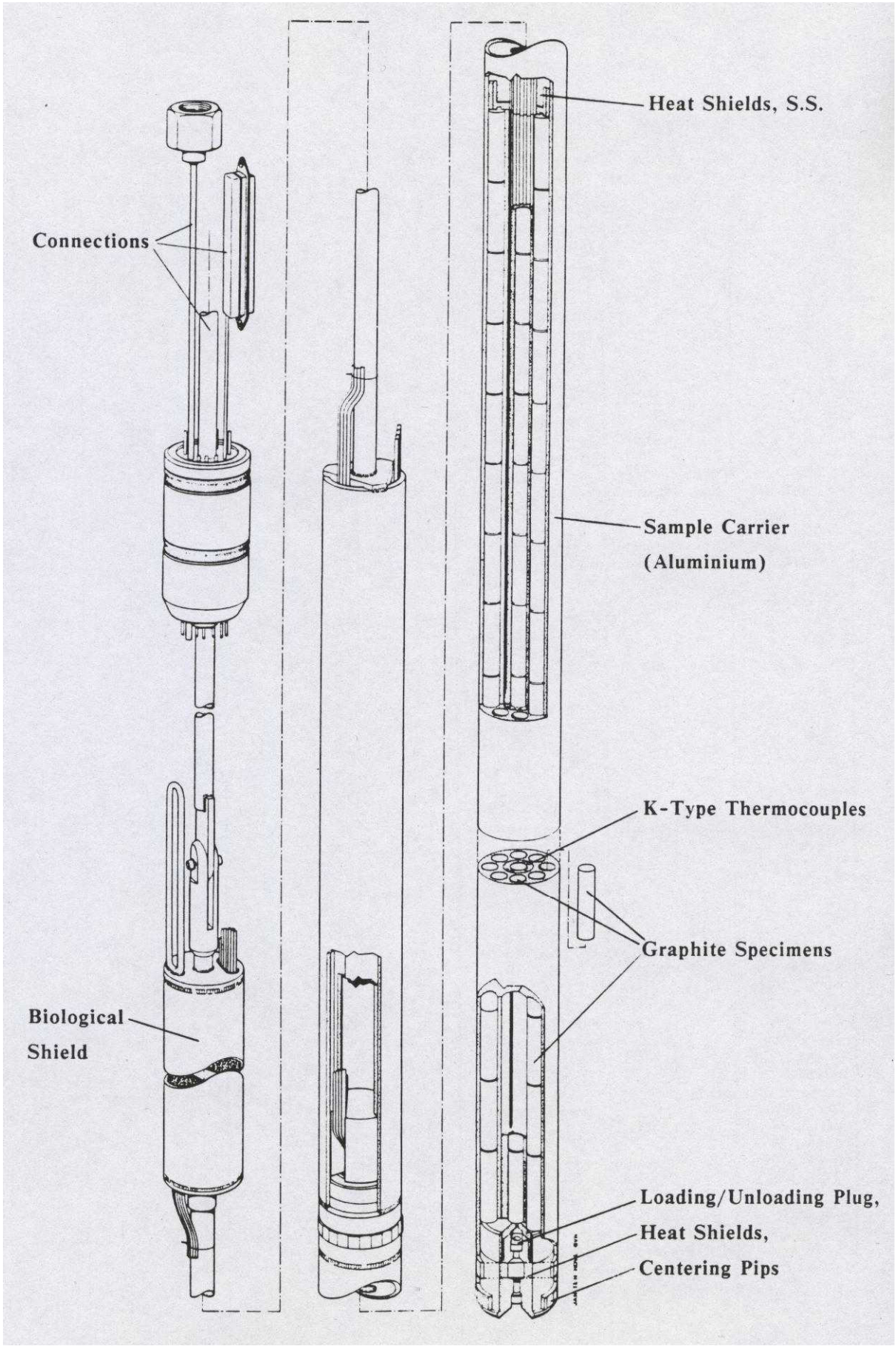

Fig. 17 Graphite irradiation standard sample holder Type 1

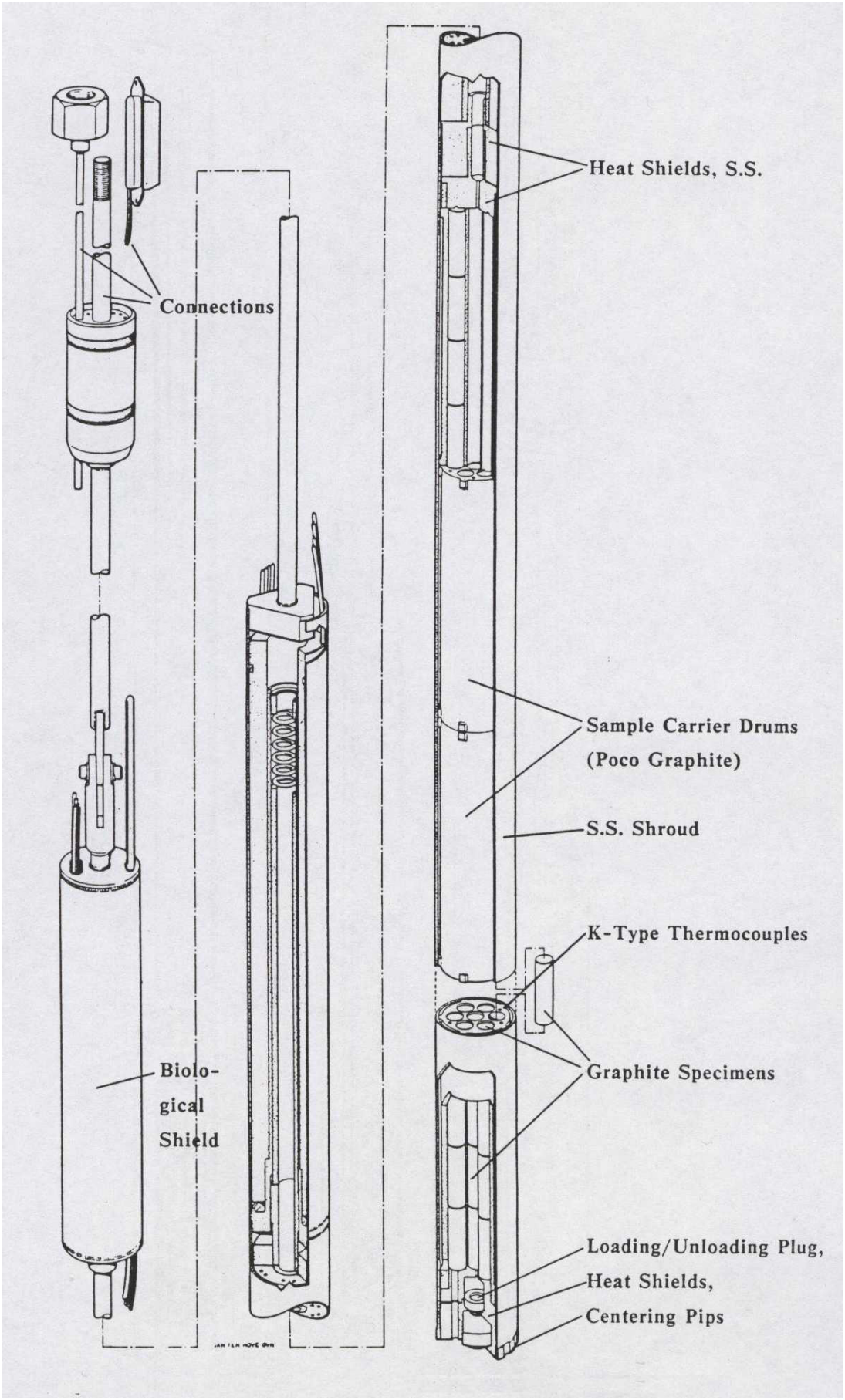

Fig. 18 Graphite irradiation standard sample holder Type 2

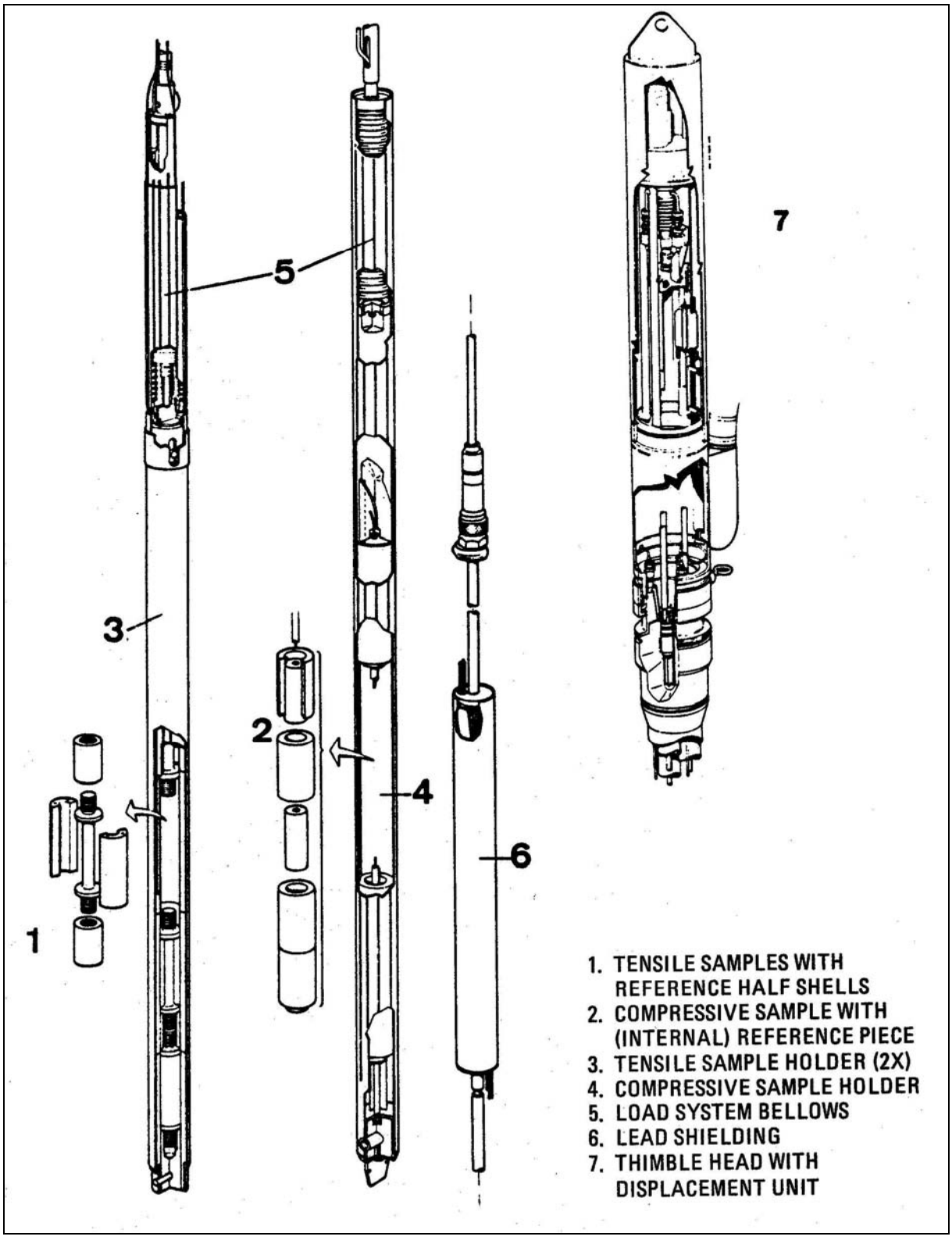

Fig. 19 DISCREET creep facility for fast neutron irradiation of tensile or compressive creep samples under a load of 5 MPa along with unloaded samples

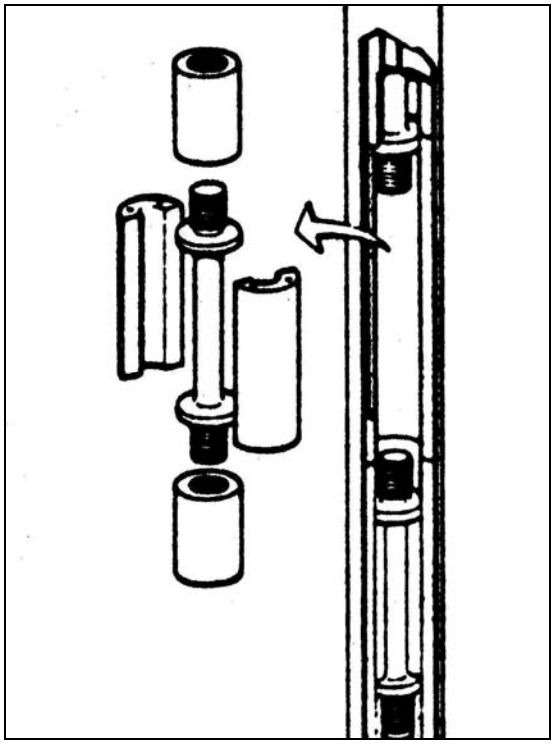

Fig. 20 Tensile creep specimens (dog-bone-shaped) with unloaded reference specimens (half-cylinders)

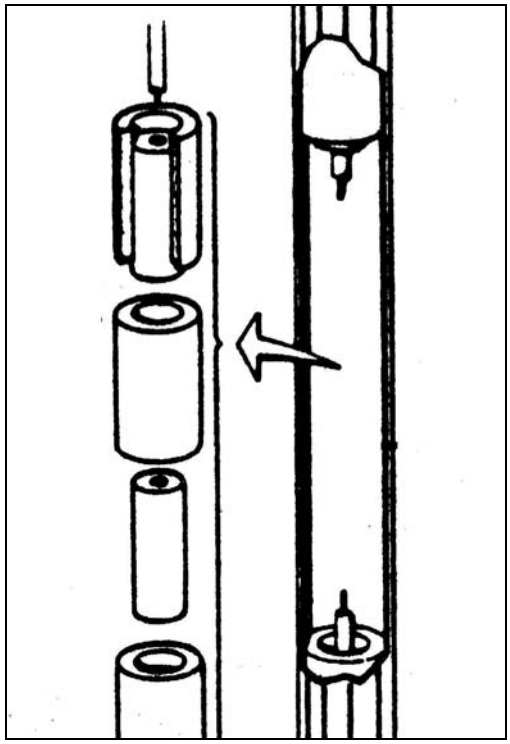

Fig. 21 Compressive creep specimens (hollow cylinders) with internal cylindrical reference specimens

4. REVIEW OF CHARACTERISATION METHODS

4.1 Size and Geometry of Specimens for HFR Petten Irradiation Experiments

The standard geometry of graphite specimens for HFR Petten irradiation experiments was cylindrical with a diameter of 6 mm and length of 25 mm or prismatic 5 mm x 5 mm x 25 mm. These dimensions sometimes are required to fulfil contradictory requirements. Irradiation specimens should be as small (in volume) as possible to make the most effective use of the available space within the irradiation capsule. They must also comply with the requirements of the standardised methods such as DIN, ASTM etc. for the determination of all physical properties under consideration. One of the most important requirements is that the smallest dimension should be at least two times the diameter of the largest structural constituent (e.g., maximum size of filler coke particles) of the graphite to be examined.

Particular aspects may be introduced by the measuring equipment, e.g., samples for measuring thermal conductivity at elevated temperatures using the modified Kohlrausch method had to be cylindrical and 32 mm long with an axial and full length bore of 1 mm diameter.

Tensile creep samples were dog-bone-shaped. The gauge length was an 8-mm-diameter cylinder 50 mm long. Unstressed reference shells of 18 mm outside diameter fitted closely round the gauge length of the tensile samples. Each half-shell was provided with a 1.6 mm diameter through hole suitable for the installation of fluence monitors. Tensile samples were interconnected by means of screwed sleeves having an outside diameter of 18 mm. The entire sample column thus fitted cleanly within an 18-mm-diameter cylinder.

For the design of the compressive creep samples it was considered of overriding importance to select a geometry with strong resistance to buckling. The outside diameter of the samples was 26 mm, which was the maximum that could be accommodated in a TRIO capsule sample carrier. A 16 mm diameter reference sample fitted within a bore of the stressed sample. A 1.6 mm diameter through hole in the reference sample was again provided for the installation of fluence monitors.

4.2 Linear Dimensions

Linear dimensions of standard graphite samples (6 mm ∅ x 25 mm) from the German irradiation programme were measured out-of-pile before and after every irradiation run at the HFR labs at

Petten as well as at the Graphite Laboratory at KFA Jülich since length and diameter are needed for the determination of many other physical properties. The Petten lab used computer-controlled automatic equipment to measure length and diameter simultaneously by means of two inductive transducers which – also computer-controlled – were actuated pneumatically. The specimens were placed side by side in fixed position on a conveying facility, which also moved forward pneumatically after the preceding measurement was finished. Thus, the measurement could be performed without laboratory staff being exposed to gamma radiation from the irradiated graphite samples. At the Jülich graphite laboratory, the length and diameter measurements were performed manually with a wall of lead bricks between the individually measured specimens and the operator. In this case, the measuring device was supplied by LEITZ Co. (vertical length meter) with an accuracy of 0.5 μm. The specimen's lower surface is sucked on a plane table while a calliper gauge is lowered onto the upper surface. The distance is measured optically applying a force of 0.6 N. The reading was automatically recorded by a data logger. From time to time the apparatus was re-calibrated using precision gauge end blocks.

The deformations of creep specimens were also measured out-of-pile in a special measuring jig at pre-determined irradiation intervals during reactor shutdown periods.[18] Experience with previous measurements on graphite indicated that a repeatability of ± 5% could reasonably be achieved. This represented a total length measurement error of about 0.01% in comparison with an expected maximum shrinkage of about 3% and is considered acceptable.

A series of jigs and fixtures specially designed for hot cell use were provided for pre- and post-irradiation measurements. A universal adapter was equipped with a displacement transducer which was connected to a direct reading display unit located outside the cell. Separate jigs, suited to the different samples, locked into the universal adapter in such a way that the face to be measured made contact with the transducer's spring loaded plunger. The system was set up and zeroed after inserting the known reference standard.

Sample dimensional measurements were taken at room temperature and in the unstressed condition. In order to translate dimensional changes to the hot stressed condition, corrections had to be applied for the irradiation-induced changes in Young's modulus and for changes in the coefficient of thermal expansion due to irradiation and creep strain. Changes in Young's modulus due to creep strain had been assumed to be negligible.

4.3 Apparent Density and Open Porosity

The apparent density (or bulk density) was calculated from the linear dimensions, and the mass of the specimens supposed that the geometry of the body was regular. A second measurement of the bulk density was performed according to DIN 51918 (German Standard; “Determination of bulk density by the buoyancy method and the accessible porosity by impregnation with water”). The accessible pores were filled with xylene (instead of water!), and the volume of the specimen was determined from its buoyancy in xylene. This measurement also yields the open porosity from the amount of xylene within the pores. Normally, the two bulk densities are identical within an error limit of 0.15%. However, specimens which are cylindrical at the beginning of irradiation at very high fast neutron fluences may take on an oval cross section because of the graphite texture, or they may bend as a consequence of inner stresses due to irradiation. In these cases, the geometrically determined bulk density is no longer correct whereas the buoyancy measurement still remains reliable.

4.4 Electrical Resistivity

The electrical resistivity was determined out-of-pile by the Petten laboratory. Again automatic equipment similar to the dimension measuring device was used. The electrical resistivity was measured using the so-called 4-point method according to DIN 51911 (“Determination of electrical resistivity by the current voltage method”). A constant current is passed through the specimen. The electrical resistivity is calculated from the voltage drop between two potential contacts on the surface of the specimen, from the total current intensity, the distance between the potential contacts, and the cross section of the specimen. The error limit of the electrical resistivity measurement is 3 to 5%.

4.5 Dynamic Young’s Modulus

Resonant longitudinal oscillations are activated by a pulse generator in the specimen to be measured. The resonance frequency of the fundamental oscillation determines the sound velocity, and the dynamic Young’s modulus is then calculated from the bulk density and the sound velocity. This method was applied out-of-pile to the irradiation specimens at the Petten laboratory again using automatic equipment. According to the respective standard DIN 51915 (“Determination of dynamic Young’s modulus of elasticity by the resonance method”) the error limit achieved by this method is about 3 to 5%.

4.6 Linear Thermal Expansion Coefficient

The coefficient of linear thermal expansion was measured in the Jülich Graphite Laboratory in accordance with DIN 51909 (“Determination of coefficient of linear thermal expansion”) using commercial push-rod dilatometers. The specimen is contained in a sample holder made of low-thermal-expansion material, such as flint glass. It is heated in a furnace and the length change is transmitted by a push-rod to an optical or electronic measuring system outside the furnace. The average linear thermal expansion coefficient is calculated from the measured length change, the original length, and the temperature change of the test specimen, taking the expansion of the sample holder and the push-rod into account. For industrial applications, the thermal expansion coefficient is mostly determined in the temperature range from room temperature to 200°C. However, for nuclear graphite the thermal expansion coefficient at operating temperature is important. Therefore, the measurement is extended from room temperature up to irradiation temperature.

One of the most favourable properties of graphite for nuclear reactor applications is its very small thermal expansion coefficient, which is smaller by a factor of about 10 than for many metals. As a consequence, it is much harder to determine and needs careful sample preparation, maintenance of the measuring device and temperature control. First of all, the dilatometer must be well calibrated and the specimen carefully adjusted within the sample holder, so that a reliable length change is measured during the whole measuring procedure. It has also been found that the temperature distribution along the axis of the furnace must be constant at least over the length of the sample, and the temperature change rate must not exceed 5 K/min in order to keep the whole specimen at the same temperature. If the test specimen is heated to temperatures above 300°C, oxidation must be avoided by applying protective gas or vacuum.

A special aspect of measuring the thermal expansion coefficient of irradiated graphite is that the irradiation temperature must not be exceeded by more than about 50 K at any time to avoid annealing of irradiation damage.

In the temperature range from 20 to 200°C or higher the accuracy of the method is about 1 to 2 % for samples longer than 20 mm.

4.7 Thermal Conductivity

For the determination of thermal conductivity, two different methods have been used at KFA Jülich. One of these is performed at about room temperature, whereas the other one can take measurements at any temperature between 100 and 1000°C, or can measure the thermal conductivity continuously in the whole temperature range under consideration.

Room temperature thermal conductivity was determined following DIN 51908 (“Determination of thermal conductivity at room temperature by means of a comparative method”). The test specimen, placed in series with a specimen of known thermal conductivity, is clamped between two measuring heads, which are kept at 20°C and 40°C, respectively. The temperature drop occurring in the reference specimen, which is measured as a thermoelectric voltage by means of a fixed differential thermocouple element, yields the thermal conductivity of the test specimen at about 30°C.

Thermal conductivity at temperatures from 100 to 1000 °C is measured according to the so-called ‘modified KOHLRAUSCH method’ described elsewhere[19]. This method only became available after 1974. Till then, many laboratories had measured thermal conductivity and its changes due to fast neutron irradiation only at room temperature, hoping that room temperature data could be converted to high temperature data just by calculations based on a convenient model. This model was presented by B.T. Kelly[20]. Many years later, when enough experimental data on the high-temperature thermal conductivity of many different nuclear graphites from the German irradiation programme had become available, G. Haag[21] verified Kelly’s model and thus made the enormous amount of room temperature data available for design calculations.

5. RADIATION DAMAGE IN NUCLEAR GRAPHITE

5.1 Structure of polycrystalline graphite

Graphite is a synthetic material exhibiting a very complex structure. It consists of almost pure carbon. Its basic structural element is the hexagonal carbon lattice, which is thermally the most stable modification. Nevertheless, a carbon body as used in most technical applications has a polycrystalline structure. This structure is determined by the structure and properties of the raw materials and by the manufacturing process. On closer examination of the surface of a piece of nuclear graphite by means of an optical microscope (Fig. 22), one can see the coke particles (sometimes called filler particles) and binder coke regions, as well as pores with sizes larger than about 10 μm between the filler particles.

After increasing the magnification by a factor of about 5000, the crystallites become visible as the main constituents of the coke particles. Between the crystallites there are micropores which are important for the thermal expansion as well as for the dimensional changes of bulk graphite due to fast neutron irradiation. Their size is about a few hundred angstroms.

After once more increasing the magnification of a fictitious microscope, one could see the graphitic lattice structure with the carbon layer planes exhibiting an interlayer spacing of 3.35 Å in an ideal graphite crystallite. This ideal graphite lattice is shown in Fig. 23.

In principle, the binder coke regions amongst the filler particles have a similar crystallite structure. However, the crystallites are much smaller and less perfect. Hence, their changes due to fast neutron irradiation are slightly different from the irradiation behaviour of filler particle crystallites.

Manufacturing of graphite is based on the main raw materials of filler coke and carbonaceous binder, which are mixed and pressed yielding large blocks typically up to 500 mm ∅ and 2000 mm long. These blocks are subjected to repeated high-temperature treatments, such as baking at about 1000°C, to remove most of the non-carbon constituents, and finally graphitisation at temperatures of 2600 to 3000 °C to achieve the highest possible crystalline structure accompanied by a release of most of the remaining impurities.

The production of polycrystalline graphite is a large-scale process, which is not fully controllable. As a consequence, the resulting products exhibit batch-to-batch and even block-to-block

variation of their properties. One of the main questions arising when new graphites are to be developed is whether there are dominant parameters determining the “character” of graphites.

No matter how different the properties of graphite may be, there are some features which are characteristic and in some cases make a typical difference between graphite and, for example, metals. First of all, attention must be directed to anisotropy, which is based on the anisotropy of the graphite single crystal (see Fig. 23), and is extremely important with respect to graphite as a nuclear material. Apart from that, it is mainly the mechanical properties of graphite which make the difference, and which define the class of materials called ceramics. Some examples will be given in the following.

Normally, graphite is rather sensitive to tensile stresses. Fracture strains are generally of the order of 0.2%. Tensile strength is much lower than compressive strength, and fracture toughness is low, too. Fracture probability can be appreciable even at low stresses as there is a large scatter of stress data. Nevertheless, graphite is very resistant to thermal shock, as a result of a high heat conductivity and a low thermal expansion coefficient, and even at the highest temperatures of interest for nuclear applications thermal creep is negligible.

5.2 Basic Effects of Radiation On the Graphite Lattice Structure

Radiation induces permanent effects in solids either by displacing atoms or by exciting electrons into higher metastable energy levels.[22]

During the fast neutron radiation bombardment of a solid, the incident particle transfers its energy either by exciting the electrons in the solid or by colliding with its atoms. Because electron excitation can occur only when the incident particle is charged, the primary interaction in the case of neutron bombardment is always a collision (Fig. 24). In a collision with a fast neutron, the struck atom will be displaced and can in turn act as an energetic bombarding particle. This moving displaced atom is called the "primary knock-on atom." If it displaces other atoms, these atoms are called "secondary knock-on atoms," etc. Knock-on atoms will generally be ionised and may therefore lose a significant portion of their energy by electron excitation.

The maximum energy which can be transferred to a nucleus of atomic weight A by a neutron of energy E in a purely elastic collision is:

$$\Delta E = \frac{4 \cdot A}{(A+1)^2} E_n$$

which for ^{12}C is ΔE = 0.284 E_n. (This large portion of neutron energy transferred in a collision between a neutron and a carbon nucleus is one of the main reasons for using graphite as a moderator in nuclear reactors.)

The energy of the neutrons covers a wide range, from thermal energy to the order of 10 MeV, with a mean energy of about 1 to 2 MeV. Every fast neutron moderated in graphite knocks several thousand atoms from their lattice sites. Residual displacement damage is the effect of neutron radiation on the graphite crystal (Fig. 25). Carbon atoms in the hexagonal layer planes are displaced to form interstitials between the layer planes, leaving vacancies within the planes, and causing the lattice to expand in the direction perpendicular to the layer planes (c-direction). The crystal lattice is severely distorted by radiation damage, and energy storage must be a real consideration. The residual displacement is largely a function of the irradiation temperature and hence the mobility of the interstitials. At cryogenic temperatures the interstitials are essentially immobile forming point defects.

On the other hand, the capability of gamma radiation to cause damage to the graphite lattice is very small. Sometimes strange effects are attributed to gamma radiation, but there is a large degree of agreement that the influence of gamma radiation is in the order of 5 % of that of fast neutrons.

As the temperature increases to around 300 to 350°C and higher, single interstitial atoms become mobile. Migrating through the lattice they can either recombine with vacancies so that the irradiation damage is removed and the c-direction expansion is reduced. Or they form interstitial clusters with the consequence that they can no longer recombine with vacancies and the c-direction expansion can no longer be annealed. As they continue to cluster, new lattice planes are formed.

At even higher temperatures (above 500°C), vacancies also become mobile and migrate to the crystallite boundaries where they disappear, causing a contraction of the crystallites in the a-direction, or they coalesce to larger vacancy clusters. These vacancy clusters are believed to cause the lattice planes to collapse, again leading to a contraction of the crystallites and hence of the piece of graphite.

The more time vacancies need to get to the crystallite boundaries, the higher is the probability of meeting a single interstitial for recombination. Therefore, more perfect crystalline graphite with a large crystallite size undergoes less radiation damage than less graphitised material. This is the main reason for reactor graphite being graphitised at temperatures close to 3000°C.

5.3 Graphite Property Changes due to Fast Neutron Irradiation

The reason for bulk dimensional changes of graphite due to fast neutron irradiation is the deformation of the graphite lattice as discussed above. The effects are monitored by measuring changes in dimension and physical properties. The purpose of this section is to discuss these changes in detail. This will be illustrated by figures which indicate typical graphite behaviour but do not necessarily describe the performance of any particular graphite. In addition, the property changes are illustrated at two irradiation temperatures T_1, T_2. Effects due to anisotropy have already been demonstrated, for example, in Fig. 1a-d, and are therefore not considered here.

5.3.1 Dimensional changes

The dimensional changes are normally expressed as isothermal curves based on room temperature measurements as shown in Fig. 26 for two irradiation temperatures $T_1 < T_2$, and without considering anisotropy, which is discussed elsewhere.

For more than 20 years solid state physics has tried to explain the radiation-induced dimensional changes of graphite by a theory based on physical properties of the crystallites. It was believed that the relative linear dimensional change with increasing fast neutron fluence can be described by the equation[23],[24]

$$\frac{1}{l_x}\frac{dl_x}{d\gamma} = A_x \frac{1}{X_c}\frac{dX_c}{d\gamma} + (1-A_x)\frac{1}{X_a}\frac{dX_a}{d\gamma}$$

where l is the length of the body in a given direction x,

γ is the fast neutron fluence,

X_a , X_c are the crystallite dimensions in the a and c axis directions, respectively,

A_x is an accommodation coefficient relevant to a direction x.

The accommodation coefficient A_x can be determined from the thermal expansion coefficient (α_x) of the graphite and that of a single crystal graphite $(\alpha_a$ and $\alpha_c)$ by the equation

$$\alpha_x = A_x\,\alpha_c + (1-A_x)\,\alpha_a$$

However, this so-called *single phase model* cannot be completely satisfactory since it does not take into account the fact that the structure of polycrystalline graphite is much more complex. Thus, the averaging techniques required to render the single-crystal dimensional changes in

polycrystalline graphite changes must include the additional effects of porosity changes and shearing stresses. This has not been achieved so far.

While the mechanism of initial shrinkage is not well understood, the effects causing shrinkage reversal to growth are at least qualitatively known. Before turn-around, the shrinkage of the dimensions leads to an increase in density and a reduction of porosity. After turn-around the volume increase occurs by an increase of porosity. Both effects, decreasing porosity before and increasing porosity after turn-around, can be observed by optical microscopy with graphites before and after irradiation (Fig. 27a-c).

5.3.2 Thermal expansion coefficient

Due to its porosity, graphite is a material with an extremely low thermal expansion. The lattice thermal expansion of the crystallites is buffered by the small and intermediate pores adjacent to the crystallites, and is therefore not entirely transferred to the bulk geometry. This mechanism is similar to events caused by fast neutron irradiation, i.e. the dimensional changes of crystallites due to radiation damage and their effect on the bulk geometry.

The changes in the thermal expansion coefficient during fast neutron irradiation are monitored by measuring the mean coefficient between 20°C and a given temperature, which may be the irradiation temperature (ambient temperature during reactor operation).

Fig. 28 shows a typical variation of the mean coefficient (20 to 120 °C) with fast neutron flux at two irradiation temperatures $T_1 < T_2$ reflecting the strong dependence upon pore structure. The initial rise results from a porosity decrease due to the c-direction growth of crystallites. It is followed by a steady decrease when new pores are increasingly generated by the shrinkage of crystallites in the a-direction. This decrease is more rapid at the higher irradiation temperature according to the higher mobility of lattice vacancies at higher temperatures. The decrease of the thermal expansion coefficient tends to level out at a low value at high fluences well beyond the point of shrinkage reversal. In this state, the bulk dimensional behaviour of graphite due to fast neutron irradiation is dominated by macroscopic pore generation which has almost no effect on thermal expansion properties.

5.3.3 Thermal conductivity

In order to maintain the safety features for which the high-temperature reactor is known, more and more attention has to be directed to the thermal conductivity of the side reflector graphite after significant fast neutron irradiation.

It is well known that thermal conductivity decreases very rapidly with increasing neutron fluence. However, a minimum thermal conductivity must be available at all times to remove the afterheat from the HTR core in case of a loss of pressure accident, thus preventing the fuel temperature from exceeding the limit of about 1600°C, at which temperature release of some fission products has been proven to start. Therefore, calculations of the temperature distribution within the reactor core during normal operation as well as in the case of severe accidents require the thermal conductivity of reflector graphite at various temperatures.

Since graphite is a metallic-type conductor of electricity[25], it might be anticipated that the electrons and holes that are responsible for the conduction of electricity would also transport heat. However, all evidence indicates that heat is transferred by lattice vibrations (phonons) rather than by electrons or holes. For example, in graphite the Wiedemann-Franz ratio (R_{WF}) defined by $R_{WF} = K \cdot \rho / T$ (K is the thermal conductivity, T the absolute temperature, and ρ the electrical resistivity) is much larger than in metals. For electronic conductors of heat, the value of R_{WF} is predicted by the theory to be a universal constant equal to 2.45 $\Omega \cdot W/K^2$. In most metals the observed value is between 2 and 3. However, in both single-crystal and polycrystalline graphite, the observed value of R_{WF} is 10 to 100 times larger. In addition, it has been found that drastic changes in the charge carrier population produced by doping graphite with boron has only a slight effect on thermal conductivity[26]. These facts imply that electronic conduction is not the primary mode of heat transfer in graphite.

It is characteristic of such processes that as the temperature is reduced the thermal conductivity becomes a function of the crystallite size. Scattering of phonons at the crystal boundaries limits the mean free path for the phonons. The thermal conductivity is given approximately by $K = {}^1/_3 \cdot C_p \cdot \lambda \cdot v$, where C_p is the specific heat, λ is the phonon mean free path, and v is the phonon velocity.

The thermal conductivity of unirradiated reactor graphite as a function of temperature, $(K_0)_T$, has a characteristic shape determined by crystallite size and a level determined by orientation, crystallite perfection, and porosity effects. Fig. 29 shows the temperature dependence for near-isotropic graphites normalised to unity at room temperature. The fact that there is a marked dependence of thermal conductivity on the measuring temperature causes a problem which was not taken seriously for a long time.

Measurements of thermal conductivity at room temperature are fairly easy. Cheap equipment is available on the market. Therefore, almost all measurements of thermal conductivity were made at room temperature, and also its behaviour under neutron irradiation was investigated at room temperature. However, this is not what engineers need to design a nuclear reactor. They must

know the thermal conductivity at operating temperatures, i.e., in the range up to 1000°C or even higher. All thermal conductivity data gathered at room temperature are useless unless there is a theory available to determine thermal conductivities at operating temperature from thermal conductivities at room temperature.

Effects of fast neutron irradiation on polycrystalline graphite can be monitored by the fractional change in thermal resistance measured at room temperature, $\left(\frac{K_0}{K} - 1\right)_{20}$, with K_0, K being the thermal conductivity before and after irradiation, respectively, as a function of irradiation fluence and irradiation temperature. The overall changes are comprised of within-crystal effects established at low fluences and superimposed structural changes at high fluences.

The initial effect of fast neutron irradiation is a rapid increase in thermal resistance $(1/K)_T$ towards a level determined by the irradiation temperature. This 'within-crystal' effect is caused by phonon scattering at irradiation-induced defects.

At higher irradiation fluxes, the thermal resistance increases further as porosity generation resulting from shrinkage reversal to growth becomes important, at a flux level which decreases with increasing irradiation temperature. Fig. 30 shows the typical pattern of thermal resistance changes, measured at room temperature, as a function of neutron fluence at two irradiation temperatures $T_1 < T_2$.

From the results of the previously mentioned study on high-temperature thermal conductivity data obtained at FZJ, two results of general importance shall be mentioned here. One is the discovery that the saturation level of the thermal resistivity curves is temperature- but not material-dependent. In other words, there is a relation between the irradiation (and hence measuring) temperature and the saturation level for all graphites so far considered (Table 4).

The second result is that the further decrease of thermal conductivity (or, the further increase of thermal resistance) at high fluences (the so-called secondary breakdown) can be related to the volume changes of the graphite due to irradiation. The coincidence of the turn-around of dimensional or volume changes and the starting point of the secondary breakdown of thermal conductivity can be clearly seen from Fig. 31 and Fig. 32, where irradiation data of the Gilsonite coke graphite IM2-24 are plotted using identically scaled fluence axes.

This proves, as said before, that the "secondary breakdown" is caused by pore generation and not by within-crystal effects.

A mathematical function to describe the secondary breakdown as exhibited in Fig. 31 and Fig. 32 is given by the equation

Irradiation Temperature T/**°C**	**Saturation Level for Measurements at Temperature T** **(K/K_0 -1) ·100**	**Saturation Level for Measurements at Room Temperature** **(K/K_0 -1) ·100**
300	-90	-93
400	-78	-87
500	-68	-80
600	-61	-75
750	-51	-70
850	-47	-69
900	-45	-68
950	-44	-67
1050	-38	-64
1250	-33	-62

Table 4 Saturation levels of relative thermal conductivity changes due to fast neutron irradiation, derived empirically from data for several different nuclear graphites

$$\left(\frac{k_0}{k}-1\right)_T = S_T + A\cdot V_R(T)\cdot(\gamma-\gamma_0) \quad \text{for } \gamma > \gamma_0 \text{ only,}$$

where

S_T is the saturation level of thermal resistivity change at irradiation temperature T,

A is a parameter to be determined empirically,

γ is the fast neutron fluence (10^{25}/m^2 (EDN)),

γ_0 is the fast neutron fluence (10^{25}/m^2 (EDN)) at turn-around.

$$V_R(\gamma,T) = \left(\frac{\Delta V}{V_0}(\gamma)\Big/(\frac{\Delta V}{V_0})_{\min}\right)_T - 1$$

$\Delta V/V_0$ is the relative volume change due to fast neutron irradiation,

$(\Delta V/V_0)_{min}$ is the maximum relative volume shrinkage at turn-around.

Using existing data, an empirical value A = -0.15 turned out to be a first approximation for different graphites and different irradiation temperatures. It needs to be checked after additional data are generated in the future.

5.3.4 Electrical resistivity

In one of the most important text books about nuclear graphite[27] one reads of the electrical resistance:

“The mean free path of the conduction electrons in unirradiated electrographites is relatively large, being limited only by scattering at the crystallite boundaries. The introduction of crystal defects by neutron and heavy-particle radiation changes the concentration of the charge carriers (electrons and holes) and also the number of scattering centers. ...

... The effects of reactor radiation on the electrical resistivity of graphite have been measured on a wide variety of materials ranging from graphitized lampblack to carefully selected single crystals. Nuclear graphites, which lie between these two extremes, have been most thoroughly studied. The data on two grades are shown in ... (Fig. 33). In contrast to most other properties, the changes in electrical resistivity rapidly approach a saturation value, and the changes thereafter occur over a long period of time. This rapid approach to saturation has been explained in terms of the relative change in the number of charge carriers and scattering centers. At low doses the increase in the concentration of positive holes is almost balanced by the decrease in the concentration of free electrons, and therefore the increase in resistivity is almost proportional to the number of scattering centers. After a relatively low dose (~200 MWd/At at 30°C), the free-electron concentration is greatly reduced and does not contribute significantly to the conductivity. At this point the increasing concentration of holes counteracts the decreasing mean free path between scattering centers, and the resistivity remains relatively constant.

Although there is little change in electrical resistivity after 200 MWd/At, the changes that continue to occur in the graphite cause the activation energy for annealing electrical resistivity to increase. Apparently the scattering centers become more complex and more difficult to anneal as the structure becomes heavily damaged.

Because the initial resistivity of graphite is strongly dependent on the degree of crystallinity, the fractional increase in resistivity caused by irradiation is also sensitive to the crystallinity. Relatively large differences in the saturation value of fractional resistivities are found, even between different grades of nuclear graphite. The differences in the graphitization temperatures of CSF and TSGBF (2800 and 2450°C, respectively) and the graphitizability of the starting cokes largely account for the different degree of crystallinity and different values of the initial electrical resistivity.”

The physical background of the effects of radiation on electrical resistivity is rather complex. However, “... The impact of changes in electrical resistivity per se on the engineering aspects of

reactor technology has been relatively minor. Such changes have introduced no problems in the operation of graphite-moderated reactors."

In 1957, Primak[28] et al. suggested the use of the electrical resistivity of graphite for monitoring the damaging by fast neutron radiation. However, Fig. 33 proves that the shape of the curves does not allow this as the initial increase is too steep and the following section is too flat.

5.3.5 Young's Modulus

Usually, the effects of fast neutron irradiation on Young's modulus E are plotted as fractional changes of this parameter, $\left(\frac{E}{E_0} - 1\right)$, as a function of irradiation fluence and irradiation temperature. As for thermal resistivity, the observed changes are the combined result of irradiation damage within the crystals established at low fluxes, and superimposed structural changes external to the crystal. For this property however, these structural effects change in character as the fluence increases.

The initial effect of fast neutron irradiation is a rapid increase to a level determined by the irradiation temperature, attributed to the pinning of mobile dislocations within the crystal basal planes by small irradiation-induced defects. At the temperature of interest, the saturation level for this crystal damage is given by data at fast neutron fluences less than about $2 \cdot 10^{21}/\text{cm}^2$. At higher fluences, the Young's modulus starts to increase again relatively slowly with fluence, attributed to a tightening of the structure caused by c-axis growth. This increase continues beyond the point at which the dimensional changes show shrinkage reversal, but eventually the pore generation associated with this phenomenon causes the Young's modulus to decrease, and ultimate values lower than the original modulus have been recorded. This decrease occurs at lower fluxes for higher irradiation temperatures, consistent with the earlier onset of shrinkage reversal. Fig. 34 shows the typical changes at two irradiation temperatures $T_1 < T_2$.

The above discussion refers to measurements at room temperature, but the temperature dependence of Young's modulus is small, and the increase above the room temperature value is only a few per cent up to 500°C.

5.3.6 Tensile Strength

Strength changes due to fast neutron irradiation are also the result of within-crystal effects at low fluences and structural changes at high fluences. If it is assumed that a crack mechanism of failure operates, the so-called Griffith-Irwin-type relationship

$$\sigma_f = \left(\frac{G_{Ic} \cdot E}{2\pi c}\right)^{1/2} = \frac{K_{Ic}}{(2\pi c)^{1/2}}$$

where G_{IC} = strain energy release rate,

K_{IC} = fracture toughness,

E = Young's modulus,

C = one-half the width of the initial defect,

σ_f = fracture stress,

implies that changes within the crystal lattice without changes in the inherent crack population should lead to a strength change proportional to the square root of the modulus change. However, structural changes external to the crystal will influence the effective maximum flaw size as well as the average crack/pore spectrum sampled by the modulus. Hence the overall effect on strength is complex and cannot be expected to depend solely on the modulus changes.

Although strength is one measure of the mechanical properties, fracture toughness is probably a better one under real conditions where stress concentrations are built into the structure. The strength of graphite, or more specifically the change in the probability of fracture, is a very important physical property in the consideration of the useful life of moderator graphite.

The data presentation Fig. 35 compares the fractional strength changes measured in uniform tension for a range of graphites with the modulus changes for a similar range of materials as a function of fast neutron fluence. Fig. 36 shows a similar correlation between relative tensile strength and fast neutron fluence deduced from brittle-ring fracture experiments. The data points are individual results on the irradiated specimens relative to the unirradiated mean for the batch.

The scatter in relative strength change is greater than that in modulus since it reflects the uncertainty in the unirradiated value for the particular specimen tested in addition to the differences between the graphite types.

The dotted curves for the lower temperature data on the strength plot Fig. 35 are either E/E_0 or $(E/E_0)^{½}$, and it is clear that the square root form is the better overall fit at this lower temperature where the pore generation component is not very severe in the fluence range examined.

At high temperatures and fluences, when pore generation is dominant, the fall in strength is greater than would be predicted by the square root relationship. In this regime, i.e. where the

development of pores causes a reduction in both strength and modulus, the changes in these properties are almost linearly related.

5.3.7 Irradiation Induced Creep

The effective lifetime of future high-temperature gas-cooled reactors may ultimately depend upon the integrity of those graphite components which are adjacent to the core and are therefore exposed to the highest fast neutron fluences. The decisive criterion for the integrity will be the magnitude of tensile stresses across the component compared to the tensile strength remaining after irradiation. These stresses are mainly caused by differential dimensional changes due to flux gradients as well as temperature transients. They continue to increase with time due to increasing neutron damage.

Considering that fracture strain of graphite is in the order of 0.2% it may be surprising that graphite can sustain dimensional changes of several percent under fast neutron irradiation without being destroyed. However, there is a mechanism to relieve such stresses which is called ‘irradiation creep’, and which is driven by an external or internal mechanical load. The effect was investigated by special irradiation experiments comparing the dimensional changes under tension as well as under compression with the dimensional changes of unstressed samples.

Fig. 37 shows the irradiation-induced creep strain, ε_c, as a function of fast neutron fluence for a range of near-isotropic graphites irradiated in BR-2 under constant compressive and constant tensile stresses of about 6 MN/m^2 within the irradiation temperature range of 300 to 650 °C.[29] The secondary creep rate for fluences above $10 \cdot 10^{20}$/cm^2 (DNE) appears to be linear with the fluence whereas the value extrapolated to zero fluence is equal to the elastic strain. Normalised to the elastic strain the data are well represented by the equation

$$\frac{\varepsilon_c}{\sigma / E_0} = 1 + 0.23\,\gamma$$

where γ is the equivalent Dido nickel fluence in units 10^{20}/cm^2,

σ is the applied stress,

E_0 is the unirradiated Young’s modulus obtained in a static test to stress σ.

The same expression relating creep and elastic strain was also found in the BR-2 reactor for more anisotropic graphites with widely differing Young’s moduli, and was further substantiated both by comparisons with other experimental data and by experiments on samples pre-oxidised

to different weight losses, producing large modulus reductions.[30] In addition, there is no evidence of temperature dependence in the range from 300 to 650°C.

Irradiation creep may also affect some material properties. There is believed to be a lower coefficient of thermal expansion (CTE) for tensile and a higher CTE for compressive creep compared to that for unloaded specimens.

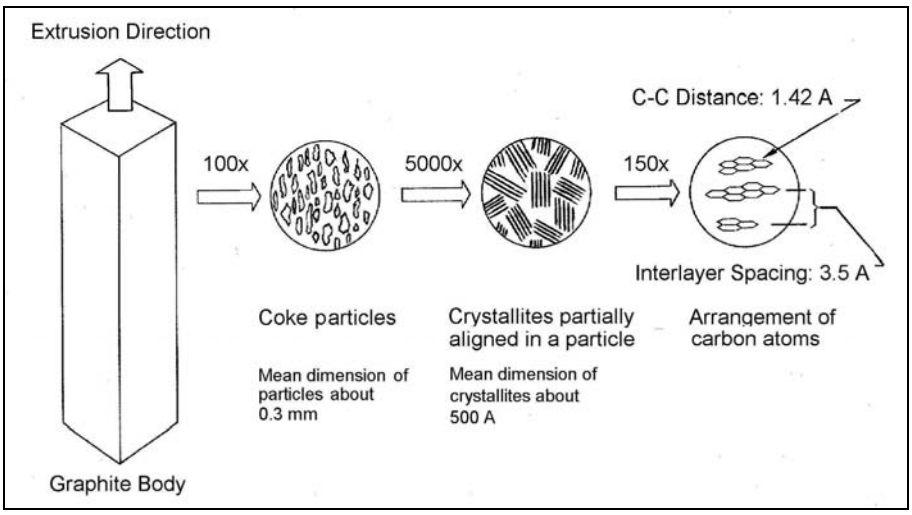

Fig. 22 Polycrystalline structure of artificial graphite [31]

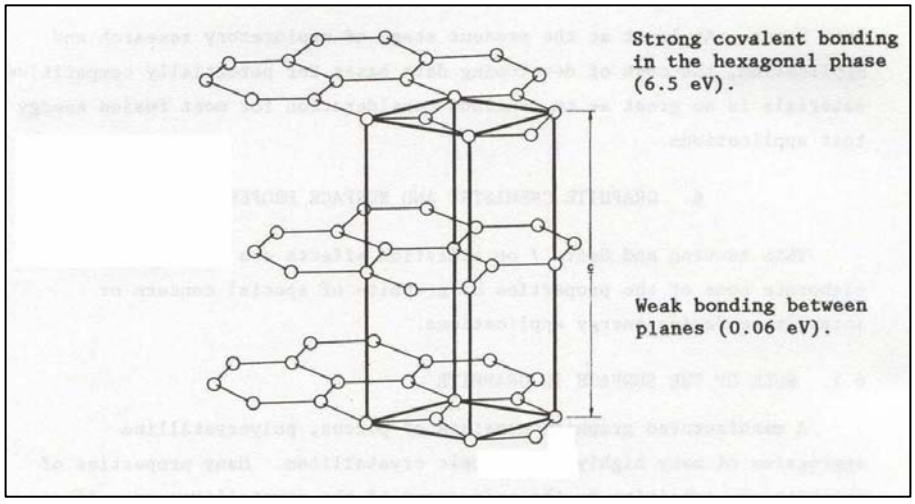

Fig. 23 Graphite single crystal structure [32]

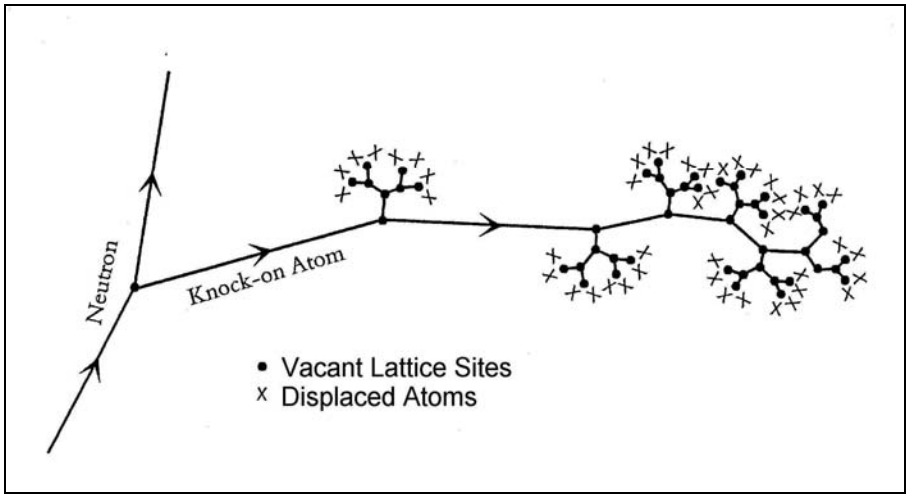

Fig. 24 Radiation damage spikes in graphite

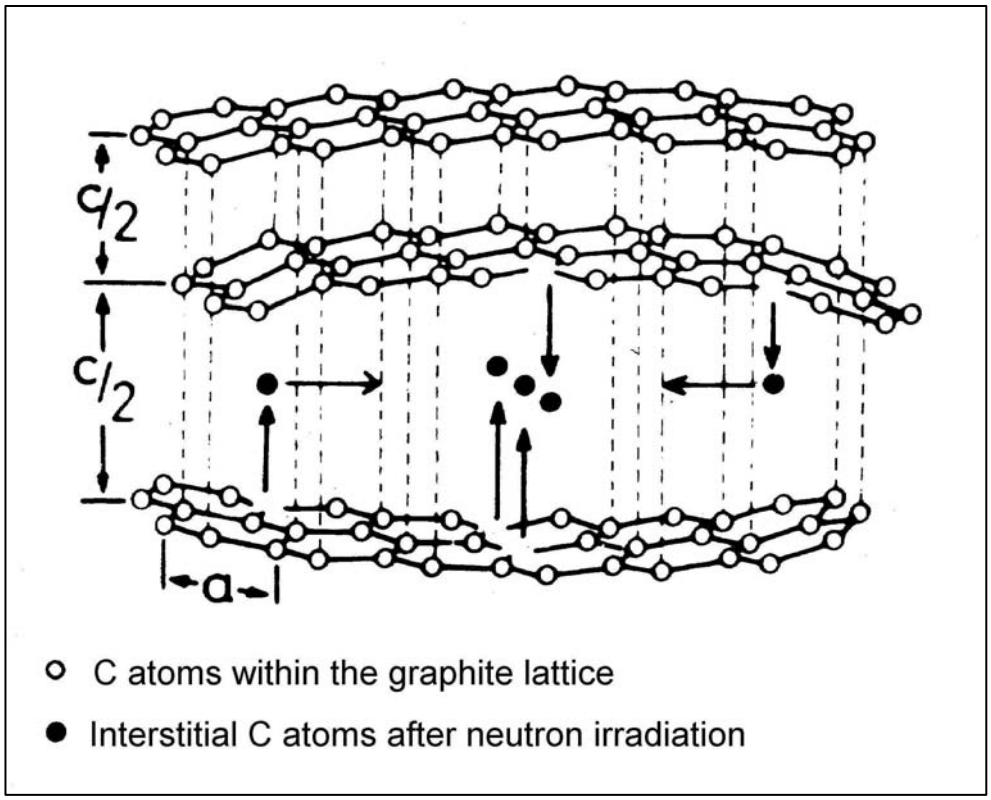

Fig. 25 Graphite crystallite radiation damage

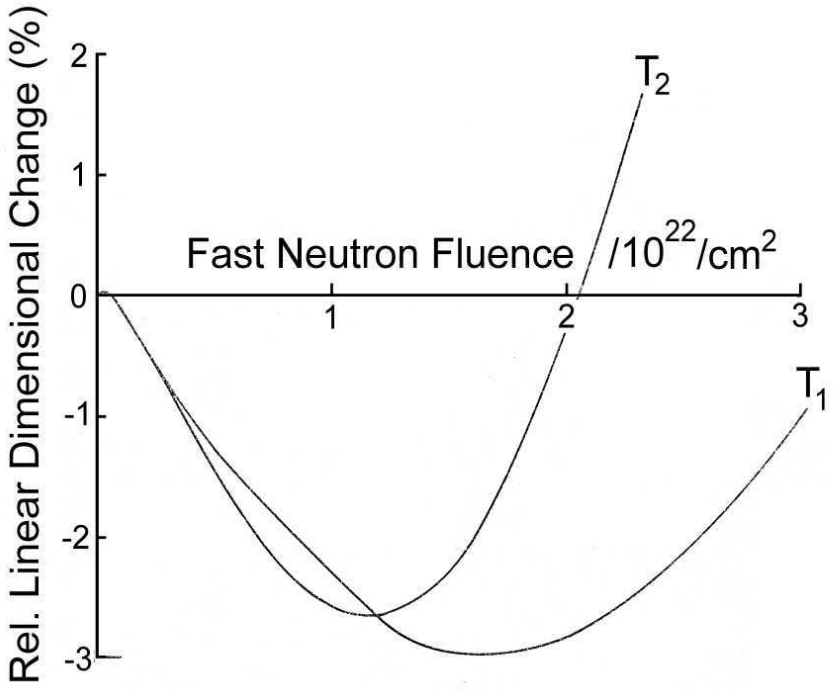

Fig. 26 Relative linear dimensional changes due to fast neutron irradiation for two different irradiation temperatures $T_1 < T_2$

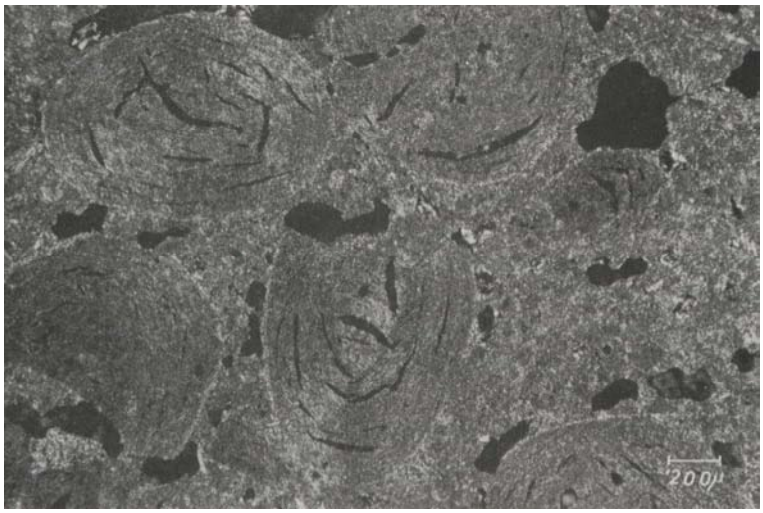

Fig. 27a Pores in unirradiated Gilsonite graphite

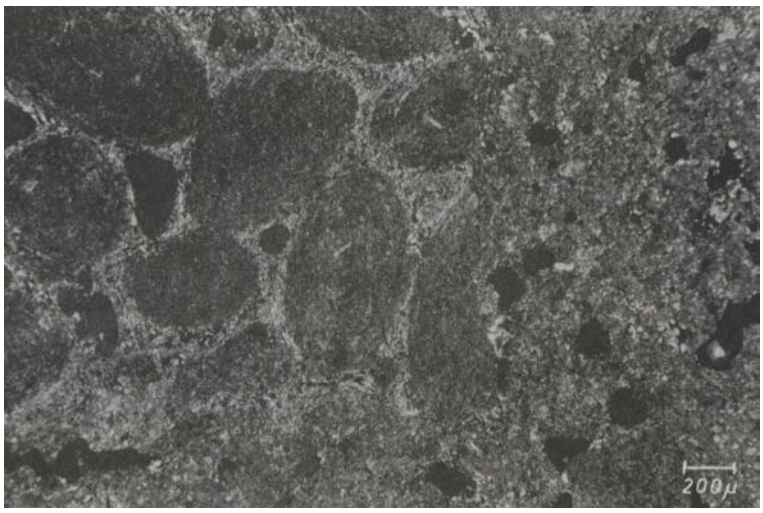

Fig. 27b Pores in Gilsonite graphite irradiated to turn-around

Fig. 27c Pores in Gilsonite graphite irradiated beyond turn-around

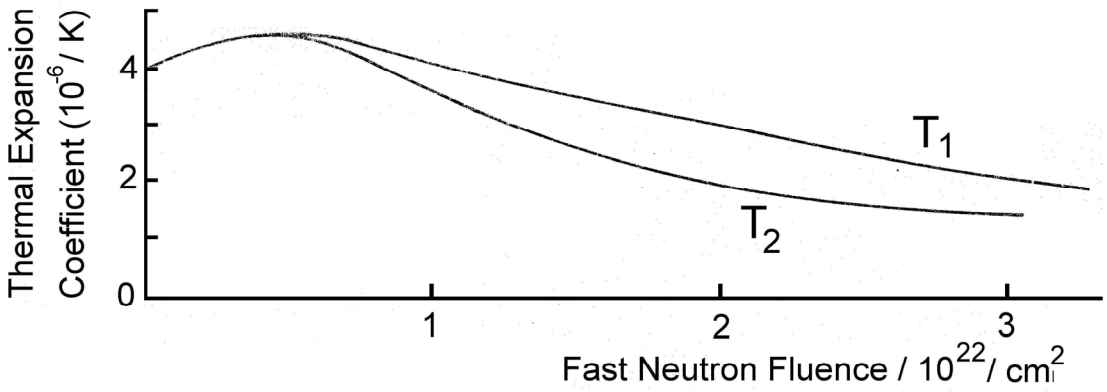

Fig. 28 Thermal expansion coefficient (CTE) as a function of fast neutron fluence for two different irradiation temperatures $T_1 < T_2$.

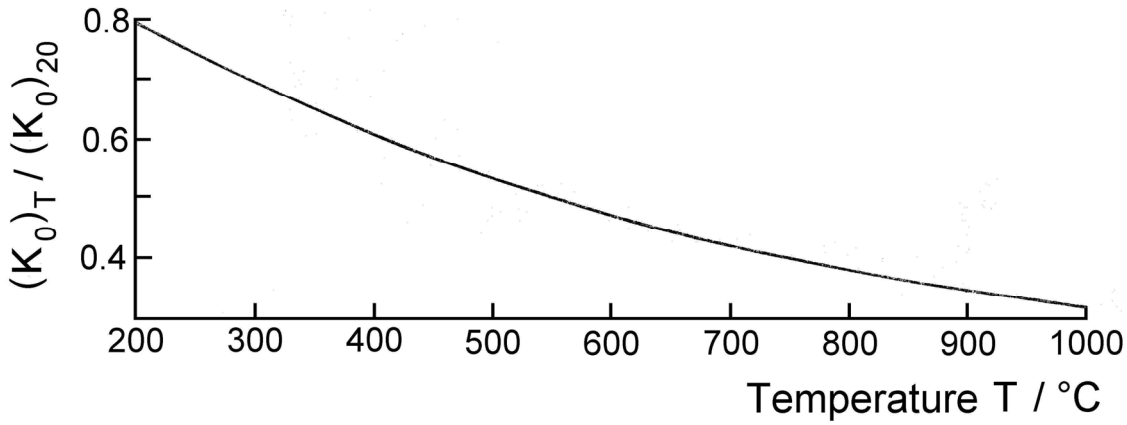

Fig. 29 Thermal conductivity of unirradiated graphite vs measuring temperature

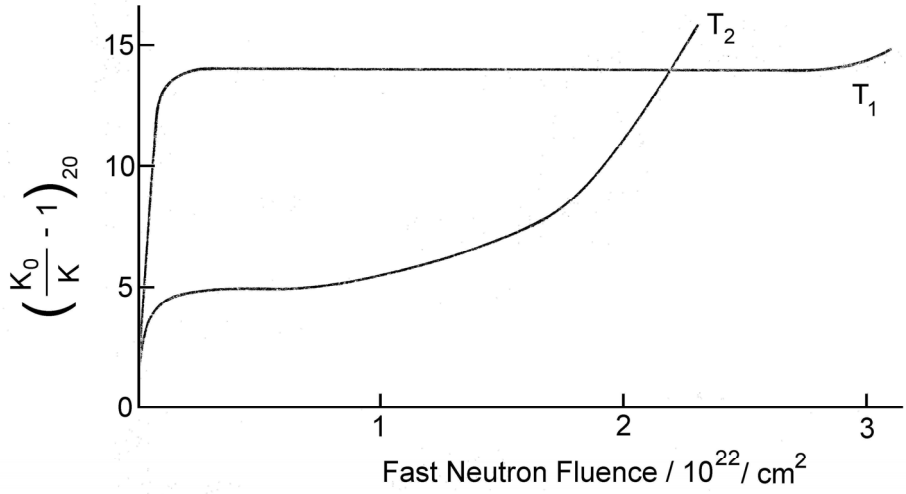

Fig. 30 Thermal resistivity changes of graphite due to fast neutron irradiation for two different irradiation temperatures $T_1 < T_2$

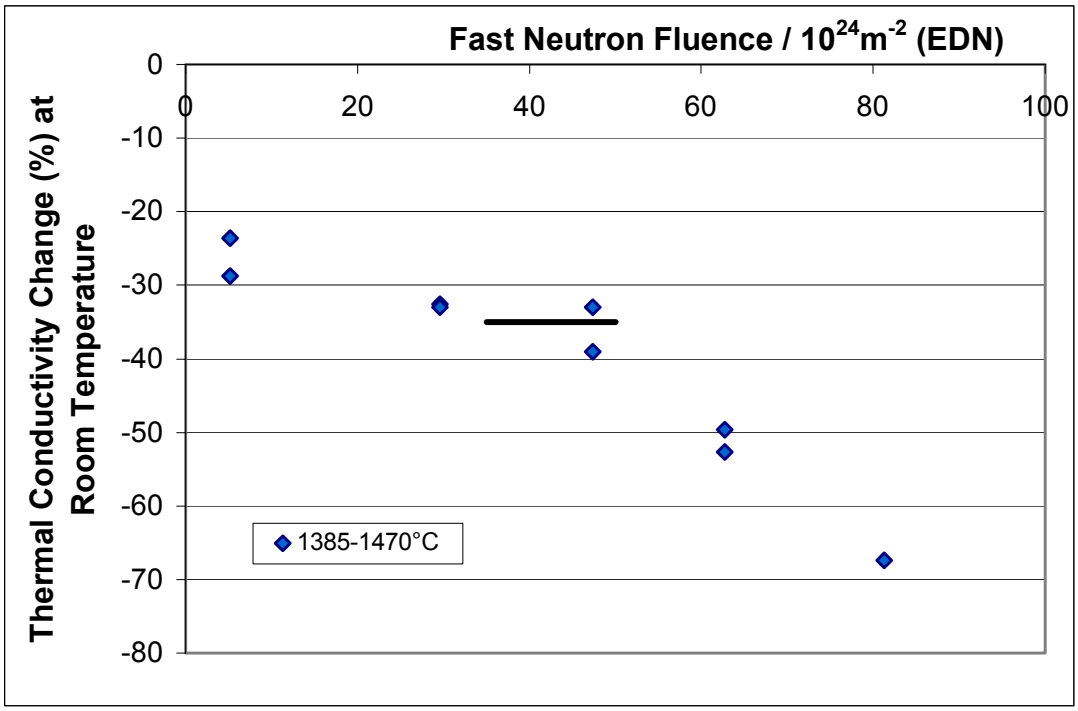

Fig. 31 Thermal conductivity changes of IM2-24 graphite due to fast neutron irradiation at about 1400°C, measured at room temperature

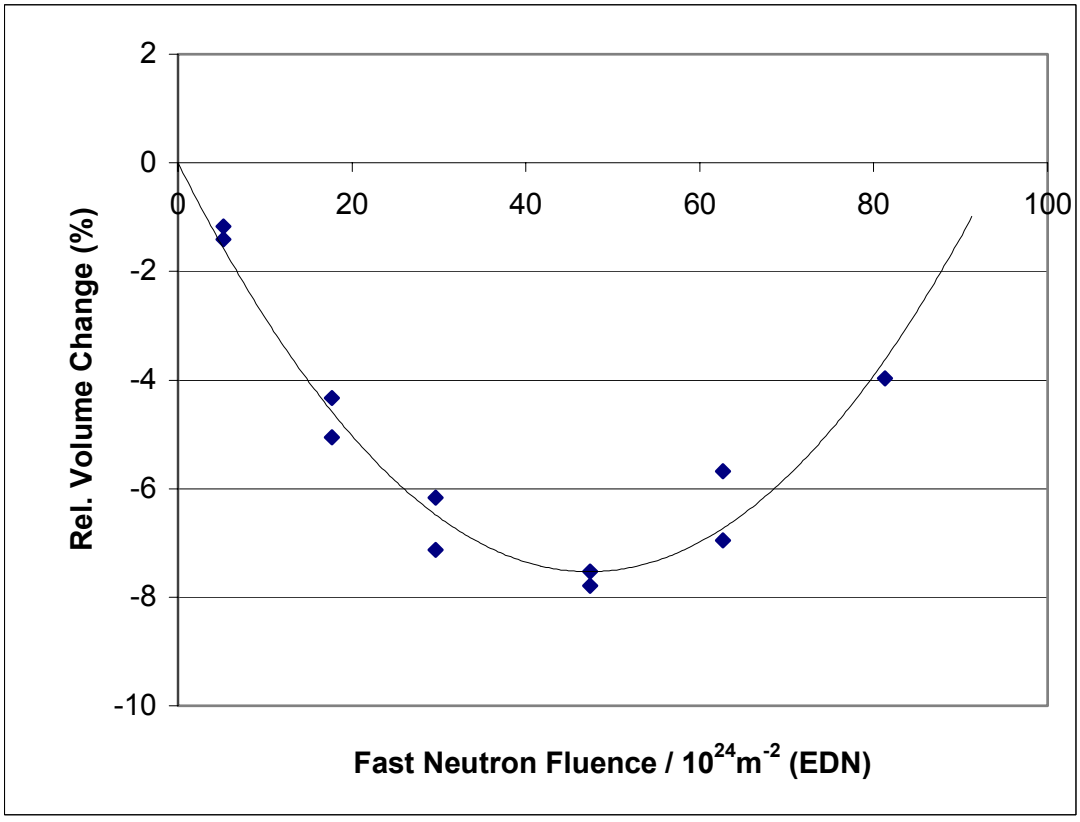

Fig. 32 Relative volume changes of IM2-24 graphite due to fast neutron irradiation at about 1400°C

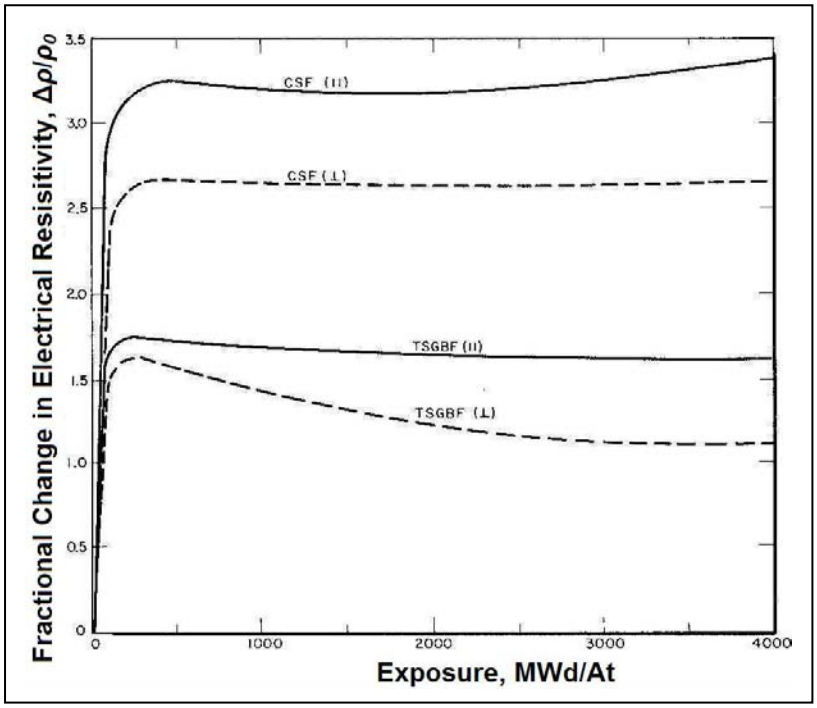

Fig. 33
Fractional change in room temperature electrical resistivity of CSF and TSGBF graphites due to irradiation [33]

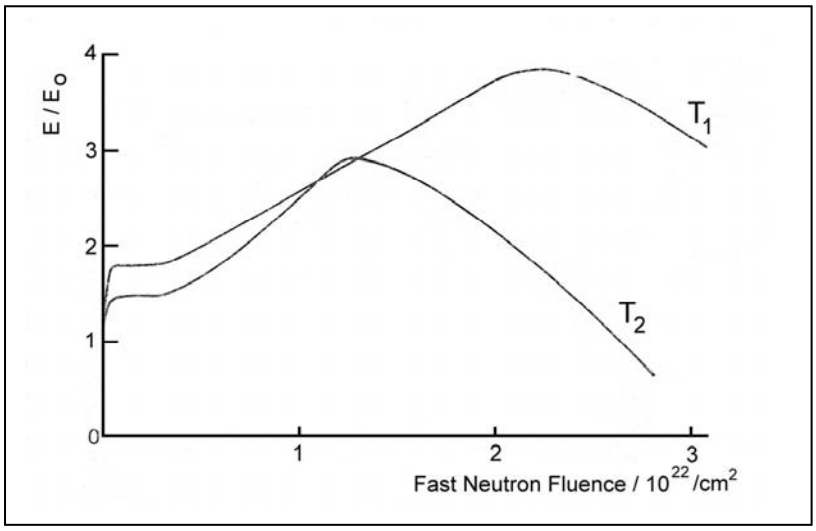

Fig. 34
Young's modulus changes of graphite due to fast neutron irradiation for two different irradiation temperatures $T_1 < T_2$

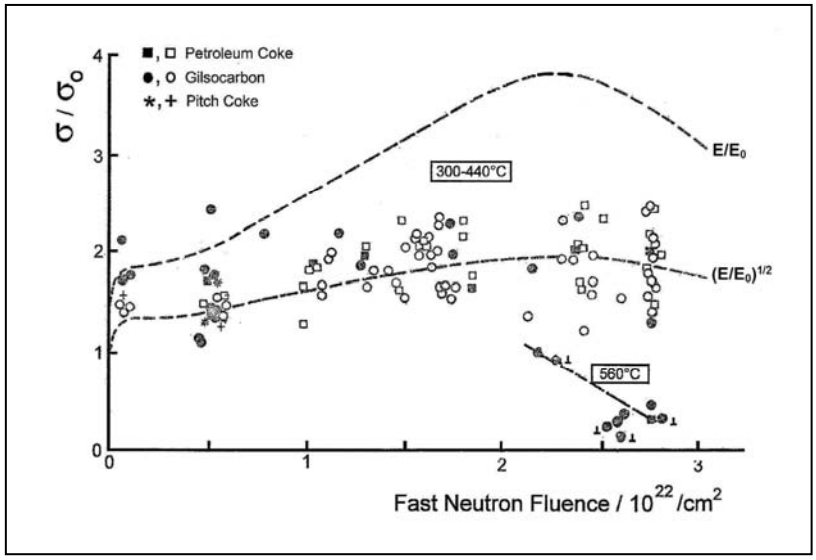

Fig. 35
Tensile strength changes of graphite due to fast neutron irradiation at 300 to 440°C and around 560°C. [34]

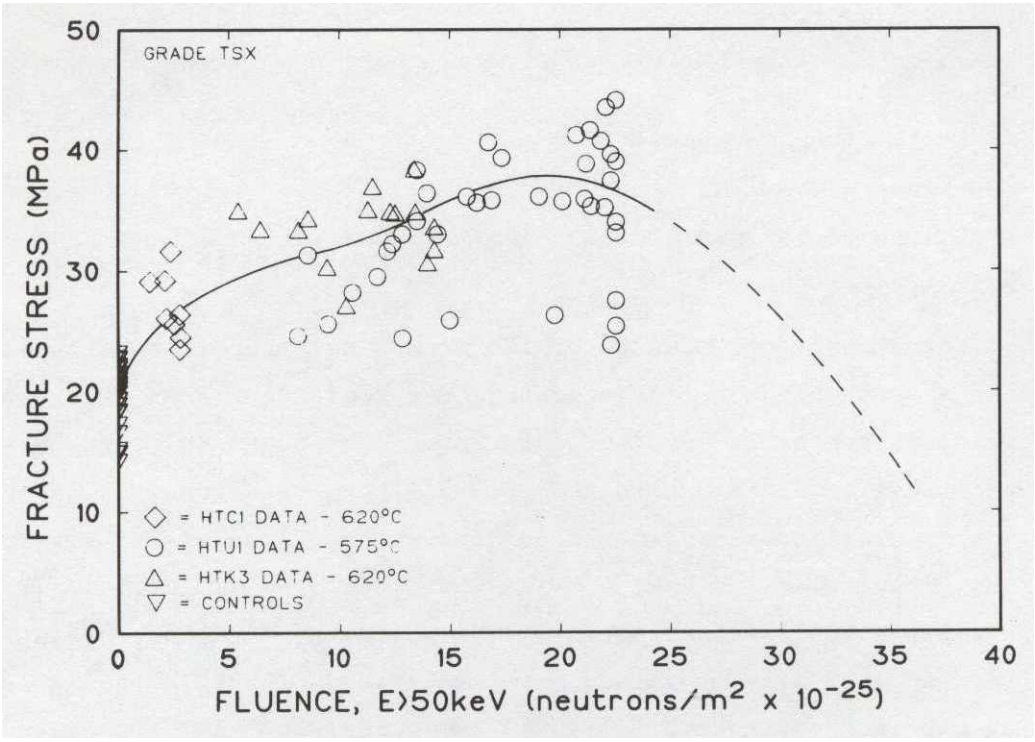

Fig. 36 Brittle-ring fracture strength of TSX graphite irradiated at 575°C [35]

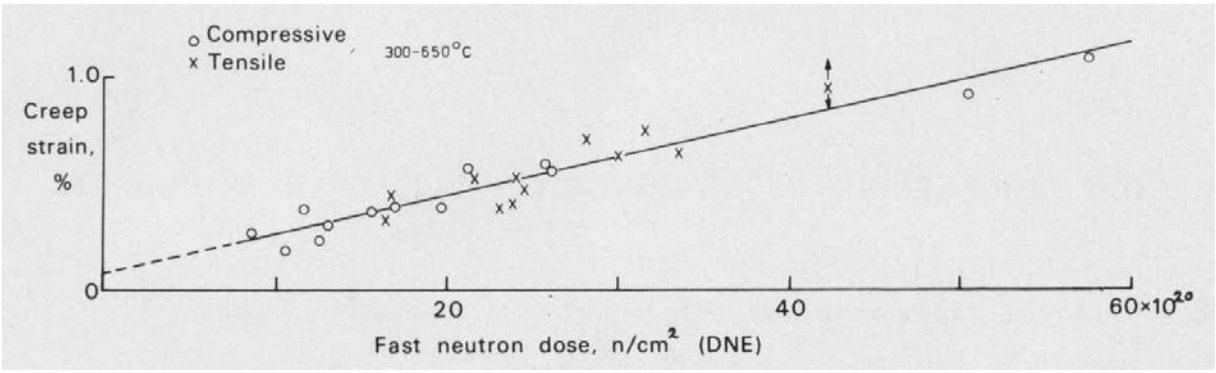

Fig. 37 Irradiation-induced creep strain of isotropic graphites under constant stress (6.2 MN/m^2) [36]

6. IRRADIATION BEHAVIOUR OF ATR-2E GRAPHITE

6.1 Basic Property Changes

6.1.1 Dimensional and Volume Changes

In general, there are two features of graphite relevant for assessing its anisotropy and hence its applicability in nuclear reactor technology if the material is to be exposed to fast neutron irradiation. One is its anisotropy factor, which is defined as the ratio of the two thermal expansion coefficients $\alpha_{\perp}/\alpha_{||}$ with $\alpha_{\perp} > \alpha_{||}$ in the two main crystallographic directions. This factor serves to determine whether a graphite is worth being irradiation-tested. After the irradiation behaviour has been investigated, the difference in the dimensional changes in the two main crystallographic directions is expected to reflect the as-manufactured anisotropy indicated by the anisotropy factor.

The dimensional changes of ATR-2E graphite due to fast neutron irradiation, which are demonstrated in Appendix B, Fig. B1, B6, B11, B16, B21 do still exhibit a remaining anisotropy, which is in good agreement with an anisotropy factor $\alpha_{\perp}/\alpha_{||}$ = 1.12 as manufactured. However, compared to the dimensional behaviour of graphites used in the early stages of graphite reactor technology (see Fig. 1a,b ; Fig. 2a,b; Fig. 3; Fig. 4) progress is obvious. The statistics of the ATR-2E data points at all four temperatures is good, and allows to fit in polynomials, which in most cases are of the 3rd order if minor details at extremely low fluences are not considered.

Three parameters of the regression lines are important for design purposes. (i) The *turn-around fluences* in both crystallographic directions give a first orientation about the presumable operational lifetime of parts of the reactor core produced from the material under consideration. The higher the turn-around fluence is the higher the end-of-life fluence may be.

However, comparing the two dimensional change curves for samples cut parallel and perpendicular to the pressing direction it appears that the turn-around is delayed by (ii) higher maximum shrinkage, which is the second important parameter of dimensional change plots. The advantage of a later turn-around can easily be destroyed by higher stresses due to higher values of differential shrinkage or higher shrinkage rates. Moreover, there are indications from other graphites that the expansion rate behind the turn-around might increase with increasing maximum shrinkage, which also would worsen the stress situation within graphite parts exposed to flux gradients. Therefore, allowing a higher maximum shrinkage and thus increasing the “life-

time" of a graphite is generally a double-edged measure which can only be justified by detailed stress analyses.

(iii) The third important parameter of dimensional change curves is the zero passage where the specimens return to their pre-irradiation dimension and net expansion begins. Roughly speaking, this point is sometimes called "lifetime fluence", which is a misleading interpretation as the end-of-life can only be assessed by stress analysis. To be more precise, one should state that the fluence at zero passage in combination with the expansion rate and maximum shrinkage may be an indicator of the lifetime of that graphite compared to other graphites.

As far as the volume change is concerned, it is calculated from the bulk density changes which have been determined as the geometrical density as well as according to the buoyancy method (Archimedes' principle) to yield more reliable information. In general, the relative volume changes should be a combination of the dimensional changes in both directions. As a first approximation one might assume that for a near-isotropic extruded graphite and small relative linear dimensional changes the relative volume change is given by the equation

$$\frac{\Delta V}{V_0} \approx \frac{\Delta l_{parallel}}{l_{0,parallel}} + 2 \cdot \frac{\Delta l_{perp}}{l_{0,perp}}$$

This equation is in good agreement with the accompanying plots (Fig. B2, B7, B12, B17 in the Appendix).

6.1.2 Young's Modulus Changes

Young's modulus behaves according to the description of its general behaviour with increasing fast neutron fluence given in Chapter 5.3.5, although the initial rapid increase cannot in all cases be verified by data points. Unfortunately, at 600°C irradiation temperature (Fig. B18) the scatter of the data points is rather large for no obvious reason and the resulting pattern is not typical. The best data sets are those for 400, 500 and 750 °C irradiation temperature (Fig. B8, B13 and B22).

At the three temperatures, the maximum fluences are high enough to show an effect which has not yet been discussed in detail in the literature. Beyond the peak at about 20 dpa the Young's modulus does not drop more and more rapidly towards, or even beyond, its initial value indicating that as a result of the structural changes due to irradiation damage the material

becomes weaker and weaker. On the contrary, it levels off and the expected destruction is markedly delayed. The reason for that may be creep processes as the creep coefficient has been observed to increase at very high fluences[37]. Since with increasing fluence the strength of irradiated graphite is assumed to be directly proportional to the Young's modulus, this effect might be helpful for increasing the effective lifetime of graphite. At present, however, there are not sufficient high fluence data available to confirm the existing ideas about the mechanics of graphite under such extreme conditions. Therefore, lifetime assessments must make more pessimistic assumptions even if there is some hope that graphite in real applications might turn out to be stronger than expected.

6.1.3 Electrical Resistivity Changes

Why has the electric resistance been measured in the framework of irradiation testing? One reason is that a graphite sample can exhibit unexpected properties. The most frequent causes are inhomogeneity of the material from which the sample is taken, unfavourable dimensions with respect to the measuring device or the applied method, mechanical damage during handling, or simply error of measurement. As the available time between two subsequent irradiation tests may be rather short, strange results cannot always be detected early enough to repeat the measurement. In this situation it can be helpful to measure the electric resistance in addition to the relevant properties.

Another reason for measuring the electric resistance is the relation to thermal resistivity. It is known that the Wiedemann-Franz law describes this relation for metallic conductors. However, the thermal conductivity is determined to a greater extent by phonon scattering rather than by the transport of electric charge carriers. Nevertheless, there is an indirect correlation between the two properties caused by the polycrystallinity of reactor graphite. The transport of charge carriers from crystallite to crystallite proceeds along the same paths as the transport of phonons. They are both influenced by the contact between the crystallites within the graphite body. Since the measurement of thermal conductivity is technically difficult its error probability is high, and, therefore, the measurement of electric resistance has been considered to be desirable.

Finally, it has become apparent that electrical resistivity data have never been used to back up thermal conductivity data. Nevertheless, this has been observed in order to check for unexpected effects, e.g., cracks within the specimens etc. Fig. B5, B10, B15, and B20 display the data exhibiting the typical shape of such curves as shown in Fig. 33. However, the clear difference between fractional changes $\Delta\rho/\rho_0$ for specimens cut parallel and perpendicular was

not found in case of ATR-2E. The existence of an anisotropy of the fractional changes of resistivity as shown in Fig. 33 means the following:

$$\text{if} \qquad \left(\frac{\Delta\rho}{\rho_0}\right)_{perp} < \left(\frac{\Delta\rho}{\rho_0}\right)_{par}$$

$$\text{then} \qquad \left(\frac{\rho^*}{\rho_0}\right)_{perp} < \left(\frac{\rho^*}{\rho_0}\right)_{par}$$

$$\text{and} \qquad \left(\frac{\rho^*_{perp}}{\rho^*_{par}}\right) < \left(\frac{\rho_{0\,perp}}{\rho_{0\,par}}\right)$$

i.e., the anisotropy factor of electrical resistivity after irradiation is smaller than before irradiation. It is possible that this is true for very anisotropic graphite such as CSF or TSGBF graphites (see Table 1). If there is a mechanism which decreases the anisotropy it might not be observable for graphites which are already isotropic.

Another difference between Fig. 33 and the electrical resistivity plots for ATR-2E graphite in the appendix is the existence of a “secondary increase” at very high fast neutron fluences, which has been discussed before for thermal conductivity.

6.1.4 Thermal Expansivity Changes

At all four irradiation temperatures, the thermal expansion coefficient measured between room temperature and irradiation temperature behaves as expected (see Figs. B4, B9, B14, B19). The number of data points is much smaller than for the other properties under consideration in this chapter because the measuring procedure takes a lot of time, and the gap between two subsequent irradiations is very limited.

6.1.5 Thermal Conductivity Changes

It has been mentioned before that until about 1975 most of the thermal conductivity measurements on fast-neutron-irradiated graphite were performed at room temperature on the assumption that with an appropriate model it would be possible to derive thermal conductivity data at operational temperatures from them by calculation. At that time, a measuring device for thermal conductivity measurements up to 1000°C according to a modified Kohlrausch method became available at KFA Jülich (Germany), Institute for Reactor Materials[38], and from that time on, all investigations of the irradiation behaviour of thermal conductivity in the framework of the

German nuclear graphite development programme were based on direct measurements at irradiation temperature.

For the four ranges of irradiation temperatures the thermal conductivity data for ATR-2E graphite are presented in Table 5. Normally, all thermal conductivity measurements using the modified Kohlrausch method started at a temperature of about 100 °C and recorded the data in steps of roughly 100 K.

The data as measured were presented in the form

Measuring Temp. (°C)	99	198	297	397	496	596	695	795	895	995
Thermal Cond. (W/(cm K))	1.130	1.020	0.856	0.773	0.688	0.630	0.584	0.535	0.502	0.462

Irradiated specimens were measured up to a maximum temperature of 50 to 100 K below irradiation temperature in order to avoid thermal annealing of radiation damage. Therefore, the exact thermal conductivity values at irradiation temperature had to be extrapolated using a suitable function. It was found that the expression

$$k(T) \quad = \quad a_0 + \frac{a_1}{T^2} + a_2 \cdot e^{\left(\frac{-1250}{T}\right)}$$

with coefficients a_i (i = 1,2,3) to be determined by regression analysis is an excellent approach to the measured data. For low temperatures $k(T)$ is proportional to $1/T^2$, and for temperatures in the range of the irradiation temperatures and higher $k(T)$ decreases exponentially with increasing measuring temperature. At temperatures around room temperature, thermal conductivity has a maximum. Its exact location on the temperature axis depends upon the mean free-path of the phonons, and is therefore depending upon the degree of damage due to fast neutron irradiation. The above equation describes this maximum also very well. Fig. 38 shows regression curves according to the above equation with the associated measured data points.

Fig. 39 demonstrates that the data points agree very well with the general saturation levels (horizontal lines) given in Table 4. For the lowest irradiation temperatures (300 and 400 °C) where the thermal conductivity exhibits the largest relative decreases anyway, there is no indication of a secondary breakdown which, according to volume turn-around (see Chapter 5.3.3), would be expected to begin at the right end of the horizontal bars. At 500 and 600 °C irradiation temperature, however, there is a marked secondary breakdown, which is in good agreement with volume turn-around, as can be seen from Fig. 40 and Fig. 41.

This relation between the secondary breakdown and the relative volume changes in combination with the material-independent saturation levels can be used to assess the thermal conductivity changes of a graphite due to irradiation even if no directly measured data are available.

6.1.6 Irradiation-Induced Creep

One of the major aspects of the deformation behaviour of graphite under conditions prevailing in a high-temperature reactor is irradiation-induced creep. Although in reality graphite parts in the reactor experience external and internal stresses caused by differential deformation due to neutron flux and temperature gradients, the majority of graphite irradiation experiments are performed without subjecting the specimens to external loads. The intricacy of irradiation creep facilities coupled with the high specific costs and the possibility of premature failure of the device or specimen have given rise to the situation that the general creep data available in the literature are very limited compared to those available for the changes in the physical and mechanical properties of graphite under irradiation.

Irradiation-induced creep reduces stresses prevailing within graphite parts. For many years design rules existed in the UK for incorporating irradiation creep of graphite into stress analyses for highly irradiated graphite reactor components. These design rules were based on data from UKAEA creep experiments[39],[40] (see Chapter 5.3.7) and a theoretical model[41]. However, the data only cover the low fluence range up to about 8 dpa.

This did not satisfy the requirements of advanced high-temperature reactor designs mostly using large graphite blocks which are exposed to much higher end-of-life fluences of fast neutrons than in former graphite reactor designs. Therefore, KFA Jülich performed a new series of creep irradiation experiments in HFR Petten with ATR-2E graphite under tensile and compressive load. The maximum fast neutron fluences achieved were about 28 dpa, and the irradiation temperatures were 300 and 500 °C, which were the most interesting temperatures for the pebble-bed reactor designs under discussion at that time. All test specimens were taken in the direction parallel to extrusion from a single block from the second production batch to obtain the maximum amount of comparable data.[42]

This new series of irradiation experiments under creep conditions was aimed to test the existing creep model with respect to much higher fast neutron fluences, to compare the creep behaviour under compression to that under tensile strength, and to investigate in detail the creep model developed by Kelly and Brocklehurst[43], and by Kelly and Foreman[44]. If this model was correct

then an inverse proportionality between creep coefficient and Young's modulus up to the highest achievable fluences should once again be observed.

A standard design of reloadable irradiation thimble had been well proven at Petten. Three independently controllable sample holders could be irradiated simultaneously in any one of the HFR core or reflector positions. Two sample holders, one for tensile and one for compressive tests, were designed for operation at 500°C and one tensile sample holder for operation at 300°C.

The arrangement of the samples in the DISCREET creep facility is shown in Fig. 19, Fig. 20 and Fig. 21 for the tensile as well as the compressive creep experiments.

In both cases, the arrangement guaranteed that creep samples and the accompanying reference samples were irradiated under the same conditions (temperature, fast neutron flux). Therefore, the respective dimensional changes can be directly compared and the creep strain is simply the difference between the dimensional changes of stressed and unstressed samples corrected for thermal expansion and Young's modulus.

The dimensional changes of stressed and unstressed samples are given in Tables 6 to 9. However, from the point of view of quality assurance it must be stated that these data could not be taken directly from a written source such as a laboratory protocol, report, article in a journal etc. The numerical data rather had to be recovered from published diagrams[45,46]. Nevertheless, the accuracy of the method applied is good enough to regard the recovered data as being equivalent to measured data.

It is known from the literature that "the creep strain is taken to be the difference in the length changes at the irradiation temperature of stressed and unstressed specimens, i.e. measurements at room temperature on unstressed samples are corrected for thermal expansion and modulus changes taking place under the irradiation." [47] It is assumed that the creep strain plotted in Fig. 46 is in accordance with this definition, since Cundy et al. say that plots like Figs. 42, 43, 44 and 45 show "... both the corrected measurement points and the curvilinear least squares fits." [48]

Fig. 42 and Table 6 show the results of a series of irradiations of ATR-2E graphite at 550°C to investigate the creep behaviour under compressive load. All the graphite specimens were cut with their axes parallel to the extrusion direction, i.e., parallel to the preferred orientation of the filler particles. In this case, the shrinkage due to fast neutron irradiation, which is represented by the reference samples, is increased as expected by applying a mechanical load of 5 MPa. The difference between corresponding data points is the creep strain, which is the key parameter for irradiation-induced creep.

In Fig. 43, the effect of an external tensile load of 5 MPa on ATR-2E graphite at 500°C irradiation temperature is demonstrated. Since graphite is weakest in tensile load, most creep experiments reported in the literature were performed using tensile conditions. It was expected that creep strain limits would be reached earlier for tension than for compression. Therefore, it might be more difficult to attain high fluence values without failure of one of the tensile samples, and hence of the whole chain. This was another reason to rely not only upon tensile creep experiments but to incorporate compressive creep investigations into the programme.

Again, the specimens were cut with their axes parallel to the extrusion direction. This time, due to the tensile stress, the axial shrinkage of the specimens decreases as the samples are elongated by the external load (Table 7; Fig. 43). The evaluation of the data points belonging to the stressed and unstressed samples again yields the creep strain. It should be pointed out that there is a difference between the two curves for the reference samples in Fig. 42 and Fig. 43 that is attributed to the difference in irradiation temperature.

A third series of irradiations was performed at 300°C to investigate the influence of temperature on the creep effect. Again, ATR-2E graphite samples were cut parallel to extrusion and irradiated under an external axial tensile load of 5 MPa. The numerical results of the determination of irradiation-induced strain for both stressed and unstressed samples are given in Table 8, and the related graph is displayed in Fig. 44.

Finally, the dimensional changes of the samples used in the compression creep experiment at 550°C irradiation temperature were not only measured in the longitudinal but also in the transverse direction. The idea is that a cylindrical specimen which is compressed along its axis should swell in the radial direction. This is indeed observed as Fig. 45 demonstrates. Without external load the samples would shrink like the white data points representing the normal dimensional changes of ATR-2E graphite perpendicular to extrusion. When the axial compressive load of 5 MPa is applied the overall shrinkage in diameter becomes smaller as the expected expansion in diameter is superimposed.

Since the data in Table 9 were originally obtained from the same specimens as the data in Table 6, the fluence values should be exactly the same. However, as described above, the numerical data had to be recovered from the existing graphs. For the samples in the compressive creep irradiations this was done independently for the longitudinal and the transverse strain data. The differences between the corresponding pairs of data indicate that the accuracy of the recovered data is satisfying.

Fig. 46 combines all the creep strain data. A first rough examination of the graphs leads to the conclusion that there is not much difference between (i) compressive and tensile creep strain,

and (ii) 300°C and 500°C tensile creep strain. However, a closer examination of the high fluence data should reveal whether the “old” creep model, which was verified at fast fluences up to about 8 dpa, stills hold at fluences three times as high.

Fig. 47 shows a similar diagram as published by Cundy et al.[49]

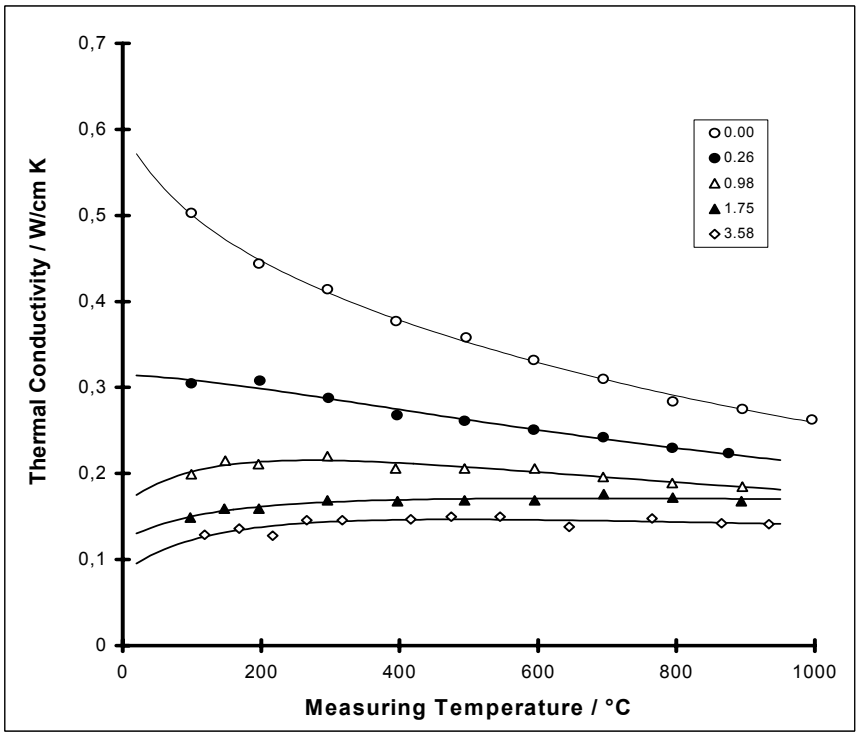

Fig. 38 Thermal conductivity of a nuclear graphite as a function of measuring temperature before irradiation (0.00) , and after irradiation at 950°C to fast neutron fluences 0.26, 0.98, 1.75, and $3.58 \cdot 10^{25}/m^2$ (EDN).

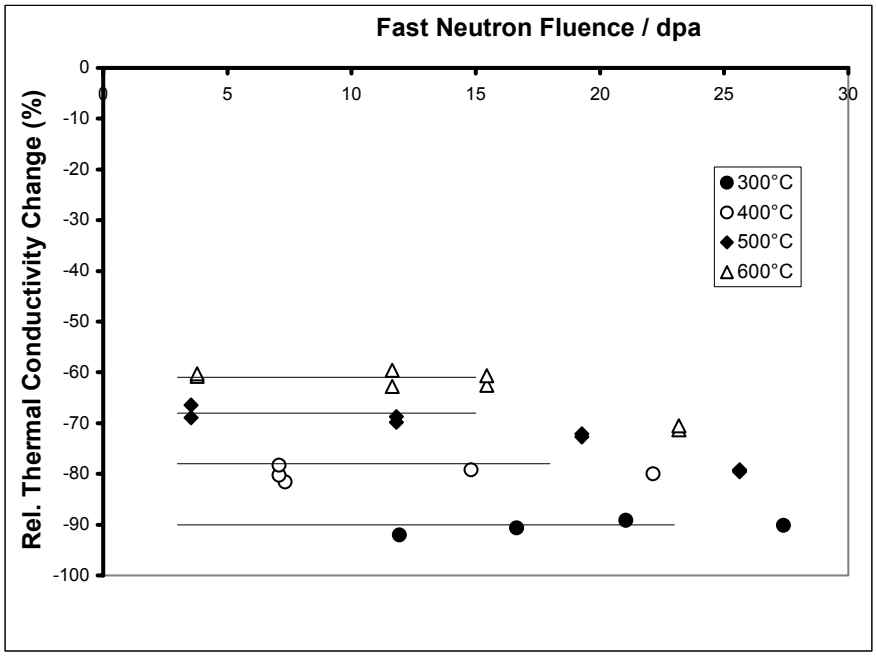

Fig. 39 Thermal conductivity change of ATR-2E graphite due to fast neutron irradiation at different irradiation temperatures of 300, 400, 500, and 600 °C according to Table 5; the horizontal lines indicate the saturation levels.

Irradiation & Measuring Temperature (°C)	**Fast Neutron Fluence (dpa)**	**Orientation** (with regard to extruding direction)	**Thermal Conductivity (W/cm K)**	**Thermal Conductivity Change (K/K_0 -1) (%)**
300	0	parallel	110.25	
300	11.93	parallel	8.83	-92.0
300	21.04	parallel	12.00	-89.1
300	0	perpendicular	86.32	
300	16.65	perpendicular	8.11	-90.6
300	27.40	perpendicular	8.50	-90.2
400	0	parallel	105.67	
400	7.33	parallel	19.50	-81.6
400	0	parallel	101.47	
400	7.08	parallel	20.00	-80.3
400	0	perpendicular	85.40	
400	7.08	perpendicular	18.58	-78.3
400	14.81	perpendicular	17.81	-79.2
400	22.14	perpendicular	17.13	-80.0
500	0	parallel	86.53	
500	3.54	parallel	26.93	-68.9
500	11.80	parallel	26.10	-69.8
500	19.27	parallel	24.10	-72.2
500	25.63	parallel	17.64	-79.6
500	0	perpendicular	77.36	
500	3.54	perpendicular	25.96	-66.4
500	11.80	perpendicular	24.23	-68.7
500	19.27	perpendicular	21.15	-72.7
500	25.63	perpendicular	16.08	-79.2
600	0	parallel	72.21	
600	3.78	parallel	28.36	-60.7
600	11.64	parallel	26.91	-62.7
600	15.44	parallel	27.02	-62.6
600	23.18	parallel	20.73	-71.3
600	0	perpendicular	78.63	
600	3.78	perpendicular	31.22	-60.3
600	11.64	perpendicular	31.82	-59.5
600	15.44	perpendicular	30.95	-60.6
600	23.18	perpendicular	23.18	-70.5

Table 5 Data on irradiation temperature, fast neutron fluence, thermal conductivity at irradiation temperature, and relative thermal conductivity change of ATR-2E graphite parallel and perpendicular to the extruding direction due to irradiation.

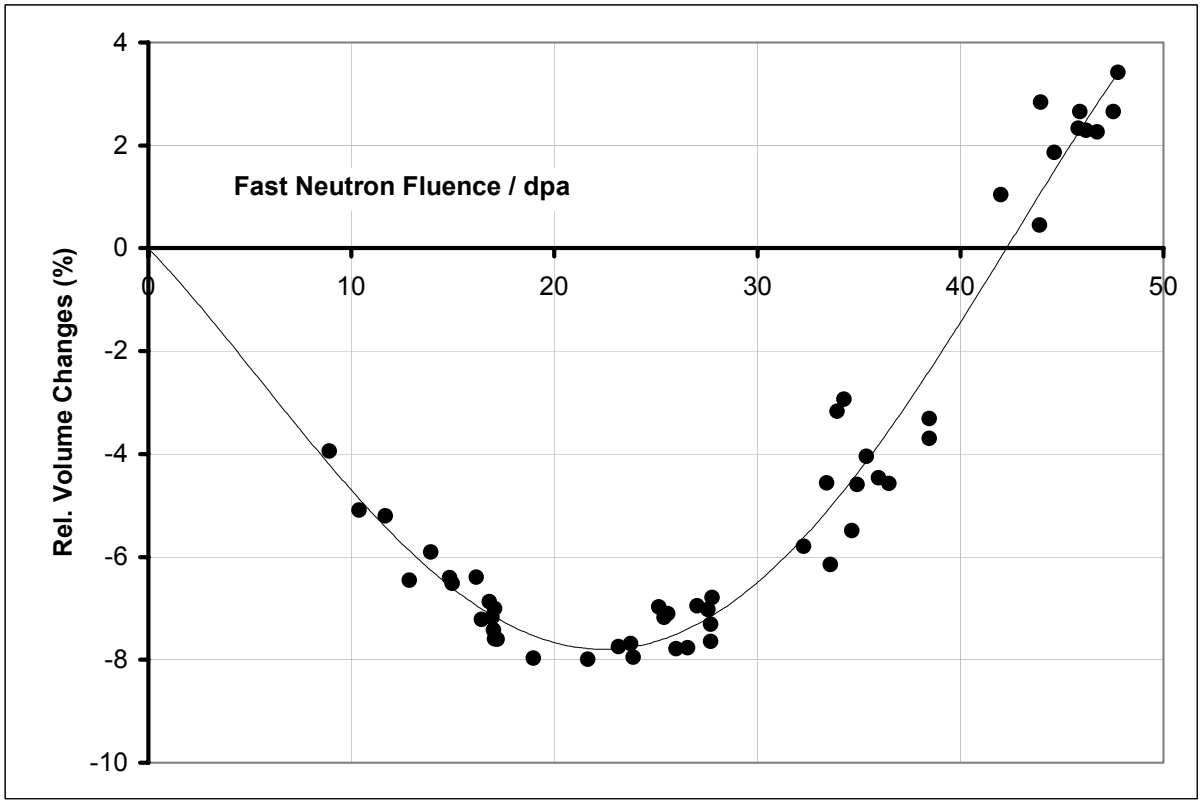

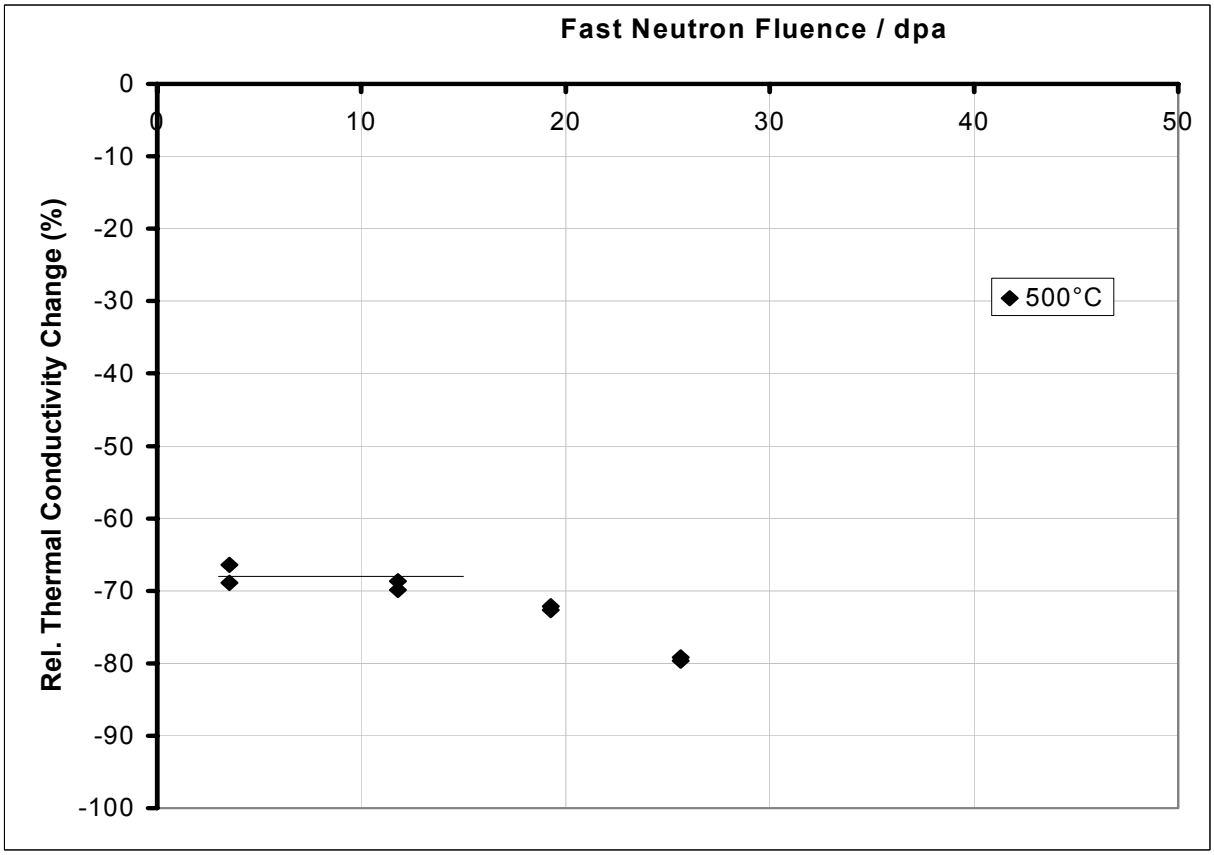

Fig. 40 ATR-2E graphite: Relation between maximum volume shrinkage and secondary breakdown of thermal conductivity at 500°C.

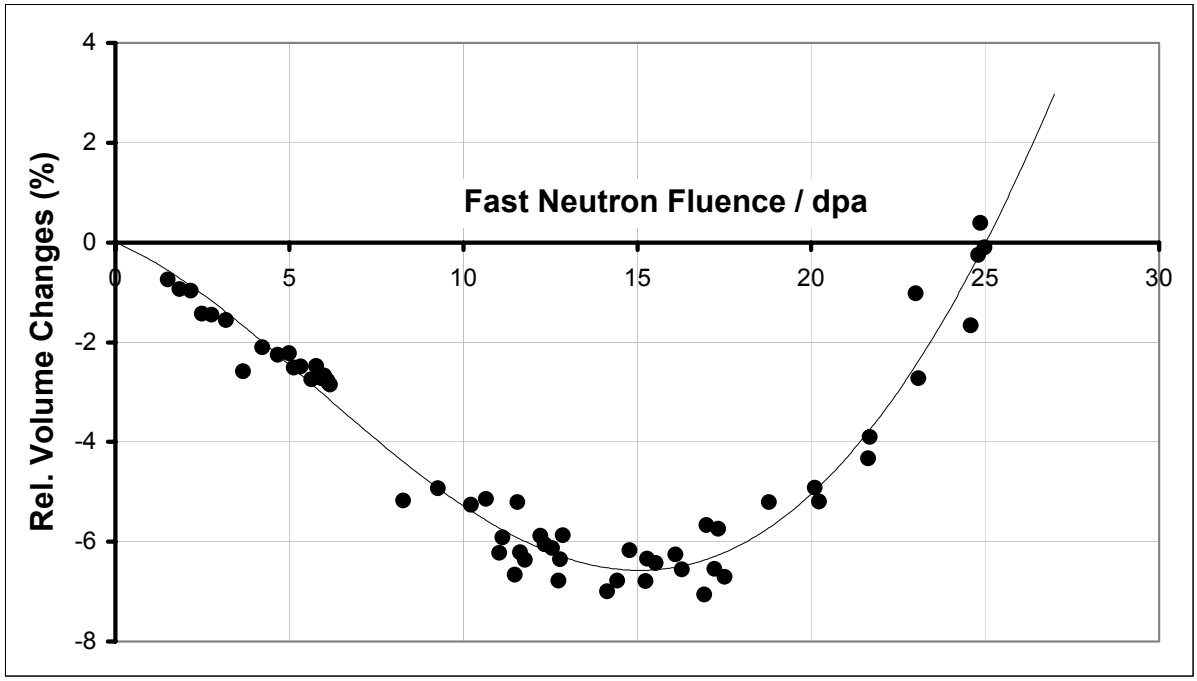

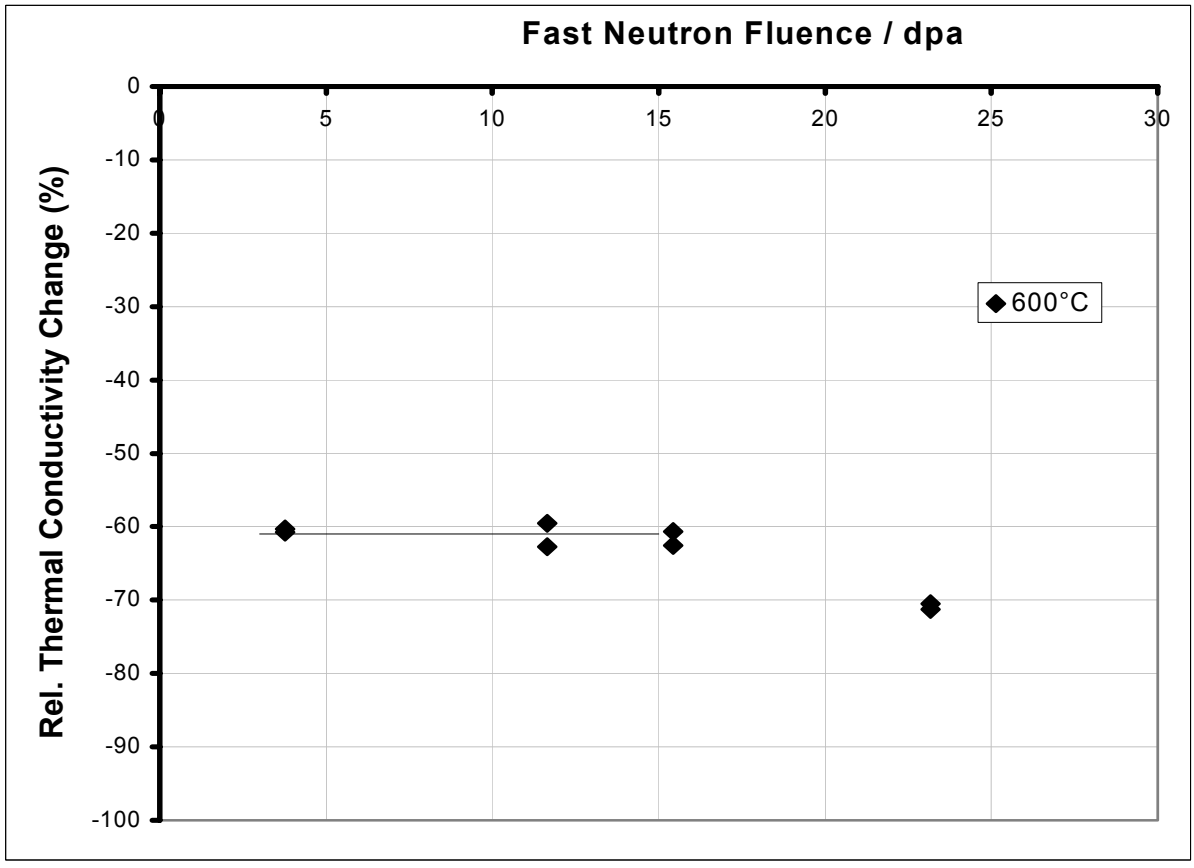

Fig. 41 ATR-2E graphite: Relation between maximum volume shrinkage and start of secondary breakdown of thermal conductivity at 600°C.

Irradiation Temperature (°C)	Fast Neutron Fluence (dpa)	Rel. Linear Dimensional Changes $\Delta l/l_0$ (%) (unstressed)	Rel. Linear Dimensional Changes $\Delta l/l_0$ (%) (stressed)	Creep Strain (%)
550	0.29	-0.07	-0.18	-0.11
550	0.41	-0.10	-0.21	-0.11
550	0.54	-0.15	-0.24	-0.09
550	1.66	-0.34	-0.56	-0.22
550	2.02	-0.42	-0.65	-0.23
550	2.21	-0.38	-0.61	-0.23
550	2.34	-0.49	-0.73	-0.24
550	2.38	-0.44	-0.77	-0.33
550	2.52	-0.56	-0.82	-0.26
550	2.67	-0.55	-0.77	-0.22
550	2.76	-0.56	-0.87	-0.31
550	3.92	-0.82	-1.26	-0.44
550	4.90	-1.06	-1.49	-0.43
550	5.04	-0.94	-1.39	-0.45
550	5.55	-1.19	-1.69	-0.50
550	5.75	-1.11	-1.67	-0.56
550	6.09	-1.28	-1.81	-0.53
550	6.23	-1.25	-1.77	-0.52
550	6.33	-1.29	-1.84	-0.55
550	6.41	-1.33	-1.86	-0.53
550	6.62	-1.35	-1.87	-0.52
550	8.16	-1.76	-2.45	-0.69
550	9.87	-2.05	-2.77	-0.72
550	10.00	-1.96	-2.65	-0.69
550	10.95	-2.21	-3.05	-0.84
550	11.29	-2.13	-2.97	-0.84
550	12.05	-2.33	-3.12	-0.79
550	12.13	-2.28	-3.07	-0.79
550	12.32	-2.41	-3.20	-0.79
550	12.41	-2.40	-3.29	-0.89
550	12.62	-2.31	-3.15	-0.84
550	12.92	-2.36	-3.18	-0.82
550	14.69	-2.51	-3.45	-0.94
550	15.16	-2.57	-3.49	-0.92
550	15.17	-2.63	-3.52	-0.89
550	16.66	-2.51	-3.41	-0.90
550	16.74	-2.62	-3.65	-1.03
550	16.92	-2.53	-3.56	-1.03
550	17.91	-2.57	-3.47	-0.90
550	17.95	-2.48	-3.49	-1.01
550	18.04	-2.55	-3.55	-1.00
550	18.09	-2.50	-3.47	-0.97
550	18.54	-2.57	-3.52	-0.95

Table 6 Dimensional changes of ATR-2E graphite (with grain) irradiated at 550°C. Stressed samples under 5 MPa compressive load (continued →)

Irradiation Temperature (°C)	Fast Neutron Fluence (dpa)	Rel. Linear Dimensional Changes $\Delta l/l_0$ (%) (unstressed)	Rel. Linear Dimensional Changes $\Delta l/l_0$ (%) (stressed)	Creep Strain (%)
550	19.01	-2.39	-3.41	-1.02
550	19.20	-2.30	-3.22	-0.92
550	19.28	-2.36	-3.35	-0.99
550	19.85	-2.18	-3.33	-1.15
550	20.10	-2.17	-3.35	-1.18
550	20.38	-2.22	-3.05	-0.83
550	21.29	-2.01	-3.16	-1.15
550	21.56	-1.96	-3.16	-1.20
550	22.08	-1.91	-3.08	-1.17
550	22.58	-1.52	-2.76	-1.24
550	22.73	-1.53	-3.02	-1.49
550	22.74	-1.78	-2.79	-1.01
550	22.98	-1.67	-2.90	-1.23
550	24.49	-1.19	-2.36	-1.17
550	24.75	-1.12	-2.41	-1.29
550	25.30	-0.93	-2.20	-1.27
550	26.07	-0.73	-2.10	-1.37
550	26.22	-0.58	-1.94	-1.36

Table 6 Dimensional changes of ATR-2E graphite (with grain) irradiated at 550°C. Stressed samples under 5 MPa compressive load

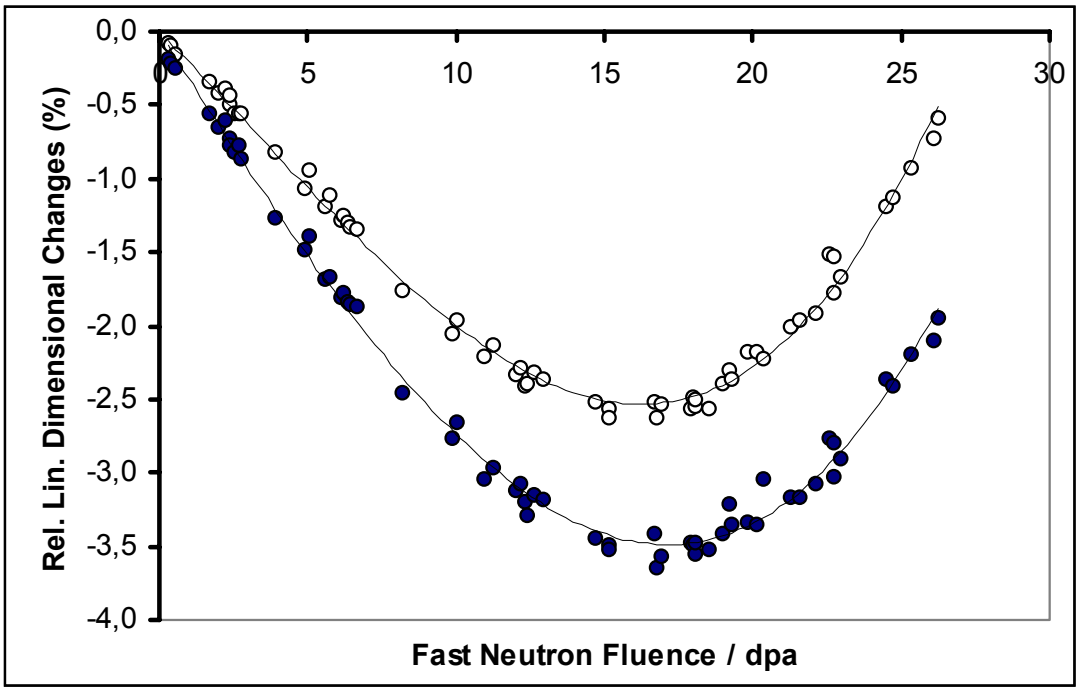

Fig. 42 Dimensional changes of ATR-2E graphite irradiated at 550°C. – Data from Table 6

Black data points: Samples under 5 MPa compressive load
White data points: Unloaded reference samples

Irradiation Temperature (°C)	Fast Neutron Fluence (dpa)	Rel. Linear Dimensional Changes $\Delta l/l_0$ (%) (unstressed)	Rel. Linear Dimensional Changes $\Delta l/l_0$ (%) (stressed)	Creep Strain (%)
500	0.32	-0.07	0.03	0.10
500	0.48	-0.06	0.05	0.11
500	0.50	-0.10	0.02	0.12
500	1.56	-0.36	-0.02	0.34
500	2.02	-0.33	-0.04	0.29
500	2.13	-0.27	-0.11	0.16
500	2.15	-0.41	0.05	0.45
500	2.28	-0.35	-0.01	0.35
500	2.40	-0.45	-0.15	0.30
500	2.47	-0.42	-0.09	0.34
500	3.39	-0.71	-0.25	0.45
500	4.95	-1.05	-0.55	0.50
500	6.01	-1.05	-0.61	0.44
500	6.13	-1.15	-0.64	0.51
500	6.92	-1.43	-0.70	0.73
500	7.03	-1.36	-0.71	0.65
500	7.65	-1.28	-0.47	0.81
500	8.01	-1.48	-0.84	0.64
500	8.01	-1.71	-0.89	0.82
500	8.09	-1.55	-0.68	0.87
500	8.87	-1.58	-0.58	1.01
500	9.47	-1.93	-1.21	0.72
500	10.12	-2.04	-1.40	0.65
500	11.21	-2.36	-1.49	0.87
500	11.46	-2.37	-1.59	0.78
500	11.46	-2.45	-1.62	0.83
500	12.29	-2.16	-1.17	1.00
500	12.37	-2.48	-1.53	0.94
500	12.89	-2.53	-1.87	0.67
500	13.01	-2.51	-1.43	1.08
500	14.07	-2.54	-1.39	1.14
500	16.82	-2.98	-2.14	0.84
500	16.96	-2.81	-1.95	0.86
500	16.97	-2.93	-1.85	1.08
500	18.58	-2.96	-1.87	1.09
500	19.75	-2.87	-1.71	1.16
500	20.28	-2.69	-1.41	1.28
500	20.29	-2.81	-1.49	1.33
500	22.35	-2.63	-1.33	1.31
500	23.03	-2.23	-0.45	1.79
500	26.80	-1.16	0.77	1.93

Table 7 Dimensional changes of ATR-2E graphite (with grain) irradiated at 500°C. Stressed samples under 5 MPa tensile load

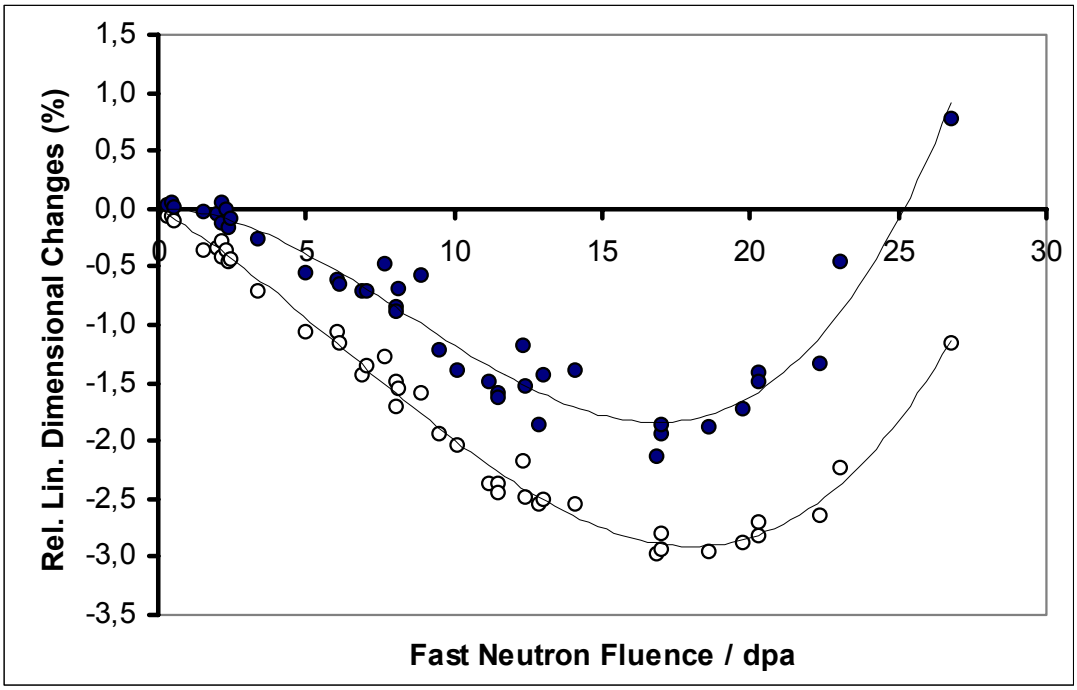

Fig. 43 Dimensional changes of ATR-2E graphite irradiated at 500°C. – Data from Table 7

Black data points: Samples under 5 MPa tensile load
White data points: Unloaded reference samples

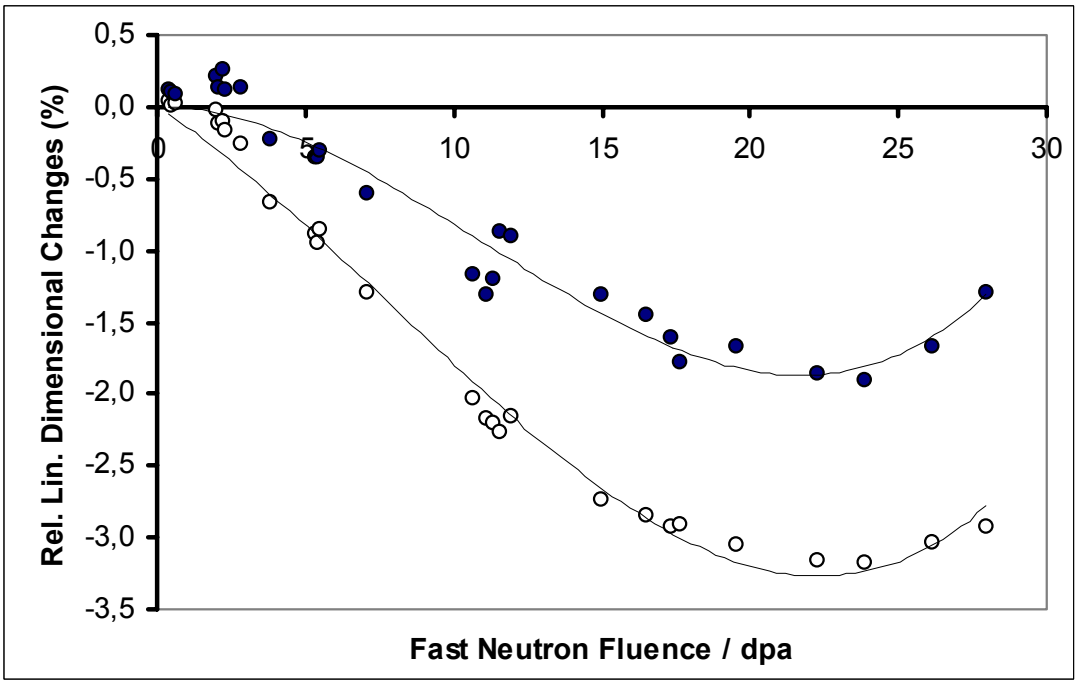

Fig. 44 Dimensional changes of ATR-2E graphite irradiated at 300°C. – Data from Table 8

Black data points: Samples under 5 MPa tensile load
White data points: Unloaded reference samples

Irradiation Temperature (°C)	Fast Neutron Fluence (dpa)	Rel. Linear Dimensional Changes $\Delta l/l_0$ (%) (unstressed)	Rel. Linear Dimensional Changes $\Delta l/l_0$ (%) (stressed)	Creep Strain (%)
300	0.37	0.05	0.12	0.07
300	0.49	0.01	0.11	0.10
300	0.61	0.03	0.09	0.06
300	2.00	-0.01	0.22	0.23
300	2.03	-0.11	0.13	0.24
300	2.19	-0.09	0.26	0.35
300	2.30	-0.16	0.13	0.28
300	2.79	-0.25	0.14	0.39
300	3.76	-0.65	-0.23	0.42
300	5.31	-0.88	-0.35	0.52
300	5.41	-0.94	-0.34	0.60
300	5.47	-0.84	-0.30	0.54
300	7.09	-1.29	-0.60	0.69
300	10.60	-2.03	-1.17	0.86
300	11.10	-2.16	-1.30	0.86
300	11.35	-2.19	-1.19	1.00
300	11.54	-2.26	-0.87	1.39
300	11.92	-2.15	-0.90	1.25
300	15.00	-2.74	-1.30	1.44
300	16.47	-2.84	-1.44	1.40
300	17.31	-2.92	-1.60	1.32
300	17.59	-2.91	-1.77	1.14
300	19.55	-3.04	-1.67	1.38
300	22.25	-3.15	-1.86	1.29
300	23.88	-3.17	-1.90	1.27
300	26.12	-3.03	-1.67	1.37
300	27.97	-2.93	-1.28	1.64

Table 8 Dimensional changes of ATR-2E graphite (with grain) irradiated at 300°C. Stressed samples under 5 MPa tensile load

Irradiation Temperature (°C)	Fast Neutron Fluence (dpa)	Rel. Linear Dimensional Changes $\Delta l/l_0$ (%) (unstressed)	Rel. Linear Dimensional Changes $\Delta l/l_0$ (%) (stressed)	Creep Strain (%)
550	3.97	-0.76	-0.53	0.24
550	4.95	-0.87	-0.61	0.26
550	5.08	-0.83	-0.55	0.28
550	5.61	-0.99	-0.69	0.30
550	5.80	-0.99	-0.73	0.26
550	6.13	-1.08	-0.72	0.35
550	6.24	-1.03	-0.73	0.30
550	6.45	-1.07	-0.81	0.26

Table 9 Transverse dimensional changes of ATR-2E graphite (across grain) irradiated at 550°C. Samples with 5 MPa tensile stress in 'with grain' direction. (continued →)

Irradiation Temperature (°C)	Fast Neutron Fluence (dpa)	Rel. Linear Dimensional Changes $\Delta l/l_0$ (%) (unstressed)	Rel. Linear Dimensional Changes $\Delta l/l_0$ (%) (stressed)	Creep Strain (%)
550	6.67	-1.09	-0.81	0.28
550	8.20	-1.36	-1.07	0.28
550	9.94	-1.44	-1.17	0.27
550	10.07	-1.57	-1.12	0.45
550	10.98	-1.45	-1.22	0.23
550	11.29	-1.65	-1.34	0.30
550	12.02	-1.52	-1.24	0.28
550	12.15	-1.58	-1.24	0.34
550	12.37	-1.60	-1.37	0.23
550	12.36	-1.82	-1.41	0.41
550	12.55	-1.68	-1.41	0.27
550	12.93	-1.67	-1.40	0.27
550	14.68	-1.52	-1.31	0.21
550	15.16	-1.68	-1.35	0.33
550	15.17	-1.84	-1.28	0.56
550	16.66	-1.09	-0.96	0.14
550	16.75	-1.52	-1.14	0.38
550	16.93	-1.60	-1.30	0.30
550	17.89	-1.20	-0.90	0.30
550	17.95	-1.38	-1.01	0.38
550	18.05	-1.32	-0.92	0.40
550	18.09	-1.00	-0.83	0.16
550	18.63	-1.20	-0.93	0.27
550	19.09	-1.17	-0.92	0.25
550	19.28	-0.83	-0.29	0.54
550	19.34	-1.12	-0.89	0.24
550	19.93	-0.41	-0.25	0.16
550	20.18	-0.68	-0.49	0.19
550	20.45	-0.16	-0.01	0.15
550	21.35	0.03	0.14	0.10
550	21.62	-0.03	0.14	0.17
550	22.13	0.26	0.33	0.07
550	22.79	0.24	0.27	0.04
550	22.80	0.57	0.69	0.12
550	22.67	0.75	0.90	0.16
550	23.06	0.45	0.39	-0.06
550	24.37	1.51	1.63	0.12
550	24.64	1.59	1.64	0.05
550	25.16	1.97	1.81	-0.16
550	25.94	1.85	1.93	0.07
550	26.20	2.05	2.01	-0.04

Table 9 Transverse dimensional changes of ATR-2E graphite (across grain) irradiated at 550°C. Samples with 5 MPa compressive stress in ‘with grain’ direction.

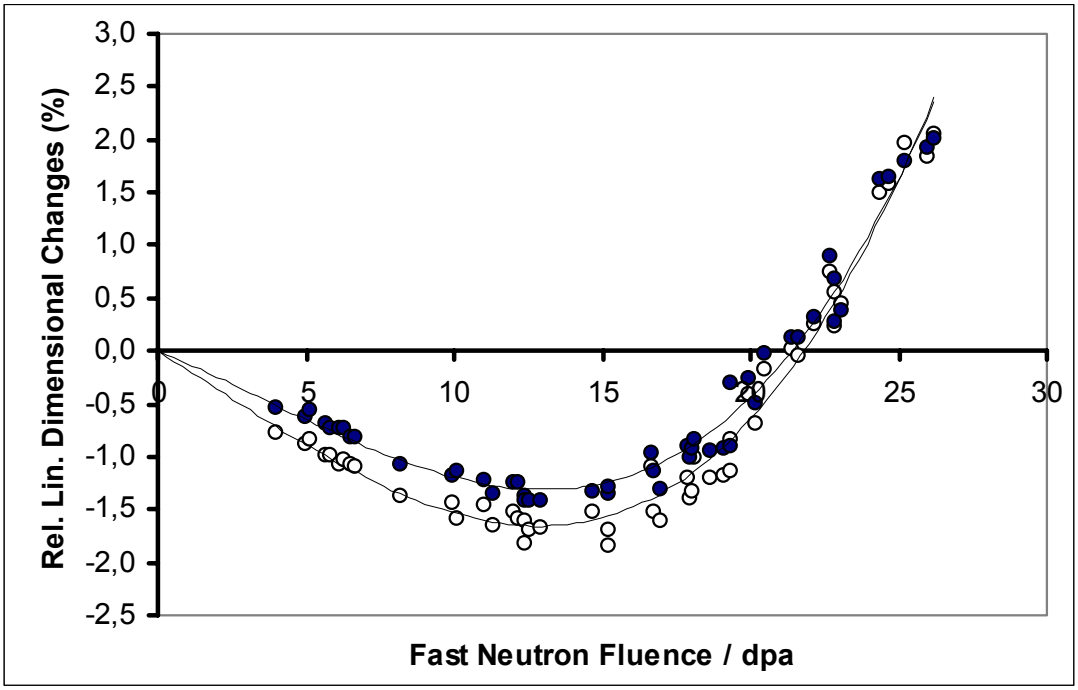

Fig. 45 Transverse dimensional changes of ATR-2E graphite vs fast neutron fluence irradiated at 550°C. – Data from Table 9

Black data points: Samples under 5 MPa axial compressive load
White data points: Unloaded reference samples

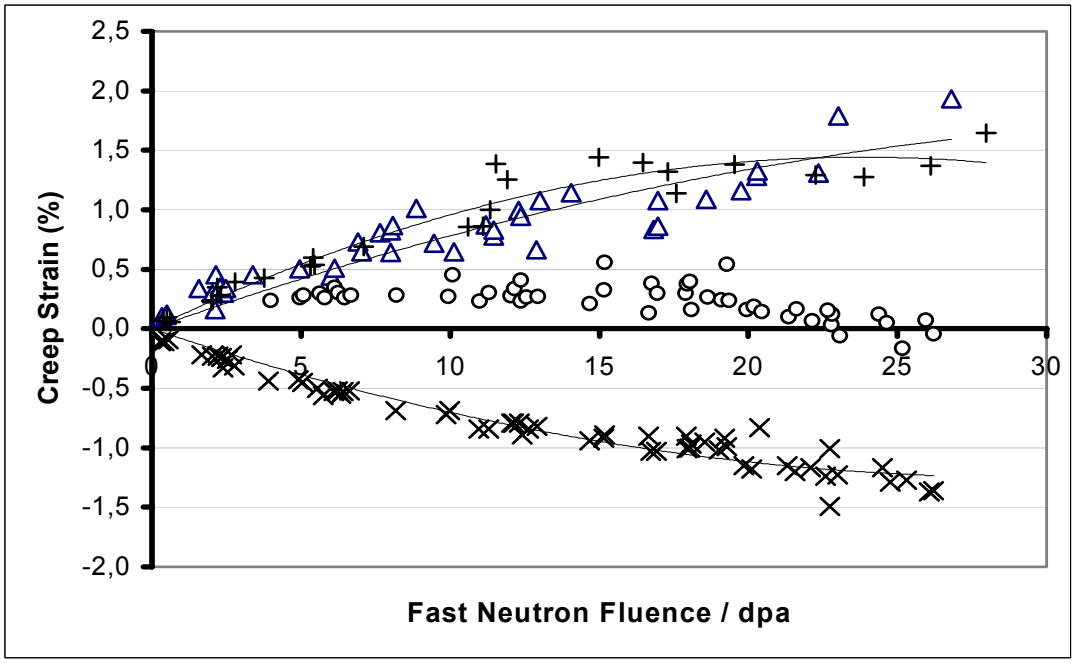

Fig. 46 Creep strain of ATR-2E graphite vs fast neutron fluence under different irradiation conditions – Data from Tables 6 to 9

+ : With grain; irr.temp. 300°C; tensile stress, with grain, 5 MPa.
Δ : With grain; irr.temp. 500°C; tensile stress, with grain, 5 MPa.
o : Across grain; irr.temp. 550°C; compressive stress, with grain, 5 MPa.
x : With grain; irr.temp. 550°C; compressive stress, with grain, 5 MPa.

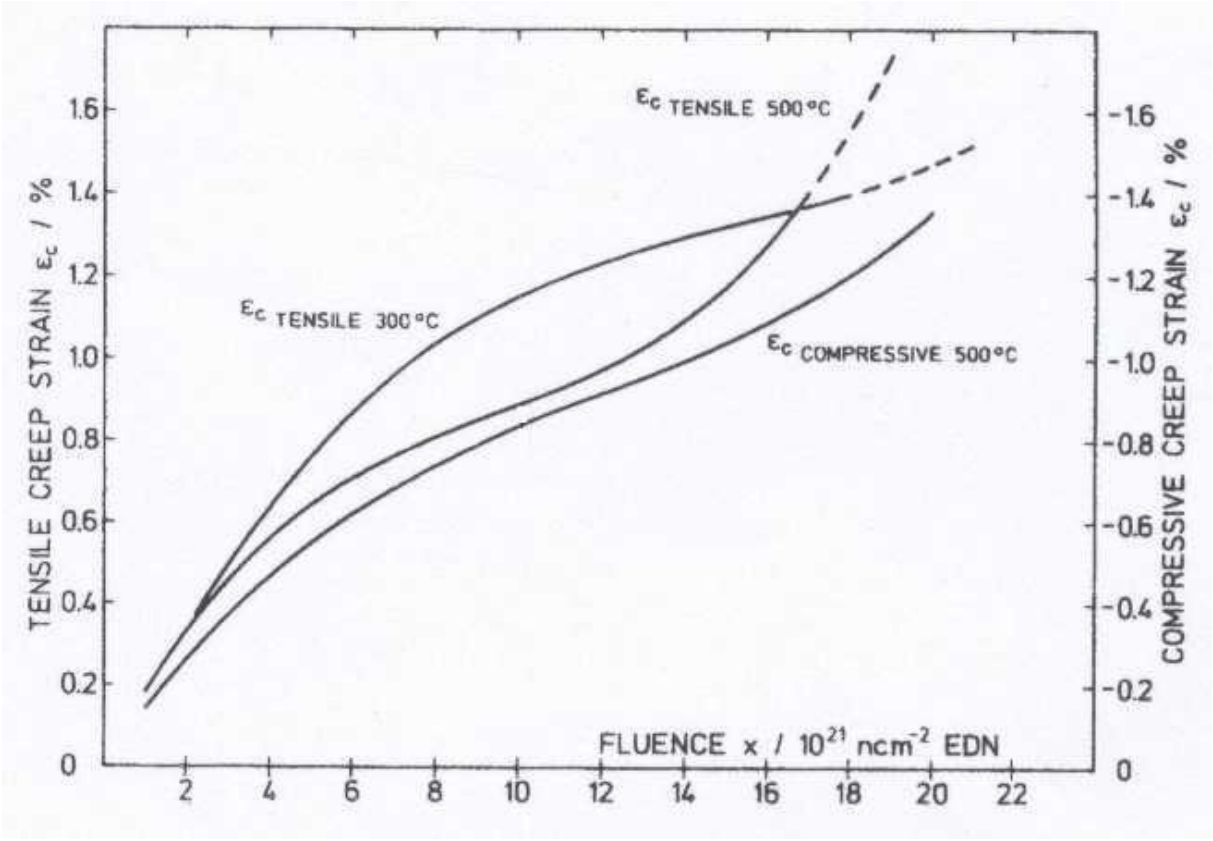

Fig. 47 Tensile and compressive creep strain of ATR-2E graphite vs fast neutron fluence irradiated at 300 and 500°C

7. INFLUENCE OF PRESSING TECHNIQUE ON PROPERTIES OF NEAR-ISOTROPIC GRAPHITE

Two graphites made from the same special pitch coke, one extruded (ATR-2E), the other one vibro-moulded (ATR-2R), were included in the German nuclear graphite irradiation programme. They are a nice pair of graphites for investigating the influence of the two pressing techniques on their physical properties and finally on their irradiation behaviour. Both graphites have already been mentioned in Chapter 2 when the screening test in HFIR with six candidate graphites and the decision in favour of ATR-2E as a reference material were discussed.

As shown in Table 3, some of the properties as communicated by the manufacturer are similar, others are markedly different. First of all, the different densities (1.80 g/cm^3 for ATR-2E; 1.71 g/cm^3 for ATR-2R) and thermal conductivities (around 170 W/(m·K) for ATR-2E; around 115 W/(m·K) for ATR-2R) catch the eye and favour extrusion in both cases. Surprisingly, the strength data of ATR-2R are not at all impaired by the low bulk density, which may indicate different size distributions of the coke particles and/or a good homogeneity of the vibrated material.

Table 10 shows averages and standard deviations of some physical properties of ATR-2R and ATR-2E graphite irradiation samples as measured prior to irradiation. They are in good agreement with the corresponding data in Table 3.

From the corresponding properties of the two sets of irradiation specimens it is now concluded that the irradiation behaviour of the two graphites in HFIR, Oak Ridge, and in HFR, Petten, should be comparable to a certain extent, but in the case of potential differences one has to take into account the fact that the irradiation conditions are better defined in HFR (thermocouple temperature measurements, continuous temperature control, fluence monitoring, etc.), and that there is a difference in fast neutron flux density (in HFIR flux density is higher by a factor of 2 to 3).

From all the physical properties of graphite monitored in fast neutron irradiation experiments the dimensional changes are the most suitable ones for determining even small differences between very similar grades. Therefore, the dimensional changes of ATR-2E and ATR-2R graphites are displayed in Fig. 48 to 63 along with their related volume changes for different irradiation temperatures of 300, 400, 500, and 600 °C.

The interpretation of the data leads to the same conclusion at all irradiation temperatures: Compared to ATR-2E, ATR-2R graphite exhibits (i) a smaller maximum shrinkage, (ii) an earlier

turn-around from shrinkage to expansion, and (iii) an earlier return to the initial dimensions which – as mentioned already - is sometimes taken as a rough indication for the operational lifetime of the graphite.

Graphite Grade	**Orien-tation**	**N**		**Young's Modulus** (GPa)	**Electrical Resistivity** ($\Omega \cdot \mu m$)	**Bulk Density** (g/cm^3)	**Thermal Expansivity** ($10^{-6}/K$)
ATR-2R	parallel	52	Average:	9.45	12.27	*par.*+	5.42 (N=22)
			Stand.Dev.:	0.573	0.590	*perp.:*	0.169
ATR-2R	perpend.	59	Average:	9.00	12.88	1.724	5.74 (N=20)
			Stand.Dev.:	0.516	0.668	0.0460	0.253
			Anisotropy:	1.05	1.05		1.06
ATR-2E	parallel	60	Average:	9.27	7.06	*par.*+	4.51 (N=17)
			Stand.Dev.:	0.665	0.367	*perp.:*	0.189
ATR-2E	perpend.	60	Average:	8.90	7.47	1.800	5.00 (N=19)
			Stand.Dev.:	0.496	0.299	0.0322	0.134
			Anisotropy:	1.04	1.06		1.11

Table 10 Comparison of various physical properties of ATR-2R and ATR-2E graphites (N = number of samples involved)

From the close relation between the two graphites – they are both manufactured from the "same" pitch coke (as far as different batches of coke can be identical) – one would expect very similar initial shrinkage rates. Later, it turned out that ATR-2E graphite shrinks longer and hence reaches its turn-around later and at a higher maximum shrinkage. At turn-around both graphites start expanding more and more rapidly. Since for ATR-2R graphite this expansion begins at a lower fluence and at lower maximum shrinkage it inevitably returns to its initial dimensions earlier than ATR-2E graphite.

After all, the only basic difference in irradiation-induced dimensional changes of the two graphites is the location of turn-around, which is known to be dependent upon the binder coke content in the sense that more binder increases the shrinkage due to irradiation.

Extruded graphite may contain more binder to make the green mixture less viscous for pressing. On the other hand, a small binder content is very important if larger graphite blocks are to be

manufactured. During baking volatile products arise from the pyrolysis of the binder. They form the larger pores within the structure of polycrystalline graphite through which they can escape from the graphite body. Otherwise, the graphite body might be destroyed. Therefore, the amount of binder cannot be varied at will.

Another indication of basic differences between the two graphites is electrical resistivity, which is markedly higher for ATR-2R. The reason for that could be a lower graphitisation temperature, which would also affect the dimensional behaviour under fast neutron irradiation in accordance with the data.

At least for smaller graphite blocks, consideration might be given to using more binder according to the idea that some more binder might improve the dimensional behaviour of vibration-moulded graphite due to irradiation. However, introducing more binder by impregnation with coal tar pitch would not be the right solution since it has been found that additional impregnation increases the density but does not change the irradiation-induced dimensional behaviour.

Finally, it should to be mentioned that around 1977, when both graphites were manufactured, there was much more experience with the extrusion rather than with the vibration moulding procedure. This may have changed in the meantime so that graphite manufacturers may be able to incorporate better irradiation behaviour into modern vibrated graphites.

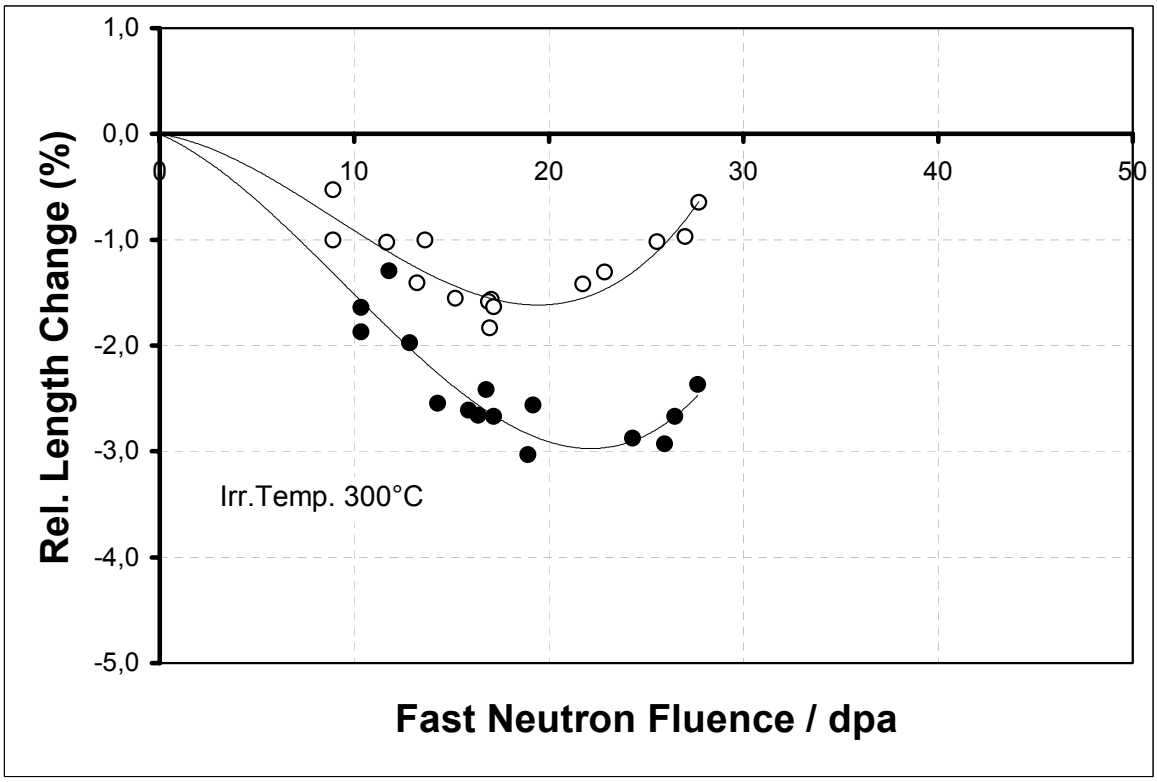

Fig. 48 ***ATR-2R***: Dimensional changes due to fast neutron irradiation at 300°C
(white data points: perpendicular; black data points: parallel to grain orientation)

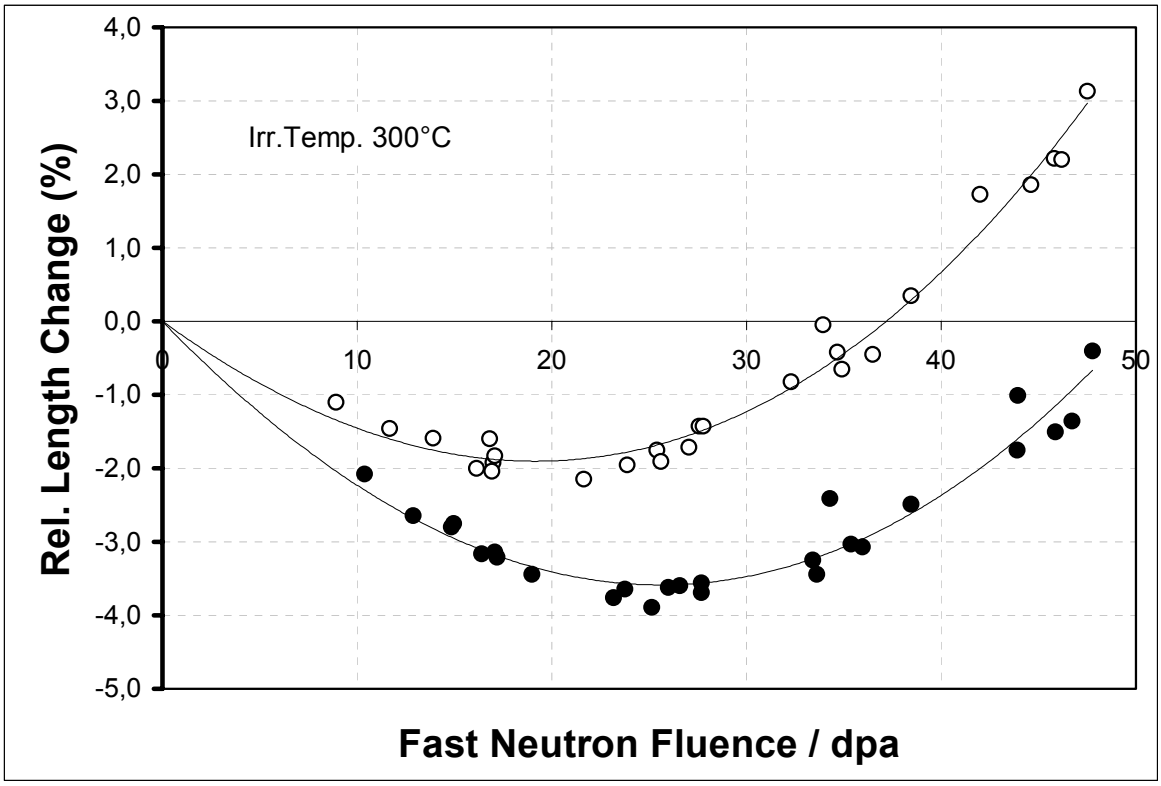

Fig. 49 ***ATR-2E***: Dimensional changes due to fast neutron irradiation at 300°C
(white data points: perpendicular; black data points: parallel to grain orientation)

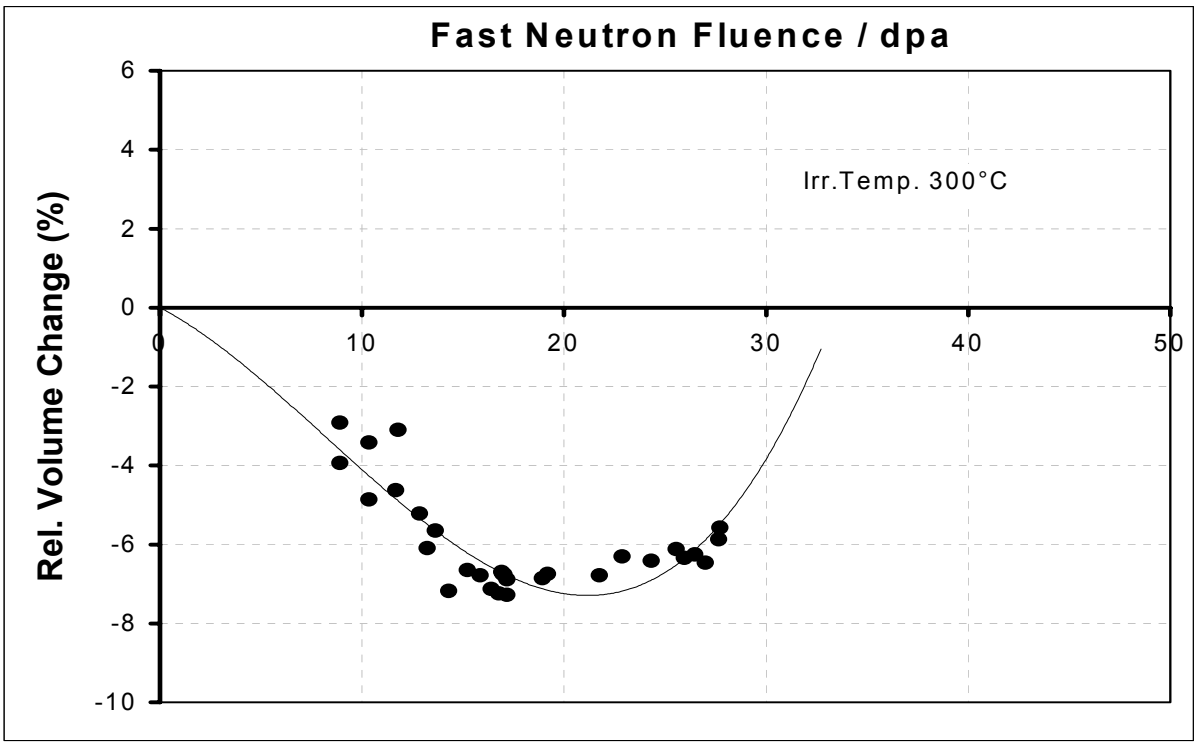

Fig. 50 ***ATR-2R***: Volume changes due to fast neutron irradiation at 300°C

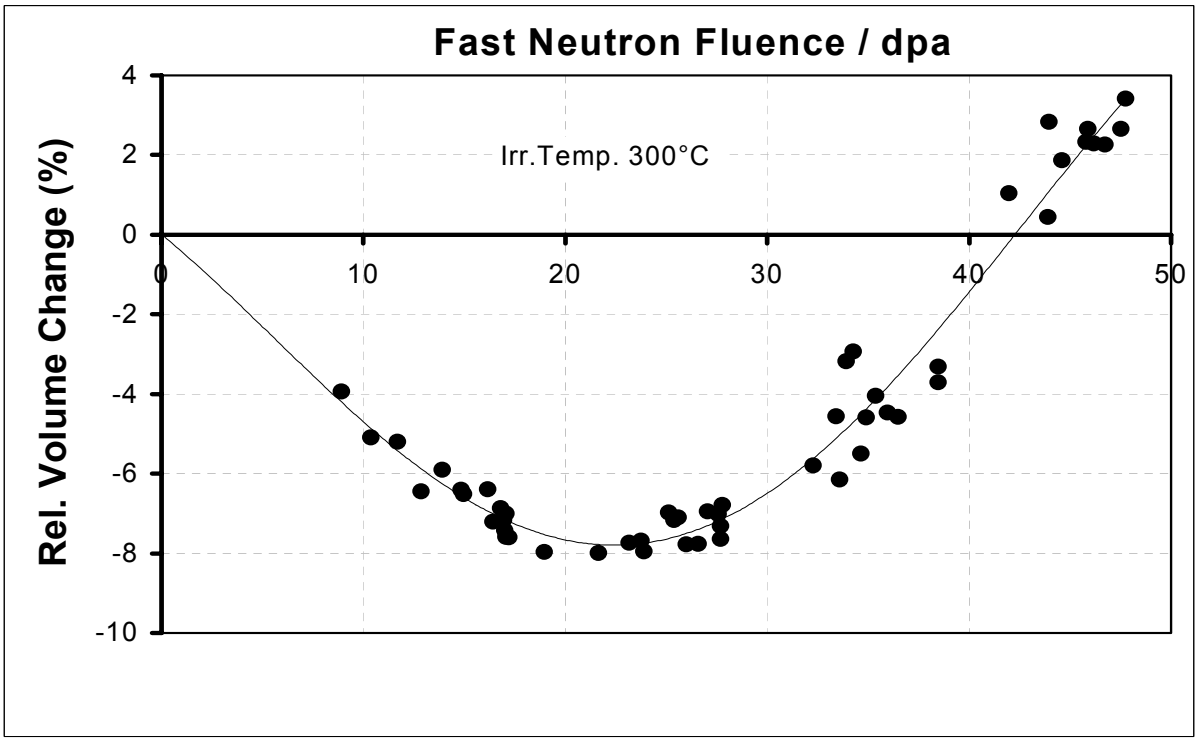

Fig. 51 ***ATR-2E***: Volume changes due to fast neutron irradiation at 300°C

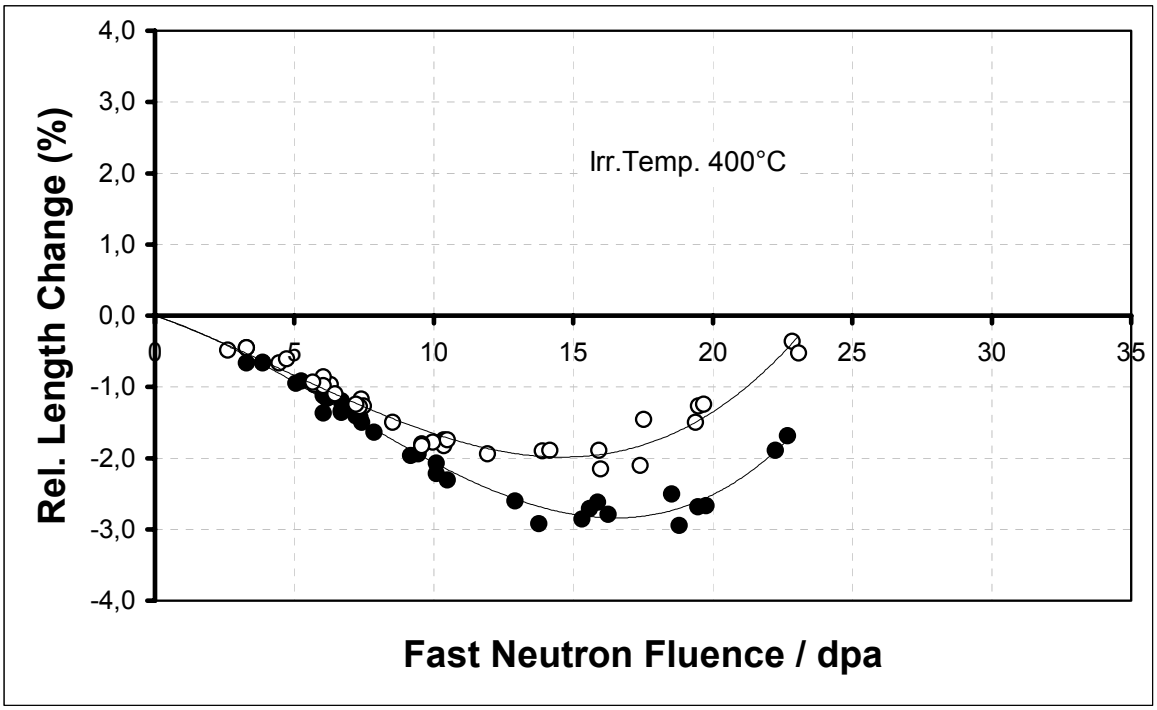

Fig. 52 ***ATR-2R***: Dimensional changes due to fast neutron irradiation at 400°C
(white data points: perpendicular; black data points: parallel to grain orientation)

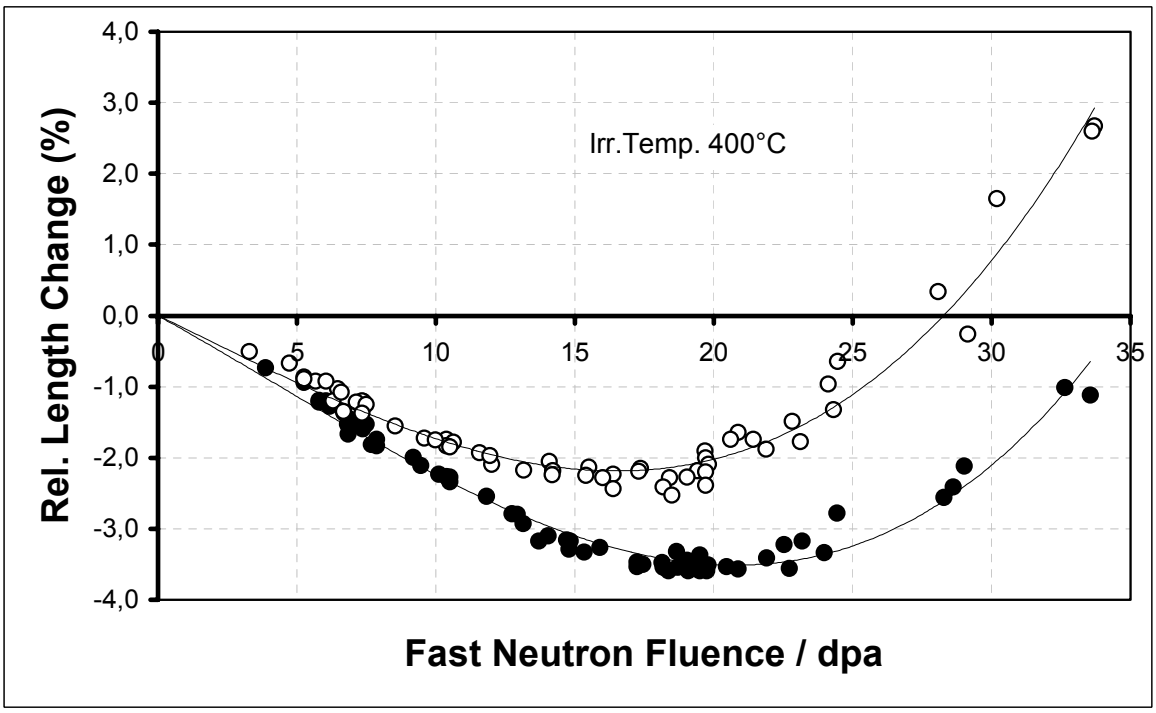

Fig. 53 ***ATR-2E***: Dimensional changes due to fast neutron irradiation at 400°C
(white data points: perpendicular; black data points: parallel to grain orientation)

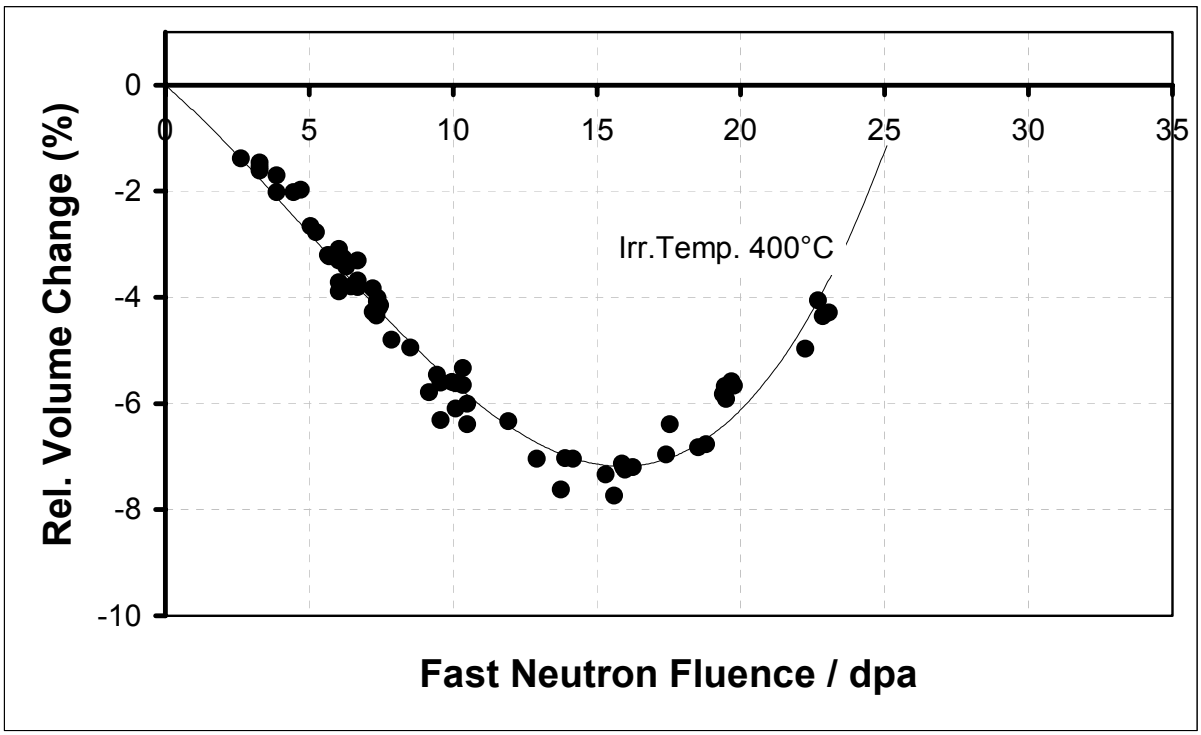

Fig. 54 ***ATR-2R***: Volume changes due to fast neutron irradiation at 400°C

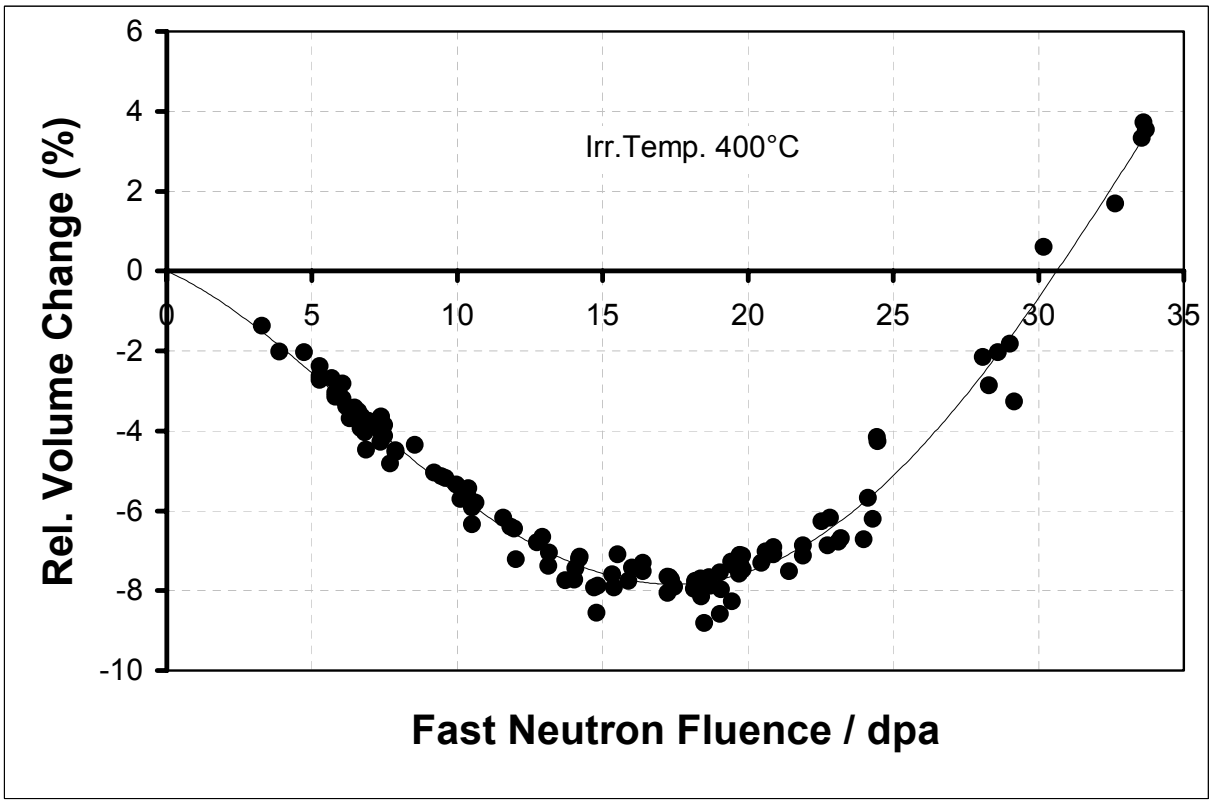

Fig. 55 ***ATR-2E***: Volume changes due to fast neutron irradiation at 400°C

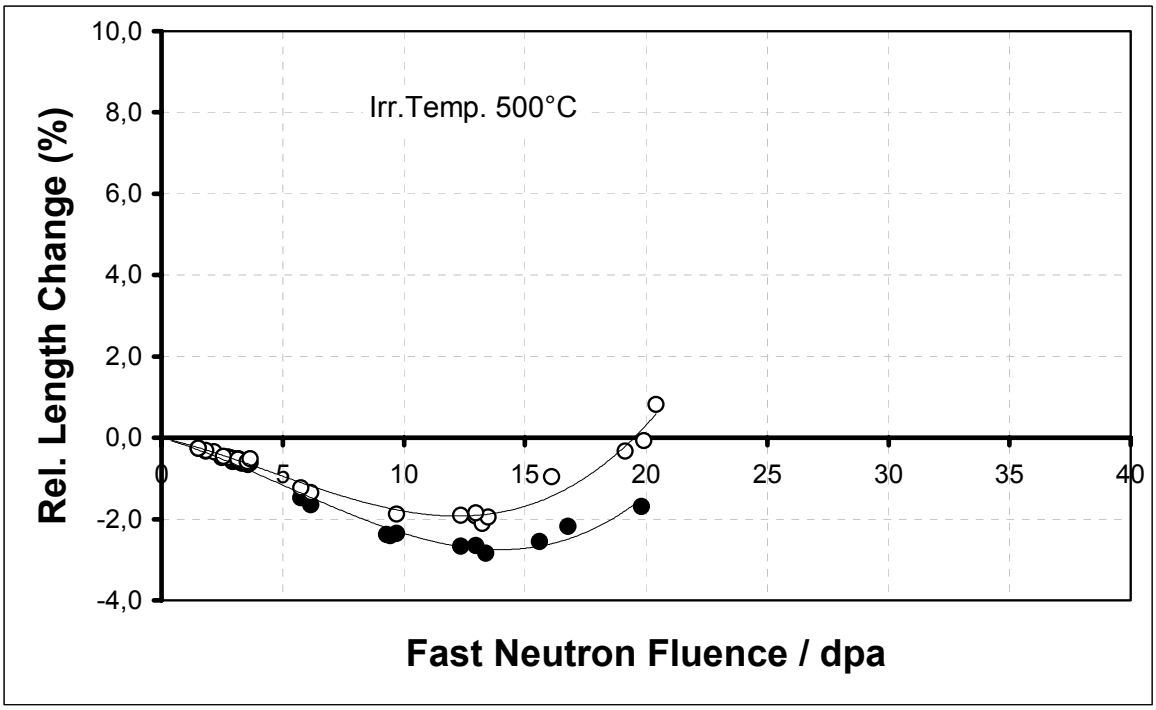

Fig. 56 ***ATR-2R***: Dimensional changes due to fast neutron irradiation at 500°C
(white data points: perpendicular; black data points: parallel to grain orientation)

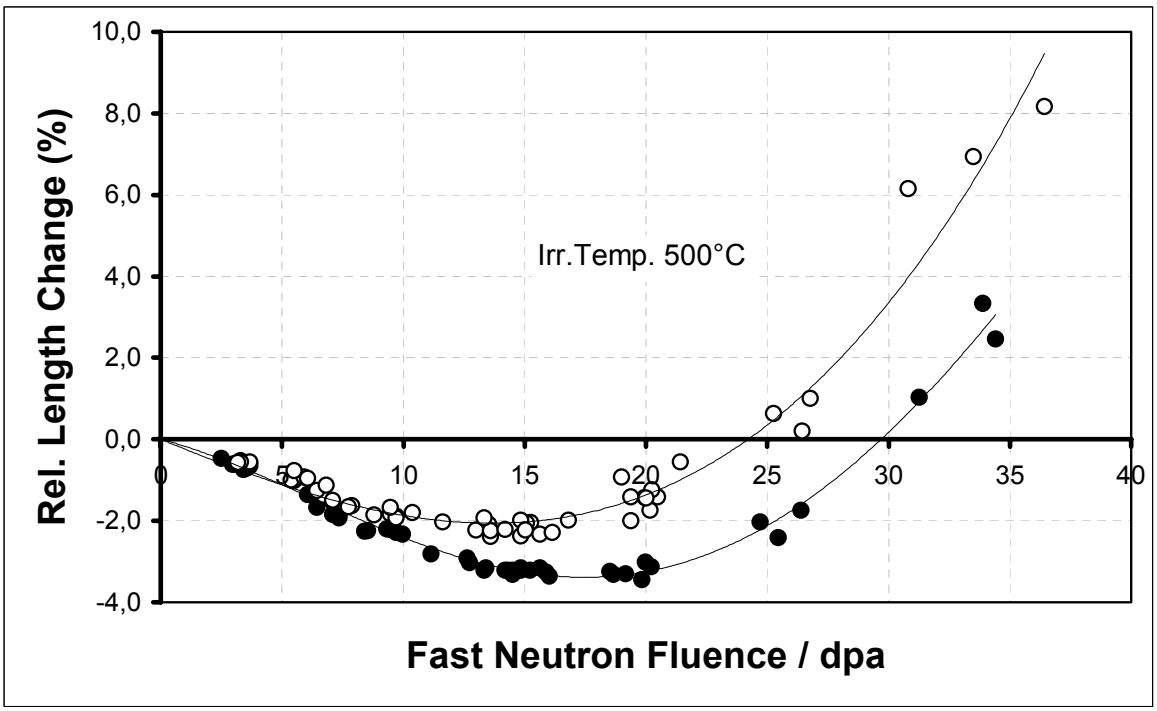

Fig. 57 ***ATR-2E***: Dimensional changes due to fast neutron irradiation at 500°C
(white data points: perpendicular; black data points: parallel to grain orientation)

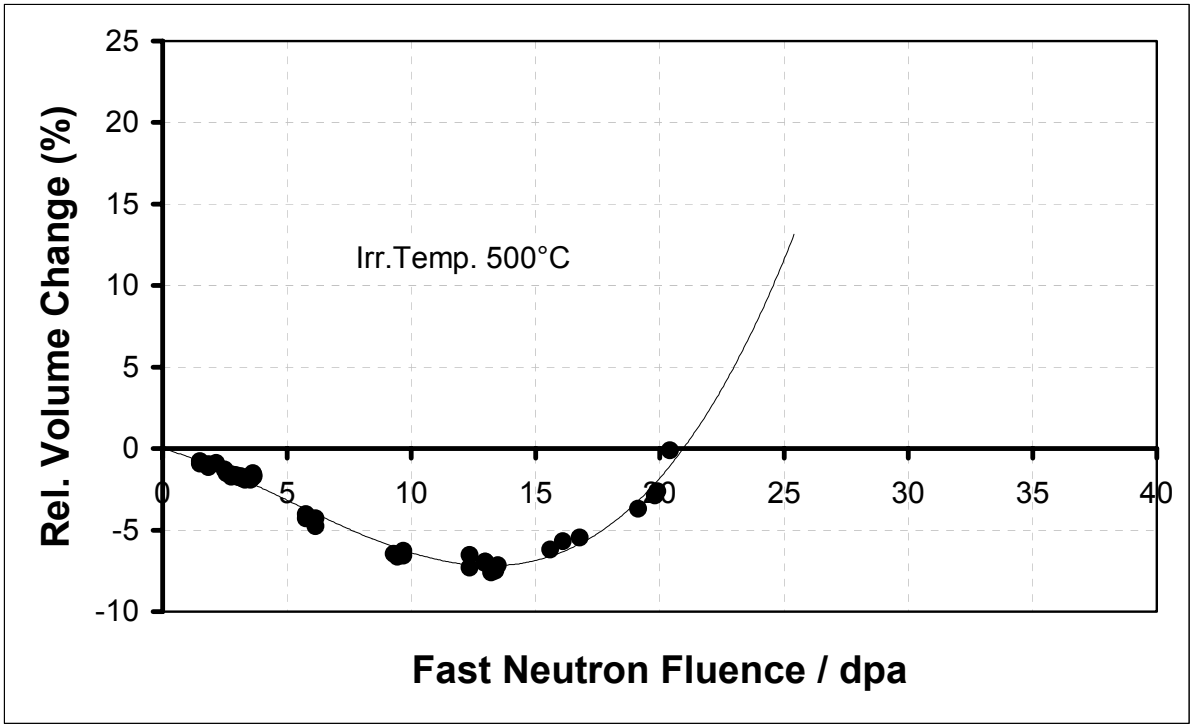

Fig. 58 ***ATR-2R***: Volume changes due to fast neutron irradiation at 500°C

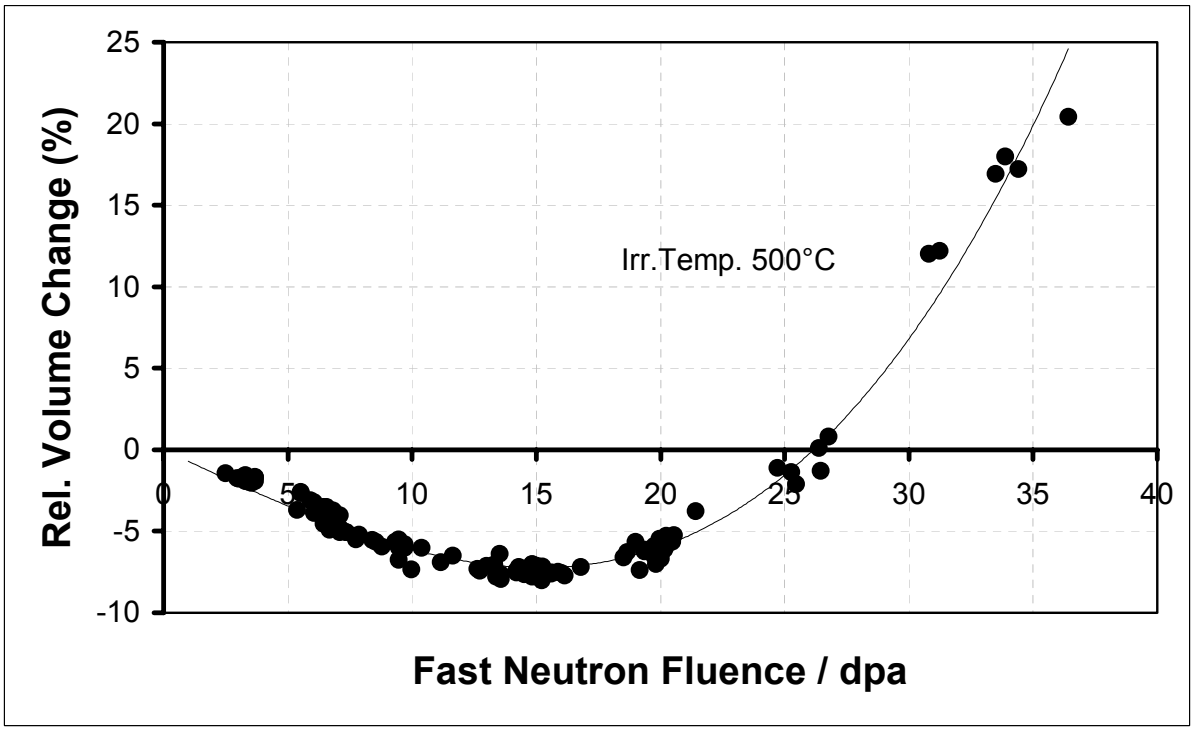

Fig. 59 ***ATR-2E***: Volume changes due to fast neutron irradiation at 500°C

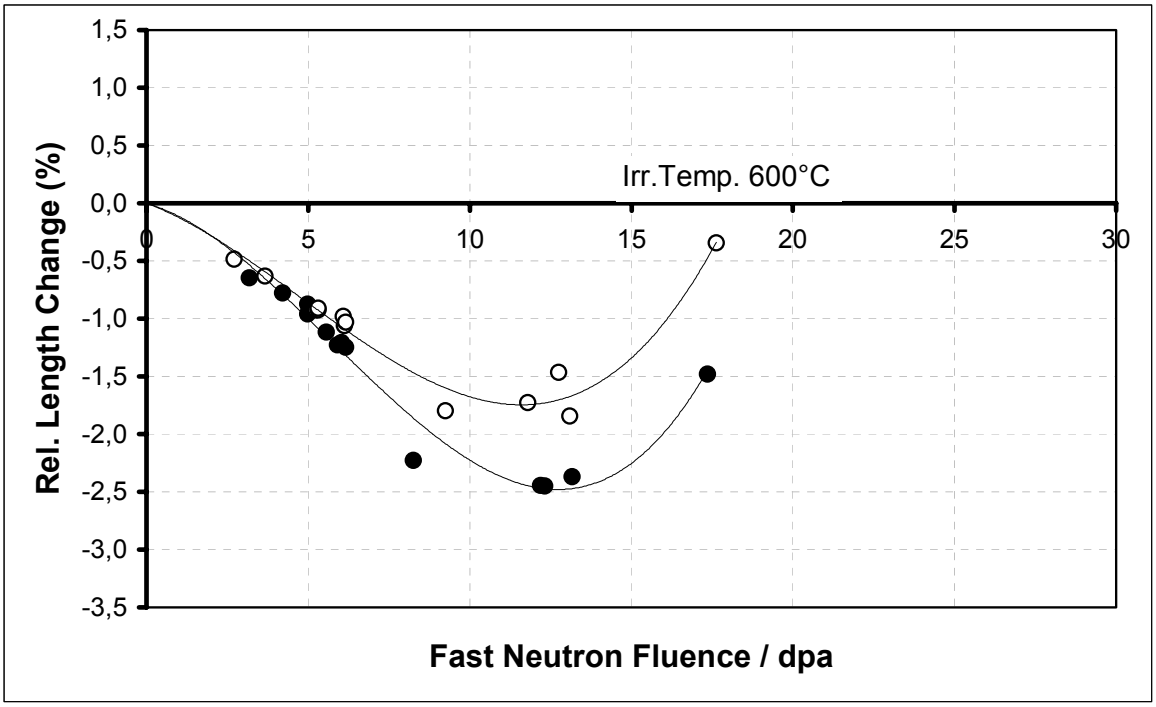

Fig. 60 ***ATR-2R***: Dimensional changes due to fast neutron irradiation at 600°C
(white data points: perpendicular; black data points: parallel to grain orientation)

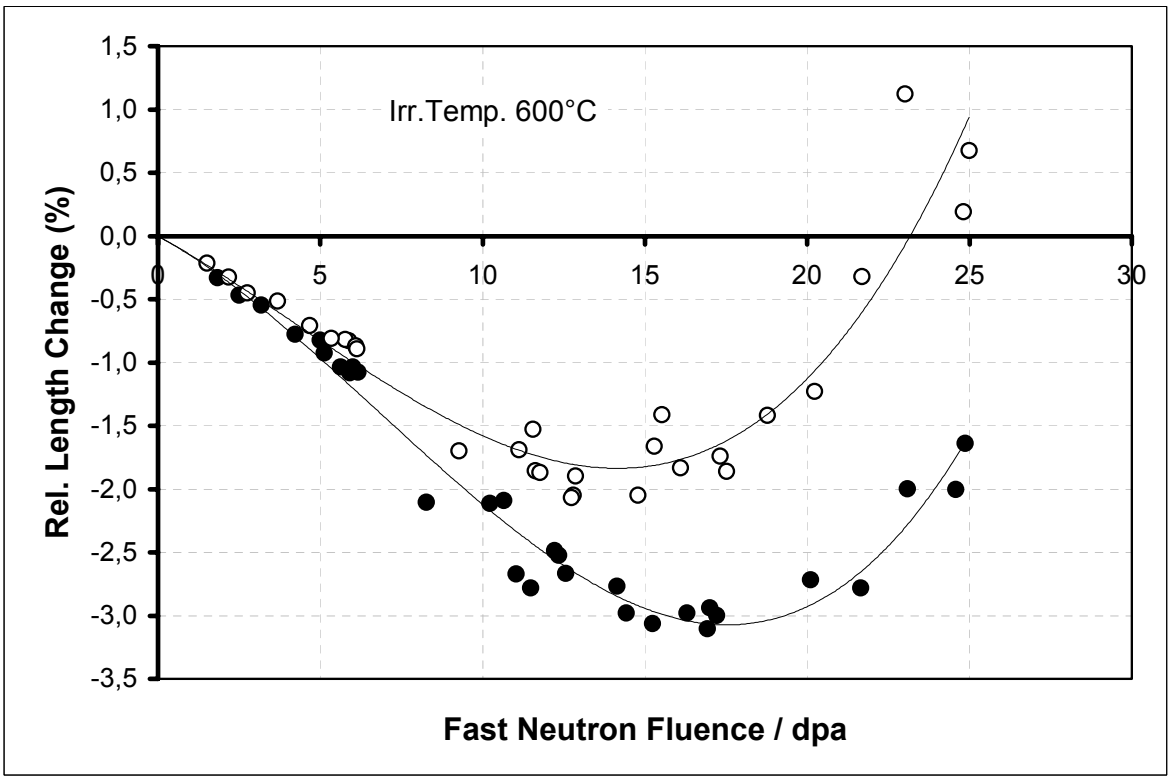

Fig. 61 ***ATR-2E***: Dimensional changes due to fast neutron irradiation at 600°C
(white data points: perpendicular; black data points: parallel to grain orientation)

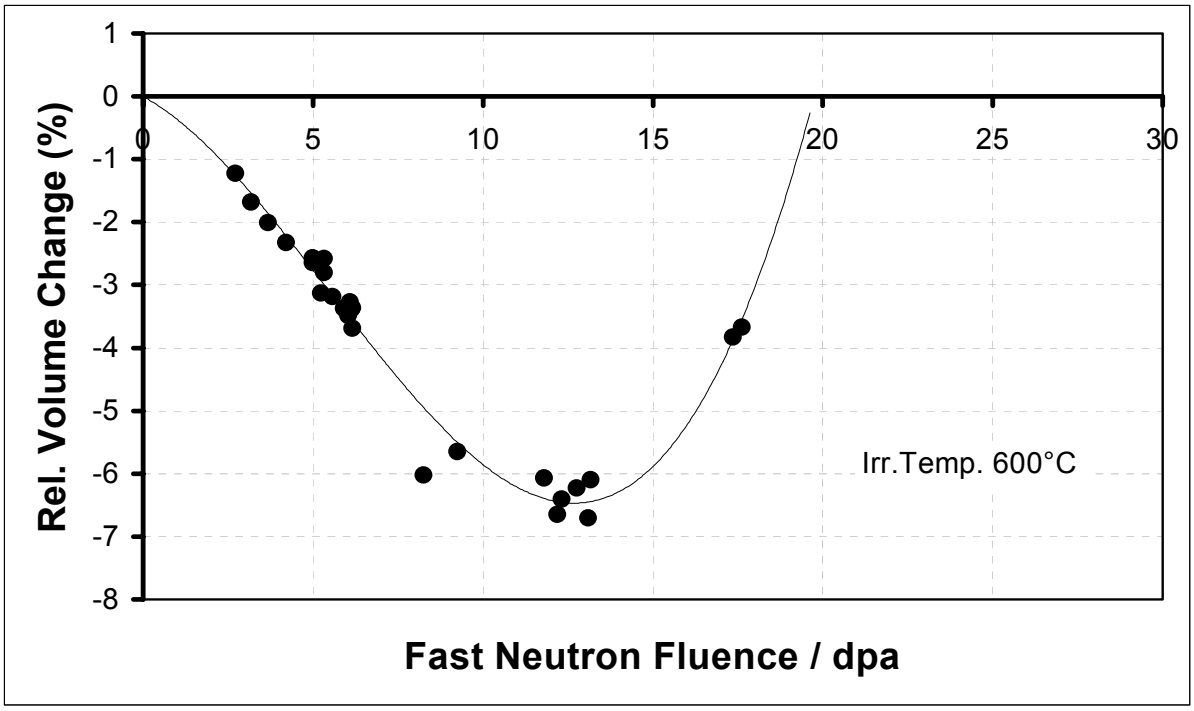

Fig. 62 ***ATR-2R***: Volume changes due to fast neutron irradiation at 600°C

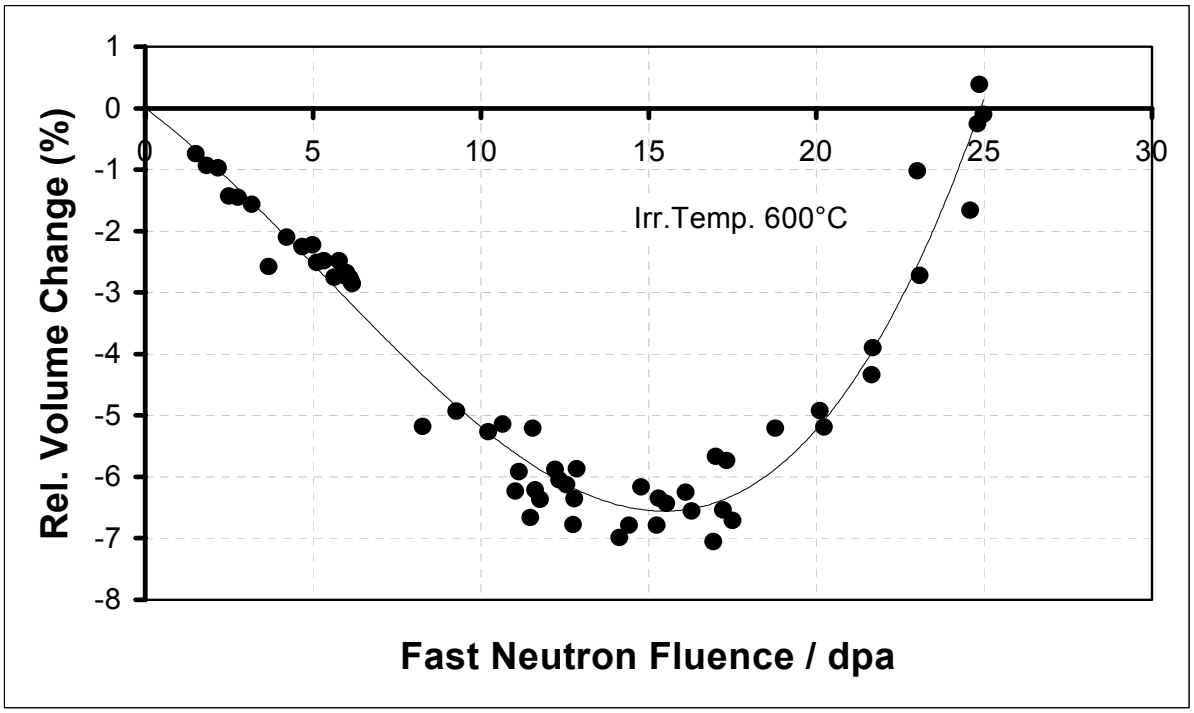

Fig. 63 ***ATR-2E***: Volume changes due to fast neutron irradiation at 600°C

8. CONCLUSION

From 1975 to about 1990, ATR-2E was one of the outstanding nuclear graphites. It was developed exclusively for reactor applications and was tested in great detail. However, for various reasons not many data were published at that time. This report is intended to present all the data available at present (see Appendix B) and thus to remedy the situation.

The amount of information still available today will allow

- graphite manufacturing companies to develop and produce successor materials with similar or better properties,
- reactor engineers and designers to use the old information and data for their design work, thus for an intermediate period of time replacing data not yet available for the current materials.
- licensing and experts organisations to understand that present HTR projects use new high-quality graphites which, even without knowing the entire database, represent an advanced state of the art, and should be considered as proven technology.

As far as nuclear graphite is concerned, the situation is much better today than it was in the past when the graphite reactor concepts Magnox, AVR, RBMK, Peach Bottom, and even AGR, Fort St. Vrain and THTR, were realised. None of these reactors were built with such a level of scientific and technological background. This should give good prospects for the success of the new HTR projects as far as moderator and reflector graphite is concerned.

Appendix A

A. OXIDATION BEHAVIOUR OF ATR-2E GRAPHITE

In connection with analyses of severe air ingress accidents in high-temperature gas-cooled reactors, the oxidation behaviour of ATR-2E graphite deserves some consideration. In the framework of investigations on hypothetical accidents with air ingress, Hinssen, Katscher and Moormann obtained data on the kinetics of chemical reactions of oxygen with the fuel element matrix[50], manufactured by the HOBEG company, and the reactor graphites ASR-1RS, ASR-1RG, V483T, and ATR-2E[51], all manufactured by the former SIGRI Elektrographit company. The parameters were

- temperatures approx. 680 to 930 °C,
- gas pressure 1.5 bar constant, with helium as the carrier gas,
- oxygen partial pressures 0.015 to 0.15 bar.

All graphites showed relatively small, but temperature-dependent differences in their reactivities with ASR-1RG exhibiting the worst oxidation behaviour at 400°C and ATR-2E in the range from 700 to 900°C. However, these differences were not attributed to differences in raw material properties, manufacturing parameters, or other final product properties, so that one cannot learn from the oxidation behaviour of the old graphites how to improve new graphites with respect to their behaviour during air ingress accidents.

Moreover, if the differences in oxidation behaviour are small as in the case of ATR-2E compared to the other graphites, they are overlapped by the uncertainties of the assumptions about possible accident parameters, as Hinssen et al. stated in the final remarks of their second report.

Appendix B

Tables of Basic Property Changes of ATR-2E Graphite

The following data on the irradiation behaviour of ATR-2E graphite were obtained within the framework of the German R & D programme “Hochtemperatur-Brennstoff-Kreislauf (HBK)” (High-Temperature Reactor Fuel Cycle). From about 1977 until 1991, numerous irradiation experiments were performed in HFR Petten by the former Kernforschungsanlage Jülich GmbH (KFA, now Forschungszentrum Jülich GmbH, FZJ), Institut für Reaktorwerkstoffe (IRW, Institute for Reactor Materials). In the past, these data were never published completely. Instead, they were carefully stored electronically by the author, a former member of IRW. Thus, the data survived the end of the German gas-cooled reactor programme in the early 1990s.

The precision of the physical property data is in accordance with the respective DIN standards given in chapter 4.

According to an existing model the fast fluence data were derived from the measured time dependent activities of a set of flux monitors and from the neutronic spectrum of the test reactor. Details are given in section 3.4. For fast fluences resulting from several individual irradiation steps the overall precision cannot easily be defined. Originally, all fluences were calculated as “Dido Nickel Equivalent (DNE)” fluences. For this report they were converted to “displacements-per-atom (dpa)” units applying the widely accepted formula 1 dpa = $7.63*10^{24}/m^2$ (DNE).

As for the irradiation temperatures, they were originally measured continuously by means of thermocouples, and evaluated statistically as median temperatures on condition that the deviations of the individual temperature data from the nominal value were less than 50 K. After each irradiation step the resulting irradiation temperature was calculated as an average of all preceding median temperatures weighted by the respective incremental fluence values.

Irradiation Temperature (°C)	Fast Neutron Fluence (dpa)	Rel. Linear Dimensional Changes $\Delta l/l_0$ (%)	Pre-Irrad. Bulk Density (g/cm^3)	Rel. Volume Changes $\Delta V/V_0$ (%)	Young's Modulus E		Electrical Resistivity R		Thermal Expansivity α	
					Pre-Irrad. E_o (GPa)	Rel. Change E/E_o	Pre-Irrad. R_0 ($\Omega \cdot \mu m$)	Rel. Change $\Delta R/R_0$ (%)	Pre-Irrad. α_0 (10^{-6}/K)	Rel. Change $\Delta\alpha/\alpha_0$ (%)
300	8.92	-1.10	1.830	-3.94	9.39	1.91	7.19	246	4.86	21.2
300	16.99	-1.92	1.830	-7.42	9.39	3.07	7.19	205	4.86	6.2
300	25.39	-1.75	1.830	-7.17	9.39	4.20	7.19	204	4.86	-16.5
299	33.92	-0.05	1.830	-3.17			7.19	229		
310	16.80	-1.60	1.835	-6.87	8.66	3.13	7.50	199	4.72	5.3
308	27.56	-1.43	1.835	-7.02	8.66	3.79	7.50	181	4.72	-24.4
309	38.45	0.35	1.835	-3.31	8.66	4.14	7.50	222	4.72	-35.8
305	47.52	3.13	1.835	2.66	8.66	2.63	7.50	303		
305	17.06	-1.83	1.778	-7.00	8.08	3.26	7.89	194		
303	27.76	-1.43	1.778	-6.79	8.08	4.62	7.89	180		
300	13.91	-1.59	1.820	-5.90	8.69	2.57	7.56	219		
302	23.88	-1.95	1.820	-7.95	8.69	3.65	7.56	176		
303	34.65	-0.42	1.820	-5.49	8.69	4.42	7.56	204		
303	45.80	2.22	1.820	2.33	8.69	3.17	7.56	285		
305	16.93	-2.04	1.828	-7.17	9.41	3.28	7.18	198		
301	27.03	-1.71	1.828	-6.95	9.41	3.47	7.18	192		
302	36.48	-0.45	1.828	-4.57	9.41	4.24	7.18	212		
301	46.18	2.20	1.828	2.29	9.41	2.66	7.18	301		
300	11.68	-1.46	1.797	-5.20	8.76	2.20	7.57	227		
302	21.65	-2.15	1.797	-7.99	8.76	3.36	7.57	181		
303	32.28	-0.82	1.797	-5.79	8.76	4.45	7.57	201		
301	41.98	1.73	1.797	1.04	8.76	2.79	7.57	282		
305	16.14	-2.00	1.857	-6.39	9.81	3.03	6.90	210		
301	25.59	-1.91	1.857	-7.10			6.90	240		
302	34.91	-0.65	1.857	-4.59	9.81	4.39	6.90	211		
301	44.61	1.86	1.857	1.87	9.81	2.76	6.90	282		

Table B1 ATR-2E – physical property changes due to fast neutron irradiation **perpendicular to extrusion. Irradiation temperatures 299 to 310 °C**

Irradiation Temperature (°C)	Fast Neutron Fluence (dpa)	Rel. Linear Dimensional Changes $\Delta l/l_0$ (%)	Pre-Irrad. Bulk Density (g/cm^3)	Rel. Volume Changes $\Delta V/V_0$ (%)	Young's Modulus E		Electrical Resistivity R		Thermal Expansivity α	
					Pre-Irrad. E_o (GPa)	Rel. Change E/E_o	Pre-Irrad. R_0 ($\Omega \cdot \mu m$)	Rel. Change $\Delta R/R_0$ (%)	Pre-Irrad. α_0 (10^{-6}/K)	Rel. Change $\Delta\alpha/\alpha_0$ (%)
300	10.37	-2.08	1.765	-5.09	7.96	2.05	7.93	230	4.27	19.0
300	18.96	-3.44	1.765	-7.97	7.96	3.68	7.93	197	4.27	-4.0
300	26.57	-3.60	1.765	-7.76	7.96	4.38	7.93	201	4.27	-30.4
298	34.27	-2.41	1.765	-2.93	7.96	2.89	7.93	261		
305	17.06	-3.14	1.734	-7.59	8.29	3.28	7.46	207	4.24	0.9
303	27.69	-3.56	1.734	-7.31	8.29	3.65	7.46	198	4.24	-25.9
304	38.45	-2.49	1.734	-3.70	8.29	3.68	7.46	258	4.24	-29.7
302	47.76	-0.40	1.734	3.42	8.29	2.29	7.46	359		
305	17.19	-3.21	1.790	-7.60	8.55	3.30	7.37	203		
303	27.69	-3.69	1.790	-7.64	8.55	4.48	7.37	195		
305	14.83	-2.80	1.822	-6.40	9.77	2.60	6.76	225		
307	25.13	-3.89	1.822	-6.97	9.77	3.58	6.76	198		
305	35.37	-3.03	1.822	-4.04	9.77	3.95	6.76	244		
304	45.87	-1.50	1.822	2.66	9.77	2.67	6.76	328		
305	16.40	-3.16	1.778	-7.21	9.19	3.04	7.16	209		
301	25.98	-3.62	1.778	-7.78	9.19	3.32	7.16	203		
302	35.96	-3.07	1.778	-4.46	9.19	4.00	7.16	242		
302	46.72	-1.36	1.778	2.26	9.19	2.52	7.16	320		
300	12.86	-2.64	1.793	-6.45	8.93	2.43	7.24	223		
304	23.16	-3.76	1.793	-7.74	8.93	3.55	7.24	195		
303	33.40	-3.25	1.793	-4.56	8.93	4.07	7.24	235		
302	43.94	-1.01	1.793	2.84	8.93	2.36	7.24	332		
300	14.96	-2.75	1.796	-6.51	9.40	2.63	6.91	231		
298	23.75	-3.64	1.796	-7.68	9.40	4.05	6.91	204		
300	33.60	-3.44	1.796	-6.15	9.40	4.54	6.91	221		
299	43.90	-1.75	1.796	0.45	9.40	2.78	6.91	300		

Table B2 ATR-2E – physical property changes due to fast neutron irradiation **parallel to extrusion.**
Irradiation temperatures 298 to 307 °C

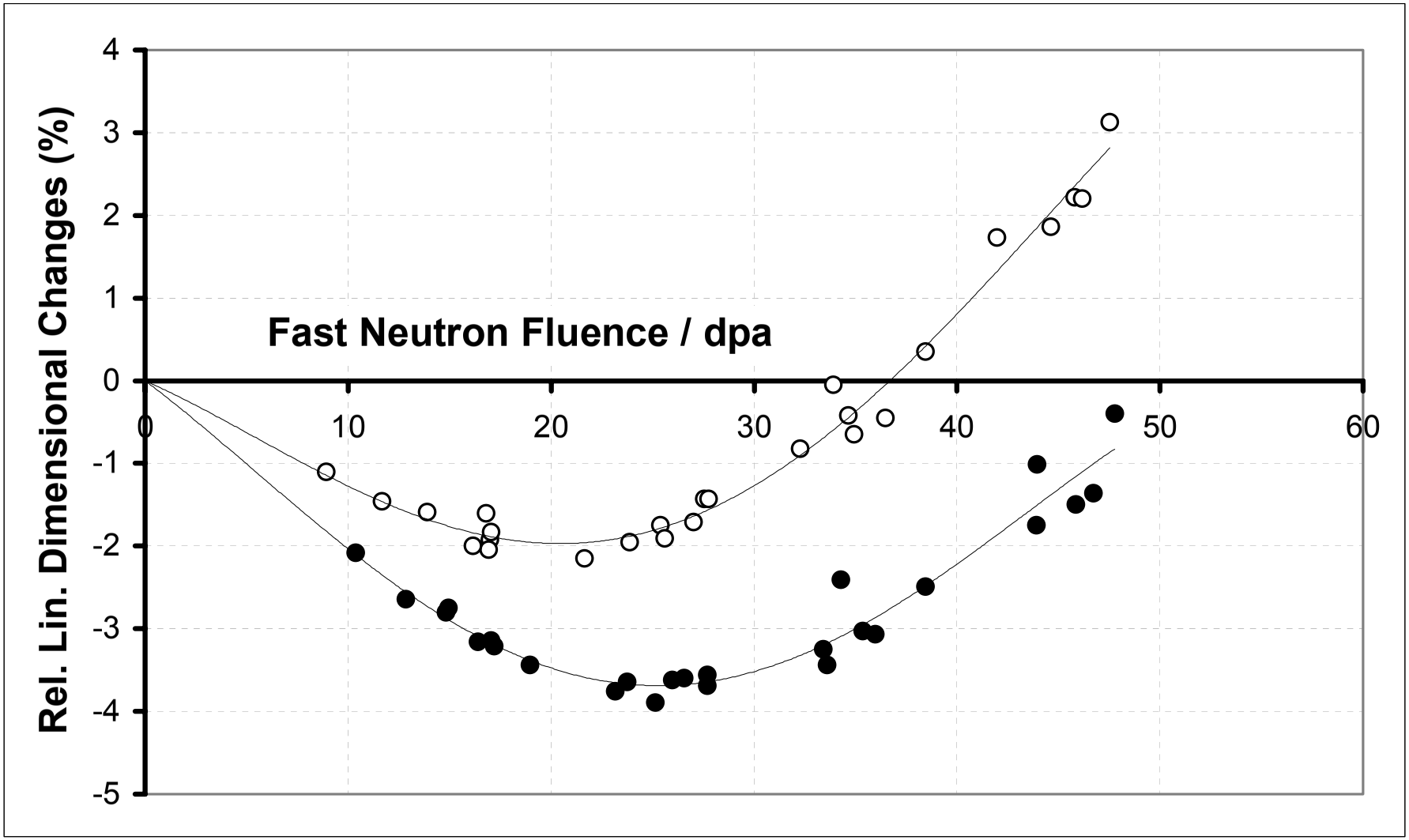

Fig. B1 **ATR-2E** – Linear dimensional changes due to fast neutron irradiation; perpendicular (white circles) and parallel (black circles) to extrusion. **Irradiation temperature about 300 °C** (data from Table B1 and B2)

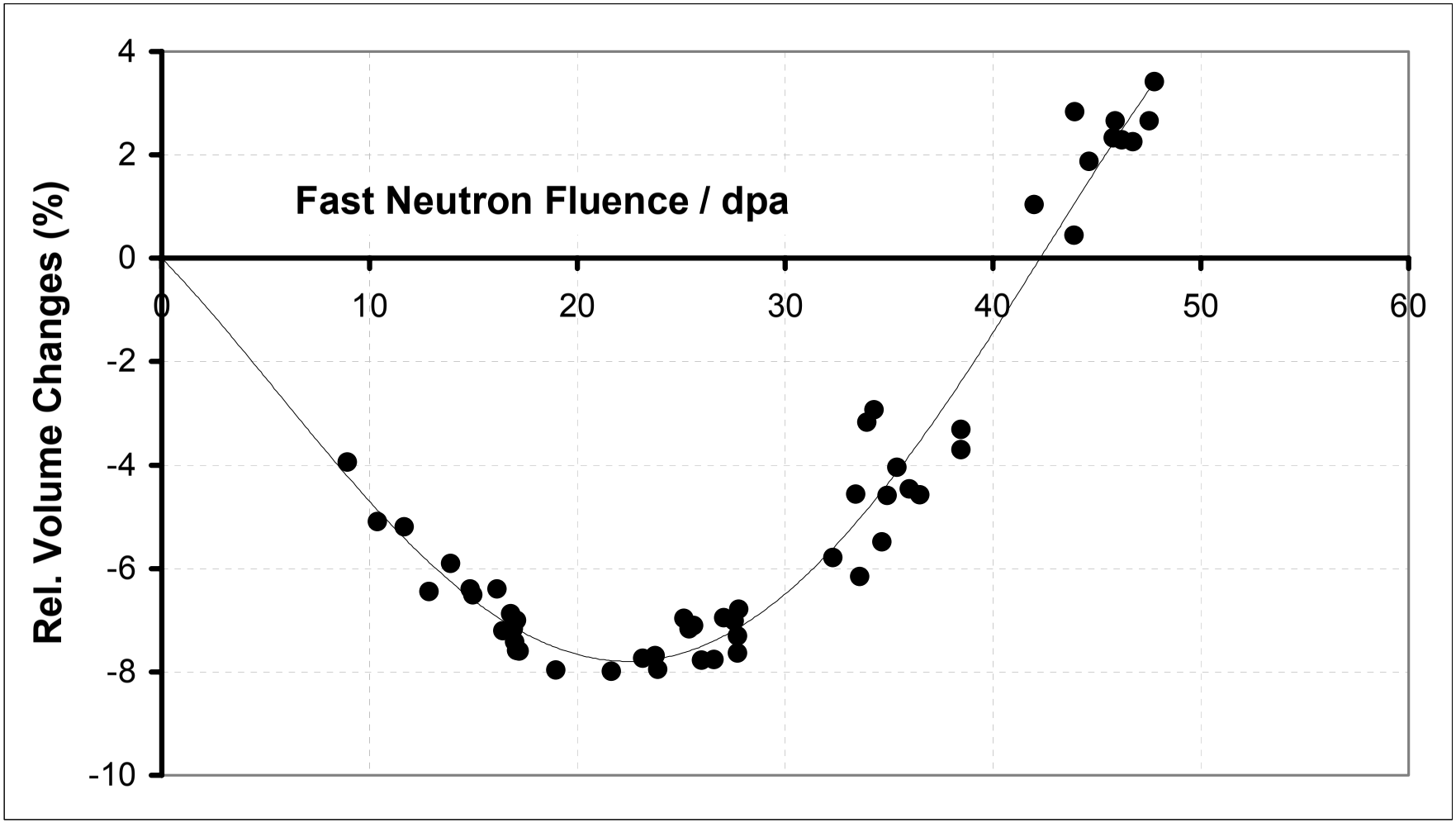

Fig. B2 **ATR-2E** – Relative volume changes due to fast neutron irradiation.
Irradiation temperature about 300 °C (data from Table B1 and B2)

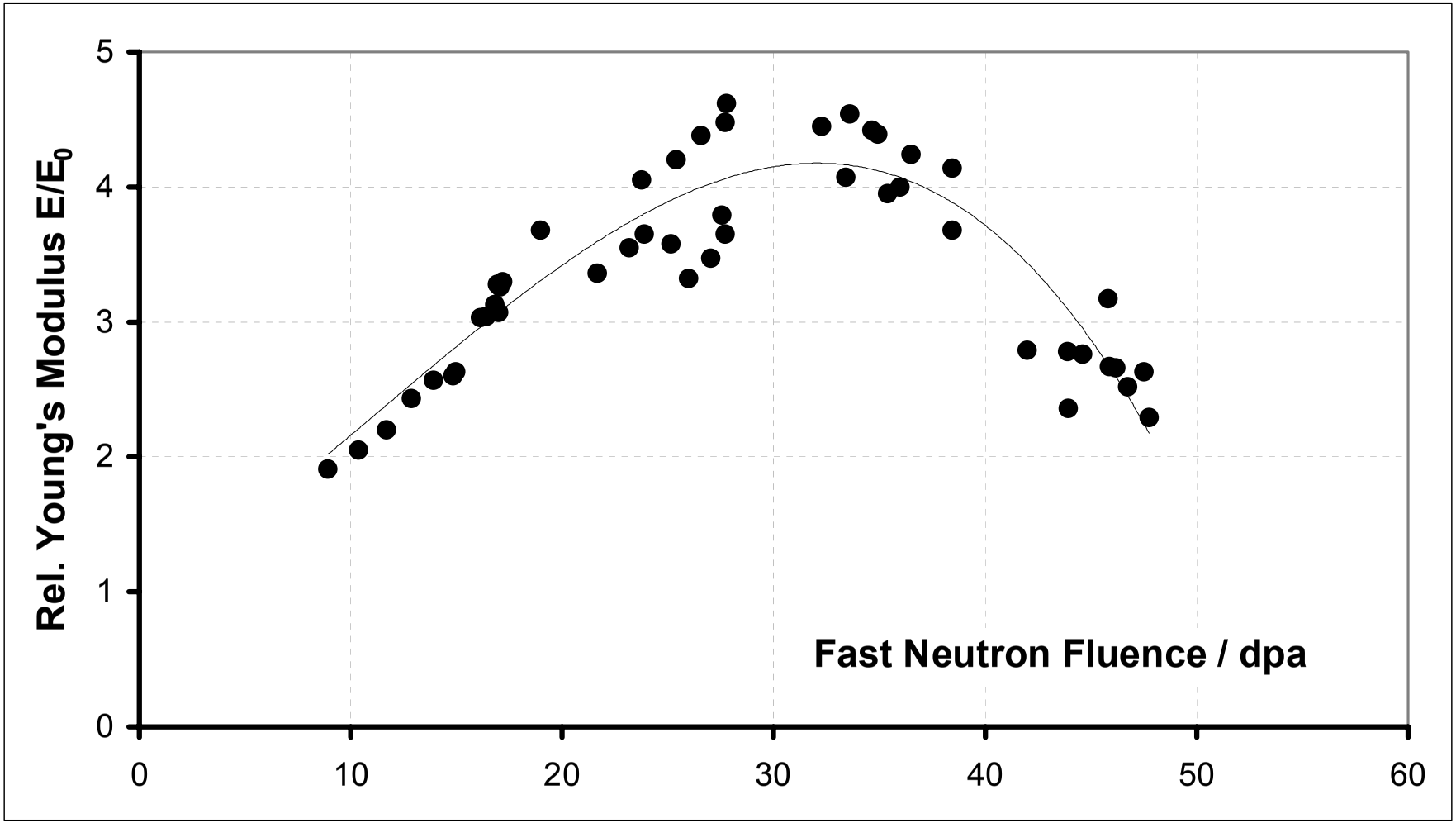

Fig. B3 **ATR-2E** – Relative Young's modulus changes due to fast neutron irradiation.
Irradiation temperature about 300 °C (data from Table B1 and B2)

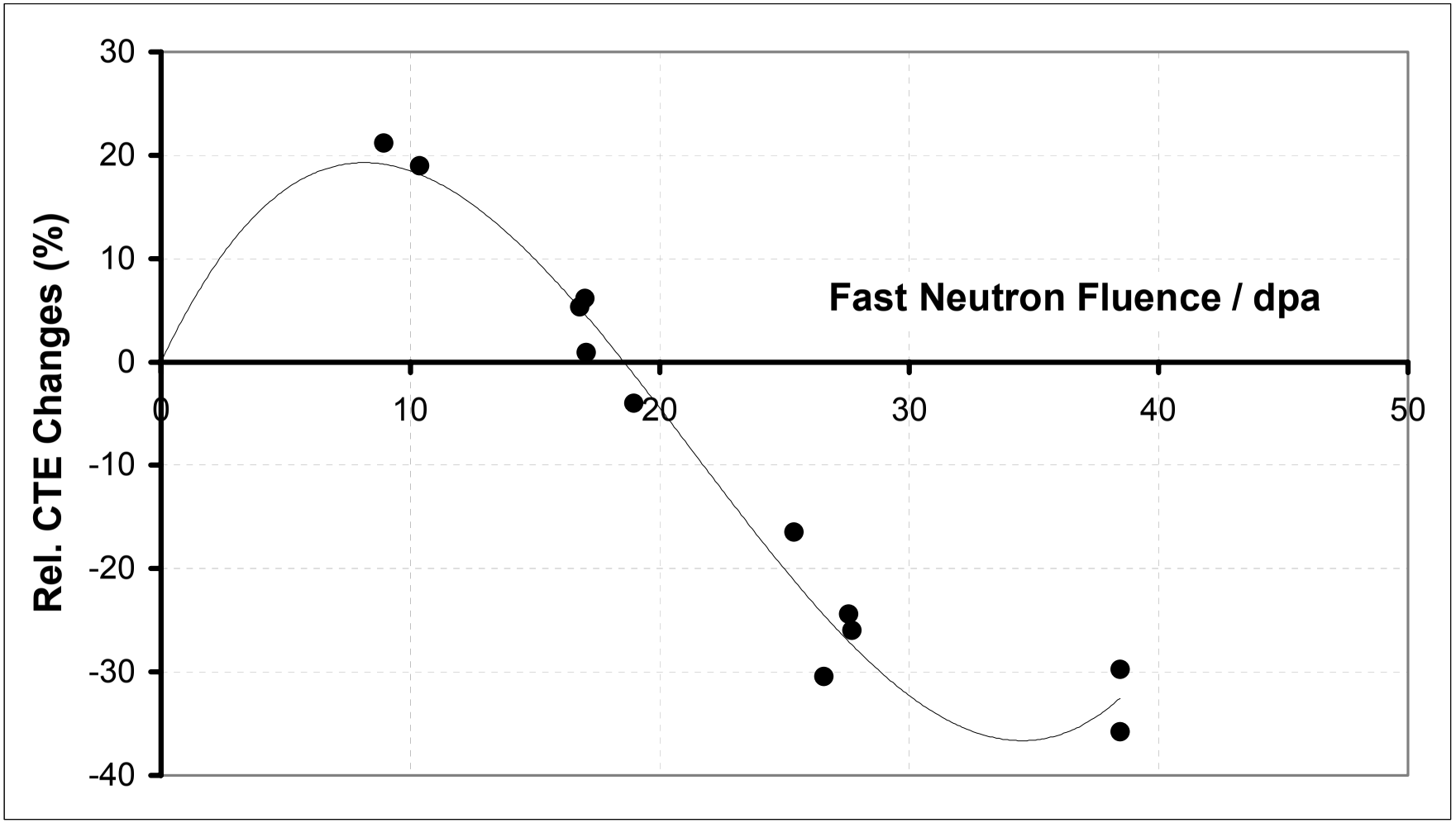

Fig. B4 **ATR-2E** – Relative thermal expansivity (CTE) changes due to fast neutron irradiation.
Irradiation temperature about 300 °C (data from Table B1 and B2)

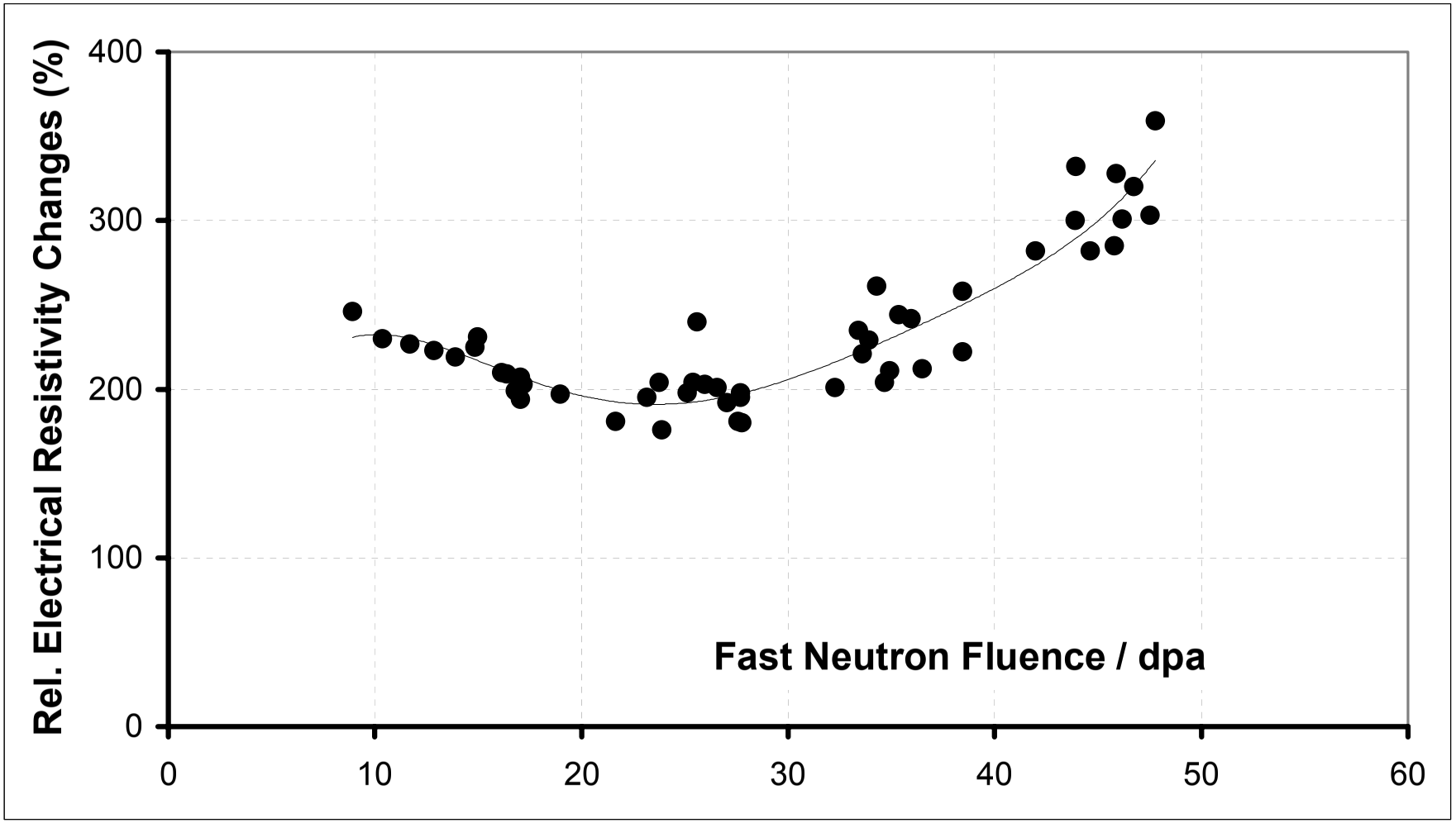

Fig. B5 **ATR-2E** – Relative electrical resistivity changes due to fast neutron irradiation.
Irradiation temperature about 300 °C (data from Table B1 and B2)

Irradiation Temperature (°C)	Fast Neutron Fluence (dpa)	Rel. Linear Dimensional Changes $\Delta l/l_0$ (%)	Pre-Irrad. Bulk Density (g/cm^3)	Rel. Volume Changes $\Delta V/V_0$ (%)	Young's Modulus E		Electrical Resistivity R		Thermal Expansivity α	
					Pre-Irrad. E_o (GPa)	Rel. Change E/E_o	Pre-Irrad. R_0 ($\Omega \cdot \mu m$)	Rel. Change $\Delta R/R_0$ (%)	Pre-Irrad. α_0 (10^{-6}/K)	Rel. Change $\Delta\alpha/\alpha_0$ (%)
395	6.46	-1.03	1.839	-3.42	8.76	2.49	7.44	211	4.73	28.3
392	14.07	-2.05	1.839	-7.44	8.76	3.35	7.44	195	4.73	3.2
392	19.69	-1.90	1.839	-7.33	8.76	4.25	7.44	191	4.73	-21.8
392	20.87	-1.64	1.839	-6.91	8.76	4.00	7.44	193	4.73	-27.2
396	30.18	1.65	1.839	0.60	8.76	2.72	7.44	281	4.73	-30.5
405	7.38	-1.21	1.850	-3.64	9.56	2.53	7.12	209	4.90	24.5
400	15.51	-2.13	1.850	-7.09	9.56	3.49	7.12	198	4.90	-6.9
401	22.83	-1.49	1.850	-6.17	9.56	4.40	7.12	197	4.90	-31.2
401	24.12	-0.96	1.850	-5.67	9.56	3.71	7.12	212	4.90	-35.0
400	33.70	2.67	1.850	3.55	9.56	2.57	7.12	298	4.90	-37.2
390	3.28	-0.50	1.841	-1.37	9.48	2.17	7.15	225	4.68	29.3
400	6.30	-1.20	1.841	-3.69	9.48	2.51	7.15	222	4.68	12.7
400	12.01	-2.09	1.841	-7.22	9.48	3.08	7.15	201	4.68	8.8
400	13.15	-2.17	1.841	-7.04	9.48	3.26	7.15	204	4.68	2.7
400	21.42	-1.74	1.841	-7.51	9.48	4.07	7.15	199	4.68	-29.1
405	10.37	-1.74	1.803	-5.43	8.64	2.76	7.55	209	4.92	12.6
403	19.71	-2.00	1.803	-7.11	8.64	4.24	7.55	199	4.92	-24.8
403	20.60	-1.74	1.803	-7.01	8.64	4.02	7.55	205	4.92	-25.7
405	28.08	0.34	1.803	-2.15	8.64	3.03	7.55	257	4.92	-47.5
405	7.35	-1.20	1.808	-3.67	8.55	2.49	7.64	223	4.89	21.6
408	16.38	-2.23	1.808	-7.30	8.55	3.79	7.64	196	4.89	-9.2
407	17.36	-2.15	1.808	-7.72	8.55	3.84	7.64	200	4.89	-17.2
405	24.45	-0.64	1.808	-4.26	8.55	3.31	7.64	236	4.89	-31.4
405	6.59	-1.08	1.821	-3.51	8.67	2.47	7.31	220		
397	14.20	-2.18	1.821	-7.16	8.67	3.33	7.31	203		
395	19.82	-2.09	1.821	-7.47	8.67	4.24	7.31	196		

Table B3 ATR-2E – physical property changes due to fast neutron irradiation **perpendicular to extrusion.**
Irradiation temperatures 390 to 415 °C (continued)

Irradiation Temperature (°C)	Fast Neutron Fluence (dpa)	Rel. Linear Dimensional Changes $\Delta l/l_0$ (%)	Pre-Irrad. Bulk Density (g/cm^3)	Rel. Volume Changes $\Delta V/V_0$ (%)	Young's Modulus E		Electrical Resistivity R		Thermal Expansivity α	
					Pre-Irrad. E_o (GPa)	Rel. Change E/E_o	Pre-Irrad. R_0 ($\Omega \cdot \mu m$)	Rel. Change $\Delta R/R_0$ (%)	Pre-Irrad. α_0 (10^{-6}/K)	Rel. Change $\Delta\alpha/\alpha_0$ (%)
405	5.25	-0.86	1.821	-2.64	8.79	2.40	7.45	221		
402	10.63	-1.78	1.821	-5.79	8.79	2.81	7.45	207		
403	17.30	-2.19	1.821	-7.66	8.79	4.05	7.45	198		
405	5.67	-0.92	1.828	-2.68	9.46	2.40	7.18	216		
405	11.57	-1.93	1.828	-6.17	9.46	2.87	7.18	207		
405	18.40	-2.28	1.828	-8.14	9.46	4.13	7.18	190		
405	7.13	-1.22	1.754	-3.85	7.90	2.49	8.01	211		
400	15.39	-2.25	1.754	-7.92	7.90	3.50	8.01	199		
398	21.89	-1.88	1.754	-6.87	7.90	4.29	8.01	195		
405	5.25	-0.89	1.826	-2.72	9.53	2.40	7.08	221		
410	7.48	-1.25	1.794	-3.85	8.40	2.49	7.69	211		
402	16.01	-2.28	1.794	-7.43	8.40	3.53	7.69	197		
401	23.11	-1.77	1.794	-6.78	8.40	4.34	7.69	193		
401	24.30	-1.32	1.794	-6.20	8.40	3.70	7.69	207		
402	33.62	2.60	1.794	3.72	8.40	2.19	7.69	338		
405	8.53	-1.55	1.751	-4.35	8.14	2.60	7.92	215		
405	18.18	-2.41	1.751	-7.76	8.14	4.10	7.92	184		
405	9.58	-1.72	1.818	-5.18	9.47	2.69	7.07	214		
405	19.42	-2.18	1.818	-7.28	9.47	4.18	7.07	199		
405	10.37	-1.83	1.815	-5.72	8.70	2.23	7.61	204		
403	19.71	-2.20	1.815	-7.12	8.70	4.27	7.61	192		
405	10.50	-1.85	1.768	-6.34	8.58	2.86	7.66	203		
403	19.03	-2.27	1.768	-8.58	8.58	4.25	7.66	187		
395	9.97	-1.75	1.817	-5.35	9.60	2.72	7.05	211		
397	18.50	-2.53	1.817	-8.81	9.60	4.14	7.05	187		
397	19.70	-2.39	1.817	-7.58	9.60	4.08	7.05	200		

Table B3 ATR-2E – physical property changes due to fast neutron irradiation **perpendicular to extrusion.**
Irradiation temperatures 390 to 415 °C (continued)

Irradiation Temperature (°C)	Fast Neutron Fluence (dpa)	Rel. Linear Dimensional Changes $\Delta l/l_0$ (%)	Pre-Irrad. Bulk Density (g/cm^3)	Rel. Volume Changes $\Delta V/V_0$ (%)	Young's Modulus E		Electrical Resistivity R		Thermal Expansivity α	
					Pre-Irrad. E_o (GPa)	Rel. Change E/E_o	Pre-Irrad. R_0 ($\Omega \cdot \mu m$)	Rel. Change $\Delta R/R_0$ (%)	Pre-Irrad. α_0 (10^{-6}/K)	Rel. Change $\Delta\alpha/\alpha_0$ (%)
400	29.15	-0.26	1.817	-3.26	9.60	3.22	7.05	247		
405	7.35	-1.37	1.789	-4.28	8.87	2.54	7.55	222		
408	16.38	-2.44	1.789	-7.52	8.87	3.87	7.55	196		
415	4.72	-0.67	1.799	-2.03	8.53	2.27	7.77	235		
409	11.94	-1.97	1.799	-6.45	8.53	2.82	7.77	208		
405	6.04	-0.92	1.795	-2.81	9.10	2.40	7.28	238		
405	14.19	-2.24	1.795	-7.20	9.10	2.46	7.28	209		
405	6.67	-1.35	1.778	-3.93	8.90	2.60	7.30	235		

Table B3 ATR-2E – physical property changes due to fast neutron irradiation **perpendicular to extrusion. Irradiation temperatures 390 to 415 °C**

Irradiation Temperature (°C)	Fast Neutron Fluence (dpa)	Rel. Linear Dimensional Changes $\Delta l/l_0$ (%)	Pre-Irrad. Bulk Density (g/cm^3)	Rel. Volume Changes $\Delta V/V_0$ (%)	Young's Modulus E		Electrical Resistivity R		Thermal Expansivity α	
					Pre-Irrad. E_o (GPa)	Rel. Change E/E_o	Pre-Irrad. R_0 ($\Omega \cdot \mu m$)	Rel. Change $\Delta R/R_0$ (%)	Pre-Irrad. α_0 (10^{-6}/K)	Rel. Change $\Delta\alpha/\alpha_0$ (%)
385	6.05	-1.20	1.814	-3.19	9.85	2.20	6.72	225	4.31	26.8
385	13.14	-2.93	1.814	-7.38	9.85	3.13	6.72	215	4.31	0.6
386	18.19	-3.54	1.814	-7.79	9.85	3.98	6.72	212	4.31	-25.9
387	19.44	-3.49	1.814	-8.26	9.85	3.95	6.72	215	4.31	-31.8
393	29.02	-2.12	1.814	-1.82	9.85	3.12	6.72	286	4.31	-41.8
410	7.48	-1.53	1.764	-4.12	8.50	2.49	7.45	212	4.29	25.3
403	14.70	-3.16	1.764	-7.92	8.50	3.44	7.45	204	4.29	-11.2
402	21.90	-3.41	1.764	-7.12	8.50	4.31	7.45	210	4.29	-37.4
402	23.19	-3.17	1.764	-6.69	8.50	3.80	7.45	227	4.29	-36.4
398	32.64	-1.01	1.764	1.69	8.50	2.67	7.45	326	4.29	-37.2
395	3.87	-0.73	1.743	-2.02	8.30	2.26	7.60	232	4.17	31.4
400	7.68	-1.81	1.743	-4.81	8.30	2.57	7.60	230	4.17	10.6
400	13.71	-3.17	1.743	-7.74	8.30	3.37	7.60	203	4.17	-10.1
400	14.79	-3.29	1.743	-8.55	8.30	3.58	7.60	209	4.17	-12.4
400	22.53	-3.22	1.743	-6.26	8.30	3.75	7.60	227	4.17	-35.4
405	10.50	-2.34	1.828	-5.86	9.92	2.72	6.70	216	4.63	2.71
403	19.49	-3.59	1.828	-7.37	9.92	4.10	6.70	202	4.63	-26.58
403	20.47	-3.53	1.828	-7.31	9.92	3.94	6.70	209	4.63	-32.76
405	28.61	-2.41	1.828	-2.03	9.92	3.08	6.70	274	4.63	-38.72
405	7.87	-1.74	1.756	-4.53	9.10	2.52	7.25	226	4.70	7.7
408	17.24	-3.47	1.756	-8.05	9.10	3.89	7.25	209	4.70	-22.2
407	18.14	-3.48	1.756	-7.95	9.10	3.92	7.25	205	4.70	-28.1
405	24.44	-2.78	1.756	-4.15	9.10	3.24	7.25	250	4.70	-41.2
405	6.94	-1.46	1.792	-3.75	9.52	2.45	6.95	220		
395	14.03	-3.10	1.792	-7.73	9.52	3.27	6.95	209		
394	19.08	-3.59	1.792	-7.96	9.52	4.09	6.95	207		

Table B4 ATR-2E – physical property changes due to fast neutron irradiation **parallel to extrusion.**
Irradiation temperatures 385 to 410 °C (continued)

Irradiation Temperature (°C)	Fast Neutron Fluence (dpa)	Rel. Linear Dimensional Changes $\Delta l/l_0$ (%)	Pre-Irrad. Bulk Density (g/cm^3)	Rel. Volume Changes $\Delta V/V_0$ (%)	Young's Modulus E		Electrical Resistivity R		Thermal Expansivity α	
					Pre-Irrad. E_o (GPa)	Rel. Change E/E_o	Pre-Irrad. R_0 ($\Omega \cdot \mu m$)	Rel. Change $\Delta R/R_0$ (%)	Pre-Irrad. α_0 (10^{-6}/K)	Rel. Change $\Delta\alpha/\alpha_0$ (%)
405	5.79	-1.19	1.837	-3.04	10.44	2.39	6.63	220		
408	11.82	-2.54	1.837	-6.40	10.44	2.87	6.63	213		
407	18.67	-3.32	1.837	-7.66	10.44	4.13	6.63	198		
405	6.18	-1.27	1.820	-3.38	10.02	2.44	6.58	226		
410	12.74	-2.79	1.820	-6.79	10.02	2.98	6.58	219		
408	19.74	-3.59	1.820	-7.35	10.02	4.22	6.58	208		
400	6.82	-1.53	1.780	-4.03	8.77	2.43	7.25	221		
397	14.83	-3.17	1.780	-7.88	8.77	3.36	7.25	213		
395	20.87	-3.57	1.780	-7.09	8.77	4.19	7.25	207		
405	5.79	-1.22	1.801	-3.15	9.82	2.41	6.82	222		
410	7.36	-1.59	1.814	-4.01	10.01	2.47	6.70	218		
402	15.89	-3.26	1.814	-7.76	10.01	3.45	6.70	209		
400	22.73	-3.56	1.814	-6.87	10.01	4.27	6.70	210		
400	23.98	-3.34	1.814	-6.71	10.01	3.75	6.70	230		
401	33.56	-1.12	1.814	3.34	10.01	2.46	6.70	340		
405	9.19	-1.99	1.811	-5.04	9.14	2.61	6.92	225		
405	19.03	-3.44	1.811	-7.55	9.14	4.04	6.92	214		
405	10.10	-2.23	1.795	-5.71	9.05	2.71	7.25	211		
405	19.79	-3.51	1.795	-7.12	9.05	4.13	7.25	206		
405	10.50	-2.27	1.848	-5.91	10.56	2.76	6.47	215		
403	19.49	-3.37	1.848	-7.31	10.56	3.21	6.47	209		
400	10.37	-2.26	1.795	-5.67	9.50	2.73	6.90	217		
398	18.37	-3.59	1.795	-7.69	9.50	4.06	6.90	203		
390	9.45	-2.11	1.796	-5.14	9.11	2.65	6.92	230		
392	17.45	-3.50	1.796	-7.90	9.11	3.86	6.92	207		
393	18.70	-3.54	1.796	-7.87	9.11	3.93	6.92	193		

Table B4 ATR-2E – physical property changes due to fast neutron irradiation **parallel to extrusion.**
Irradiation temperatures 385 to 410 °C (continued)

Irradiation Temperature (°C)	Fast Neutron Fluence (dpa)	Rel. Linear Dimensional Changes $\Delta l/l_0$ (%)	Pre-Irrad. Bulk Density (g/cm^3)	Rel. Volume Changes $\Delta V/V_0$ (%)	Young's Modulus E		Electrical Resistivity R		Thermal Expansivity α	
					Pre-Irrad. E_o (GPa)	Rel. Change E/E_o	Pre-Irrad. R_0 ($\Omega \cdot \mu m$)	Rel. Change $\Delta R/R_0$ (%)	Pre-Irrad. α_0 (10^{-6}/K)	Rel. Change $\Delta\alpha/\alpha_0$ (%)
397	28.28	-2.56	1.796	-2.86	9.11	3.23	6.92	274		
405	7.87	-1.83	1.796	-4.49	9.56	2.37	6.89	227		
408	17.24	-3.53	1.796	-7.65	9.56	3.93	6.89	210		
410	5.25	-0.94	1.830	-2.37	9.97	2.22	6.74	244		
407	12.93	-2.80	1.830	-6.65	9.97	2.30	6.74	219		
405	6.69	-1.37	1.788	-13.35	8.98	2.99	7.12	242		
405	15.33	-3.33	1.788	-7.59	8.98	3.50	7.12	210		
405	6.85	-1.67	1.795	-4.47	8.81	2.56	7.17	239		

Table B4 ATR-2E – physical property changes due to fast neutron irradiation **parallel to extrusion. Irradiation temperatures 385 to 410 °C**

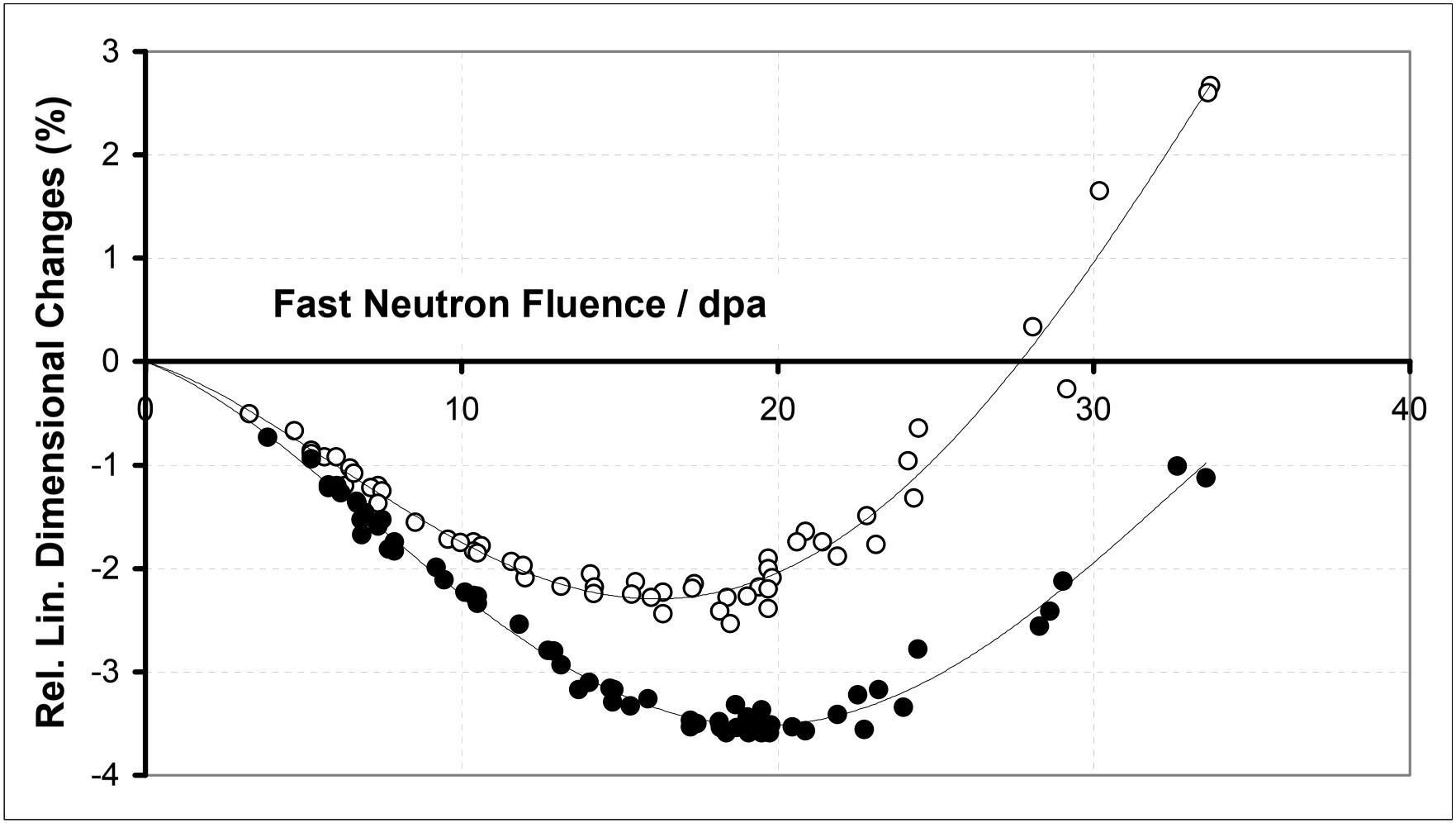

Fig. B6 **ATR-2E** – Linear dimensional changes due to fast neutron irradiation; perpendicular (white circles) and parallel (black circles) to extrusion. **Irradiation temperature about 400 °C** (data from Table B3 and B4)

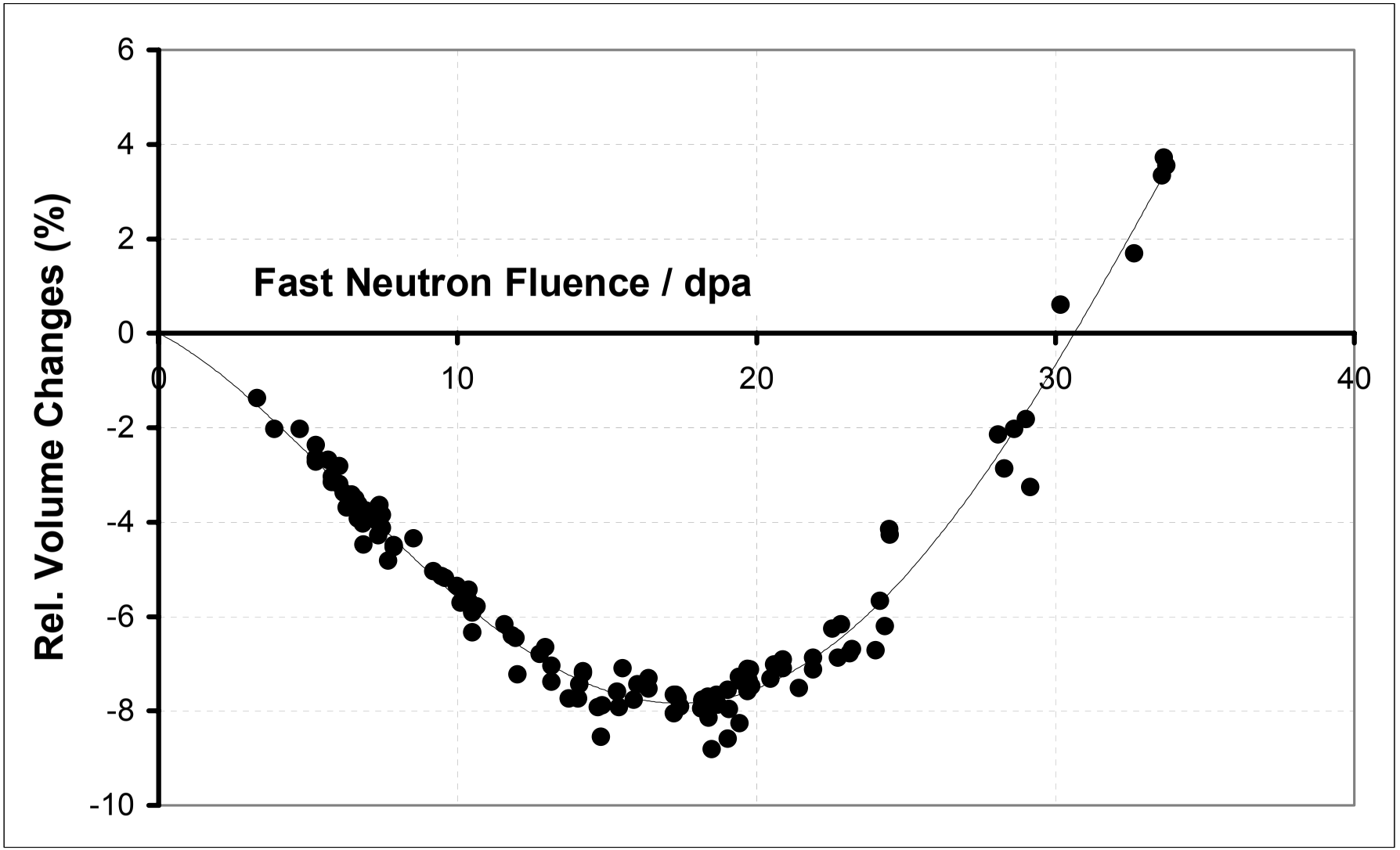

Fig. B7 **ATR-2E** – Relative volume changes due to fast neutron irradiation.
Irradiation temperature about 400 °C (data from Table B3 and B4)

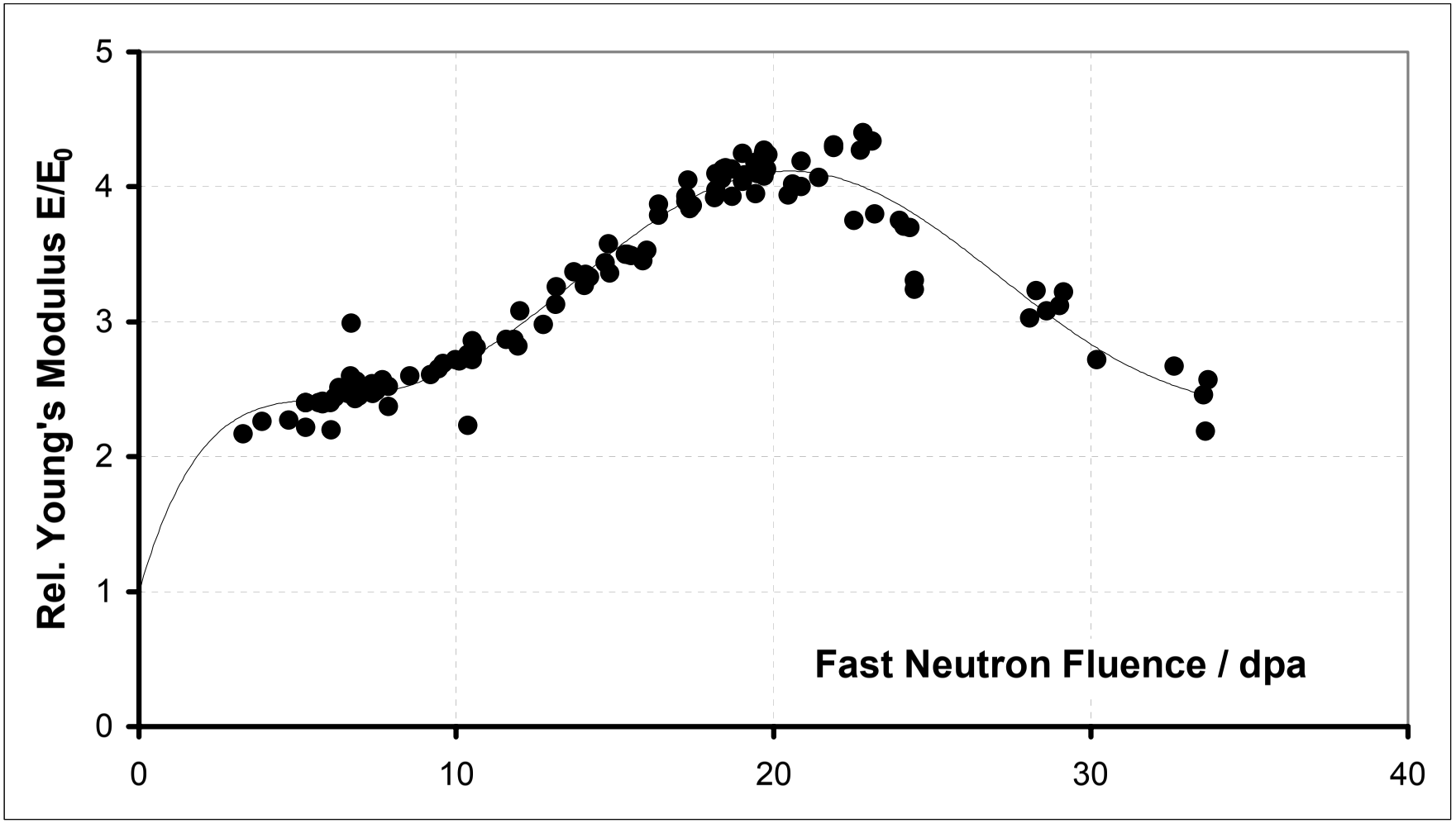

Fig. B8 **ATR-2E** – Relative Young's modulus changes due to fast neutron irradiation.
Irradiation temperature about 400 °C (data from Table B3 and B4)

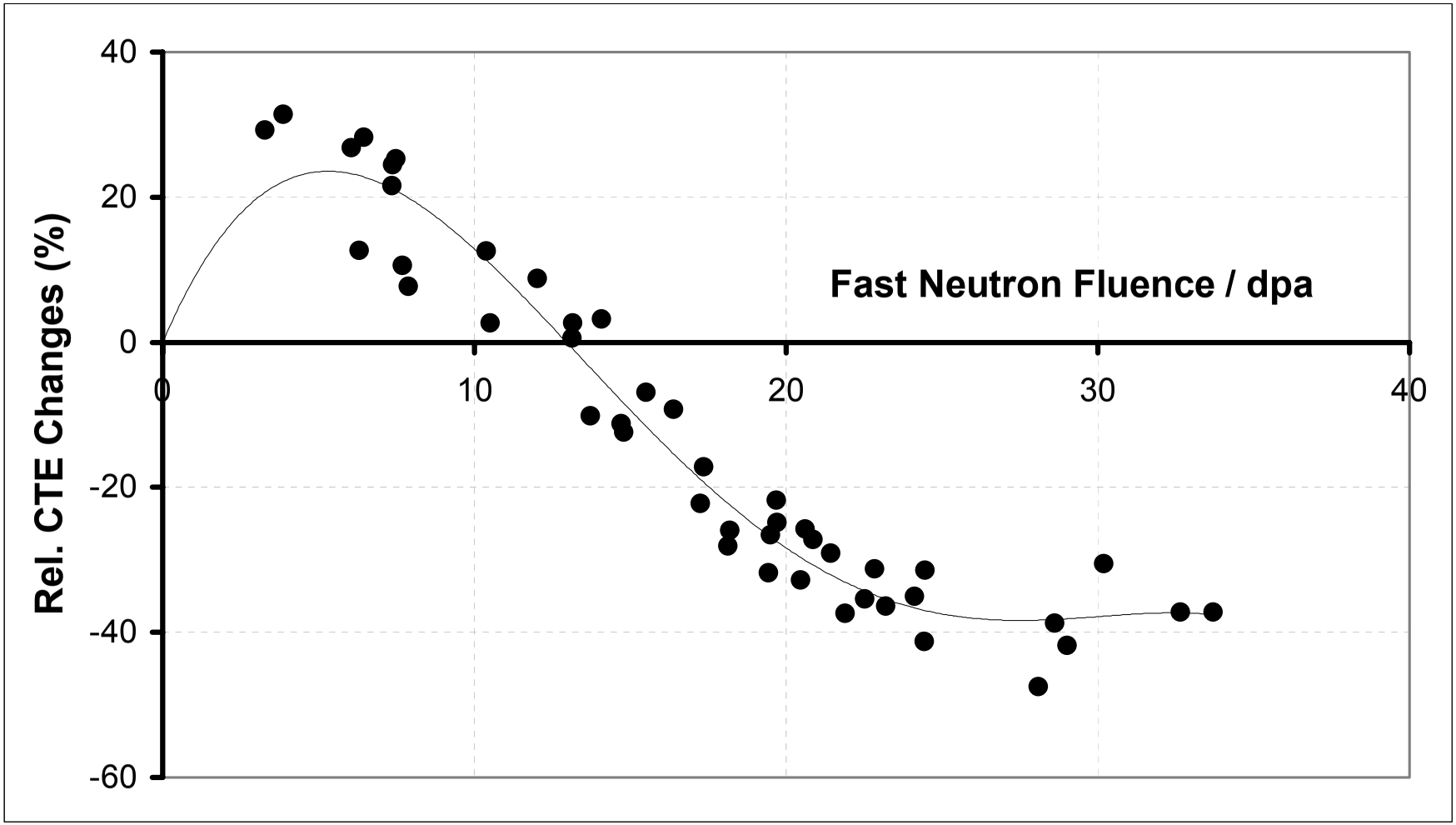

Fig. B9 **ATR-2E** – Relative thermal expansivity (CTE) changes due to fast neutron irradiation.
Irradiation temperature about 400 °C (data from Table B3 and B4)

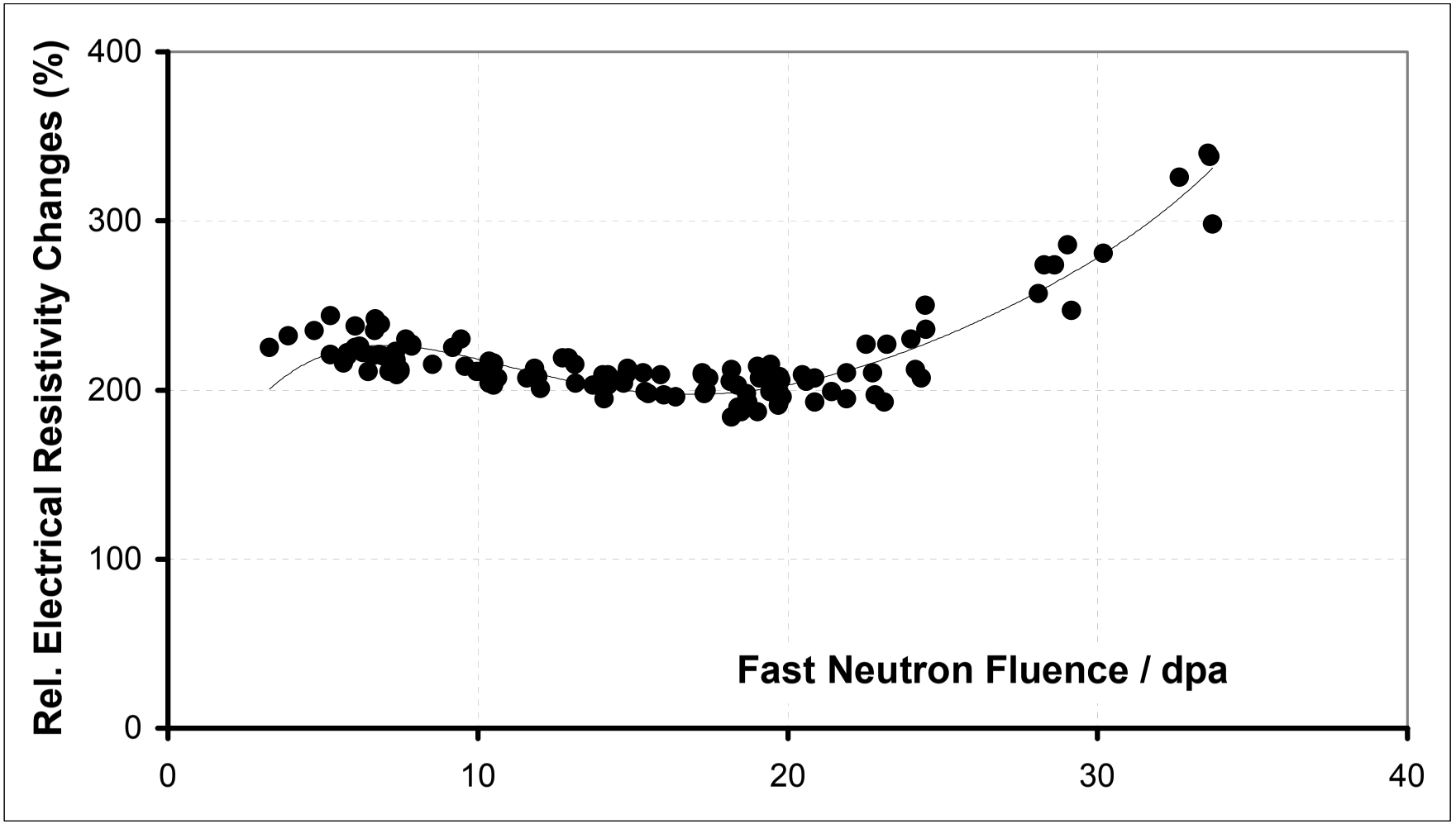

Fig. B10 **ATR-2E** – Relative electrical resistivity changes due to fast neutron irradiation.
Irradiation temperature about 400 °C (data from Table B3 and B4)

Irradiation Temperature (°C)	Fast Neutron Fluence (dpa)	Rel. Linear Dimensional Changes $\Delta l/l_0$ (%)	Pre-Irrad. Bulk Density (g/cm^3)	Rel. Volume Changes $\Delta V/V_0$ (%)	Young's Modulus E		Electrical Resistivity R		Thermal Expansivity α	
					Pre-Irrad. E_o (GPa)	Rel. Change E/E_o	Pre-Irrad. R_0 ($\Omega \cdot \mu m$)	Rel. Change $\Delta R/R_0$ (%)	Pre-Irrad. α_0 (10^{-6}/K)	Rel. Change $\Delta\alpha/\alpha_0$ (%)
480	3.67	-0.60	1.848	-1.70	8.92	2.13	7.36	225	5.03	21.3
491	13.52	-2.09	1.848	-6.39	8.92	3.14	7.36	201	5.03	-6.6
494	19.95	-1.42	1.848	-6.34	8.92	3.82	7.36	204	5.03	-23.7
496	25.26	0.64	1.848	-1.36	8.92	2.96	7.36	257	5.03	-30.2
497	36.42	8.17	1.848	20.42	8.92	1.16	7.36	553	5.03	-29.4
520	3.28	-0.52	1.838	-1.54	9.37	2.05	7.24	231	4.98	20.5
505	7.87	-1.63	1.822	-5.20	8.69	2.35	7.44	207		
503	15.24	-2.04	1.822	-7.16	8.69	3.54	7.44	196	5.43	-23.4
495	10.37	-1.80	1.810	-6.01	8.78	2.51	7.44	209	5.11	3.1
497	16.80	-1.99	1.810	-7.20	8.78	3.64	7.44	203	5.11	-19.4
480	3.67	-0.56	1.782	-1.67	8.86	2.13	7.54	223		
502	12.99	-2.23	1.782	-7.14			7.54	199		
501	20.47	-1.41	1.782	-5.66	8.86	3.66	7.54	215		
500	26.77	1.01	1.782	0.82	8.86	2.76	7.54	276		
520	3.28	-0.56	1.775	-1.91	8.79	2.03	7.62	225		
525	3.18	-0.57	1.804	-1.68	8.72	2.03	7.60	224		
495	5.38	-0.99	1.755	-3.71	7.82	2.23	8.28	210		
498	11.63	-2.02	1.755	-6.51	7.82	2.65	8.28	193		
500	6.69	-1.41	1.839	-4.39	9.83	2.29	6.97	216		
508	13.58	-2.39	1.839	-7.92	9.83	3.21	6.97	194		
504	26.44	0.21	1.839	-1.31	9.83	2.97	6.97	263		
500	6.69	-1.37	1.724	-4.92	7.62	2.32	8.39	198		
508	13.58	-2.24	1.724	-7.64			8.39	184		
500	9.71	-1.88	1.798	-5.96	9.44	2.52	7.46	203		
502	15.62	-2.32	1.798	-7.53			7.46	189		
501	20.16	-1.74	1.798	-6.12	9.44	3.73	7.46	199		

Table B5 ATR-2E – physical property changes due to fast neutron irradiation **perpendicular to extrusion.**
Irradiation temperatures 480 to 525 °C (continued)

Irradiation Temperature (°C)	Fast Neutron Fluence (dpa)	Rel. Linear Dimensional Changes $\Delta l/l_0$ (%)	Pre-Irrad. Bulk Density (g/cm^3)	Rel. Volume Changes $\Delta V/V_0$ (%)	Young's Modulus E		Electrical Resistivity R		Thermal Expansivity α	
					Pre-Irrad. E_o (GPa)	Rel. Change E/E_o	Pre-Irrad. R_0 ($\Omega \cdot \mu m$)	Rel. Change $\Delta R/R_0$ (%)	Pre-Irrad. α_0 (10^{-6}/K)	Rel. Change $\Delta\alpha/\alpha_0$ (%)
495	9.45	-1.82	1.707	-6.74	7.89	2.51	7.22	257		
502	14.83	-2.37	1.707	-7.27			7.22	237		
502	19.37	-2.00	1.707	-6.22	7.89	3.71	7.22	246		
495	9.71	-1.92	1.795	-6.00	9.29	2.50	7.30	212		
497	16.14	-2.28	1.795	-7.72	9.29	3.61	7.30	204		
510	7.74	-1.65	1.830	-5.49	9.18	2.37	7.21	218	5.01	8.6
508	15.09	-2.06	1.830	-7.31	9.18	3.63	7.21	202	5.01	-19.2
505	21.42	-0.56	1.830	-3.76	9.18	3.40	7.21	233	5.01	-26.1
505	6.43	-1.26	1.845	-4.56	8.89	2.30	7.34	227	5.13	15.2
508	13.32	-1.93	1.845	-7.09			7.34	200	5.13	-13.3
508	18.99	-0.93	1.845	-5.65	8.89	3.65	7.34	209	5.13	-24.6
505	30.80	6.15	1.845	12.01	8.89	1.58	7.34	449	5.13	-25.6
495	9.45	-1.67	1.833	-5.98	8.87	2.45	7.50	208	5.04	9.3
502	14.83	-1.99	1.833	-7.05			7.50	192	5.04	-10.5
502	19.37	-1.42	1.833	-6.14	8.87	3.68	7.50	202	5.04	-21.0
505	7.09	-1.50	1.805	-5.07	8.99	2.36	7.30	224	4.89	15.5
505	14.20	-2.21	1.805	-7.53	8.99	3.44	7.30	207	4.89	-13.7
508	20.24	-1.24	1.805	-5.28	8.99	3.66	7.30	226	4.89	-25.8
505	33.49	6.94	1.805	16.94	8.99	1.31	7.30	552	4.89	-26.7
525	8.79	-1.85	1.837	-5.96	9.71	2.43	7.00	215		
515	15.03	-2.23	1.837	-7.12	9.71	3.52	7.00	200		
513	20.01	-1.44	1.837	-6.68	9.71	3.70	7.00	214		
495	6.82	-1.12	1.841	-3.73	9.03	2.25	7.82	212		
500	5.91	-0.92	1.845	-3.10	9.05	2.19	7.65	221		
505	5.51	-0.77	1.835	-2.57	8.89	2.06	7.76	219		
515	6.04	-0.95	1.833	-3.20	9.36	2.16	7.54	220		

Table B5 ATR-2E – physical property changes due to fast neutron irradiation **perpendicular to extrusion. Irradiation temperatures 480 to 525 °C**

Irradiation Temperature (°C)	Fast Neutron Fluence (dpa)	Rel. Linear Dimensional Changes $\Delta l/l_0$ (%)	Pre-Irrad. Bulk Density (g/cm^3)	Rel. Volume Changes $\Delta V/V_0$ (%)	Young's Modulus E		Electrical Resistivity R		Thermal Expansivity α	
					Pre-Irrad. E_o (GPa)	Rel. Change E/E_o	Pre-Irrad. R_0 ($\Omega \cdot \mu m$)	Rel. Change $\Delta R/R_0$ (%)	Pre-Irrad. α_0 (10^{-6}/K)	Rel. Change $\Delta\alpha/\alpha_0$ (%)
570	2.49	-0.47	1.785	-1.43	8.49	2.06	7.03	230	4.33	19.4
495	3.54	-0.71	1.786	-2.03	9.37	2.08	7.02	229	4.41	21.1
495	13.39	-3.15	1.786	-7.77	9.37	3.04	7.02	207	4.41	-7.0
497	19.82	-3.44	1.786	-7.02			7.02	211	4.41	-26.8
500	25.46	-2.41	1.786	-2.11	9.37	2.94	7.02	270	4.41	-29.5
500	3.41	-0.74	1.765	-1.96	9.20	2.05	7.27	228	4.50	18.0
507	11.15	-2.81	1.765	-6.92	9.20	2.76	7.27	207	4.50	-4.0
506	18.50	-3.24	1.765	-6.59			7.27	209	4.50	-26.7
506	24.70	-2.03	1.765	-1.13	9.20	2.93	7.27	271	4.50	-31.8
504	34.41	2.46	1.765	17.21	9.20	1.34	7.27	534	4.50	-28.7
510	8.53	-2.24	1.788	-5.66	9.35	2.37	7.03	213	4.90	-4.9
505	16.02	-3.35	1.788	-7.57			7.03	197	4.90	-30.2
475	3.67	-0.66	1.790	-1.94	8.74	2.13				
500	3.41	-0.69	1.768	-1.84	9.03	2.07	7.13	229		
507	12.73	-3.03	1.768	-7.40	9.03	3.00	7.13	209		
505	20.21	-3.13	1.768	-5.96			7.13	219		
500	26.38	-1.75	1.768	0.11	9.03	2.78	7.13	289		
535	2.95	-0.61	1.796	-1.75	8.89	2.06	7.24	241		
535	3.02	-0.61	1.774	-1.79	9.17	1.99	7.06	233		
500	9.97	-2.33	1.831	-7.36	10.36	2.47	6.62	214		
500	15.88	-3.26	1.831	-7.49			6.62	210		
500	6.04	-1.35	1.785	-3.89	8.54	2.25	7.30	204		
505	12.62	-2.92	1.785	-7.29			7.30	203		
500	7.35	-1.89	1.816	-5.06	9.53	2.32	6.84	216		
505	14.51	-3.21	1.816	-7.65	9.53	3.37	6.84	209		
500	7.35	-1.93	1.790	-5.07	9.45	2.32	6.91	214		

Table B6 ATR-2E – physical property changes due to fast neutron irradiation **parallel to extrusion.**
Irradiation temperatures 475 to 535 °C (continued)

Irradiation Temperature (°C)	Fast Neutron Fluence (dpa)	Rel. Linear Dimensional Changes $\Delta l/l_0$ (%)	Pre-Irrad. Bulk Density (g/cm^3)	Rel. Volume Changes $\Delta V/V_0$ (%)	Young's Modulus E		Electrical Resistivity R		Thermal Expansivity α	
					Pre-Irrad. E_o (GPa)	Rel. Change E/E_o	Pre-Irrad. R_0 ($\Omega \cdot \mu m$)	Rel. Change $\Delta R/R_0$ (%)	Pre-Irrad. α_0 (10^{-6}/K)	Rel. Change $\Delta\alpha/\alpha_0$ (%)
505	14.51	-3.32	1.790	-7.51			6.91	198		
500	9.71	-2.29	1.841	-5.81	10.31	2.50	6.62	220		
502	15.62	-3.16	1.841	-7.61			6.62	205		
501	20.54	-0.71	1.841	-5.25	10.31	3.69	6.62	221		
495	9.45	-2.20	1.799	-5.76	10.04	2.46	6.73	225		
499	14.83	-3.16	1.799	-7.77	10.04	3.27	6.73	214		
499	19.75	-0.99	1.799	-6.53	10.04	3.72	6.73	213		
500	9.32	-2.20	1.794	-5.65	8.04	2.40	7.49	236		
500	15.22	-3.22	1.794	-8.01	8.04	3.35	7.49	240		
505	6.43	-1.67	1.740	-4.33	8.76	2.30	7.20	243	4.33	20.8
508	13.32	-3.21	1.740	-7.06	8.76	3.16	7.20	220	4.33	-6.9
507	18.65	-3.32	1.740	-6.28	8.76	3.64	7.20	229	4.33	-23.8
504	31.25	1.03	1.740	12.22	8.76	1.52	7.20	488	4.33	-28.0
495	9.45	-2.21	1.821	-5.51	9.76	2.45	6.82	222	4.67	4.3
502	14.83	-3.22	1.821	-7.03	9.76	3.31	6.82	209	4.67	-15.4
502	19.75	-1.11	1.821	-5.92	9.76	3.73	6.82	217	4.67	-29.3
505	7.09	-1.84	1.823	-4.80	9.88	2.31	6.66	233	4.41	11.8
505	14.20	-3.22	1.823	-7.41	9.88	3.37	6.66	214	4.41	-15.2
508	19.97	-3.01	1.823	-5.45	9.88	3.59	6.66	240	4.41	-26.8
505	33.88	3.34	1.823	17.99	9.88	1.31	6.66	543	4.41	-31.4
520	8.40	-2.25	1.795	-5.55	9.42	2.36	6.90	228		
510	14.30	-3.22	1.795	-7.19	9.42	3.28	6.90	208		
506	18.90	-1.02			9.42	3.59	6.90	217		
500	7.09	-1.54	1.698	-4.04	7.99	2.23	8.20	221		
500	19.16	-3.30	1.698	-7.38	7.99	3.75	8.20	190		
500	6.43	-1.32	1.764	-3.51	9.06	2.20	7.39	227		

Table B6 ATR-2E – physical property changes due to fast neutron irradiation **parallel to extrusion.**
Irradiation temperatures 475 to 535 °C (continued)

Irradiation Temperature (°C)	Fast Neutron Fluence (dpa)	Rel. Linear Dimensional Changes $\Delta l/l_0$ (%)	Pre-Irrad. Bulk Density (g/cm^3)	Rel. Volume Changes $\Delta V/V_0$ (%)	Young's Modulus E		Electrical Resistivity R		Thermal Expansivity α	
					Pre-Irrad. E_o (GPa)	Rel. Change E/E_o	Pre-Irrad. R_0 ($\Omega \cdot \mu m$)	Rel. Change $\Delta R/R_0$ (%)	Pre-Irrad. α_0 (10^{-6}/K)	Rel. Change $\Delta\alpha/\alpha_0$ (%)
490	5.51	-1.01	1.791	-2.66	8.74	2.11	7.59	230		
510	6.56	-1.33	1.763	-3.52	8.93	2.14	7.89	207		

Table B6 ATR-2E – physical property changes due to fast neutron irradiation **parallel to extrusion.**
Irradiation temperatures 475 to 535 °C

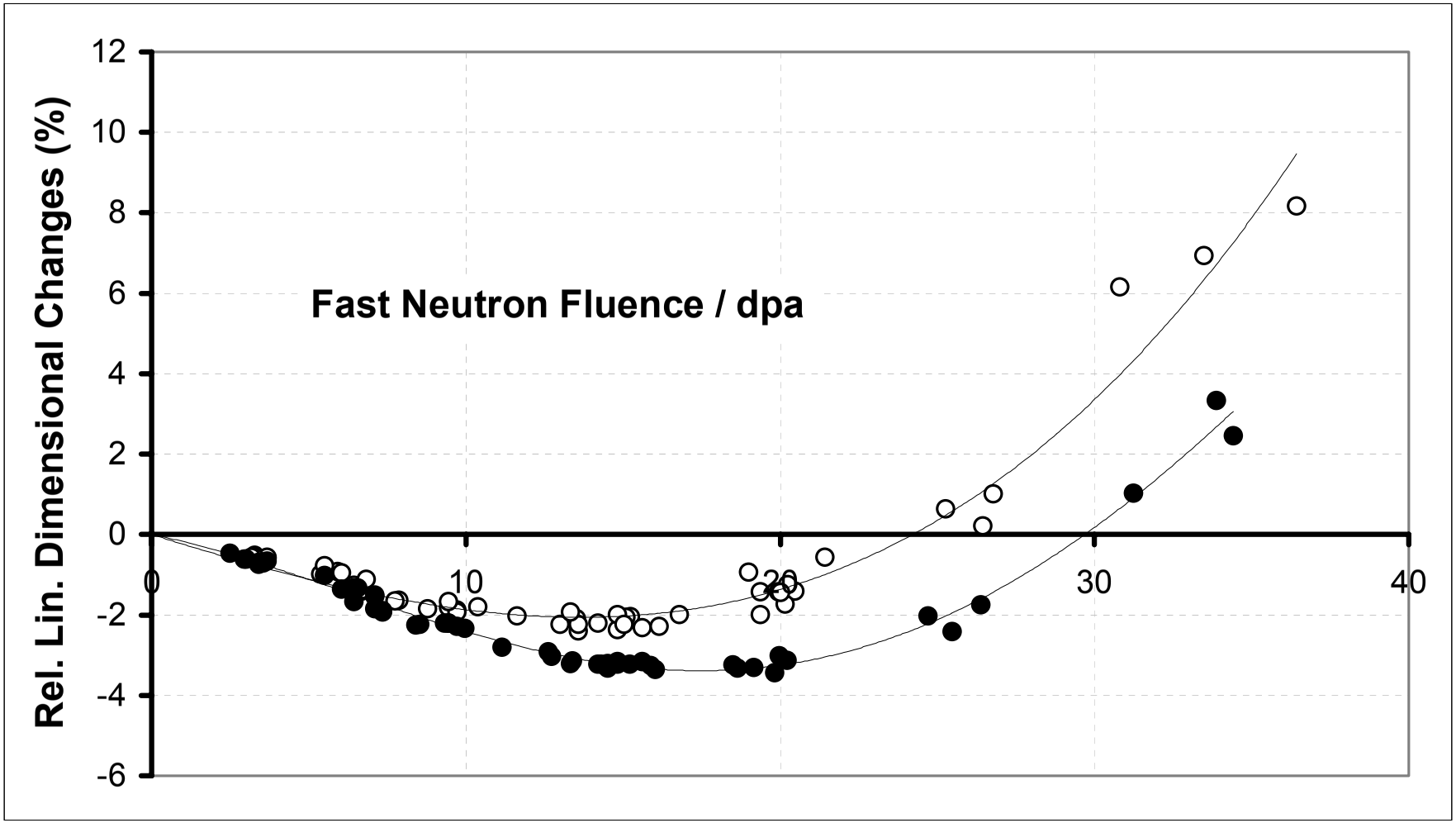

Fig. B11 **ATR-2E** – Linear dimensional changes due to fast neutron irradiation; perpendicular (white circles) and parallel (black circles) to extrusion. **Irradiation temperature about 500 °C** (data from Table B5 and B6)

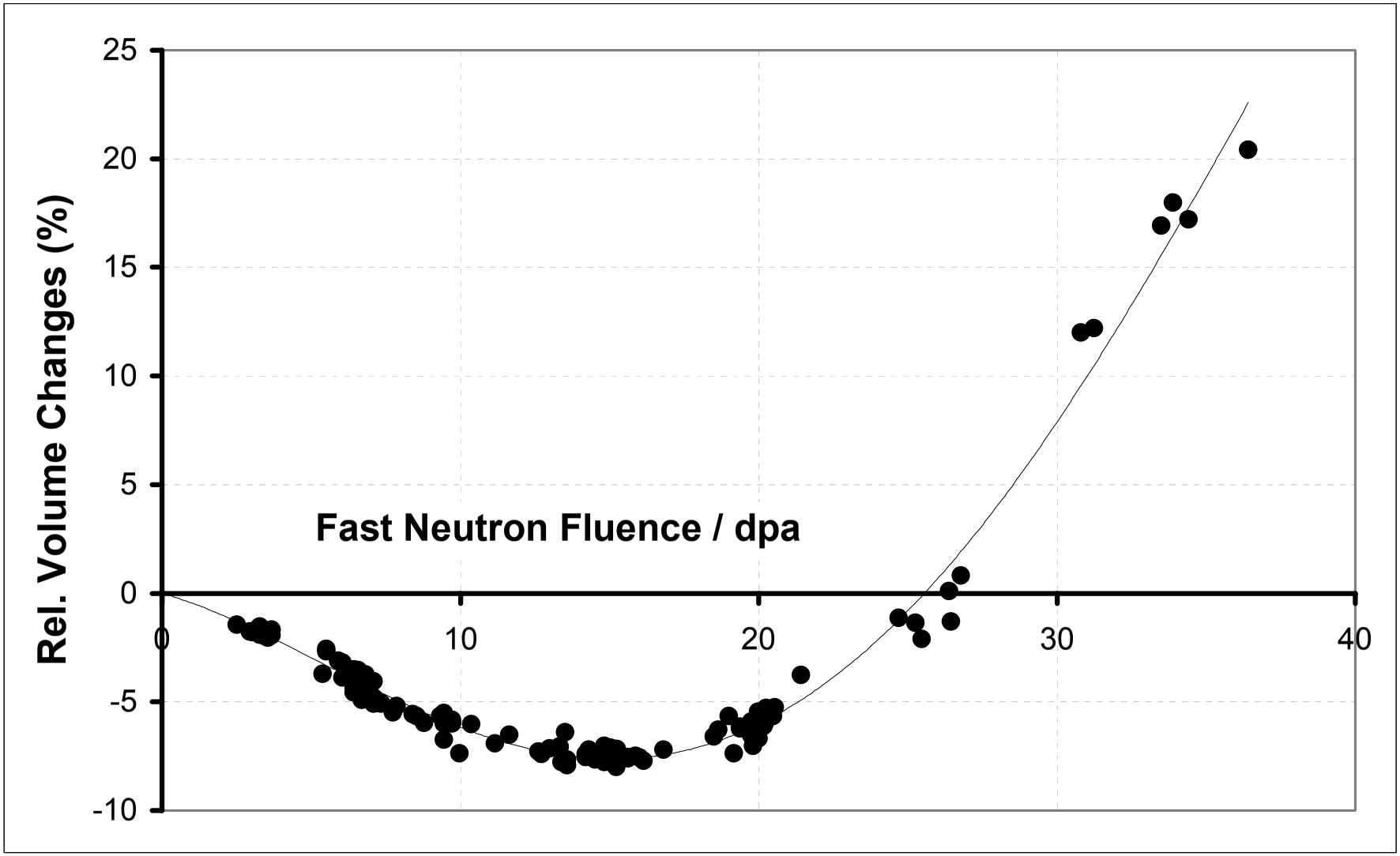

Fig. B12 **ATR-2E** – Relative volume changes due to fast neutron irradiation.
Irradiation temperature about 500 °C (data from Table B5 and B6)

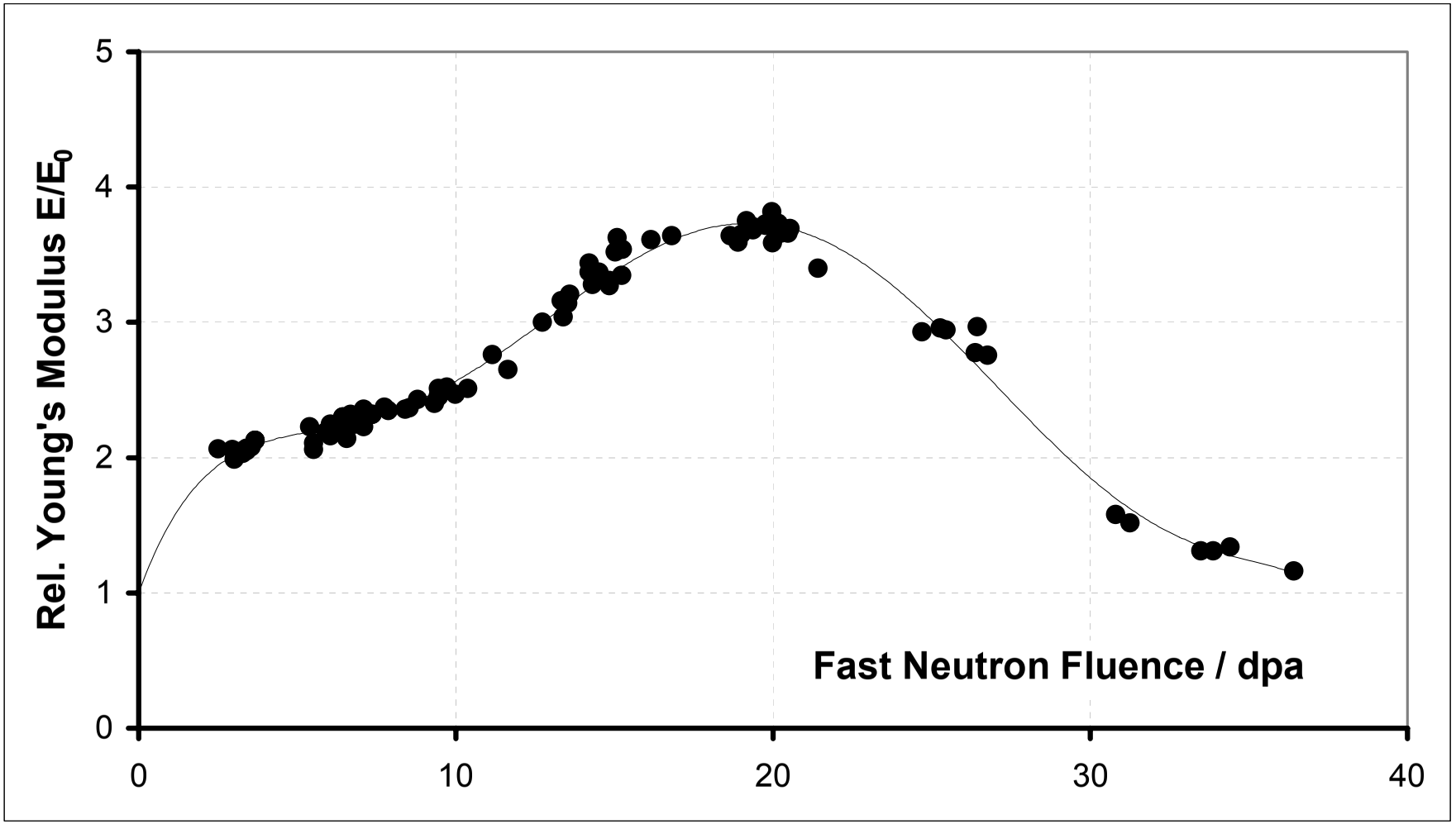

Fig. B13 **ATR-2E** – Relative Young's modulus changes due to fast neutron irradiation.
Irradiation temperature about 500 °C (data from Table B5 and B6)

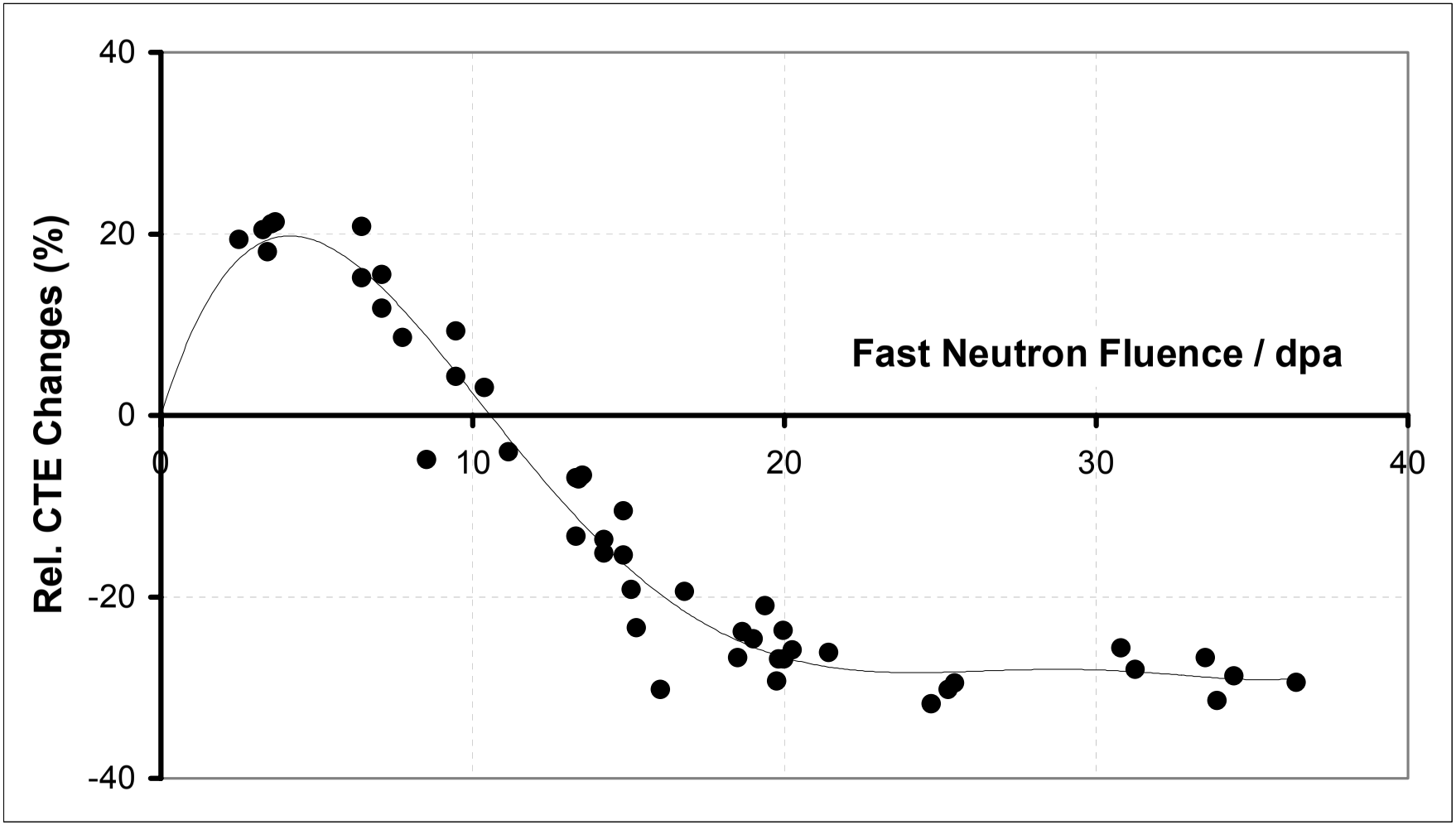

Fig. B14 **ATR-2E** – Relative thermal expansivity (CTE) changes due to fast neutron irradiation.
Irradiation temperature about 500 °C (data from Table B5 and B6)

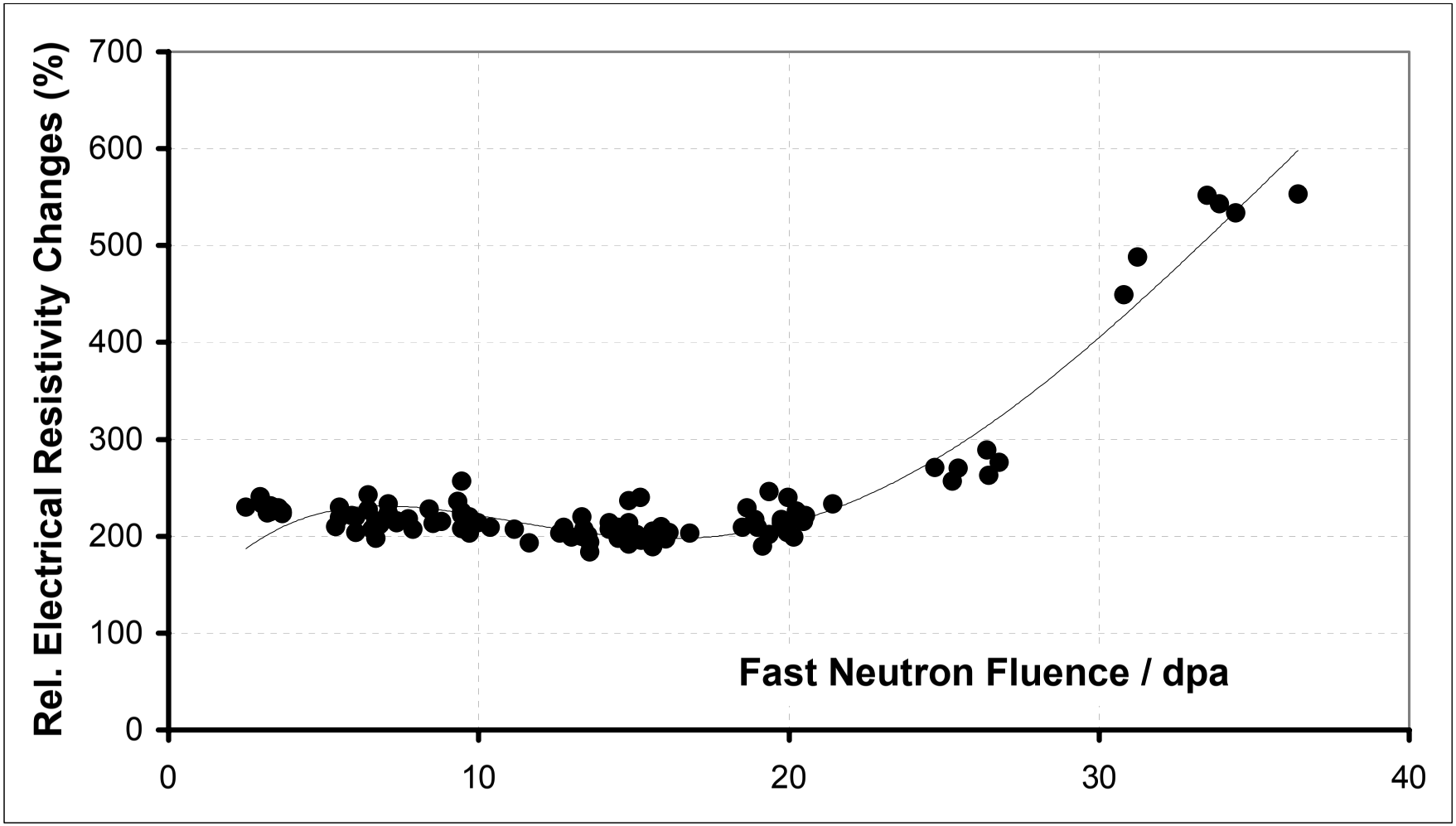

Fig. B15 **ATR-2E** – Relative electrical resistivity changes due to fast neutron irradiation.
Irradiation temperature about 500 °C (data from Table B5 and B6)

Irradiation Temperature (°C)	Fast Neutron Fluence (dpa)	Rel. Linear Dimensional Changes $\Delta l/l_0$ (%)	Pre-Irrad. Bulk Density (g/cm^3)	Rel. Volume Changes $\Delta V/V_0$ (%)	Young's Modulus E		Electrical Resistivity R		Thermal Expansivity α	
					Pre-Irrad. E_o (GPa)	Rel. Change E/E_o	Pre-Irrad. R_0 ($\Omega \cdot \mu m$)	Rel. Change $\Delta R/R_0$ (%)	Pre-Irrad. α_0 (10^{-6}/K)	Rel. Change $\Delta\alpha/\alpha_0$ (%)
570	2.17	-0.33	1.834	-0.97	9.02	1.83	7.37	218	5.06	16.5
600	3.67	-0.51	1.841	-2.58	9.13	1.85	7.32	239	5.05	17.8
593	11.55	-1.53	1.841	-5.21	9.13	2.28	7.32	212	5.05	-1.6
595	15.29	-1.66	1.841	-6.34	9.13	2.27	7.32	204	5.05	-23.2
596	21.68	-0.32	1.841	-3.90	9.13	2.69	7.32	214	5.05	-35.6
595	5.88	-0.83	1.801	-2.70	8.38	1.99	7.77	217	5.05	19.2
607	11.13	-1.69	1.801	-5.92	8.38	2.63	7.77	206	5.05	-15.4
602	15.52	-1.41	1.801	-6.43	8.38	2.70	7.77	195	5.05	-29.3
601	23.01	1.12	1.801	-1.02	8.38	2.79	7.77	261	5.05	-41.8
600	5.77	-0.82	1.831	-2.48	9.42	1.95	7.20	214	5.05	17.0
606	12.86	-1.90	1.831	-5.87	9.42	2.63	7.20	205	5.05	-19.0
604	17.32	-1.74	1.831	-5.74	9.42	2.30	7.20	196	5.05	-32.3
603	24.80	0.19	1.831	-0.25	9.42	2.20	7.20	270	5.05	-35.8
565	1.51	-0.21	1.797	-0.74	8.66	1.75	7.54	210		
555	2.76	-0.45	1.793	-1.45	8.90	1.92	7.36	224		
600	6.09	-0.87	1.702	-2.76	8.18	1.96	7.86	222		
605	12.78	-2.05	1.702	-6.35	8.18	2.74	7.86	209		
602	17.51	-1.86	1.702	-6.71	8.18	2.57	7.86	200		
602	24.99	0.67	1.702	-0.10	8.18	2.70	7.86	278		
605	4.67	-0.71	1.774	-2.25	8.75	1.95	7.62	218		
614	11.63	-1.85	1.774	-6.21	8.75	2.49	7.62	205		
608	14.78	-2.05	1.774	-6.17	8.75	2.38	7.62	198		
606	20.22	-1.23	1.774	-5.19	8.75	2.71	7.62	221		
600	6.13	-0.89	1.786	-2.82	8.94	1.99	7.60	217		
605	11.77	-1.87	1.786	-6.37	8.94	2.56	7.60	202		
601	16.10	-1.83	1.786	-6.25	8.94	2.57	7.60	194		

Table B7 ATR-2E – physical property changes due to fast neutron irradiation **perpendicular to extrusion. Irradiation temperatures 555 to 614 °C** (continued)

Irradiation Temperature (°C)	Fast Neutron Fluence (dpa)	Rel. Linear Dimensional Changes $\Delta l/l_0$ (%)	Pre-Irrad. Bulk Density (g/cm^3)	Rel. Volume Changes $\Delta V/V_0$ (%)	Young's Modulus E		Electrical Resistivity R		Thermal Expansivity α	
					Pre-Irrad. E_o (GPa)	Rel. Change E/E_o	Pre-Irrad. R_0 ($\Omega \cdot \mu m$)	Rel. Change $\Delta R/R_0$ (%)	Pre-Irrad. α_0 (10^{-6}/K)	Rel. Change $\Delta\alpha/\alpha_0$ (%)
600	5.33	-0.81	1.796	-2.48	9.04	1.97	7.33	218		
596	9.27	-1.70	1.796	-4.93	9.04	2.23	7.33	215		
597	12.74	-2.07	1.796	-6.78	9.04	2.25	7.33	210		
598	18.78	-1.42	1.796	-5.21	9.04	2.68	7.33	219		

Table B7 ATR-2E – physical property changes due to fast neutron irradiation **perpendicular to extrusion.**
Irradiation temperatures 555 to 614 °C

Irradiation Temperature (°C)	Fast Neutron Fluence (dpa)	Rel. Linear Dimensional Changes $\Delta l/l_0$ (%)	Pre-Irrad. Bulk Density (g/cm^3)	Rel. Volume Changes $\Delta V/V_0$ (%)	Young's Modulus E		Electrical Resistivity R		Thermal Expansivity α	
					Pre-Irrad. E_o (GPa)	Rel. Change E/E_o	Pre-Irrad. R_0 ($\Omega \cdot \mu m$)	Rel. Change $\Delta R/R_0$ (%)	Pre-Irrad. α_0 (10^{-6}/K)	Rel. Change $\Delta\alpha/\alpha_0$ (%)
570	2.49	-0.47	1.785	-1.43	8.49	2.06	7.03	230	4.43	19.4
600	4.21	-0.77	1.789	-2.10	8.65	1.81	7.34	219	4.48	16.7
593	12.22	-2.49	1.789	-5.88	8.65	2.19	7.34	215	4.48	-10.0
598	16.29	-2.98	1.789	-6.55	8.65	2.08	7.34	254	4.48	-26.8
598	23.08	-2.00	1.789	-2.72	8.65	2.36	7.34	248	4.48	-33.3
595	5.63	-1.03	1.793	-2.74	9.32	1.97	7.02	225	4.58	14.0
606	10.22	-2.11	1.793	-5.26	9.32	2.21	7.02	221	4.58	-0.7
603	14.42	-2.98	1.793	-6.78	9.32	2.13	7.02	211	4.58	-25.1
602	21.64	-2.78	1.793	-4.33	9.32	2.50	7.02	245	4.58	-33.4

Table B8 ATR-2E – physical property changes due to fast neutron irradiation **parallel to extrusion.**
Irradiation temperatures 570 to 610 °C (continued)

Irradiation Temperature (°C)	Fast Neutron Fluence (dpa)	Rel. Linear Dimensional Changes $\Delta l/l_0$ (%)	Pre-Irrad. Bulk Density (g/cm^3)	Rel. Volume Changes $\Delta V/V_0$ (%)	Young's Modulus E		Electrical Resistivity R		Thermal Expansivity α	
					Pre-Irrad. E_o (GPa)	Rel. Change E/E_o	Pre-Irrad. R_0 ($\Omega \cdot \mu m$)	Rel. Change $\Delta R/R_0$ (%)	Pre-Irrad. α_0 (10^{-6}/K)	Rel. Change $\Delta\alpha/\alpha_0$ (%)
600	6.00	-1.03	1.825	-2.67	10.27	1.96	6.57	223	4.87	9.7
610	12.56	-2.66	1.825	-6.12	10.27	2.70	6.57	215	4.87	-22.0
606	17.22	-3.00	1.825	-6.54	10.27	2.09	6.57	218	4.87	-38.6
604	24.86	-1.64	1.825	0.39	10.27	2.25	6.57	279	4.87	-42.3
570	1.84	-0.33	1.758	-0.93	8.74	1.81	7.27	228		
600	6.17	-1.08	1.806	-2.85	8.58	1.97	7.42	216		
605	12.34	-2.52	1.806	-6.05	8.58	2.45	7.42	212		
601	16.93	-3.10	1.806	-7.05	8.58	2.52	7.42	195		
601	24.58	-2.00	1.806	-1.66	8.58	2.43	7.42	272		
605	5.12	-0.92	1.813	-2.51	10.04	1.91	6.75	220		
595	5.92	-1.08	1.820	-2.72	10.18	1.95	6.54	229		
602	11.04	-2.67	1.820	-6.23	10.18	2.58	6.54	220		
600	15.24	-3.06	1.820	-6.79	10.18	2.14	6.54	216		
600	4.99	-0.82	1.842	-2.22	10.40	1.99	6.52	225		
592	8.27	-2.10	1.842	-5.18	10.40	2.27	6.52	221		
596	11.48	-2.78	1.842	-6.66	10.40	2.10	6.52	207		
597	16.99	-2.94	1.842	-5.67	10.40	2.01	6.52	223		
605	3.18	-0.55	1.777	-1.56	9.49	1.87	6.95	224		
601	10.66	-2.09	1.777	-5.14	9.49	2.22	6.95	221		
599	14.13	-2.77	1.777	-6.99	9.49	2.25	6.95	218		
599	20.10	-2.71	1.777	-4.92	9.49	2.08	6.95	229		

Table B8 ATR-2E – physical property changes due to fast neutron irradiation **parallel to extrusion.**
Irradiation temperatures 570 to 610 °C

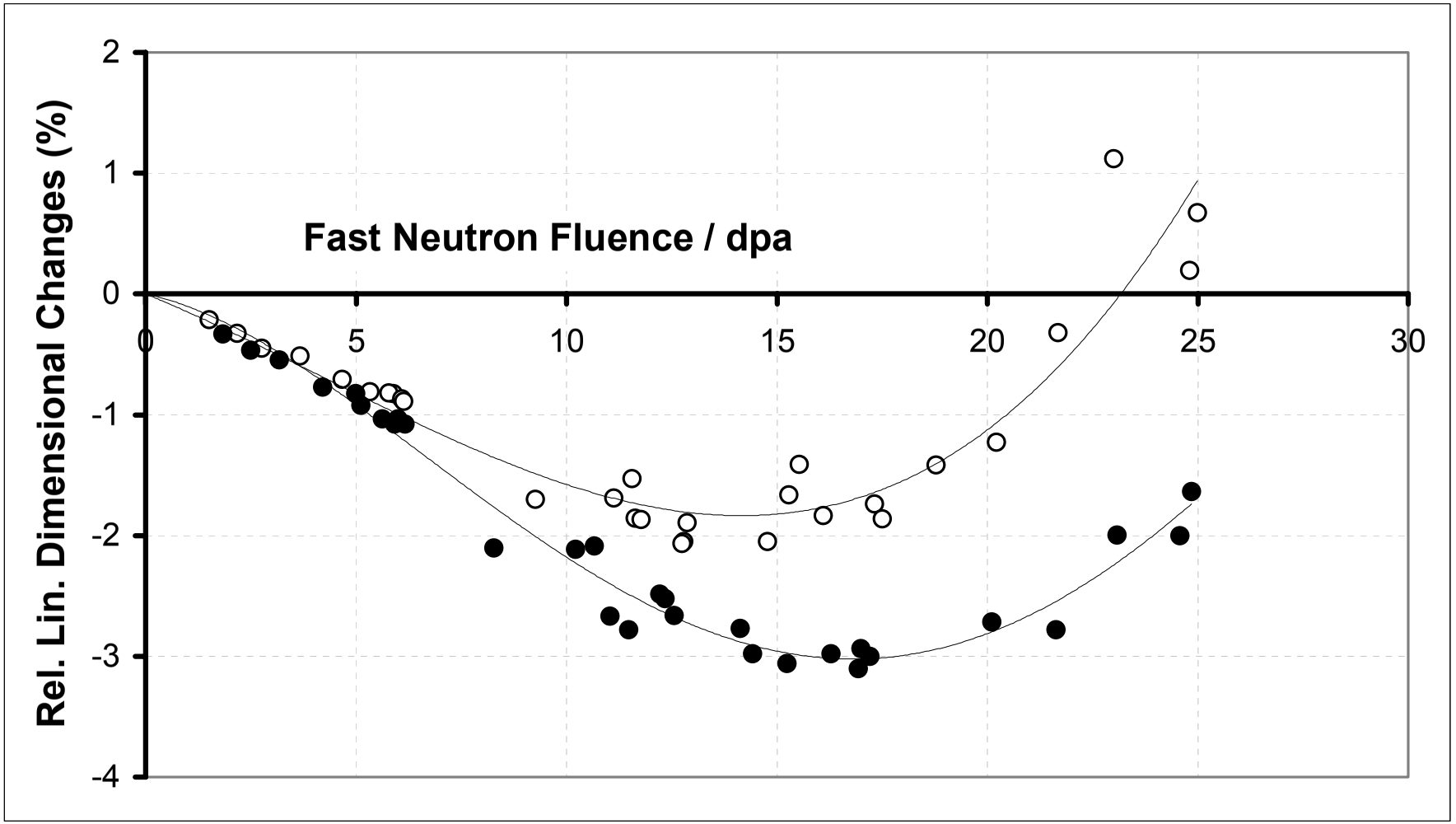

Fig. B16 **ATR-2E** – Linear dimensional changes due to fast neutron irradiation; perpendicular (white circles) and parallel (black circles) to extrusion. **Irradiation temperature about 600 °C** (data from Table B7 and B8)

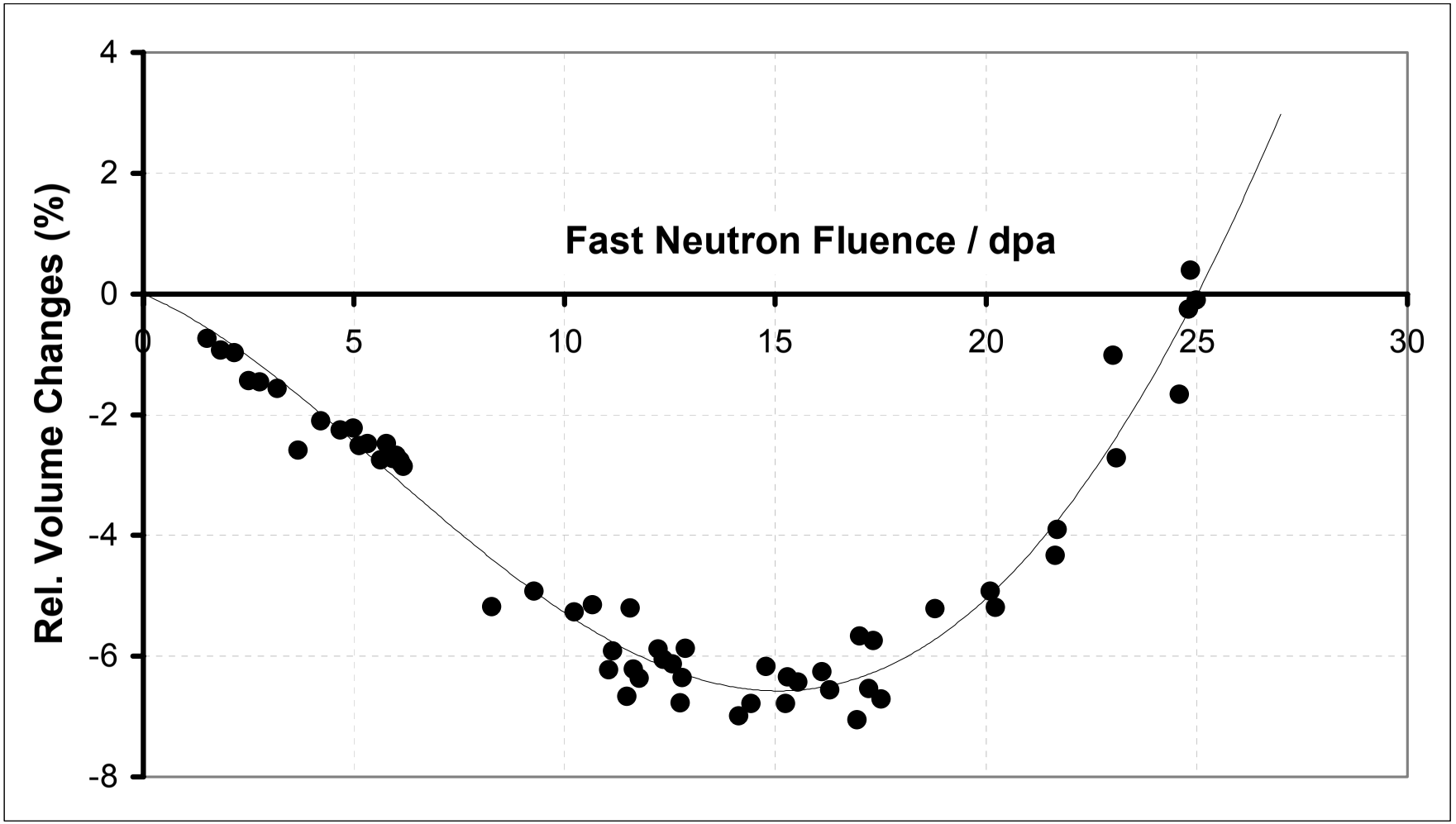

Fig. B17 **ATR-2E** – Relative volume changes due to fast neutron irradiation.
Irradiation temperature about 600 °C (data from Table B7 and B8)

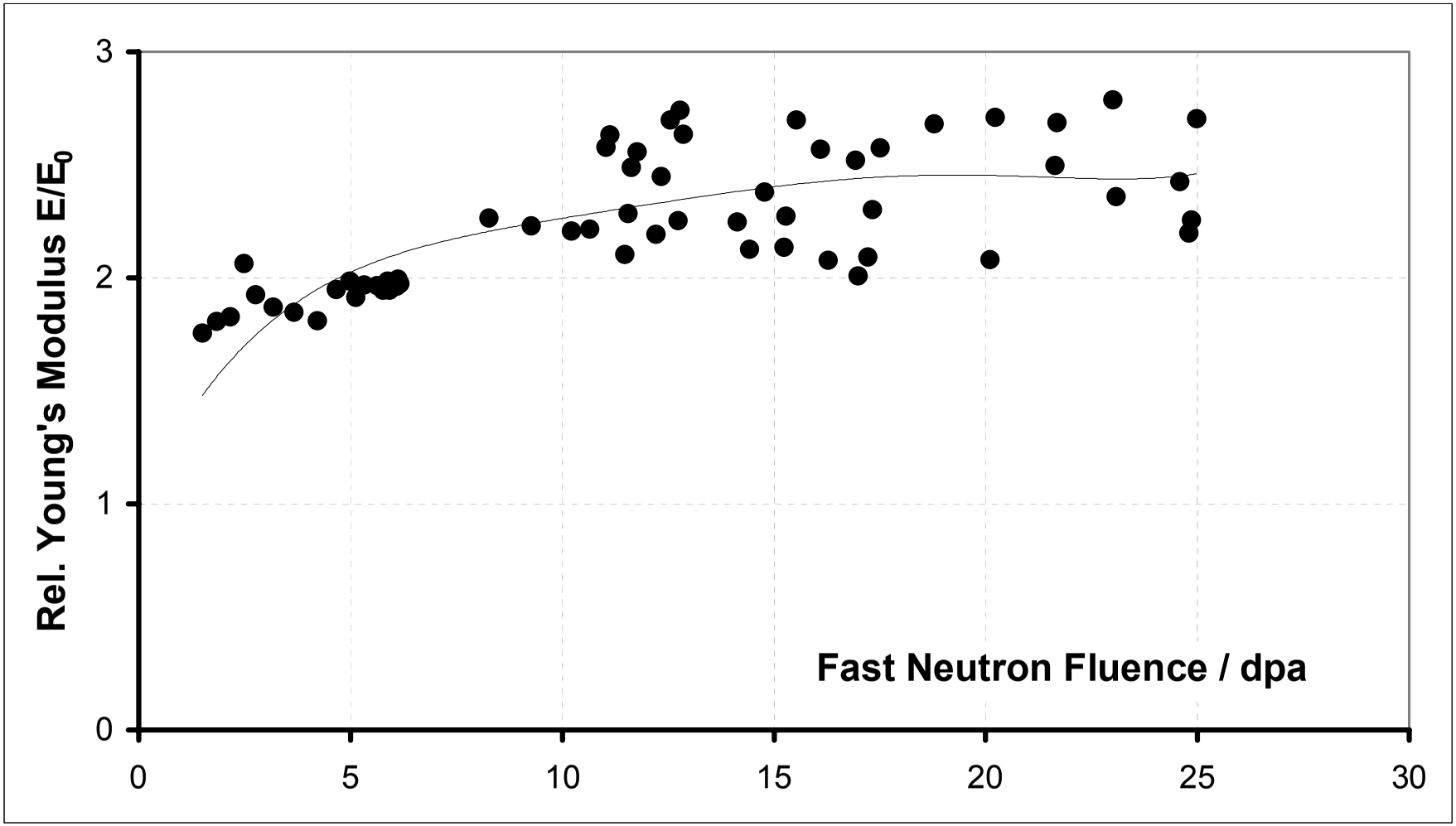

Fig. B18 **ATR-2E** – Relative Young's modulus changes due to fast neutron irradiation.
Irradiation temperature about 600 °C (data from Table B7 and B8)

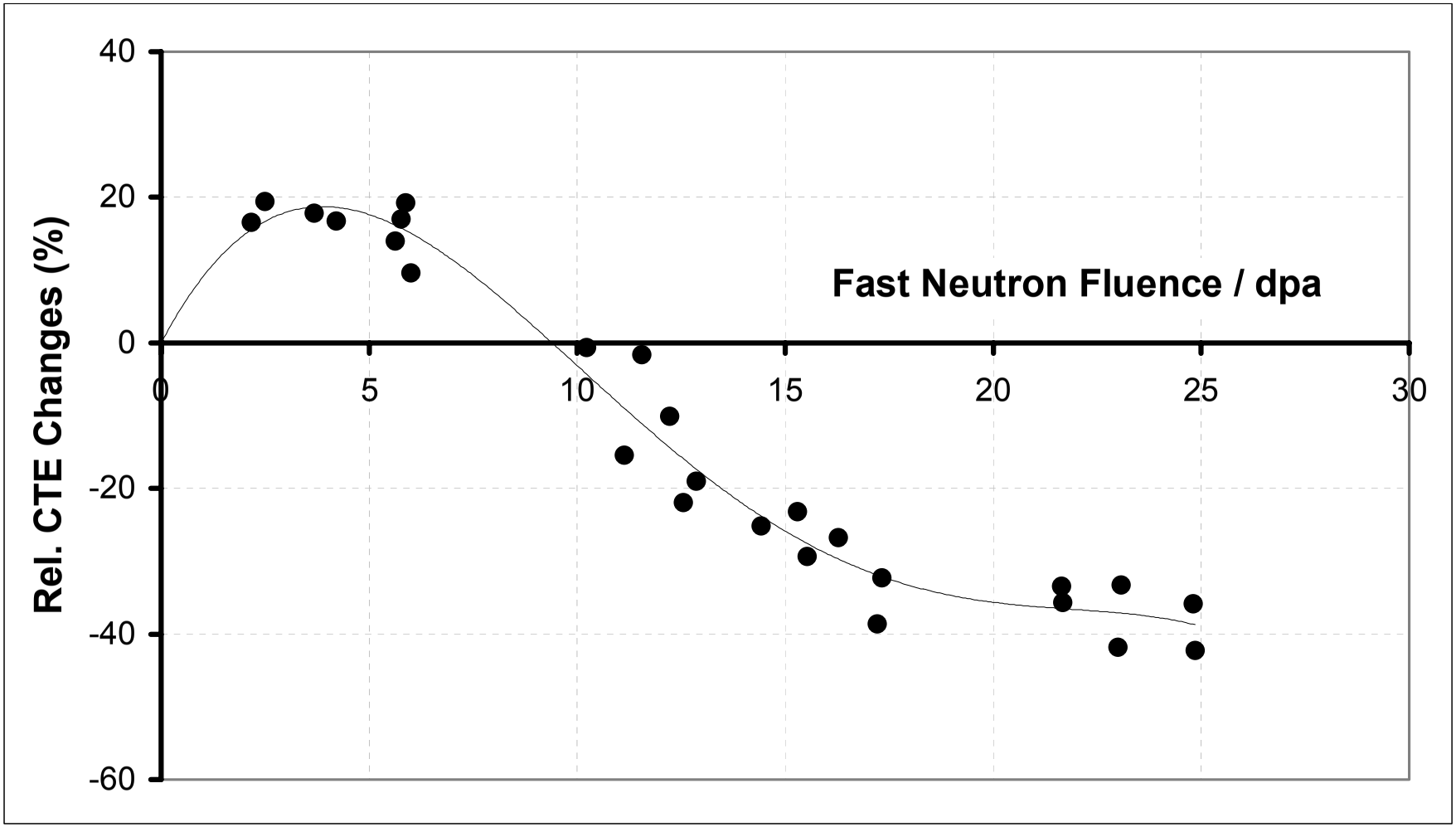

Fig. B19 **ATR-2E** – Relative thermal expansivity (CTE) changes due to fast neutron irradiation.
Irradiation temperature about 600 °C (data from Table B7 and B8)

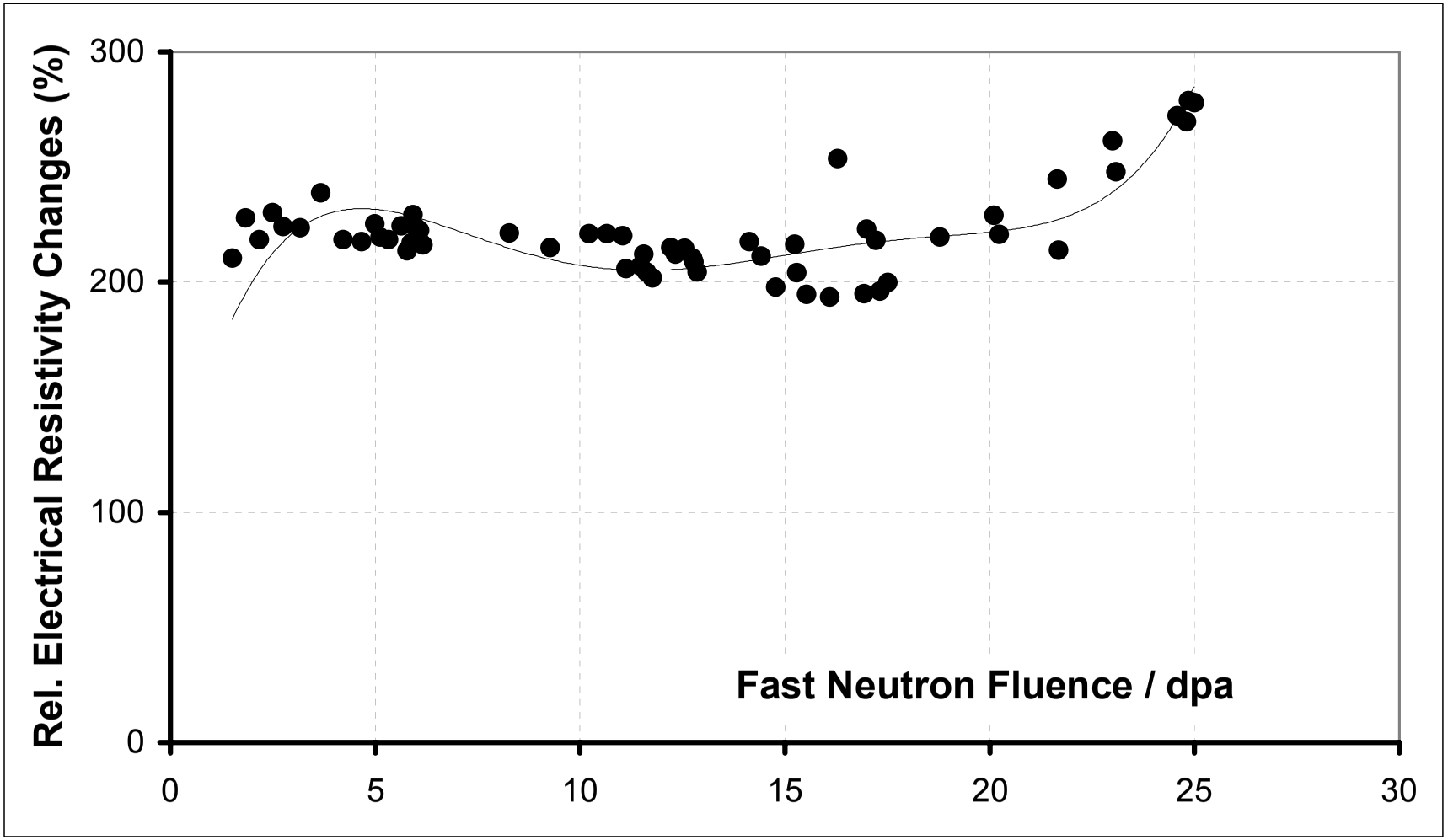

Fig. B20 **ATR-2E** – Relative electrical resistivity changes due to fast neutron irradiation. **Irradiation temperature about 600 °C** (data from Table B7 and B8)

Irradiation Temperature (°C)	Fast Neutron Fluence (dpa)	Rel. Linear Dimensional Changes $\Delta l/l_0$ (%)	Pre-Irrad. Bulk Density (g/cm^3)	Rel. Volume Changes $\Delta V/V_0$ (%)	Young's Modulus E		Electrical Resistivity R		Thermal Expansivity α	
					Pre-Irrad. E_o (GPa)	Rel. Change E/E_o	Pre-Irrad. R_0 ($\Omega \cdot \mu m$)	Rel. Change $\Delta R/R_0$ (%)	Pre-Irrad. α_0 (10^{-6}/K)	Rel. Change $\Delta\alpha/\alpha_0$ (%)
750°	1.76	-0.17				1.65				
750°	2.19	-0.29				1.62				
750°	2.54	-0.32				1.66				
750°	3.36	-0.56				1.59				
750°	3.76	-0.57				1.60				
750°	4.47	-0.77				1.68				
750°	4.69	-0.86				1.67				
750°	7.99	-1.30				1.93				
750°	11.18	-1.57				2.30				
750°	12.19	-1.49				2.32				
750°	12.19	-1.59				2.52				
750°	16.43	-0.62				2.25				
750°	16.75	-0.76				2.30				
750°	17.11	-1.13				2.48				
750°	22.58	1.84				0.93				
750°	22.44	4.32				1.31				

Table B9 ATR-2E – dimensional and dynamic Young's modulus changes due to fast neutron irradiation **parallel to extrusion.**
Irradiation temperature around **750°C**

Irradiation Temperature (°C)	Fast Neutron Fluence (dpa)	Rel. Linear Dimensional Changes $\Delta l/l_0$ (%)	Pre-Irrad. Bulk Density (g/cm^3)	Rel. Volume Changes $\Delta V/V_0$ (%)	Young's Modulus E		Electrical Resistivity R		Thermal Expansivity α	
					Pre-Irrad. E_o (GPa)	Rel. Change E/E_o	Pre-Irrad. R_0 ($\Omega \cdot \mu m$)	Rel. Change $\Delta R/R_0$ (%)	Pre-Irrad. α_0 (10^{-6}/K)	Rel. Change $\Delta\alpha/\alpha_0$ (%)
750°	1.79	-0.13				1.56				
750°	2.26	-0.15				1.57				
750°	2.65	-0.29				1.61				
750°	3.75	-0.43				1.68				
750°	4.11	-0.47				1.67				
750°	4.68	-0.45				1.67				
750°	4.68	-0.47				1.57				
750°	5.11	-0.65				1.66				
750°	5.57	-0.49				1.67				
750°	10.08	-0.82				2.09				
750°	10.26	-0.63				2.18				
750°	13.30	-0.74				2.52				
750°	13.83	-0.31				2.52				
750°	14.64	0.20				2.67				
750°	17.75	0.92				2.03				
750°	18.16	1.86				2.25				
750°	19.72	3.70				1.85				

Table B10 ATR-2E – dimensional and dynamic Young's modulus changes due to fast neutron irradiation **perpendicular to extrusion.** **Irradiation temperature** around **750°C**

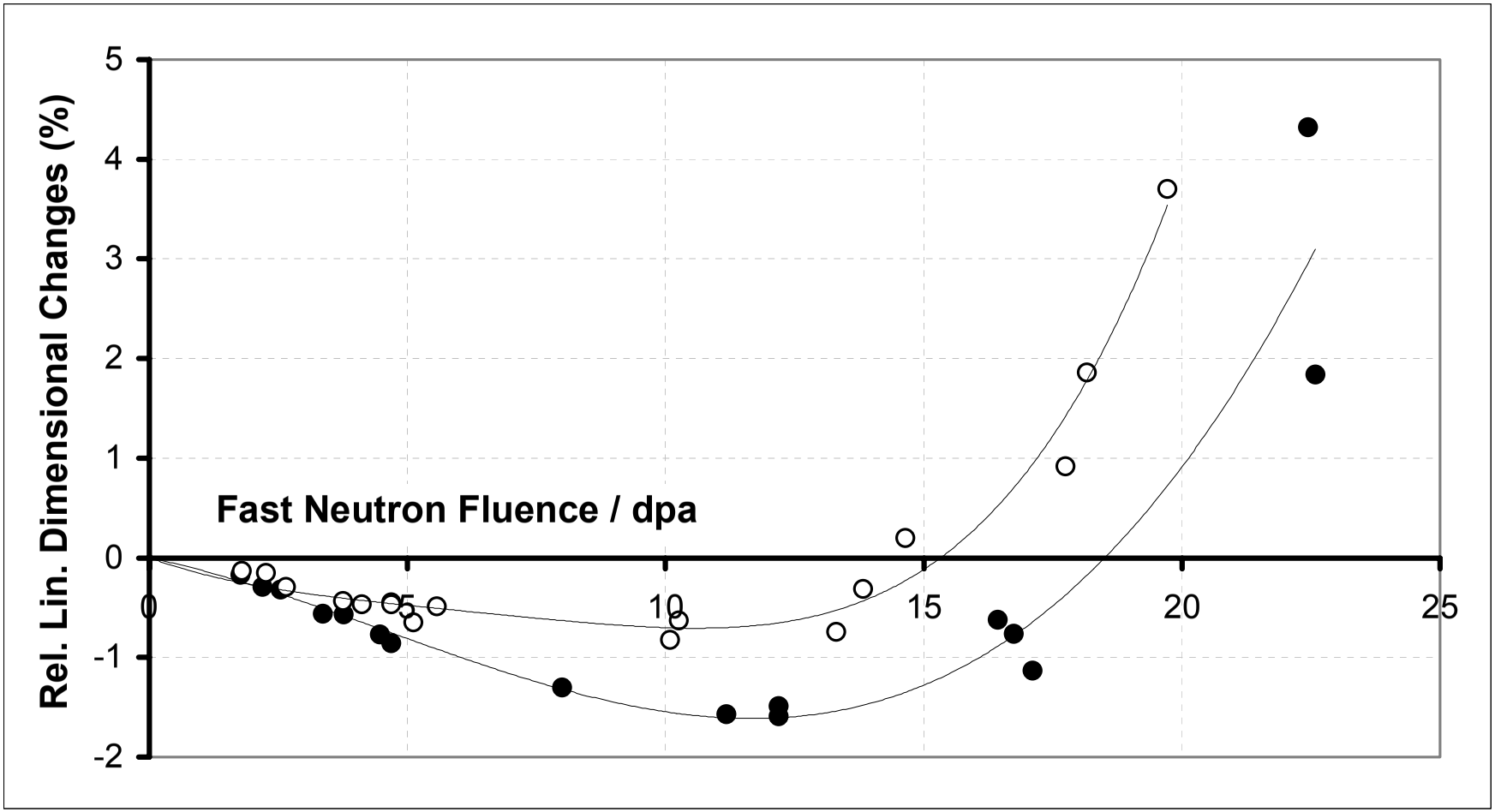

Fig. B21 **ATR-2E** – Linear dimensional changes due to fast neutron irradiation; perpendicular (white circles) and parallel (black circles) to extrusion. **Irradiation temperature about 750 °C** (data from Table B9 and B10)

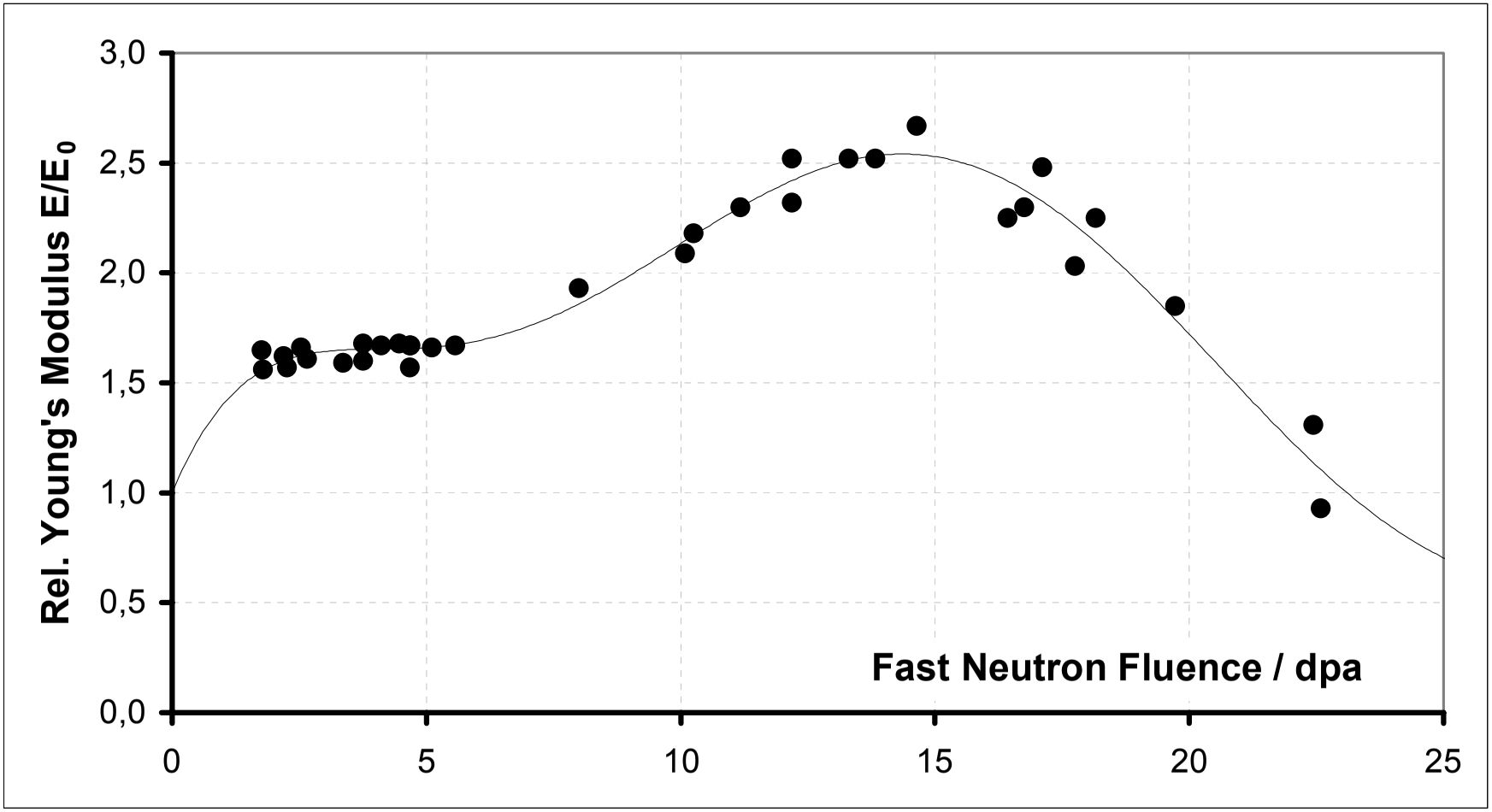

Fig. B22 **ATR-2E** – Relative Young's modulus changes due to fast neutron irradiation.
Irradiation temperature about 750 °C (data from Table B9 and B10)

9. References

[1] R.E. Nightingale, H.H. Yoshikawa, H.H.W. Losty, in: Nightingale (Editor), Nuclear Graphite, Academic Press 1962, Chapter 6 Physical Properties, p.185

[2] T.J. Neubert et al., *Neutron-induced Decomposition of Graphite. I. Fundamentals*, USAEC Report ANL-5472, Argonne National Laboratory, January 1956.

[3] R.E. Nightingale, H.H. Yoshikawa, H.H.W. Losty, in: Nightingale (Editor), Nuclear Graphite, Academic Press 1962, Chapter 6 Physical Properties, p.185

[4] J. W. Helm, Carbon 1966, Vol. 3, pp. 493-501

[5] G. Haag et al., *Results of the Visual In-pile Inspection of the Inner Graphite Reflector of the AVR*, Paper presented at the IAEA Specialists Meeting on Graphite Component Structural Design, Japan Atomic Energy Research Institute, Japan, September 8-11, 1986

[6] Charles L. Mantell, Carbon and Graphite Handbook, 1968, pp. 417-419

[7] W.C. Morgan, W.J. Gray, BNWL-1672 UC-25

[8] S. Wilkening, Various vibration methods for the forming of carbon products, Extended Abstracts 13th Biennial Conf. on Carbon, Irvine, (1977) p. 330.

[9] H. Rosswurm, G. Pietzka, W. Ulsamer, Anisotropie von Formkörpern in Abhängigkeit vom Koks und von den Herstellungsbedingungen, Preprints CARBON ’72, Baden-Baden (1972), p. 403

[10] G. Haag, D. Mindermann, G. Wilhelmi, H. Persicke, W. Ulsamer, Development of reactor graphite, J. Nucl. Mat. **171** (1990) 41-48.

[11] M.F. O’Connor, G. Haag, W.P. Eatherly, C.R. Kennedy, Suitability Tests for Reflector Graphites, Preprints CARBON ’80, Baden-Baden (1980), p. 583.

[12] See 10.

[13] P. Fraipont: Joint Research Centre, Institute for Advanced Materials/Petten Site, Technical Note “D 85, Standard Sample Holder Type 2, 3, 4 and 5 for Intermediate and High Temperature Irradiations of Graphite”, Design and Safety Report P/F1/91/11, August 1991.

[14] P. Fraipont: Joint Research Centre, Institute for Advanced Materials/Petten Site, Technical Note “D 85, Standard Sample Holder Type 1 for 300°C to 450°C Irradiations of Graphite”, Design and Safety Report P/F1/91/9, August 1991.

[15] H. Rother: User manual for WRZ1 (two dimensional heat transfer code), personal communication, unpublished

[16] Baard, J.H., Voorbraak, W.P., “Neutron Metrology in the HFR – Graphite Irradiation D85-54”, ECN-CX--91-032

[17] Freudenreich, W.E., Nolthenius, H.J.: „Neutron Spectrum Unfolding Code SANDP01“, unpublished laboratory note FYS/RASA-87/17 (June 1987).

[18] R. Lölgen, F. Mason, J. Nucl. Mat. 65 (1977), 131-141

[19] L. Binkele, High Temp. – High Press., **4**, 401 (1972)

[20] B.T. Kelly, The thermal conductivity of graphite. Chemistry and Physics of Carbon 5, (1969) 119

[21] G. Haag, "Thermal Conductivity of Graphite Irradiated With Medium and High Neutron Fluences", Proceedings of International Congress on Advances in Nuclear Power Plants (ICAPP’03), Córdoba, Spain, May 4-7, 2003, Paper 3094

[22] D.R. de Halas, in: Nightingale (Editor), Nuclear Graphite, Academic Press 1962, Chapter 7, Theory of Radiation Effects in Graphite, p. 195

[23] J.H.W. Simmons, Radiation Damage in Graphite, Pergamon Press (1965)

[24] B.T. Kelly, Physics of Graphite, Applied Science Publishers (1981)

[25] R.E. Nightingale, in: Nightingale (Editor), Nuclear Graphite, Academic Press 1962, Chapter 6, Structure, p. 120

[26] J.C. Bowman et al., X-Ray and Low Temperature Thermal Conductivity Study of Defects in Graphite, *Conf. Industrial Carbon and Graphite*, *London (1957),* Abstracts pp. 52-59, Society of Chemical Industry, London, 1958.

[27] R.E. Nightingale, H.H. Yoshikawa, H.H.W. Losty, in: Nightingale (Editor), Nuclear Graphite, Academic Press 1962, Chapter 10 Radiation Effects on Electrical and Thermal Properties, p.295

[28] W. Primak. L.H. Fuchs, Fast Neutron Damaging in Nuclear Reactors. I. Radiation Damage Monitoring with the Electrical Conductivity of Graphite, Nucl. Sci. and Eng. 2, 49-56 (1957)

[29] J.E. Brocklehurst, R.G. Brown, Constant stress irradiation creep experiments on graphite in BR-2, Carbon **7** (1969) 487

[30] B.T. Kelly, J.E. Brocklehurst, Analysis of irradiation creep in reactor graphite. Proc. 3rd Conf. On Industrial Carbon and Graphite, S.C.I. London (1971) 363.

[31] R.E. Nightingale, in: Nightingale (Editor), Nuclear Graphite, Academic Press 1962, Chapter 5, Structure, p. 88

[32] R.E. Nightingale, in: Nightingale (Editor), Nuclear Graphite, Academic Press 1962, Chapter 5, Structure, p. 89

[33] R.E. Nightingale, H.H. Yoshikawa, H.H.W. Losty, in: Nightingale (Editor), Nuclear Graphite, Academic Press 1962, Chapter 10 Radiation Effects on Electrical and Thermal Properties

[34] B.T. Kelly, Irradiation Damage in Graphite due to Fast Neutrons in Fission and Fusion Systems, edited and completed by B.J. Marsden and K. Hall, to be published

[35] W.P. Eatherly, private communication

[36] B.T. Kelly, J.E. Brocklehurst, UKAEA Reactor Group Studies of Irradiation-Induced Creep in Graphite, J. Nucl. Mat. **65** (1977) 79-85

[37] M.R. Cundy, G. Kleist, D. Mindermann, Irradiation induced creep in graphite with respect to the flux effect and the high fluence behaviour. Paper to the International Conf. on Carbon and Graphite 'CARBONE 84', Bordeaux, France, July 1984.

[38] See 19.

[39] B.S. Gray, et al. The irradiation-induced plasticity of graphite under constant stress. TRG Report 1071(C). Carbon **5**, 173 (1967)

[40] See 36

[41] B.T. Kelly, A.J.E. Foreman, The theory of irradiation creep in reactor graphite – the dislocation pinning-unpinning model. Carbon **12**, 151 (1974)

[42] M.R. Cundy, G. Kleist, M.F. O'Connor, G. Pott, Irradiation Creep in Graphite at 500°C, Proc. 5th London International Carbon and Graphite Conference, Vol. II, Soc. of Chem. Industry, 1978, p. 959

[43] See 36.

[44] See 41.

[45] See 37.

[46] G. Haag, Irradiation-Induced Creep in Graphite and Use of Creep Data in Reactor Design, 1st International Nuclear Graphite Specialists Meeting (INGSM), Oak Ridge, Tenn., U.S.A., September 2000.

[47] B.T. Kelly, J.E. Brocklehurst, UKAEA Reactor Group Studies of Irradiation-Induced Creep in Graphite, J. Nucl. Mat. **65** (1977) 79-85

[48] See 37.

[49] See 37.

[50] H.-K. Hinssen, W. Katscher, R. Moormann: Kinetik der Graphit/Sauerstoff-Reaktion im Porendiffusionsbereich; Teil 1: Matrixmaterialien A3-3 und A3-27, Berichte der Kernforschungsanlage Jülich, Jül – 1875, November 1983

[51] H.-K. Hinssen, W. Katscher, R. Moormann: Kinetik der Graphit/Sauerstoff-Reaktion im Porendiffusionsbereich; Teil 2: Graphite V483T, ASR-1RS, ASR-1RG und ATR-2E, Berichte der Kernforschungsanlage Jülich, Jül – 2052, April 1986

Forschungszentrum Jülich
in der Helmholtz-Gemeinschaft

Jül-4183
Oktober 2005
ISSN 0944-2952